

SHAPE COEXISTENCE IN THE NEUTRON-RICH NICKEL ISOTOPES NEAR $N = 40$

By

Christopher John Prokop

A DISSERTATION

Submitted to
Michigan State University
in partial fulfillment of the requirements
for the degree of

Chemistry - Doctor of Philosophy

2016

ABSTRACT

SHAPE COEXISTENCE IN THE NEUTRON-RICH NICKEL ISOTOPES NEAR $N = 40$

By

Christopher John Prokop

The evolution of nuclear structure with changing proton and neutron number is of common interest across the nuclear science community. Within the shell model, protons and neutrons occupy collections of single-particle states separated by relatively large energy gaps, giving rise to the so called “magic” numbers. Analogous to the noble gases in chemistry, which have enhanced chemical inertness, unstable nuclei possessing closed-shell nucleon configurations are generally spherical in shape and exhibit increased stability. Closed shell nuclei exhibit larger nucleon separation energies, and when radioactive they have longer half-lives. The energy of the single-particle states also migrate with changing numbers of protons and neutrons due to strong proton-neutron residual interactions. The migration of single-particle energies leads to shell evolution and can drive nuclei from spherical to deformed shapes.

Within a single nucleus, the redistribution of nucleons can give rise to intruder states possessing different shapes than that of the ground state configuration. These intruder states owe their existence to the delicate balance between the cost of exciting nucleons into the higher-lying single-particle states and the stabilizing effect of residual proton-neutron interactions. If the energy of the intruder state descends far enough, states with nucleon configurations associated with different nuclear shapes can coexist at similar excitation energy in a phenomenon called shape coexistence. In even-even nuclei, the hallmark of shape coexistence is multiple low-lying 0^+ states.

Recently, the Ni isotopic chain has been the focus of many experimental and theoretical

investigations studying the evolution of nuclear structure away from stability. In particular, ^{68}Ni has elicited significant attention due to the presence of both the $Z = 28$ proton shell closure and the $N = 40$ neutron subshell closure. In ^{68}Ni , three 0^+ states, with energies of 0, 1603, and 2511 keV have been identified. Advanced shell-model calculations, utilizing the full $fp_{g_{9/2}}d_{5/2}$ model space for both protons and neutrons, predict a spherical 0_1^+ ground state, oblate-deformed 0_2^+ state, and prolate-deformed 0_3^+ state. The configuration of the oblate-deformed 0_2^+ state is predicted to be predominately the excitation of two neutrons across $N = 40$ into the $0\nu g_{9/2}$ orbit, while the the prolate-deformed 0_3^+ state is expected to contain multiple particle-hole excitations dominated by the excitation of two protons across $Z = 28$ into the $0\pi f_{5/2}$ orbit.

Transitioning to ^{70}Ni , with the addition of only two neutrons, the same shell-model calculations predict the prolate deformed 0^+ state to drop precipitously from the measured energy of 2511 keV in ^{68}Ni down to a predicted energy of 1525 keV in ^{70}Ni . This is explained by the reduction of the energy spacing between the $0\pi f_{7/2}$ and $0\pi f_{5/2}$ single-particle states due to the strengthening of the attractive $0\nu g_{9/2} - 0\pi f_{5/2}$ and repulsive $0\nu g_{9/2} - 0\pi f_{7/2}$ monopole interactions of the tensor force with increased occupancy of the $0\nu g_{9/2}$ orbital.

In order to validate these predictions and experimentally investigate shape coexistence in $^{68,70}\text{Ni}$, two complimentary experiments were performed at the National Superconducting Cyclotron Laboratory. As a result of these experiments, a new (0_2^+) state was discovered at 1567-keV in ^{70}Ni , in good agreement with theoretical predictions. Transition probabilities deduced from new lifetime and branching ratio measurements of 0^+ states in $^{68,70}\text{Ni}$ provide stringent tests for competing theoretical descriptions. These results constitute the first quantitative descriptions of these 0^+ states and support the predictions of shape coexistence in $^{68,70}\text{Ni}$.

In loving memory of my father Harold D. Prokop

ACKNOWLEDGMENTS

The list of people that have been instrumental to my success in graduate school, presented herein, is long and without a doubt not exhaustive so I would like to begin by thanking everyone as a whole for their contributions, both large and small, that made this dissertation possible.

First, I would like to thank my advisor Sean Liddick for your continuous support throughout my tenure as a graduate student. The guidance and training you have given me has been instrumental for preparing my for road ahead. Your willingness to answer the countless, perhaps even some foolish, questions during the many times I stopped by your office has been greatly appreciated. Thank you for being approachable and always willing to help.

Before moving onto anyone else I would like to thank my father Harold. So much of who I have become is directly because of you and no amount of words can express how much I miss you. There are countless life skills I learned working with you on enumerable household projects. I attribute a lot of my problem solving ability to your teaching. Outside of work my abilities as a competent mechanic and carpenter are a direct result of the time I spent with you. Despite being surrounded by very intelligent people on a daily basis during graduate school I always regarded you as one of the most intelligent people I know. Though I know you were always proud of me, I cant help but wish you were here to see me graduate.

Next I want to thank my mom Carla who is without a doubt the most caring and compassionate person I know. Any time I have a problem, whether personal or professional, I know I can turn to you for help. Words cannot express how much I appreciate you. Losing my father, one day after my 27th birthday and just two months before my thesis experiment, was the hardest thing I have ever experienced and makes all of graduate school (including

writing this dissertation) look like a walk in the park on a warm summer day. I cant imagine what that was like for you mom but somehow you remained positive and supportive. You belong in a special category among people mom and I owe you an infinite debt of gratitude.

I cant continue without thanking my little sister Lindsey. You are certainly the funniest person I know. Whenever I am stressed, tired, depressed, or a combination thereof I can talk to you and somehow feel better almost instantly. People always refer to us as "twins eight years apart" so its no surprise I am very proud of you. I know loosing dad was hard on you as well so I appreciate you helping mom around the house and for helping me with projects when I come home. I know that you and mom are always in my corner.

Next I want to thank my wonderful girlfriend Alex. I love you and I appreciate your support and companionship throughout our relationship. By virtue of coming into my life in my third year of graduate school you have had the fine privilege of dealing with me during the more stressful portion of it and I thank you for going through it with me. I appreciate the times you kept me company in my office some of those days when I was working late. Though I am sure there were more interesting or exciting things you could have done, I am glad you spent the time with me. You make my life better and I look forward to our future together.

While graduate school tends to minimize free time for activities such as video games, I want to say thanks to my cousins Tyler and Trevor for always being there when the opportunity presents itself. Playing Call Of Duty, Grand Theft Auto, and Battlefield with you guys has always been stress relief in its finest form. I also want to thank Juan Manfredi for being an excellent friend, colleague, and roommate throughout graduate school.

I want to thank Ben Crider for being my colleague and friend. With each of us responsible for running one of the complimentary experiments discussed in this dissertation there

were many long hours of collaborative work. I appreciate your assistance obtaining the results presented herein and your and companionship throughout. I also want to thank the remaining members of the beta-decay group and all others who sat shift on either experiment. Science is certainly a collaborative effort and without your help these results would not be possible.

I want to thank Robert Janssens and Bill Walters for their contributions to manuscript drafts and for the letters of recommendation you wrote for me when I was searching for postdoc positions. I also want to thank Alex Brown and Morten Hjorth-Jenson for providing me with theory calculations and for helping me understand the underlying nuclear physics concepts behind them.

Looking back on what lead me to graduate school I want to thank my undergraduate research advisor Andrew Roberts. It was working with him that gave me my first experience working in nuclear science and the desire to pursue a career in the field. I also want to thank Trent Vorlicek for suggesting I attend the department of energy nuclear summer school. It was there that I met Paul Mantica and it was through interacting with him I chose to come to Michigan State. Paul also deserves a second thank you for serving as the second reader on my guidance committee. I would like to thank the other two members of my committee, Dave Morrissey and Remco Zegers, for their service.

Even before college I was inspired by some wonderful educators. First and foremost I thank Mark Franta for being an excellent physics teacher and for providing me the inspiration to major in physics. I also want to thank Roger Schoenfelder, Tom Plocker, and Cindy Allevan for there outstanding teaching in Chemistry, Math, and English, respectively.

Last but not least I want to thank all the people that perform the day-to-day operations at the lab. I thank the beam physicists, cyclotron operators, design group, machinists, office

staff, and all others that contribute to the successful operation of the lab. Without these people none of the science would be possible. There is certainly something to be proud of being part of a world class facility such as the NSCL and its been a wonderful experience working with you all.

TABLE OF CONTENTS

LIST OF TABLES	xii
LIST OF FIGURES	xv
Chapter 1 Introduction	1
1.1 Nuclear Shell Structure	1
1.2 Nuclear Shell Evolution	4
1.3 Nuclear Shape Coexistence	6
1.4 Nuclear Structure Near $N = 40$ and $Z=28$	7
1.5 Goals of the Experiment	11
Chapter 2 Nuclear Decay Modes	12
2.1 β Decay	12
2.1.1 β -Delayed Particle Emission	18
2.2 γ Decay	19
2.3 Internal Conversion	22
2.4 Internal Pair Formation	24
2.5 $E0$ Transitions	24
Chapter 3 Experimental Description	28
3.1 Isotope Production, Identification, and Delivery at the National Superconducting Cyclotron Laboratory (NSCL)	29
3.2 NSCL e14039 Experimental Setup	31
3.3 NSCL e14057 Experimental Setup	33
3.4 NSCL Digital Data Acquisition System (DDAS)	36
3.4.1 Triggering	36
3.4.2 Energy Extraction	38
3.4.3 Fast Timing Capabilities of DDAS	39
3.5 Planar Germanium Double-Sided Strip Detector (GeDSSD)	42
3.5.1 Instrumentation and Triggering Conditions	42
3.5.2 Event Localization and Correlation	43
3.5.3 Crosstalk Calibration	46
3.5.4 Energy Calibration	50
3.5.5 Pulse Shape Analysis	52
3.6 Segmented Plastic Scintillator and Position-Sensitive Photo-Multiplier Tube (PSPMT)	64
3.6.1 Instrumentation and Triggering Conditions	64
3.6.2 Event Localization and Correlation	65
3.6.3 Pulse Shape Analysis	70
3.7 Segmented Germanium Array (SeGA)	73

3.7.1	SeGA Instrumentation and Triggering Conditions	73
3.7.2	SeGA Energy Calibrations	74
3.7.3	SeGA Absolute Efficiency Calibrations	75
3.8	Lanthanum Bromide Array	81
3.8.1	Instrumentation and Triggering Conditions	81
3.8.2	LaBr ₃ Energy Calibrations	81
3.8.3	Absolute LaBr ₃ Efficiency Calibrations	83
3.9	Level Lifetime Measurement Techniques	84
3.9.1	Time Walk Corrections	84
3.9.2	Depth of Interaction Corrections	88
3.9.3	New Analysis Method for $\beta\gamma$ Lifetime Techniques	92
3.9.4	Demonstration of the Technique on a Prompt Transition	94
3.9.5	Benchmarking the Technique on a Two Excited States with Known Lifetimes	97
Chapter 4 Experimental Results		104
4.1	Decay of ⁶⁸ Co	104
4.1.1	Decay of the Long-Lived ⁶⁸ Co Isomer	104
4.1.2	Half-Life Measurements	130
4.1.2.1	Assessing Spurious Correlations	130
4.1.2.2	“Exclusion Technique” for Correlations	131
4.1.2.3	Half-Life of ⁶⁸ Fe	135
4.1.2.4	Half-Life of the Long-Lived ⁶⁸ Co Isomer	140
4.1.2.5	$A = 68$ Decay Curves	142
4.1.2.6	Half-Life of the 0_2^+ state in ⁶⁸ Ni	146
4.1.2.7	Half-Life of the 0_3^+ state in ⁶⁸ Ni	149
4.2	Decay of ⁷⁰ Co	153
4.2.1	β -Decaying Isomers in ⁷⁰ Co	157
4.2.2	$A = 70$ Decay Curves	165
4.2.3	⁷⁰ Co Isomer Deconvolution	167
4.2.4	Decay of the Short-Lived ⁷⁰ Co Isomer	176
4.2.5	Decay of the Long-Lived ⁷⁰ Co Isomer	180
4.2.6	Half-Life of the (0_2^+) state in ⁷⁰ Ni	189
Chapter 5 Discussion and Outlook		196
5.1	Shape Coexistence in ^{68,70} Ni	196
5.2	Analysis of β -Decay Strength and Intensity Distributions in ^{68,70} Ni	200
5.2.1	Short-Lived, High-Spin, ⁷⁰ Co Isomer	202
5.2.2	Long-Lived, Low-Spin, ⁷⁰ Co Isomer	204
5.2.3	Long-Lived, Low-Spin, ⁶⁸ Co Isomer	207
5.3	Outlook	211

APPENDICES	213
Appendix A Identification of Additional Peaks Observed in Pulse Shape Analysis Not Affiliated With the $0_2^+ \rightarrow 0_1^+$ Transition in ^{68}Ni	214
Appendix B $\beta\gamma\gamma$ and $\beta\gamma\gamma$ -double-pulse Coincidences Observed Following the β - Decay of the Long-Lived, Low-Spin, ^{68}Co Isomer	219
Appendix C $\beta\gamma\gamma$ Coincidences Observed Following the β -Decay of the Short-Lived, High-Spin, ^{70}Co Isomer.	245
Appendix D $\beta\gamma\gamma$ Coincidences Observed Following the β -Decay of the Long-Lived, Low-Spin, ^{70}Co Isomer.	250
BIBLIOGRAPHY	257

LIST OF TABLES

Table 2.1:	β -decay selection rules, adapted from Ref. [25]	14
Table 2.2:	Classification of β -decay transitions and associated $\log_{10}(f_0t)$ values, adapted from Ref. [24].	17
Table 2.3:	Selection rules and electromagnetic transition rates, assuming a single-particle transition from an initial state to a final state, for the first four multipolarities of electric and magnetic transitions. λ is the multipolarity of the transition, $\Delta\pi$ is the change in parity between the initial and final states, E_γ is the γ -ray energy in MeV, and A is the mass number of the nucleus. [24].	22
Table 3.1:	Number of ions of each isotope implanted into the GeDSSD crystal over the nine days of beamtime during e14039.	33
Table 3.2:	Number of ions of each isotope implanted into the segmented plastic scintillator over the six days of beamtime during e14057.	35
Table 3.3:	Ratios of induced signals in the GeDSSD by strip n on adjacent strips $(n + 1)$ or $(n - 1)$. When multiplied by the signal amplitude of strip n these values correct the amplitude of the signal present on strips $n + 1$ or $n - 1$	48
Table 3.4:	Summing corrections used for absolute efficiency calibration with SRM source. Total efficiencies at a given energy E are denoted as $[E]$ while photo-peak efficiencies are denoted as $\{E\}$. The corrected efficiency is obtained by dividing the experimental efficiency by the value of the summing correction.	77
Table 3.5:	Values used in Eq. 3.10 to parameterize the γ -ray detection efficiency of SeGA for e14039 and 14057.	80
Table 4.1:	Energies and absolute intensities of the γ -ray transitions placed in ^{68}Ni following the β decay of the long-lived, low-spin, ^{68}Co isomer selectively populated by the β decay of ^{68}Fe . The energies of the initial and final states for each transition are also listed.	112
Table 4.2:	Summary of observed γ -ray coincidences following the β decay of the long-lived, low-spin, ^{68}Co isomer populated by the β decay of ^{68}Fe	116

Table 4.3:	Energies and absolute intensities of γ -ray transitions placed ^{68}Ni , detected in coincidence with the $0_2^+ \rightarrow 0_1^+$ $E0$ transition, following the β decay of the long-lived, low-spin, ^{68}Co isomer. The energies of the initial and final states between which each transition occurs are also listed.	123
Table 4.4:	Energies and relative intensities ($I_\gamma^{1139.2} = 100\%$) of unplaced γ -ray transitions coincident with the $0_2^+ \rightarrow 0_1^+$ $E0$ transition, following the β decay of the long-lived, low-spin, ^{68}Co isomer.	124
Table 4.5:	Summary of $\beta\gamma\gamma$ -double-pulse coincidences in ^{68}Ni following the decay of the long-lived, low-spin, ^{68}Co isomer.	124
Table 4.6:	Summary of unplaced γ rays potentially affiliated with the decay of the long-lived, low-spin, ^{68}Co isomer.	129
Table 4.7:	Decay curve integration results and correction factors for ^{68}Ni in each experiment. The “corrected” number of decays is obtained by multiplying the integrated number of counts by the spurious correlation and exclusion technique correlation factors. The corrected number of decays is then directly comparable to the non-exclusion analysis β -delayed γ -ray statistics.	146
Table 4.8:	Decay curve fit results and correction factors for ^{70}Ni in e14039. The “corrected” number of decays is obtained by multiplying the integrated number of counts by the spurious correlation and exclusion technique correlation factors. The corrected number of decays is then directly comparable to the non-exclusion analysis β -delayed γ -ray statistics.	167
Table 4.9:	Energies and absolute intensities of the γ -ray transitions identified in ^{70}Ni following the β decay of the short-lived, high-spin, ^{70}Co isomer. The energies of the initial and final states between which each transition occurs are also listed.	177
Table 4.10:	Summary of γ -ray coincidences observed following the decay of the short-lived, high-spin, ^{70}Co isomer.	178
Table 4.11:	Energies and absolute intensities of the γ -ray transitions identified in ^{70}Ni following the β decay of the long-lived, low-spin, ^{70}Co isomer. The energies of the initial and final states between which each transition occurs are also listed.	181

Table 4.12:	Summary of γ -ray coincidences observed following the decay of the long-lived, low-spin, ^{70}Co isomer.	188
Table 4.13:	Summary of unplaced γ rays potentially affiliated with the decay of the long-lived, low-spin, ^{70}Co isomer.	189
Table 5.1:	Half-lives, branching ratios, and either absolute $B(E2)$ in $e^2\text{fm}^4$ or $\rho^2(E0)$, depending on the nature of the transition.	197

LIST OF FIGURES

Figure 1.1:	(a) First ionization energy plotted as a function of atomic number. The noble-gas elements and their atomic numbers, corresponding to closed electron shell configurations, are labeled. All ionization energies were taken from Ref. [2]. (b) Differential neutron separation energies as a function of neutron number for a variety of even-even nuclei adapted from Ref. [3]. Nuclei along the same isotopic chains are connected with lines.	2
Figure 1.2:	Schematic representation of the effect of the monopole component of the tensor force.	4
Figure 1.3:	Shell evolution along the Hg isotopic chain	6
Figure 1.4:	Systematics of (a) 2_1^+ state energies and (b) $B(E2; 0_1^+ \rightarrow 2_1^+)$ values as a function of neutron number for the Cr, Fe, and Ni isotopes. Data taken from Ref. [13].	8
Figure 3.1:	Schematic representation of the Coupled Cyclotron Facility (CCF) [36] and A1900 fragment separator [37] at NSCL	29
Figure 3.2:	Normalized implantation depth distributions for ^{68}Fe and ^{70}Co ions deposited inside the GeDSSD crystal during e14039.	31
Figure 3.3:	Particle identification plot for ions deposited in the GeDSSD crystal during e14039. The data shown were obtained from the energy loss information provided by the first PIN detector and the TOF measured between the extended focal plane scintillator in the A1900 and the first PIN detector. As a condition on the plot, the GeDSSD had to record coincident implant energy deposition in at least one front and one back strip.	32
Figure 3.4:	Normalized implantation depth distributions for ^{68}Fe and ^{70}Co ions deposited inside the segmented plastic scintillator during e14057.	33
Figure 3.5:	Particle identification plot for ions deposited in the segmented plastic scintillator during e14057. The data shown were obtained from the energy loss information provided by the first PIN detector and the TOF measured between the scintillator at the dispersive image of the A1900 and the first PIN detector. As a condition on the plot, the segmented plastic scintillator had to record implant energy deposition.	34

Figure 3.6:	Example of DDAS digital filtering algorithms. A sample detector signal acquired from the planar GeDSSD by a 14-bit 250 MSPS is shown in black. The response of the DDAS trigger-filter algorithm is shown in dark red along with the user-defined trigger filter threshold illustrated as a black dashed line. Shown in dark blue is the response of the DDAS energy filter algorithm. Key points in time related to triggering and energy extraction are labeled.	37
Figure 3.7:	Example of the DDAS digital constant fraction discriminator (CFD) algorithm. A sample detector signal acquired from a LaBr ₃ detector by a 12-bit 500 MSPS is shown in black. The response of the DDAS CFD algorithm is shown in red along with the user-defined CFD threshold illustrated as a black dashed line. Key points in time related to precision time extraction are labeled.	40
Figure 3.8:	DDAS Electronics time resolution for LaBr ₃ detector type signals, generated by a Agilent 33522A arbitrary waveform generator, as a function of input signal amplitude relative to the dynamic range of the ADC. For signal amplitudes occupying >10 % of the ADC dynamic range the electronics contribution to the detector system time resolution is essentially negligible.	41
Figure 3.9:	Two-dimensional histogram showing the maximum low-gain front channel vs. the maximum low-gain back channel for all low-gain events in e14039. Projections onto the front- and back-strip axes are shown to the right and above the two-dimensional histogram, respectively. There is a clear region of missing events due to charge trapping as a result of crystal damage.	44
Figure 3.10:	Two-dimensional histogram showing the maximum high-gain front channel vs. the maximum high-gain back channel for all high-gain events in e14039. Projections onto the front- and back-strip axes are shown to the right and above the two-dimensional histogram, respectively. The region of missing events due to charge trapping as a result of crystal damage is less evident due to the fact that the electrons and γ rays can travel outside the localized damaged region and can deposit energy across the depth of the detector.	45
Figure 3.11:	Representative crosstalk example for the GeDSSD showing (b) a full energy deposition of a 662-keV γ ray in strip 11. Panels (a) and (c) show induced signals in strips 10 and 12 respectively. These induced signals yield low-energy peaks in the GeDSSD strip energy spectra and must be calibrated out.	46

Figure 3.12:	Representative sample of crosstalk calibrations using strip 10 on the back of the GeDSSD. Panels (a) and (b) show the ratio of the signal induced on strips 9 and 11, respectively, by a signal present on strip 10.	47
Figure 3.13:	Results of the crosstalk calibration for a representative strip of the back of the GeDSSD. The uncorrected and corrected spectra for ^{137}Cs are shown in (a) and (b), respectively. For each spectrum an inset expands the low energy region and demonstrates the existence and subsequent removal of the crosstalk induced peaks.	49
Figure 3.14:	Uncalibrated, crosstalk corrected, energy spectra for all 16 back strips of the GeDSSD for a ^{137}Cs source. Strips 4 through 9 clearly exhibit multiple peaks which result from differences in charge collection along the damaged regions of those strips. Energies were obtained from the DDAS digital filter.	50
Figure 3.15:	Energy spectra of GeDSSD back strip 7 taken with a ^{137}Cs source and histogrammed by interaction location from the front of the GeDSSD. The black, green, cyan, magenta, red, and blue spectra correspond to positions along the length of back strip 7 based on the coincident signal in front strips 1, 4, 7, 10, 13, and 16, respectively. The location of the 662-keV photopeak is identical for strips 1, 13, and 16 but is lower in energy for strip 4. Events occurring in back strip 7 localized to strips 7 and 10 on the front do not display a photopeak.	51
Figure 3.16:	Calibrated, crosstalk corrected, energy spectra for all 16 back strips of the GeDSSD for a ^{137}Cs source.	52
Figure 3.17:	Selected level scheme for ^{68}Ni showing the first two levels and the $E0$ transition that connects them.	53
Figure 3.18:	Example double-pulse signal recorded in the GeDSSD during e14039.	53
Figure 3.19:	Response of the trigger filter algorithm used for transient rejection in the analysis to (a) large-amplitude single pulse, (b) low-amplitude single pulse, (c) negative transient, and (d) positive transient GeDSSD signals. Detector signals are shown in black while the trigger filter responses are shown in red. Trigger filter responses have been reduced by a factor of ten and the baseline of the signal has been added.	55
Figure 3.20:	Sample response of the GeDSSD to a single event recorded using a ^{137}Cs source.	56

Figure 3.21:	Distribution of χ^2 divided by signal amplitude (χ_n^2) for the fit of high-gain GeDSSD signals with a single detector pulse. All fits above the red dashed line are fit with the linear combination of two single detector pulses while all fits below the red solid line are considered good single-pulse events.	56
Figure 3.22:	Single-pulse fit results for a variety of different signal types in the GeDSSD. (a) Good fit of a single pulse by a single-pulse fit. (b) Fit of a transient with a single pulse. (c) Fit of a low amplitude signal with a single-pulse fit. (d) Fit of a double-pulse event with a single pulse. Detector signals are shown in black while the fits are shown in red. The χ_n^2 is labeled on each fit.	57
Figure 3.23:	Energy spectrum obtained from the fit of GeDSSD signals by a single template detector signal where $\chi_n^2 < 250$. Most of the counts are from the continuous electron energy distributions from β decay and from Compton-scattered γ rays. The peak at 92.6-keV is from the decay of the 93.3-keV $1/2^-$ state in ^{67}Zn and 141.4-keV transition comes from the decay of the 242.6-keV isomeric state in ^{70}Cu . The 185.0-keV, 239.2-keV, and 352.1-keV are room background lines from ^{226}Ra , ^{212}Pb , and ^{214}Pb , respectively.	58
Figure 3.24:	Plot of double-pulse χ_n^2 obtained from the fits of GeDSSD signals using a linear combination of two single detector pulses.	59
Figure 3.25:	Plot of χ_n^2 vs. energy of the second pulse for the GeDSSD obtained from the double-pulse fitting method.	60
Figure 3.26:	Panels (a) through (c) display GeDSSD signals, shown in black, with the double-pulse fit, shown in red, overlaid for three signal types that fail the double-pulse fit but pass the χ_n^2 test. The values obtained from the various χ^2 metrics used for this analysis, described in the text, are labeled on each panel. One or more of the additional χ^2 cuts reject each signal in (a) through (c). A good double-pulse fit is shown in (d) with the same set of χ^2 metrics as (a) through (c). The fit in (d) passes all metrics. In all panels the signals are shown in black while the best double-pulse fit to each signal is shown in red.	60

Figure 3.27:	(a) Distribution of χ_{nT}^2 values. (b) Distribution of χ_{nLE}^2 values. (c) Distribution of χ_{nLEL}^2 values. The red vertical lines in (a) through (c) represent the upper limit of acceptability for each respective χ^2 value, with acceptable values being below the red line in each case. (d) Plot of the ratio (single-pulse fit / double-pulse fit) of χ_n^2 vs. energy of the second pulse obtained from the double-pulse fitting method. Values below the red horizontal line are acceptable double-pulse events.	61
Figure 3.28:	Energy spectrum displaying the energy of the (a) first and (b) second rise of the double-pulse signals. The energies were obtained from the amplitudes of the constituent pulses of double-pulse fits satisfying the χ^2 criteria, and were calibrated using the techniques described in Section 3.5.4.	62
Figure 3.29:	Plot of the energy of the second rise of the double pulses on the x axis for each back strip of the GeDSSD on the y axis.	63
Figure 3.30:	Response of the PSPMT to a single ion implantation event in the segmented plastic scintillator. Each box shows the digitized detector signal from a pixel of the PSPMT. The height of each box is 16384 ADC units (1 V full scale range) and the width is 500 ns	66
Figure 3.31:	Two-dimensional histogram showing the active row vs. active column in the PSPMT, determined in the center of gravity algorithm, for all implantation events recorded in e14057. Projections onto the active-row and active-column axes are shown to the right and above the two-dimensional histogram, respectively.	68
Figure 3.32:	Two-dimensional histogram showing the active row vs. active column in the PSPMT, determined in the center of gravity algorithm, for all decay events recorded in e14057. Projections onto the active-row and active-column axes are shown to the right and above the two-dimensional histogram, respectively.	69
Figure 3.33:	(a) Sample double-pulse event recorded during e14057. (b) Same double-pulse event as in (a) shown in black with an overlay of the scaled trigger filter algorithm shown in red. The zero crossing points of the trigger filter algorithm are used to identify subsequent triggers and extract timing information. (c) Overlay of the dynamic threshold, shown in green, discussed in the text. (d) Scaled response of the energy filter algorithm used to extract the energy of each pulse.	70

Figure 3.34:	Creation of a “dynamic” threshold to mitigate subsequent triggering from the ringing of the scintillator during the double-pulse search. The red line is the threshold and all events below threshold are considered as ringing events while events above are from potential double-pulse events in the PSPMT.	71
Figure 3.35:	Energy spectrum displaying the energy of the second constituent pulse of the double-pulse signals recorded in e14057.	72
Figure 3.36:	SeGA energy calibration residuals for each of the 16 individual detectors from a representative run taken during experiment e14039.	74
Figure 3.37:	(a) SeGA energy calibration residuals for all 16 detectors combined over the same representative run used in Fig. 3.36. (b) SeGA energy calibration residuals for all 16 detectors combined for all runs over the duration of e14039.	75
Figure 3.38:	Efficiency ratios (Simulation/Experiment) for γ rays of the SRM source with SeGA in the “beta-SeGA” configuration.	77
Figure 3.39:	Efficiency ratios (Simulation/Experiment) for γ rays of the SRM source placed downstream of the planar GeDSSD with SeGA in the final e14039 experimental configuration.	78
Figure 3.40:	Efficiency ratios (Simulation/Experiment) for γ rays of the SRM source placed upstream of the segmented plastic scintillator with SeGA in the final e14057 experimental configuration.	79
Figure 3.41:	Simulated SeGA γ -ray detection efficiencies for $A=68$ nuclei in experiments e14039 (black squares) and e14057 (red circles). The depth of ions in were taken from Figs. 3.2 and 3.4 for e14039 and e14057, respectively, while the implant x and y distributions are from Figs. 3.9 and 3.31 for e14039 and e14057, respectively. Symbols represent simulation results while lines are sixth-order polynomial fits to the simulation results used for interpolation.	80
Figure 3.42:	Energy calibration residuals for the individual ten LaBr ₃ detectors over a representative group of six runs during e14057.	82
Figure 3.43:	(a) LaBr ₃ energy calibration residuals for all 10 detectors combined over the same representative group of runs used in Fig. 3.42. (b) SeGA energy calibration residuals for all 16 detectors combined for all runs over the duration of e14039.	82
Figure 3.44:	Ratio of γ -ray efficiencies (LaBr ₃ / SeGA) as a function of energy.	83

Figure 3.45:	(a) Two-dimensional histogram of the dynode signal amplitude plotted against the LaBr ₃ - PSMPT dynode time difference for a single LaBr ₃ detector gated on either the 1173.2- or 1332.5-keV γ photopeak in that detector. (b) Plot of centroid position, extracted from fitting the projection of each bin in a) onto the time-difference axis. A high-order polynomial, shown in red, was used for interpolation between the data to extract the time walk as a function of dynode signal amplitude.	86
Figure 3.46:	(a) Two-dimensional histogram of the LaBr ₃ energy plotted against the LaBr ₃ - PSMPT dynode time difference for a single LaBr ₃ detector gated on dynode amplitudes between 20 and 500 ADC units. (b) Plot of centroid position for each LaBr ₃ energy bin, extracted from fitting the projection of each bin in (a) onto the time-difference axis. A high order polynomial, shown in red, was used extract the time walk as a function of LaBr ₃ energy.	88
Figure 3.47:	(a) LaBr ₃ energy spectrum for all ten detectors, gated on dynode amplitudes of >60 and <500 ADC units, in the region around 1077.4 keV. The peak and background regions used for this analysis are denoted with red solid and red dashed lines, respectively.	89
Figure 3.48:	(a) Background-subtracted two-dimensional dynode signal amplitude vs. time-difference spectrum for the 1077.4-keV peak in the experimental data. (b) The two-dimensional dynode signal amplitude vs. time-difference spectrum for the ⁶⁰ Co source measurements for the same energy gate as a).	90
Figure 3.49:	(a) Sigma (in ns) as a function of dynode signal amplitude shown in blue circles for the experimental data and as black squares for the source data presented in Figs. 3.48a and 3.48b, respectively. (b) The ratio (experiment/source) of sigma values from a) as a function of dynode signal amplitude. The fit to the data represents the DOI correction for the time resolution.	91
Figure 3.50:	(a) LaBr ₃ energy vs. time difference and (b) vs. LaBr ₃ energy dynode amplitude, respectively, for the same LaBr ₃ energy range as in Fig. 3.47. The same 1064- to 1094-keV peak and 1110- to 1140-keV background regions illustrated in Fig. 3.47 are shown again by red solid and dashed lines, respectively. Panels (c) and (d) show the projections of a) and b) onto the time-difference and dynode amplitude axes respectively, for the peak region between the solid red lines. Panels (e) and (f) show the projections of (a) and (b) onto the time-difference and dynode amplitude axes respectively, for the background region between the dashed red lines.	95

Figure 3.51:	Dynode signal amplitude distribution for the LaBr ₃ - dynode coincidences between 1064 and 1094 keV. This distribution is obtained by subtracting the data in Fig. 3.50f, scaled by s , from Fig. 3.50d. The counts at each dynode energy, E_p , at this specific γ energy, E_γ , are P_{E_p, E_γ} from Eq. (3.11).	96
Figure 3.52:	Results of the fitting technique for the 1077.4-keV state in ⁶⁸ Zn. The total time-difference spectrum for the 1064- to 1094-keV LaBr ₃ energy region, also shown in Fig. 3.50c, is shown in black. The scaled background time-difference spectrum over the 1110- to 1140-keV LaBr ₃ energy region is shown in blue, while the total fit of the detector response for the counts under the peak is shown in red and the total fit is shown in cyan.	97
Figure 3.53:	LaBr ₃ energy spectrum for all ten detectors, gated on dynode amplitudes of >60 and <500 ADC units, in the region around 594.3 keV. The peak and background regions used for the analysis are denoted with red solid and red dashed lines, respectively.	98
Figure 3.54:	Distribution of χ^2 values obtained from a comparison of the total fit, $R(t, t_0, \tau, E_\gamma, E_p)$, and the experimental data, shown as cyan and black in Fig. 3.55, respectively, for fourteen half-life values equally distributed about the minimum. The distribution is fit with a second order polynomial shown in red. The location of the minimum represents the half-life of the state and the second derivative of the fit is the error on that value. A half-life of 135(26) ps is obtained for the 915.3-keV state in ⁶⁹ Ni which agrees with the previously measured value of 120(34) ps [53].	99
Figure 3.55:	Results of the fitting technique for the 915.3-keV state in ⁶⁹ Ni. The total time-difference spectrum for the 574- to 614-keV LaBr ₃ energy region is shown in black. The scaled background time-difference spectrum over the 620- to 660-keV LaBr ₃ energy region is shown in blue, while the total fit of the detector response for the counts under the peak is shown in red and the total fit is shown in cyan.	100
Figure 3.56:	LaBr ₃ energy spectrum for all ten detectors, gated on dynode amplitudes of >60 and <500 ADC units, in the region around 448.5 keV. The peak and background regions used for the analysis are denoted with red solid and red dashed lines, respectively.	101

- Figure 3.57: Distribution of χ^2 values obtained from a comparison of the total fit and the experimental data, shown as cyan and black in Fig. 3.55, respectively, for fourteen half-life values equally distributed about the minimum. The distribution is fit with a second order polynomial shown in red resulting in a lifetime of 1.04(6) ns for the 2677-keV state in ^{70}Ni 102
- Figure 3.58: Results of the fitting technique for the 2677-keV state in ^{70}Ni . The total time-difference spectrum for the 396- to 424-keV LaBr₃ energy region is shown in black. The scaled background time-difference spectrum over the 434- to 462-keV LaBr₃ energy region is shown in blue, while the total fit of the detector response for the counts under the peak is shown in red and the total fit is shown in cyan. 103
- Figure 4.1: Decay scheme, adapted from Ref. [21], for the decay of the low-spin ^{68}Co isomer populating states in ^{68}Ni representing the extent of knowledge prior to the present work. Other low-energy levels in ^{68}Ni , not shown here, are known from reaction studies and decay spectroscopy of the high-spin ^{68}Co isomer. Three spin and parity assignments of $(1,^+, 2^-, 3^+)$ have been proposed for the low-spin ^{68}Co isomer by Refs. [12,21,55]. The 1.6(3)s half-life comes from Ref. [12], as does the <15 ns limit on the half-life of the 2511-keV 0_3^+ state. A β -delayed neutron branch of >2.6 % was reported by Ref. [21]. The β -decay Q-value was taken from Ref. [56]. All log ft values and β -decay feeding intensities were taken from Ref. [21]. The half-lives of 270(5) ns for the 1604-keV 0_2^+ state, 0.31(5) ps for the 2033-keV 2_1^+ , and 0.86(5) ms for the 2847-keV 5^- state were taken from Ref. [22]. 105
- Figure 4.2: β -delayed γ -ray spectrum recorded in SeGA within 4000 ms of an implanted ^{68}Fe ion. Transitions identified in the subsequent analysis as affiliated with the decay of ^{68}Ni are labeled with their energy while contaminating transitions, resulting from spurious correlations of the decay of other implanted nuclei, are denoted with symbols. The peaks at 1460 and 2614 keV are known background γ -rays from the decay of ^{40}K [49] and ^{208}Tl [50], respectively. The inset in (e) shows the full height of the 2032.9-keV peak truncated in the spectrum displayed in (e). 109
- Figure 4.3: Background-subtracted $\beta\gamma\gamma$ coincidence spectra gated on the 1514.3-keV $(2^+) \rightarrow 0_3^+$ transition in ^{68}Ni focusing around the 511-keV region. The background was taken below the 1514.3-keV peak to avoid the 1521.5-keV single escape peak from the 2032.9-keV γ ray. The upper range of the gate was also reduced by a couple of keV to avoid including the low-energy tail of the 1521.5-keV escape peak. 115

Figure 4.4:	Spectrum of γ rays recorded in coincidence with the detection of the $0_2^+ \rightarrow 0_1^+$ $E0$ transition in ^{68}Ni . The inset in (a) shows the full height of the 511-keV peak truncated in (a). The left and right insets in (c) show the full heights of the 1139.2- and 2422.0-keV peaks truncated in panels (b) and (c), respectively. The inset in (f) shows the 6000- to 6400-keV region of the same spectrum presented in (a) through (f). In all cases transitions are labeled with their energies and, when applicable, single and double-escape peaks are denoted with one or two stars, respectively, in addition to the energy of the peak.	119
Figure 4.5:	Spectrum of γ rays recorded in coincidence with the detection of the $0_2^+ \rightarrow 0_1^+$ $E0$ transition in ^{68}Ni focused in on the 1514.3-keV region.	121
Figure 4.6:	Decay scheme for the long-lived, low-spin, ^{68}Co isomer populated through the β decay of ^{68}Fe . States in ^{68}Ni are labeled with an energy in keV and the spin in parity (if known) on the right. On the left, β -decay branching ratios and $\log_{10} ft$ values are shown. β -decay Q-value taken from Ref. [56]. The 0.31(5) ps half-life of the 2033-keV 2_1^+ state is taken from the evaluation in Ref. [22].	125
Figure 4.7:	Motivation for the development of the exclusion technique. Two decay curves for ^{68}Fe are shown in black in (a) and (b) obtained from the analysis using the non-exclusion and exclusion correlation techniques, respectively. The decay curves have had their spurious-correlation component, determined using the techniques in Section 4.1.2.1, subtracted out and were normalized have equivalent integral numbers of counts. For each decay curve a total fit (red) was performed comprised of ^{68}Fe parent (green), ^{68}Co daughter (magenta), and ^{68}Ni granddaughter (orange) decays. The half-life of ^{68}Ni was fixed to the literature value of 29 s [22]. Fit residuals, normalized to the bin error, are shown in (c) and (d) for the total fit compared to the data in (a) and (b), for the non-exclusion and exclusion decay curve fits, respectively.	132

- Figure 4.8: Schematic view of the exclusion technique highlighting the differences with the non-exclusion correlation techniques. The time structure of implantations (black vertical lines), parent decays (red vertical lines), and daughter decay (blue vertical lines) for two implanted ions is shown. Solid and dashed lines are used to distinguish events affiliated with each different ion. Horizontal green bars represent the correlations and a gray horizontal bar represents a decay event that is outside the correlation window. In (a) the exclusion window of time is a crosshatched rectangle above the correlations. Implants removed from the analysis by the exclusion technique are labeled with an “X”. Time proceeds forward left to right indicated by the black arrow at the bottom of each panel. 134
- Figure 4.9: (a) Decay curve vs. coincident γ -ray energy, recorded in SeGA during e14039, for the region around the 161.8- and 184.3-keV peaks. (b) Projection of (a) onto the energy axis. Sets of solid red vertical lines and dashed vertical lines identify the peak and background regions, respectively, for each peak. 136
- Figure 4.10: Decay curves obtained by projecting 4.27a onto the time-difference axis over the regions of (a) 159 to 165 keV, (b) 166 to 172 keV, (c) 181 to 187 keV, and (d) 185 to 195 keV. Regions shown in (a) and (c) represent the encompass the 161.8-keV and 184.3-keV peaks, respectively, while (b) and (d) are representative backgrounds to be scaled and subtracted for each respective peak. 137
- Figure 4.11: (a) Background-subtracted γ -gated decay curve for the decay of ^{68}Fe into ^{68}Co . Gates were placed on the 161.8-keV and 184.3-keV transitions in ^{68}Co and the background, scaled appropriately and subtracted, was sampled directly above each peak. The background-subtracted data are shown in black while the spurious correlation component, obtained using the techniques in Section 4.1.2.1, is shown in blue. In cyan, a fit to the spurious correlation component is shown, and was used to represent the spurious correlations in the total fit of the data shown in red. The contribution from the decay of ^{68}Fe is shown in green. The half-life of ^{68}Fe , extracted from the fit, is 175(9) ms. This compares to the evaluated value of 188(4) ms [22]. (b) Fit residuals for the total fit compared to the data in (a) normalized to the bin error in (a). 138
- Figure 4.12: Results of the analysis run backwards in time through the data. (a) Decay curve vs. coincident γ -ray, recorded in SeGA during e14039, for the region around the 161.8- and 184.3-keV peaks. (b) Projection of (a) onto the energy axis. 139

- Figure 4.13: (a) Double-pulse-gated decay curve for the decay of ^{68}Co into ^{68}Ni . The data are shown in black while the spurious correlation component, obtained by running the analysis backwards in time and scaled by the fit, is shown in blue. In cyan, a fit to the spurious correlation component is shown, and was used to represent the spurious correlations in the best total fit of the data shown in red using the half-life of the minimum obtained from Fig. 4.14. The contribution from the decay of ^{68}Co is shown in magenta. (b) Fit residuals for the total fit compared to the data in (a) normalized to the bin error in (a). . . . 140
- Figure 4.14: Distribution of χ^2 values as a function of ^{68}Co half-life obtained from fitting the data shown in black in Fig. 4.13 with a combination of spurious correlations and the ^{68}Co daughter grow-in, described by equation (2.21). The spurious-correlation component and half-life of ^{68}Fe were fixed leaving the ^{68}Co half-life as the only free parameter. The χ^2 distribution was fit with a fifth order polynomial, shown in red, for interpolation between points. A value of 2360(130) ms was extracted for the half-life of the ^{68}Co low-spin isomer. 141
- Figure 4.15: (a) Decay curve for the decay of ions of ^{68}Fe in e14039. The data are shown in black while the spurious correlation component, obtained by running the analysis backwards in time and scaled by the fit, is shown in blue. In cyan, a fit to the spurious correlation component is shown, and was used to represent the spurious correlations in the best total fit of the data shown in red using the half-life of the minimum obtained from Fig. 4.14. The contribution from the decay of ^{68}Fe , ^{68}Co , and ^{68}Ni is shown in green, magenta, and orange, respectively. The total fit is shown in red. (b) Fit residuals for the total fit compared to the data in (a) normalized to the bin error in (a). 143
- Figure 4.16: (a) Decay curve for the decay of ions of ^{68}Fe in e14057. The data are shown in black while the spurious correlation component, obtained by running the analysis backwards in time and scaled by the fit, is shown in blue. In cyan, a fit to the spurious correlation component is shown, and was used to represent the spurious correlations in the best total fit of the data shown in red using the half-life of the minimum obtained from Fig. 4.14. The contribution from the decay of ^{68}Fe , ^{68}Co , and ^{68}Ni is shown in green, magenta, and orange, respectively. The total fit is shown in red. (b) Fit residuals for the total fit compared to the data in (a) normalized to the bin error in (a). 144

Figure 4.17:	(a) and (b) Time-difference distributions between the two constituent pulses of double pulse signals recorded in e14057 and e14039, respectively. The second pulse was restricted to amplitudes between 400 and 8000 ADC units in e14057 and energies of 400 and 2000 keV for e14039. A weighted average between the two results yields a value of 274(4) ns for the half-life of the 0_2^+ state in ^{68}Ni	148
Figure 4.18:	Spectrum of γ -rays recorded in the LaBr ₃ detectors around the 477.7-keV peak coincident with a decay event in the segmented plastic scintillator. The set of solid red and dashed red bars represent the energy windows used for the peak and background regions of interest, respectively.	149
Figure 4.19:	(a) Two-dimensional spectrum of γ -rays recorded in the LaBr ₃ detectors coincident with a decay event in the segmented plastic scintillator vs. time difference between the LaBr ₃ and segmented plastic scintillator. The solid red and dashed red bars denote the energy windows used for the peak and background regions of interest (ROI), respectively. (b) and (c) Time-difference spectra (LaBr ₃ - segmented plastic scintillator) obtained by projecting the spectrum in (a) onto the time-difference axis over the regions between the solid (peak ROI) and dashed (background ROI) red lines, respectively.	150
Figure 4.20:	χ^2 as a function of trial half-life used in each convolution fit, shown as black squares, and quadratic fit, shown in red, for interpolation between points.	151
Figure 4.21:	Best fit results for the lifetime of the 0_3^+ state in ^{68}Ni . In black and blue are the time-difference spectra for the peak and background ROIs shown in Figs. 4.19b and 4.19c, respectively. The convolution of the detector response with the best-fit half-life is shown in Red and the total fit of background plus convolution is shown in cyan.	151
Figure 4.22:	β -delayed γ -ray spectrum recorded in SeGA within 4000 ms of an implanted ^{70}Co ion. Transitions identified in the subsequent analysis as affiliated with the decay of ^{70}Ni are labeled with their energy while contaminating transitions, resulting from spurious correlations of the decay of other implanted nuclei, are denoted with symbols. The inset in (c) shows the full height of the 1259.1-keV peak cut off in spectrum shown in (c). The inset in (e) shows the full height of the 2032.9-keV peak cut off in spectrum shown in (e).	154

Figure 4.23:	(a) Decay curve vs. coincident γ -ray energy, recorded in SeGA during e14039, for the region around the 448.5-keV peak. (b) Projection of (a) onto the energy axis. Sets of solid red vertical lines and dashed vertical lines identify the peak and background regions, respectively, for each peak.	158
Figure 4.24:	(a) and (b) Decay curves obtained by projecting 4.23a onto the time-difference axis over the regions of (a) 443 to 453 keV and (b) 433 to 443 keV. The region shown in (a) encompasses the 448.5-keV peak while (b) is a representative background to be scaled and subtracted from the peak.	158
Figure 4.25:	(a) Background-subtracted, γ -gated decay curve for the decay of the short-lived, high-spin, ^{70}Co isomer into ^{70}Ni . A gate was placed on the 448.5-keV transitions in ^{70}Ni to isolated the short-lived, high-spin, isomer exclusively. The background, scaled appropriately and subtracted, was sampled directly below the peak. The background-subtracted data are shown in black while the spurious correlation component, obtained using the techniques in Section 4.1.2.1, is shown in blue. In cyan, a fit to the spurious correlation component is shown, and was used to represent the spurious correlations in the total fit of the data shown in red. The correlated contribution from the decay of ^{70}Co is shown in green. The half-life of short-lived, high-spin, ^{70}Co isomer, extracted from the fit, is 104.5(20) ms which agrees with the evaluated value of 114(7) ms [58]. (b) Fit residuals, normalized to the bin error, for the total fit compared to the data in (a).	159
Figure 4.26:	Results of the analysis run backwards in time through the data. (a) Decay curve vs. coincident γ -ray, recorded in SeGA during e14039, for the region around the 448.5-keV peak. (b) Projection of (a) onto the energy axis.	160
Figure 4.27:	(a) Decay curve vs. coincident γ -ray energy, recorded in SeGA during e14039, for the region around the 607.6-keV peak. (b) Projection of (a) onto the energy axis. Sets of solid red vertical lines and dashed vertical lines identify the peak and background regions, respectively, for each peak.	161
Figure 4.28:	(a) and (b) Decay curves obtained by projecting 4.27a onto the time-difference axis over the regions of (a) 605 to 615 keV and (b) 635 to 645 keV. The region shown in (a) encompasses the 607.6-keV peak while (b) is a representative background to be scaled and subtracted from the peak.	162

Figure 4.29: (a) Background-subtracted γ -gated decay curve for the decay of the short-lived, high-spin, ^{70}Co isomer into ^{70}Ni . A gate was placed on the 607.5-keV transitions in ^{70}Ni to isolated the short-lived, high-spin, isomer exclusively. The background, scaled appropriately and subtracted, was sampled directly below the peak. The background-subtracted data are shown in black while the spurious correlation component, obtained using the techniques in Section 4.1.2.1, is shown in blue. In cyan, a fit to the spurious correlation component is shown, and was used to represent the spurious correlations in the total fit of the data shown in red. The correlated contribution from the decay of ^{70}Co is shown in green. The half-life of short-lived, high-spin, ^{70}Co isomer, extracted from the fit, is 470(20) ms for the long-lived, low-spin, ^{70}Co isomer which is consistent with the previously measured value of 500(180) ms [12]. (b) Fit residuals, normalized to the bin error. 163

Figure 4.30: Results of the analysis run backwards in time through the data. (a) Decay curve vs. coincident γ -ray, recorded in SeGA during e14039, for the region around the 607.6-keV peak. (b) Projection of (a) onto the energy axis. 164

Figure 4.31: (a) Decay curve showing the time distribution of recorded decay events following within 4000 ms of an implanted ^{70}Co ion. A 4000 ms “exclusion window” was set following the implantation of each ion such that all subsequent ions within that window were ignored. The total fit is shown in red, the data are shown in black, and the time distribution of spurious correlations, obtained by running the analysis backwards in time, is shown in blue. The ^{70}Co parent, ^{70}Ni daughter, and ^{70}Cu granddaughter contributions are illustrated as green, cyan, and magenta lines, respectively. The short-lived isomer decay is shown as solid lines while the long-lived isomer decay is shown as a dashed line. The half-lives of ^{70}Ni and ^{70}Cu were fixed to the NNDC evaluated values of 6.0(3) s and 6.6(3) s [59], respectively. From the fit, the half-life of the short-lived ^{70}Co isomer was determined to be 104(4) ms while a half-life value of 450(13) ms was extracted for the long-lived ^{70}Co isomer. (b) Fit residuals normalized to the error in each bin. 166

Figure 4.32: (a) Decay curve showing the time distribution of recorded decay events following within 4000 ms of an implanted ^{70}Co ion gated on the 1259.1-keV ($2_1^+ \rightarrow 0_1^+$) transition. The same 4000 ms “exclusion window” was set following the implantation of each ion such that all subsequent ions within that window were ignored. The total fit is shown in red, the data are shown in black, and the scaled time distribution of spurious correlations used in Fig. 4.31, obtained by running the analysis backwards in time, is shown in blue. The ^{70}Co parent is shown in green and the short- and long-lived isomer decays are shown as solid and dashed lines, respectively. Half-lives of 106(5) and 446(42) ms were extracted from the fit for the short- and long-lived ^{70}Co isomers, respectively. These values are consistent with the 104.5(20) and 470(20) ms determined earlier in this section. (b) Fit residuals normalized to the bin error. 168

Figure 4.33: (a) Transformed decay curve showing the natural logarithm of the time distribution of recorded decay events following within 4000 ms of an implanted ^{70}Co ion gated on the 1259.0-keV ($2_1^+ \rightarrow 0_1^+$) transition. The same 4000 ms “exclusion window” was set following the implantation of each ion such that all subsequent ions within that window were ignored. The total fit is shown in red, the data are shown in black, and the scaled time distribution of spurious correlations used in Fig. 4.31, obtained by running the analysis backwards in time, is shown in blue. The ^{70}Co parent is shown in green and the short- and long-lived isomer decays are shown as solid and dashed lines, respectively. Half-lives of 104(5) and 440(50) ms for the short- and long-lived ^{70}Co isomers, respectively, were extracted from the fit. (b) Fit residuals normalized to the bin error. 170

Figure 4.34: Natural logarithm of the time difference between β decay and ^{70}Co ion implantation, shown on the y axis, is histogrammed vs. coincident β -delayed γ -ray energy from 0 to 1500 keV on the x axis. The z axis is counts per unit time difference per keV. 171

Figure 4.35: Results of fitting the projections of each energy bin onto the time axis of the two-dimensional histogram of the natural logarithm of the time difference between β decay and ^{70}Co ion implantation vs. coincident β -delayed γ -ray energy. The integral of each component is shown as a histogram. The short- and long-lived isomer contributions are shown as green and magenta, respectively, while the spurious correlation component is shown in blue. The sum of all components is shown in red and the total projection of the two-dimensional spectrum onto the energy axis is shown in black. The inset in (d) shows the full height of the 1259-keV transition cut off in (d). The inset in (e) shows the full height of the 2033-keV transition cut off in (f). 173

Figure 4.36:	Decay scheme for the short-lived, high-spin, ^{70}Co isomer. States in ^{70}Ni are labeled with an energy in keV and the spin in parity (if known) on the right. On the left, β -decay branching ratios and $\log_{10} ft$ values are shown. Q value taken from Ref. [56].	179
Figure 4.37:	Background subtracted $\beta\gamma\gamma$ coincidence spectrum gated on the 1259.1-keV ($2_1^+ \rightarrow 0_1^+$) transition within 4000 ms of the decay of ^{70}Co from (a) 0 to 2500 keV and (b) from 2500 to 5000 keV. The background was taken symmetrically either side of the 1259.1-keV peak. Coincidences affiliated with the long-lived, low-spin, ^{70}Co isomer are labeled with an energy while coincidences affiliated with the short-lived, high-spin, ^{70}Co isomer are denoted with black squares. Escape peaks are denoted with black stars and transitions seen in coincidences but not in singles are denoted with a single asterisk.	184
Figure 4.38:	Background subtracted $\beta\gamma\gamma$ coincidence spectrum gated on the 607.6-keV ($2_2^+ \rightarrow 2_1^+$) [panels (a) and (b)] and 1866.5-keV ($2_2^+ \rightarrow 0_1^+$) [panels (c) and (d)] transitions within 4000 ms of the decay of ^{70}Co . The background was taken symmetrically either side of each peak. Coincidences affiliated with the long-lived, low-spin, ^{70}Co isomer are labeled with an energy while coincidences affiliated with the short-lived, high-spin, ^{70}Co isomer are denoted with black squares. Contaminating coincidences are denoted with black upside-down triangles and labeled with the offending isotope, if known.	185
Figure 4.39:	Background subtracted $\beta\gamma\gamma$ coincidence spectrum gated on the (a) 307.6-keV and (b) 1943.8-keV transitions within 4000 ms of the decay of ^{70}Co . The background was taken symmetrically either side of the 307.6-keV peak and below the 1943.8-keV peak due to closely neighboring transitions. Coincidences affiliated with the long-lived, low-spin, ^{70}Co isomer are labeled with an energy.	186
Figure 4.40:	(a) Background subtracted $\beta\gamma\gamma$ coincidence spectrum gated on the 1943.8-keV transition within 4000 ms of the decay of ^{70}Co . (b) Beta-gated γ -ray singles spectrum within 4000 ms of the decay of ^{70}Co . Both spectra highlight the region around 1567 keV and no 1567-keV peak is observed in either spectrum.	186
Figure 4.41:	Decay scheme for the long-lived, low-spin, ^{70}Co isomer. States in ^{70}Ni are labeled with an energy in keV and the spin in parity (if known) on the right. On the left, β -decay branching ratios and $\log_{10} ft$ values are shown. ^a Q-value taken from Ref. [56].	190

Figure 4.42: (a) and (b) Spectrum of γ -rays recorded in the LaBr₃ and SeGA detectors, respectively, coincident with a ⁷⁰Co decay event in the segmented plastic scintillator. (c) Spectrum of γ -rays recorded in the LaBr₃ coincident with a decay event in the segmented plastic scintillator. (d) Spectrum shown in panel (c) gated on the 1259.1-keV transition in SeGA. In panels (c) and (d) the coincidence window between the LaBr₃ detectors and PSPMT was 50 ns and in (d) the LaBr₃-SeGA coincidence window was 600 ns. In all panels the set of solid red and dashed red bars represent the energy windows used for the peak and background regions of interest, respectively. 191

Figure 4.43: (a) Two-dimensional spectrum of γ -rays recorded in the LaBr₃ detectors coincident with a decay event in the segmented plastic scintillator vs. time difference between the LaBr₃ and segmented plastic scintillator. The solid red and dashed red bars denote the energy windows used for the peak and background regions of interest (ROI), respectively. (b) and (c) Time-difference spectra (LaBr₃ - segmented plastic scintillator) obtained by projecting the spectrum in (a) onto the time-difference axis over the regions between the solid (peak ROI) and dashed (background ROI) red lines, respectively. 192

Figure 4.44: χ^2 as a function of trial half-life used in each convolution fit, shown as black squares, and quadratic fit, shown in red, for interpolation between points. 193

Figure 4.45: Best fit results for the lifetime of the (0₂⁺) state in ⁷⁰Ni. In black and blue are the time-difference spectra for the peak and background ROIs shown in Figs. 4.43b and 4.43c, respectively. The convolution of the detector response with the best-fit half-life is shown in Red and the total fit of background plus convolution is shown in cyan. 193

Figure 5.1: Half-lives and transition strengths of the lowest four states in ⁶⁸Ni (left) and the lowest three states in ⁷⁰Ni (right) compared with predictions of advanced shell model calculations using the LNPS [21] and A3DA [68] effective interactions. Half-lives of the states, when known, are given on the upper left side of each level with the associated energies (in keV) on the lower left side. Unobserved transitions are indicated by dotted lines. Electric monopole transition strengths are given for the *E0* transitions, while *B(E2)* values, in units of *e*²*fm*⁴, are given for *E2* transitions. Experimental values for the 2₁⁺ state half-life and *B(E2)* for ⁷⁰Ni are adopted from Ref. [64]. Note that, while LNPS predictions of the ⁷⁰Ni *B(E2 : 0₂⁺ → 2₁⁺)* value have not been published so far, Ref. [69] indicates a calculated *B(E2 : 2₁⁺ → 0₁⁺)* value of 102 *e*²*fm*⁴ with this interaction (not shown). 198

Figure 5.2:	Apparent cumulative β -decay intensities deduced from the experimental decay scheme in Fig. 4.36 (black line with salmon error bars) compared with shell model calculations (dashed dark blue line). . . .	202
Figure 5.3:	Apparent cumulative β -decay intensities deduced from the experimental decay scheme in Fig. 4.36 (black line with turquoise error bars) compared with shell model calculations (dashed dark blue line).	203
Figure 5.4:	Apparent cumulative β -decay intensities deduced from the experimental decay scheme in Fig. 4.41 (black line with salmon error bars) compared with shell model calculations (dashed dark blue line). . . .	205
Figure 5.5:	Apparent cumulative β -decay intensities deduced from the experimental decay scheme in Fig. 4.41 (black line with turquoise error bars) compared with shell model calculations (dashed dark blue line).	206
Figure 5.6:	Apparent cumulative β -decay intensities deduced from the experimental decay scheme in Fig. 4.6 (black line with salmon error bars) compared with shell model calculations (dashed dark blue line). . . .	208
Figure 5.7:	Apparent cumulative β -decay intensities deduced from the experimental decay scheme in Fig. 4.6 (black line with turquoise error bars) compared with shell model calculations (dashed dark blue line).	209
Figure A.1:	(a) Coincident first rise energies of double pulses with a 92.6-keV second rise energy. (b) Gamma rays recorded in SeGA coincident with double pulses recorded in the GeDSSD with the energy of the second rise in the 92.6-keV peak.	215
Figure A.2:	Gamma rays recorded in SeGA coincident with double pulses recorded in the GeDSSD with the energy of the second rise in the 175-keV peak. The 511- and 1139.2-keV peaks, labeled with two asterisks, are coincident with the decay of the 0_2^+ state in ^{68}Ni during events where there was incomplete energy collection for the pair-production or internal conversion decay processes. The 806.2-keV peak is new and remains unidentified.	216

- Figure A.3: Gamma rays recorded in SeGA coincident with double pulses recorded in the GeDSSD with the energy of the second rise in the 190-keV peak. The 511-keV peak, labeled with two asterisks, was coincident with the decay of the 0_2^+ state in ^{68}Ni during events where there was incomplete energy collection for the pair-production or internal conversion decay processes. The 1357-keV peak was coincident with an unresolved and unidentified ≈ 200 keV second pulse energy. The 681- and 1870-keV transitions are from the 680.6-1872.3-keV γ -ray cascade that depopulates the 2552-keV state in ^{69}Cu [52]. 217
- Figure B.1: Background-subtracted $\beta\gamma\gamma$ coincidence spectra gated on the 2032.9-keV $2_1^+ \rightarrow 0_1^+$ transition in ^{68}Ni . The background was taken symmetrically either side of the 2032.9-keV peak. Coincident transitions are labeled with their energies and, when applicable, single and double-escape peaks are denoted with one or two stars, respectively, in addition to the energy of the peak. 220
- Figure B.2: Background-subtracted $\beta\gamma\gamma$ coincidence spectra gated on the (a) 709.3-keV, (b) 1139.2-keV, (c) 2742.2-keV, and (d) sum of the 709.3-, 1139.2-, and 2742.2-keV transitions. The background was taken symmetrically either side of each respective peak region. Coincident transitions are labeled with their energies and, when applicable, single-escape peaks are denoted with one star in addition to the energy of the peak. The insets in (a) and (b) show the full heights of the 2032.9-keV and 511-keV peaks truncated in (a) and (b), respectively. 222
- Figure B.3: Background-subtracted $\beta\gamma\gamma$ coincidence spectra. Coincident transitions are labeled with their energies. All insets display additional ranges of their respective spectra. The open square symbol used on (c) represents a contaminating 649.2-327.0-keV coincidence from ^{68}Co . A single asterisk after an energy label signifies the transition was observed exclusively in coincidence, and two asterisks following an energy label identifies a coincidence with contaminating transition. 224
- Figure B.4: Background-subtracted $\beta\gamma\gamma$ coincidence spectra gated on the sum of the 1282.6-keV, 1514.3-keV, 1992.1-keV, 2422.0-keV, and 4024.6-keV transitions. The background was taken symmetrically either side of each respective peak region. Coincident transitions are labeled with their energies. The inset shows a zoomed-in view of the 1500 to 1900 keV region of the spectrum. 233

- Figure B.5: Background-subtracted $\beta\gamma\gamma$ -double-pulse coincidence spectra recorded in coincidence with the detection of the $0_2^+ \rightarrow 0_1^+$ $E0$ transition in ^{68}Ni . The background was taken symmetrically either side of the peak except. The inset in (a) shows the full height of the 511-keV peak cut off in the spectrum displayed in (a). The inset in panel (k) shows the region between 2510 and 2550 keV for the spectrum in (k). The insets in panels (l) and (n) show the region between 2400 and 2440-keV for the same spectrum in each panel. The inset in (o) shows the full height of the 511-keV peak cut off in the spectrum displayed in (o). 243
- Figure C.1: Series of background subtracted $\beta\gamma\gamma$ coincidence spectra correlated to the decay of the short-lived, high-spin, ^{70}Co isomer. The background was taken symmetrically either side of the peak except where other γ rays interfered, in which case the background was taken above as close as possible to the peak of interest. Transitions affiliated with the long-lived, low-spin, ^{70}Co isomer are denoted with black squares. 246
- Figure D.1: Series of background subtracted $\beta\gamma\gamma$ coincidence spectra correlated to the decay of the long-lived, low-spin, ^{70}Co isomer. The background was taken symmetrically either side of the peak except where other γ rays interfered, in which case the background was taken above as close as possible to the peak of interest. Transitions affiliated with the short-lived, high-spin, ^{70}Co isomer are denoted with black squares. Transitions observed in coincidence but not in singles are denoted with asterisks. The insets in (l) and (m) show the $\beta\gamma\gamma$ coincidence spectra gated on the 1626-keV and 771.9-keV transitions. 251

Chapter 1

Introduction

In this chapter the fundamental forces, which dictate the structure of the atomic nucleus, are discussed. The evolution of nuclear structure, with both changing numbers of constituent nucleons as well as the redistribution of nucleons within a single nucleus, is explored. Finally, an overview of the current understanding of the region around the $N=40$ and $Z=28$ neutron subshell and proton shell closures is presented, establishing the motivation for the measurements performed in this work.

1.1 Nuclear Shell Structure

Since the discovery of the atomic nucleus by Ernest Rutherford in 1911 [1], countless experimental and theoretical investigations have been performed to explore the underlying fundamental forces governing nuclear properties. To first order, the nucleus is understood as a composite entity made of protons and neutrons bound together by the strong nuclear force. Though no analytic expression exists to describe the strong force, it is well established as a short range force with a repulsive core that saturates at longer distances.

Despite the deficiency in the understanding of the nucleon-nucleon force, various theoretical constructs have had success reproducing the robust patterns that emerge with changing numbers of nucleons. One such example is the nuclear shell model. In the shell model nucleons are organized into collections of nearly degenerate single-particle states separated

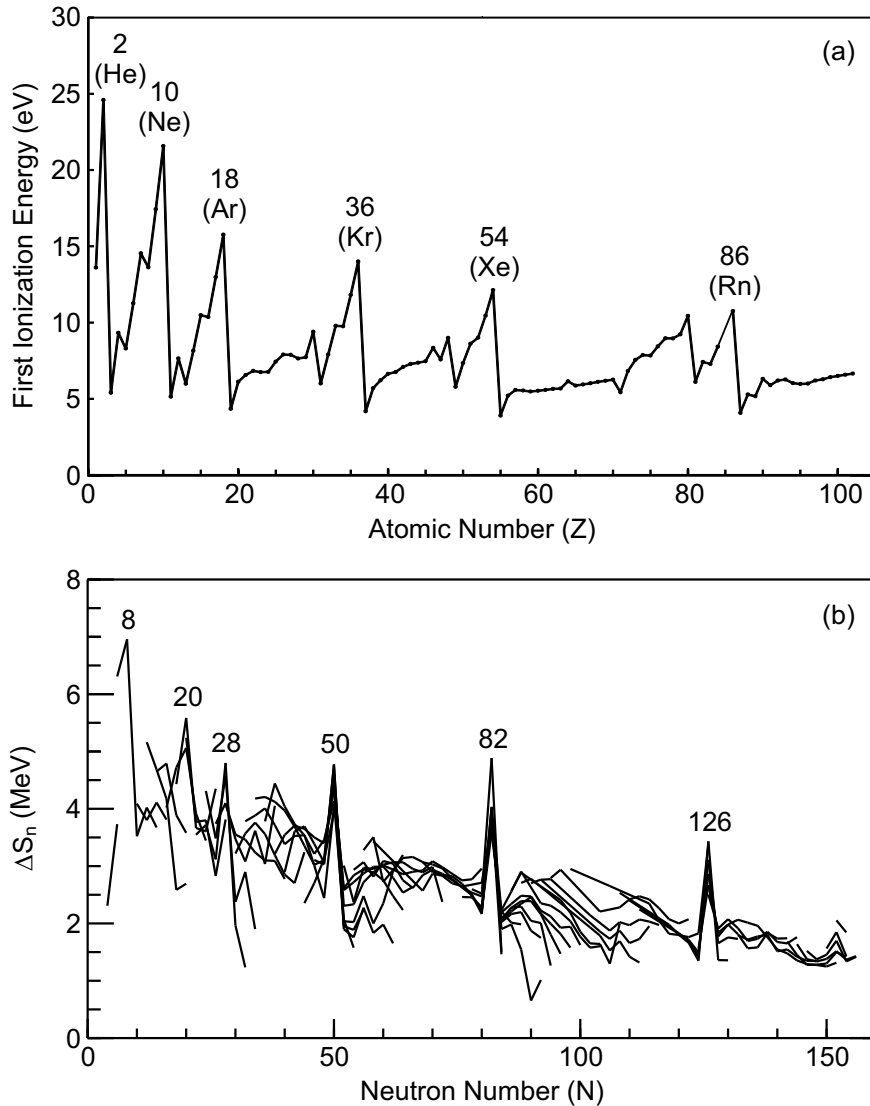


Figure 1.1: (a) First ionization energy plotted as a function of atomic number. The noble-gas elements and their atomic numbers, corresponding to closed electron shell configurations, are labeled. All ionization energies were taken from Ref. [2]. (b) Differential neutron separation energies as a function of neutron number for a variety of even-even nuclei adapted from Ref. [3]. Nuclei along the same isotopic chains are connected with lines.

by large energy gaps. This is analogous to electron shell structure in atomic systems. The effects of electronic shell structure are illustrated by the trends in the first ionization energy as a function of atomic number, shown in Fig. 1.1a. The first ionization energy refers to the amount of energy required to remove one electron from an atom. The large peaks in ionization energy at each noble gas element (atomic numbers = 2,10,18,36,54,86) represent the

complete filling of an atomic shell. In atoms, shell structure leads to the enhanced chemical stability of the noble gases. In the nuclear case, radioactive nuclei that possess completely filled proton and/or neutron shells (Z or $N = 2, 8, 20, 28, 50, 82,$ and 126 (for N), often called the “magic” numbers), are observed to exhibit enhanced stability. Empirical evidence for nuclear shell structure includes the trends in the differential one-neutron separation energy, ΔS_n , as a function of neutron number, N , shown in Fig. 1.1b. The neutron separation energy is expressed as

$$S_n = \text{BE}(N, Z) - \text{BE}(N - 1, Z), \quad (1.1)$$

where Z is the atomic number, N is the neutron number, and $\text{BE}(N - 1, Z)$ and $\text{BE}(N, Z)$ are the binding energies of neighboring nuclei along an isotopic chain. S_n represents the energy required to remove a single neutron from the nucleus. The differential neutron separation energy, ΔS_n , is the difference of neutron separation energies between nearest neighbor isotopes, and is written as

$$\Delta S_n = \text{BE}(N, Z) - \text{BE}(N - 1, Z) - [\text{BE}(N + 1, Z) - \text{BE}(N, Z)], \quad (1.2)$$

where again Z is the atomic number, N is the neutron number, and $\text{BE}(N - 1, Z)$, $\text{BE}(N, Z)$, and $\text{BE}(N + 1, Z)$ are the binding energies of three neighboring nuclei along an isotopic chain. Similar to the electron ionization energies in Fig. 1.1a, the peaks at the neutron shell closures in Fig. 1.1b provide evidence of the relatively large energy gap between single-particle states at a closed shell and the next available single-particle states. The same behavior is also observed for proton separation energies with corresponding peaks in the differential proton separation energy found at identical locations as in Fig. 1.1b (except for $Z = 126$).

1.2 Nuclear Shell Evolution

Shell structure is observed to evolve away from the valley of β stability with changing numbers of both protons and neutrons as well as with the redistribution of nucleons amongst the single particle states. The tensor force has been identified as a driving force of this evolution [4–9]. The easiest way to understand the impact of the tensor force on nuclear structure is to examine the angle-averaged, or “monopole” component, of the tensor force, written as

$$V_{ab}^T = \frac{\sum_J (2J + 1) \langle j_a j_b | V | j_a j_b \rangle_{J,T}}{\sum_J (2J + 1)}, \quad (1.3)$$

[4] where j_a and j_b are the orbits occupied by the two nucleons, each with quantum numbers n , l , and j (in a spherical potential), coupled to total angular momentum, J , and total isospin, T . The monopole component of the tensor force creates a shift in the energy of orbit j_a proportional to the occupancy of orbit j_b . Values of j can be $j_< = l - 1/2$ and $j_> = l + 1/2$. The monopole interaction is repulsive for $j_< j_<$ and $j_> j_>$ and attractive for $j_> j_<$ and $j_< j_>$. The effect of the monopole interaction on effective single-particle energies is shown schematically in Fig. 1.2.

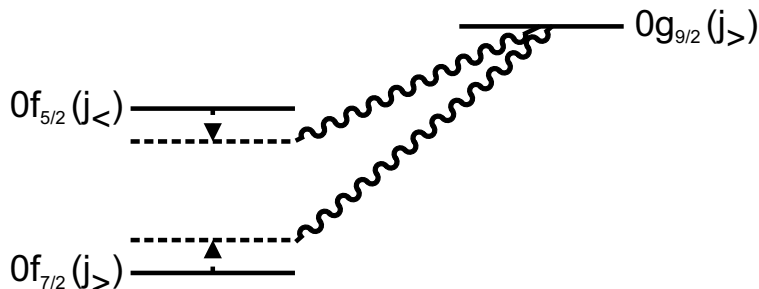


Figure 1.2: Schematic representation of the effect of the monopole component of the tensor force.

From Fig. 1.2 it can be seen that the monopole component of the tensor force reduces the energy separation of spin-orbit partners and directly influences nuclear structure in several

regions of the nuclear chart.

Nuclear shell evolution, as discussed herein, refers to two situations. The first is the migration of effective single-particle energies across an isotopic or isotonic chain due to changes in the monopole interaction of the tensor force with changing proton or neutron number. This type of shell evolution is linked to the disappearance of traditional magic numbers and the appearance of new ones [9]. One such example is the appearance of $N = 32$ and $N = 34$ semi-magic numbers in the Ca isotopes. In the Ca isotopes, the $\pi 0f_{7/2}$ orbit (where π denotes the proton orbital and ν denotes a neutron orbital) is unoccupied while in the Ni isotopes the $\pi 0f_{7/2}$ orbit is fully occupied. The strong attractive $\pi 0f_{7/2}-\nu 0f_{5/2}$ monopole interaction places the $\nu 0f_{5/2}$ orbit between the $\nu 1p_{3/2}$ and $\nu 1p_{1/2}$ orbits but in the absence of the monopole interaction the $\nu 0f_{5/2}$ is less bound and higher in energy than the $\nu 1p_{1/2}$ orbit, giving rise to the relatively large energy spacing between the $\nu 1p_{3/2}$ and $\nu 1p_{1/2}$ and $\nu 1p_{1/2}$ and $\nu 0f_{5/2}$ orbits creating the $N = 32$ and $N = 34$ semi-magic numbers [9]. Additional consequences of this will be discussed in Sec. 1.4.

The second is the change in effective single-particle energies from the monopole interaction of the tensor force due to particle-hole excitations. This type of shell evolution gives rise to low-energy intruder state configurations and a phenomenon called shape coexistence, discussed further in Sec. 1.3. One example of shell evolution giving rise to shape coexistence is provided by the Hg isotopes. Here particle-hole excitations alter the occupancy of specific single particle states. The resulting proton-neutron interactions, including the monopole interaction, drive the migration of intruder states down in excitation energy [10]. After years of detailed spectroscopy experiments, a low-lying intruder state band was observed across mid-shell for neutrons along the Hg isotopic chain. Figure 1.3, adapted from Ref. [11], shows the energy of yrast states (black, filled circles) and prolate-deformed intruder states (red,

open circles) as a function of neutron number. The coexistence of the near-spherical yrast states with the prolate-deformed intruder states is a prime example of shape coexistence.

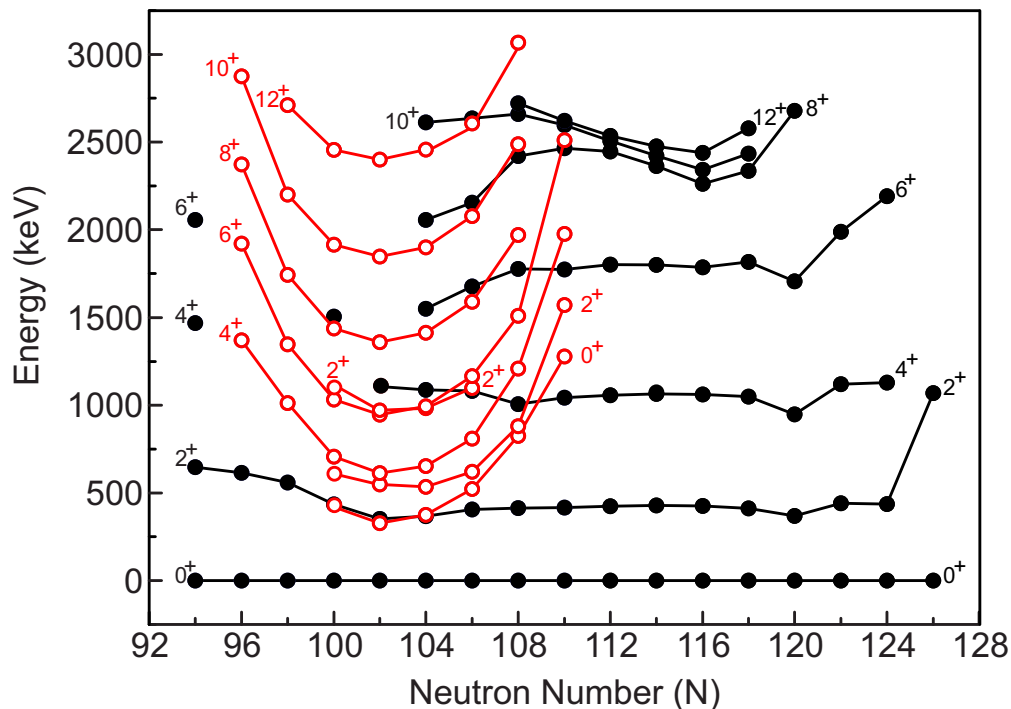


Figure 1.3: Shell evolution along the Hg isotopic chain

1.3 Nuclear Shape Coexistence

As alluded to in the previous section, shape coexistence occurs when multiple states with configurations possessing different intrinsic shapes coexist at similar excitation energy. Frequently observed near shell closures, these coexisting intruder-state configurations born of particle-hole excitations owe their existence to a delicate balance between the cost of promoting particles across a shell gap and the stabilizing effect of residual interactions such as the monopole component of the tensor force. When these competing factors are similar in magnitude the energy of normal-ordered and intruder configurations can be similar and are said to “coexist”.

Multiple low-lying 0^+ states are often a hallmark of shape coexistence in even-even nuclei and thus, spectroscopy of 0^+ states is a valuable tool for investigating shape coexistence. Of particular interest are transitions between two 0^+ states which occurs exclusively through electric monopole, $E0$, transitions, discussed further in Section 2.5. Half-lives of excited 0^+ states and decay branches are required to characterize $E0$ transitions. Also of interest are the $B(E2)$ values for $2^+ \rightarrow 0^+$ transitions. Section 2.5 discusses how ratios of $B(E2)$ values can be used to infer the degree of mixing between 0^+ states.

1.4 Nuclear Structure Near $N = 40$ and $Z=28$

The neutron-rich nuclei near the $N = 40$ neutron subshell and $Z = 28$ proton shell closures have been studied extensively by numerous theoretical and experimental investigations. The goal of this work has been to understand the rapid changes in nuclear structure with changing proton and neutron number, which appear to give rise to shape coexistence in this region. ^{68}Ni has been central to this exploration located at the $Z = 28$ proton shell closure, defined by energy gap between the $\pi 0f_{7/2}$ and $\pi 1p_{3/2}$ single particle states, and the $N = 40$ neutron subshell closure, defined by the energy gap between the neutron $\nu 1p_{1/2}$ and $\nu 0g_{9/2}$ single particle states.

Originally, the $N = 40$ neutron subshell closure was considered robust and ^{68}Ni was seen as a semi-magic nucleus based on the relatively large energy of the 2_1^+ state and low $B(E2; 0_1^+ \rightarrow 2_1^+)$ [12]. However in ^{66}Fe , with the removal of just two protons, evidence supporting a $N = 40$ neutron subshell closure quickly vanishes. In Fig. 1.4 the (a) 2_1^+ state energies and (b) $B(E2; 0_1^+ \rightarrow 2_1^+)$ values, taken from Ref. [13], are presented as a function of neutron number for the Cr, Fe, and Ni isotopes. The precipitous drop in 2_1^+ state energies

suggests a sudden onset of deformation beyond ^{68}Ni . Further, mass measurements [14] find no dip in the two neutron separation energy, a characteristic of shell closures, at $N = 40$ for any neighboring isotopes above Ni.

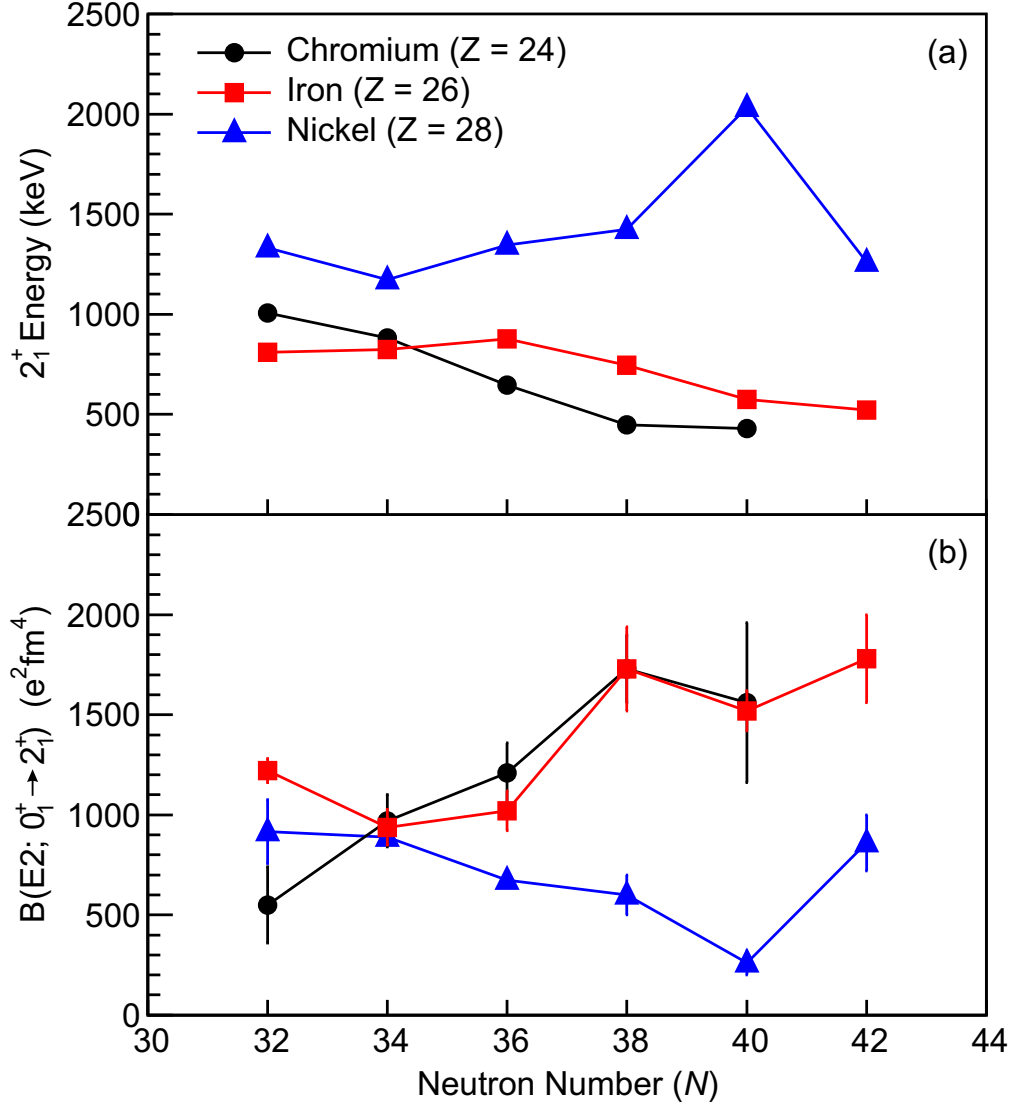


Figure 1.4: Systematics of (a) 2_1^+ state energies and (b) $B(E2; 0_1^+ \rightarrow 2_1^+)$ values as a function of neutron number for the Cr, Fe, and Ni isotopes. Data taken from Ref. [13].

Theoretically, the rapid onset of collectivity is explained by the migration of single-particle states under the changing influence of the monopole interaction of the tensor force with changing proton and neutron number [5, 9]. As protons are removed from the $\pi 0f_{7/2}$

orbit, moving from Ni to Ca, the attractive $\pi 0f_{7/2} - \nu 0f_{5/2}$ monopole interaction decreases resulting in the migration of the $\nu 0f_{5/2}$ upward in energy towards the Fermi surface, and excitations of neutrons into the $\nu 0g_{9/2}$ orbit become increasingly probable. The admixture of the $\nu 0g_{9/2}$ orbit into the ground-state wavefunction leads to deformation in the Cr and Fe isotopes, while a lack of it in ^{68}Ni preserves the spherical shape for the ground state [5, 9].

The same physics that destroys the magicity of the $N = 40$ subshell closure and drives nuclei to deformed shapes also gives rise to shape coexistence in the region. Two such examples are the odd-A Co isotopes and the even-even Ni isotopes. In ^{67}Co , a 496-ms isomeric $(1/2)^-$ state has been identified at 491.6 keV. This state can only be explained by excitations of protons into the $[321]1/2$ orbit (originating from the spherical $\pi p_{3/2}$ orbit) at prolate ($\beta > 0.2$) deformation [15]. Lower in mass along the isotopic chain, the corresponding $(1/2)^-$ state in ^{65}Co is located at 1095 keV [16]. It is believed that strong proton-neutron correlations induce deformation and lower the energy of the $(1/2)^-$ state with added neutrons [15]. The ground state of ^{67}Co is presumed spherical with a $7/2^-$ spin and parity from a $\pi 0f_{7/2}^{-1}$ configuration [15]. Therefore, ^{67}Co provides an example of spherical-prolate shape coexistence.

Transitioning to the even-even Ni isotopes, evidence of shape coexistence is building. Experimentally, three 0^+ states have been identified in ^{68}Ni at energies of 0, 1604 [17–19], and 2511 keV [12, 20]. Advanced shell-model calculations using the A3DA [7] and LNPS [5, 8] interactions over the $(0f1p0g_{9/2}1d_{5/2})^{\pi\nu}$ and $(0f1p)^{\pi}(0f1p0g_{9/2}1d_{5/2})^{\nu}$ model spaces, respectively, predict the three ^{68}Ni 0^+ states to be associated with spherical, oblate, and prolate configurations, respectively.

According to the A3DA calculations, the spherical ^{68}Ni 0_1^+ ground state contains very few particle-hole excitations across $Z = 28$ or $N = 40$ with, on average, only one neutron

in the $0\nu g_{9/2}$. The oblate-deformed 0_2^+ state contains additional excitations across the shell and subshell gaps with ≈ 0.7 protons and ≈ 2.4 neutrons excited. The work of Ref. [18] directly observed the $0_2^+ \rightarrow 0_1^+$ $E0$ transition, and using maximal mixing within the two-level mixing model obtained a difference in mean square charge radii of $\Delta\langle r^2 \rangle = 0.15\text{fm}^2$ and an absolute value of 102efm^2 for the intrinsic quadrupole moment, which agrees well with the -95efm^2 [18] and $|Q_0| = 93\text{efm}^2$ [8] from the shell-model calculations.

The A3DA calculations also predict that the 2_1^+ state is a member of a deformed rotational band built on the 0_2^+ state. Investigation of this claim requires observation of the $2_1^+ \rightarrow 0_2^+$ transition, and a measurement of the branching ratio is necessary to deduce the $B(E2)$. Limits of $<1\%$ [18] and $<0.7\%$ [21] have been placed on the branching ratio of this transition based on previous measurements. A measured half-life of $0.31(5)$ ps already exists for the 2_1^+ state in ^{68}Ni [22].

The presumed prolate-deformed 0_3^+ state is predicted to contain far more excitations with ~ 3 protons across $Z = 28$ and ~ 4 neutrons across $N = 40$ [9]. The calculations suggest that the neutrons are taken equally from the $\nu 0f_{5/2}$ and $\nu 1p_{1/2}$ orbits, both $j_<$ orbits, and placed into the $\nu 0g_{9/2}$ orbit, which is a $j_>$ orbit [9]. The result is a $\sim 33\%$ reduction in the difference in effective single-particle energies between the $\pi 0f_{7/2}$ and $\pi 0f_{5/2}$ orbits and is responsible for the increased occupancy of the $\pi 0f_{5/2}$ orbit. The predicted quadrupole moment of the 0_3^+ is $\approx 250\text{efm}^2$ [9].

Half-life predictions for the 0_3^+ state exist but vary significantly between the A3DA and LNPS calculations with values of 108 ns and 1.5 ns , respectively [21]. Experimentally, a limit of $<15\text{ ns}$ was placed on the half-life of the 0_3^+ state [12]. Additionally, the $0_3^+ \rightarrow 0_2^+$ and $0_3^+ \rightarrow 0_1^+$ $E0$ transitions in ^{68}Ni have not been observed, but branching ratio limits of $<2\%$ on the former and $<4\%$ on the total have been placed [21].

In ^{70}Ni , the A3DA calculations suggest a decrease of the 2511-keV prolate state in ^{68}Ni down to 1525 keV in ^{70}Ni . This is explained by the further decrease in the difference in effective single particle energies between the $\pi 0f_{7/2}$ and $\pi 0f_{5/2}$ orbits, with the addition of two neutrons into the $\nu 0g_{9/2}$ orbit. Prior to this work, a candidate 0_2^+ state in ^{70}Ni at 1484 keV was proposed based on unplaced γ rays observed in singles [23]. Additionally the corresponding 2^+ and 4^+ rotational band members were tentatively identified [23].

1.5 Goals of the Experiment

The purpose of the present work is to investigate the predictions of shape coexistence in the Ni isotopes near $N = 40$. To that end, two complimentary β -decay spectroscopy experiments were performed.

The first experiment was designed to observe the $2_1^+ \rightarrow 0_2^+$ transition in ^{68}Ni and measure its branching ratio in order to deduce the $B(E2 : 2_1^+ \rightarrow 0_2^+)$. Searches for other 0^+ states and $E0$ transitions were also performed.

The second experiment was designed to measure half-lives of excited nuclear states in $^{68,70}\text{Ni}$ to determine absolute $B(E2)$ values. The comparison of transition probabilities extracted from experiment with theoretical predictions would prove to be a sensitive probe of nuclear wavefunctions.

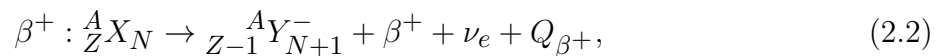
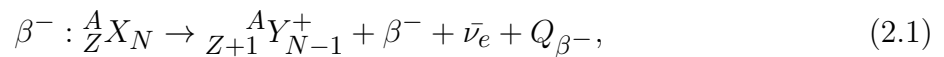
Chapter 2

Nuclear Decay Modes

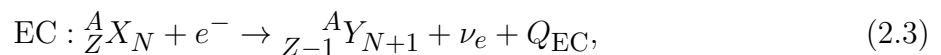
In this chapter, decay modes relevant to the nuclei of interest are discussed. The fundamental nuclear physics governing each decay mode, as well as important experimental observables, are described.

2.1 β Decay

Nuclear β decay is a process by which a nucleus of mass number A undergoes transmutation by converting a neutron to a proton or vice-versa. Three distinct β -decay processes are considered: β^- , β^+ , and electron capture (EC). These three processes transmute more exotic parent nuclei to less exotic daughter nuclei while keeping A constant with successive decays propagating along an isobaric chain towards the valley of β stability. These processes are written as:



and



where β^\pm is an electron (β^-) or positron (β^+), ν_e is an electron neutrino, $\bar{\nu}_e$ is an electron anti-neutrino, e^- is an orbital electron, and Q_{β^-} , Q_{β^+} , and Q_{EC} are the β -decay Q-values. The Q-values can be calculated using

$$Q_{\beta^-} = [M(A, Z) - M(A, Z + 1)]c^2, \quad (2.4)$$

$$Q_{\beta^+} = [M(A, Z) - M(A, Z - 1) - 2m_e]c^2, \quad (2.5)$$

and

$$Q_{EC} = [M(A, Z) - M(A, Z - 1)]c^2, \quad (2.6)$$

where $M(A, Z)$ is the mass of nucleus with A nucleons and Z protons, m_e is the mass of the electron, and c is the speed of light. Often, β decay populates some number of excited states in the daughter nucleus. The total energy released by β decay in that case is the difference between the Q-value and the excitation energy of the final state.

Nuclei relevant to the present experiments are neutron-rich and decay by β^- decay. β^- decay is possible whenever $Q_{\beta^-} > 0$. The decay energy from β^- decay is shared between the e^- , the $\bar{\nu}_e$, and the recoiling daughter nucleus. The energy of the β -decay electron is a continuous distribution ranging from zero up to Q_{β^-} (neglecting the small contributions from the $\bar{\nu}_e$ and daughter energies). The $\bar{\nu}_e$ emitted from β^- decay leaves undetected, while the emitted β -decay electron losses energy in the surrounding materials. In the present experiments, described in the following chapter, decaying nuclei are deposited into an active detector volume and the energy loss from the emitted electrons is recorded.

While the nuclei in the present study do not decay by β^+ or EC, these processes are

briefly discussed here for completeness. In β^+ decay, a proton-rich nucleus converts a proton to a neutron, emitting a positron and an electron neutrino. β^+ decay is possible whenever $Q_{\beta^+} > 0$. The decay energy from β^+ decay is shared between the e^+ , the ν_e , and the recoiling daughter nucleus. The emitted e^+ interacts with its surroundings losing energy until it annihilates with an electron, creating two 511-keV γ -rays emitted opposite in direction.

EC decay is an alternative to β^+ decay. In EC decay, a proton captures an atomic electron, typically from the inner-most shells, leaving a daughter nucleus with one fewer proton than the parent and a vacancy in a particular electron orbital. Electrons from outer orbits fill the vacancy emitting X rays or Auger electrons. Unlike β^+ decay, mono-energetic electron neutrinos are emitted.

β decay is governed by the β -decay selection rules. Allowed β decay emits the e^- and $\bar{\nu}_e$ with a relative orbital angular momentum, l , equal to zero. Higher values of l are referred to as forbidden transitions and are hindered compared to allowed transitions. Typically, the hindrance is $\sim 3 \times 10^{-4}$ for each additional unit of angular momentum [24]. In addition, the β -decay electron and the electron anti-neutrino both have intrinsic spin, s , equal to 1/2. The parallel ($S = 0$) and anti-parallel ($S = 1$) alignments of the two spins of these two particles give rise to the Fermi and Gamow-Teller decay modes, respectively. The selection rules for both Fermi and Gamow-Teller decay are shown in Table 2.1 adapted from Ref. [25].

Table 2.1: β -decay selection rules, adapted from Ref. [25]

Transition Type	$\Delta J = J_f - J_i $	$\pi_i \pi_f$
Fermi	0	+1
Gamow-Teller	1 ($J_i = 0$ or $J_f = 0$)	+1
Gamow-Teller	0,1 ($J_i > 0$ or $J_f > 0$)	+1

Often, a great deal about the underlying physics can be learned from measurement of the β -decay half-life. Denoted as $t_{1/2}$, the half-life is the average time required for half of

the radioactive nuclei in a sample to decay away, and can be expressed in terms of the decay constant, λ , as

$$t_{1/2} = \frac{\ln(2)}{\lambda}. \quad (2.7)$$

Often, several different transitions between the initial state and final states in the daughter contribute to β decay. The decay constant, λ , in Eq. (2.7) is the sum of the decay constants of all β -decay transitions, such that

$$\lambda = \sum_f \lambda_{(if)}, \quad (2.8)$$

where $\lambda_{(if)}$ is the transition probability for a particular transition between the initial parent state, i , and some final state in the daughter nucleus, f . The partial half-life of a particular transition, $t_{1/2}^{(if)}$, is then

$$t_{1/2}^{(if)} = \frac{\ln(2)}{\lambda_{(if)}}, \quad (2.9)$$

which can also be written as

$$t_{1/2}^{(if)} = \frac{t_{1/2}}{BR^{(if)}}, \quad (2.10)$$

where $t_{1/2}$ is the half-life of the initial state, i , and $BR^{(if)}$ is the branching ratio to final state f . The partial half-life can also be expressed in terms of the Fermi and Gamow-Teller reduced transition probabilities, $B(F)$ and $B(GT)$, respectively, as

$$t_{1/2}^{(if)} = \frac{2\pi^3 \hbar^7 \ln 2}{f_0(m_e^5 c^4 G_F^2)(B_F + B_{GT})}, \quad (2.11)$$

where \hbar is Planks constant divided by 2π , m_e is the electron mass, c is the speed of light, G_F is the Fermi coupling constant, and f_0 is the Fermi integral [25]. The Fermi integral

accounts for the Coulomb interaction between the emitted e^- with the daughter nucleus and can be written (using the non-relativistic Primakoff-Rosen approximation) as

$$f_0 \approx \frac{1}{30}(E_0^5 - 10E_0^2 + 15E_0 - 6) \frac{2\pi\alpha Z_f}{1 - e^{-2\pi\alpha Z_f}}, \quad (2.12)$$

where α is the fine structure constant, Z_f is the atomic number of the daughter nucleus, and E_0 is the endpoint energy. The endpoint energy can be written as

$$E_0 = \frac{E_i - E_f}{m_e c^2}, \quad (2.13)$$

where m_e is the electron mass, c is the speed of light, and E_i and E_f are the total energies of the initial and final states, respectively [25]. The reduced transition probabilities, B_F and B_{GT} , are related to the matrix elements, \mathcal{M}_F and \mathcal{M}_{GT} by

$$B_F \equiv \frac{g_V^2}{2J_i + 1} |\mathcal{M}_F|^2 \quad (2.14)$$

and

$$B_{GT} \equiv \frac{g_A^2}{2J_i + 1} |\mathcal{M}_{GT}|^2, \quad (2.15)$$

where g_A and g_V are the axial-vector and vector coupling constants. The reduced matrix elements are defined as

$$\mathcal{M}_F = (\xi_f J_f || \tau || \xi_i J_i) \quad (2.16)$$

and

$$\mathcal{M}_{GT} = (\xi_f J_f || \tau \sigma || \xi_i J_i), \quad (2.17)$$

where τ and σ are the Pauli isospin and spin operators [25], respectively.

The matrix elements contain all the nuclear physics information, and are inversely proportional to the partial half-life. From the partial half-life the comparative half-life ft can be calculated. The comparative half-life is a measure of how probable a particular β decay transition is. Typically the range in ft values is large, and thus they are expressed in \log_{10} scale. A summary of the range of $\log_{10}(f_0t)$ values associated with allowed and various types of forbidden β decay is presented in Table 2.2. It is worth mentioning that the ranges for $\log_{10}(f_0t)$ values in Table 2.2 are guidelines and some overlap exists between transition types.

Table 2.2: Classification of β -decay transitions and associated $\log_{10}(f_0t)$ values, adapted from Ref. [24].

Transition Type	Δl	ΔJ	$\Delta\pi$	$\log f_0t$
Superallowed	0	0	No	2.9 - 3.7
Allowed	0	0,1	No	4.4 - 6.0
First forbidden	1	0,1,2	Yes	6 - 10
Second forbidden	2	1,2,3	No	10 - 13
Third forbidden	3	2,3,4	Yes	≥ 15

Experimentally, the β decay half-life is often determined by fitting the activity of a sample β -decaying nuclei as a function of time. Since β decay follows first order kinetics, the decay rate is proportional to the number of radioactive nuclei present and can be written as

$$\frac{dN}{dt} = -\lambda N, \quad (2.18)$$

where λ is the decay constant, related to the half-life as given in Eq. (2.7). The number of β -decaying nuclei, N , at time, t , is given by

$$N(t) = N_0 e^{-\lambda t}, \quad (2.19)$$

where N_0 is the number of nuclei at time $t = 0$. In a chain of β -decaying nuclei the quantity of parent, daughter, and granddaughter nuclei as a function of time can be determined using

$$N_1(t) = N_{1,t=0}e^{-\lambda_1 t}, \quad (2.20)$$

$$N_2(t) = \left\{ \frac{\lambda_1}{\lambda_2 - \lambda_1} N_{1,t=0} \right\} e^{-\lambda_1 t}, N_{2,t=0} \equiv 0, \quad (2.21)$$

and

$$\begin{aligned} N_2(t) = & \left\{ \frac{\lambda_2}{\lambda_3 - \lambda_1} \frac{\lambda_1}{\lambda_2 - \lambda_1} N_{1,t=0} \right\} e^{-\lambda_1 t} - \left\{ \frac{\lambda_2}{\lambda_3 - \lambda_2} \frac{\lambda_1}{\lambda_2 - \lambda_1} N_{1,t=0} \right\} e^{-\lambda_2 t} \\ & + \left\{ \frac{\lambda_2}{\lambda_3 - \lambda_2} \frac{\lambda_1}{\lambda_3 - \lambda_1} N_{1,t=0} \right\} e^{-\lambda_3 t}, N_{2,t=0} \equiv N_{3,t=0} \equiv 0, \quad (2.22) \end{aligned}$$

[26] where the notation $N_{2,t=0} \equiv 0$ and $N_{3,t=0} \equiv 0$ signifies that no daughter or granddaughter nuclei are present at time zero.

2.1.1 β -Delayed Particle Emission

If the β -decay Q-value is large enough such that states above particle separation energies are populated, the daughter nucleus can emit nucleons or clusters of nucleons. The nuclei of interest in this study are neutron-rich, with Q-values near 12 MeV. The average neutron separation energy of the daughter nucleus is ~ 7.5 MeV, and thus β -delayed neutron emission (βn) is energetically possible. The (βn) process involves β -decaying to neutron-unbound states in the daughter nucleus, which then spontaneously emits a neutron. β -delayed neutron

emission can be written as

$${}^A_Z X_N \rightarrow {}^{A-1}_Z X_{N-1} + n + Q_n, \quad (2.23)$$

where Q_n represents the difference in total energy between the final and initial states. Following β -delayed neutron decay, excited states may be populated in the ${}^{A-1}_Z X_{N-1}$ β -delayed neutron daughter, which then decay by emitting electromagnetic radiation.

Typically, delayed neutron emission dominates over electromagnetic decays for states above the neutron separation energy. However, neutron emission can be hindered if emission of a high l -value neutron is required, or if the nuclear structure of the neutron-unbound excited state in the daughter is different than that of the beta-delayed neutron daughter. In these circumstances, electromagnetic decays can compete with neutron emission [27–29].

2.2 γ Decay

Typically, β decay populates one or more excited states in the daughter nucleus, below the nucleon separation energies, which then decay predominately by γ -ray emission. These γ rays are commonly referred to as β -delayed γ rays.

A γ -ray transition connects an initial state, i , to a final state, f , and carries with it an integer amount of angular momentum, called the multipolarity, λ , which can have values of

$$|(J_i - J_f)| \leq \lambda \leq (J_i + J_f), \quad (2.24)$$

with $\lambda \geq 1$. γ -rays have an intrinsic spin of one, therefore $\lambda = 0$ transitions are forbidden.

The transition rate for a given multipolarity, λ , of type, σ (electric or magnetic), can be

expressed as

$$T_{fi}^{(\sigma\mu)} = \sum_{m_i\mu m_f} \frac{2}{\epsilon_0\hbar} \frac{\lambda+1}{\lambda[(2\lambda+1)!!]^2} \left(\frac{E_\gamma}{\hbar c}\right)^{(2\lambda+1)} B(\sigma\lambda; \xi_i J_i \rightarrow \xi_f J_f), \quad (2.25)$$

where ϵ_0 is permittivity of free space, \hbar is Plank's constant divided by 2π , c is the speed of light, E_γ is the energy of the transition, and $B_{\sigma\lambda}$ are the reduced electromagnetic transition probabilities. The reduced electromagnetic transition probabilities are related to the matrix elements containing the magnetic and electric tensor operators, $\mathcal{M}_{\sigma\lambda}$, by

$$B(\sigma\lambda; \xi_i J_i \rightarrow \xi_f J_f) = \frac{1}{2J_i + 1} |(\xi_f J_f || \mathcal{M}_{\sigma\lambda} || \xi_i J_i)|^2. \quad (2.26)$$

The transition probability is related to the half-life of the transition by

$$t_{1/2} = \frac{\ln 2}{T_{fi}^{(\sigma\mu)}}. \quad (2.27)$$

Since the half-life of the decaying state is inversely proportional to the transition probability, and thus the matrix elements, which contain all of the information regarding the wavefunctions of the initial and final states, measurements of excited state lifetimes can directly probe nuclear structure. For example, the reduced transition probability for an $E2$ transition, in units of $e^2 b^2$, can be determined from the half-life using

$$B(E2 \uparrow; \xi_i J_i \rightarrow \xi_f J_f) = \frac{28.3 \times 10^{13} (BR)}{(t_{1/2})(E_\gamma)^5 (1 + \alpha)}, \quad (2.28)$$

from Ref. [30], where BR is the branching ratio of the $E2$ transition of interest, $t_{1/2}$ is the half-life of the decaying state in ps, E_γ is the transition energy in keV, and α is the

internal conversion coefficient, discussed in the next section.

The direction of the transition (i.e. $0^+ \rightarrow 2^+$ or $2^+ \rightarrow 0^+$) is important for determining $B(E2)$ values. In the present, work the $B(E2 \downarrow)$ values will be deduced from lifetime measurements. $B(E2 \uparrow)$ values are related to $B(E2 \downarrow)$ by

$$B(E2 \uparrow) = \frac{2J_f + 1}{2J_i + 1} B(E2 \downarrow). \quad (2.29)$$

The reduced transition probability can be simplified using a single-particle limit, referred to as Weisskopf limits, where all γ -ray transitions are presumed to result from the redistribution of a single nucleon within the nucleus. In the single-particle limit, the expressions for the reduced transition probabilities become

$$B_W(E\lambda) = \frac{1.2^{2\lambda}}{4\pi} \left[\frac{3}{(\lambda + 3)} \right]^2 A^{2\lambda/3} e^2, (\text{fm})^{2\lambda} \quad (2.30)$$

and

$$B_W(M\lambda) = \frac{10}{\pi} (1.2)^{(2\lambda-2)} \left[\frac{3}{(\lambda + 3)} \right]^2 A^{(2\lambda-2)/3} \left(\frac{\hbar}{2m_p c} \right)^2 e^2 (\text{fm})^{2\lambda-2}, \quad (2.31)$$

where A is the mass number of the nucleus, \hbar is Plank's constant divided by 2π , c is the speed of light, m_p is the mass of the proton, E_γ is the energy of the transition. The resulting reduced transition probabilities are known as Weisskopf single-particle estimates. The Weisskopf single-particle estimates for the reduced transition probabilities are typically good to within a factor of 10 for spherical nuclei [24]. A summary of γ -ray transition selection rules, with Weisskopf estimates, are shown in Table 2.3 for the first four multipolarities of electric and magnetic transition types.

Table 2.3: Selection rules and electromagnetic transition rates, assuming a single-particle transition from an initial state to a final state, for the first four multiplicities of electric and magnetic transitions. λ is the multipolarity of the transition, $\Delta\pi$ is the change in parity between the initial and final states, E_γ is the γ -ray energy in MeV, and A is the mass number of the nucleus. [24].

Name	Radiation Type	λ	$\Delta\pi$	$T_W(\sigma\lambda) \text{ (s}^{-1}\text{)}$
Electric dipole	$E1$	1	Yes	$1.03 \times 10^{14} A^{2/3} E_\gamma^3$
Magnetic dipole	$M1$	1	No	$3.15 \times 10^{13} E_\gamma^3$
Electric quadrupole	$E2$	2	No	$7.28 \times 10^7 A^{4/3} E_\gamma^5$
Magnetic quadrupole	$M2$	2	Yes	$2.24 \times 10^7 A^{2/3} E_\gamma^5$
Electric octupole	$E3$	3	Yes	$3.39 \times 10^1 A^2 E_\gamma^7$
Magnetic octupole	$M3$	3	No	$1.04 \times 10^1 A^{4/3} E_\gamma^7$
Electric hexadecapole	$E4$	4	No	$1.07 \times 10^{-5} A^{8/3} E_\gamma^9$
Magnetic hexadecapole	$M4$	4	Yes	$3.27 \times 10^{-6} A^2 E_\gamma^9$

The transition rates presented in Table 2.3 decrease as multipolarity increases. Therefore, γ -rays of lower multiplicities are generally more probable for transitions of a given energy. In addition, if an excited state can decay to multiple final states with the same spin and parity the highest energy transition will have the largest transition probability, provided that no strong differences in the matrix elements exist.

2.3 Internal Conversion

Another decay process available to excited nuclear states, which competes with γ -ray decay, is internal conversion. In this process, the excited nucleus interacts electromagnetically with an orbital electron and ejects the electron. The vacancy created by the ejected electron is filled by the outer orbital electrons, which results in X-ray or Auger electron emission. Internal conversion electrons emitted from a given transition are mono-energetic with an energy, E_{IC} , of

$$E_{IC} = (E_i - E_f) - E_{BE}, \quad (2.32)$$

where E_{BE} is the binding energy of the ejected orbital electron and E_i and E_f are the energies of the initial and final states, respectively.

The competition between internal conversion and γ -ray emission is characterized by the internal conversion coefficient, α , defined as

$$\alpha = \frac{\text{number of internal-conversion decays}}{\text{number of } \gamma\text{-ray decays}}. \quad (2.33)$$

Conversion electrons can originate from any of the K, L, M... electron shells but a K-shell electron is most probable since these electrons have the highest probability to be found at the nucleus. The total internal conversion coefficient, α_{total} , is the sum of the conversion coefficients of all available electron shells such that

$$\alpha_{\text{total}} = \alpha_{\text{K}} + \alpha_{\text{L}} + \alpha_{\text{M}} + \dots \quad (2.34)$$

Expressions for internal conversion coefficients have been derived from atomic physics and approximate values can be obtained from

$$\alpha(E\lambda) = \frac{Z^3}{n^3} \left(\frac{\lambda}{\lambda + 1} \right) \left(\frac{e^2}{4\pi\epsilon_0\hbar c} \right)^4 \left(\frac{2m_e c^2}{E} \right)^{\lambda+5/2} \quad (2.35)$$

and

$$\alpha(M\lambda) = \frac{Z^3}{n^3} \left(\frac{e^2}{4\pi\epsilon_0\hbar c} \right)^4 \left(\frac{2m_e c^2}{E} \right)^{\lambda+3/2}, \quad (2.36)$$

[24] where λ is the multipolarity of the transition, Z is the atomic number of the nucleus, n is the principal quantum number of the ejected orbital electron, m_e is the mass of the electron, c is the speed of light, ϵ_0 is permittivity of free space, \hbar is Plank's constant divided

by 2π , e is the elementary charge, and E is the energy of the transition [24]. From equations (2.35) and (2.36), one can conclude that internal conversion is most probable in heavy nuclei for lower energy transitions with higher multipolarities.

2.4 Internal Pair Formation

A third electromagnetic-decay process that competes with both γ -ray emission as well as internal conversion is internal pair formation. Internal pair formation is a process by which an electron-positron pair is directly created. The transition energy must be above 1.022 MeV to produce the electron-positron pair, and any additional energy is shared equally among the electron and positron as kinetic energy. The emitted electron and positron interact with the surrounding materials, losing energy until the positron annihilates with an electron, creating two 511-keV photons emitted in opposite directions.

Typically, the probability of internal pair production is several orders of magnitude reduced when compared with γ -ray decay. However, internal pair production is important when γ -ray decay is forbidden, such as for transitions between two 0^+ states.

2.5 $E0$ Transitions

Electromagnetic transitions that connect two states with identical spin and parities can decay via electric monopole ($E0$) transitions. $E0$ transitions take place via internal conversion or internal pair production. Typically $E0$ transitions are only observed in the decay between two 0^+ states since higher multipolarity γ -ray decays often dominate when the initial and final states have, equal, nuclear spins greater than zero. The strength of an electric monopole

transition is characterized by a dimensionless quantity, $\rho^2(E0)$, which can be written as

$$\rho^2(E0) = \left| \frac{\langle \psi_f | \hat{T}(E0) | \psi_i \rangle}{eR^2} \right|^2, \quad (2.37)$$

where ψ_i and ψ_f are the initial and final states, e is the fundamental unit of charge, R is the mean nuclear radius ($R \approx 1.2A^{1/3}$ fm), and $\hat{T}(E0)$ is the electric monopole operator defined by

$$\hat{T}(E0) = \sum_k e_k r_k^2, \quad (2.38)$$

where e_k is the effective charge for the k^{th} nucleon and r_k is the position of the k^{th} nucleon relative to the center of mass of the nucleus [31]. $\rho^2(E0)$ contains all the information about the final and initial states. Because the value of $\rho^2(E0)$ is often between 10^{-3} and 10^{-1} , it is commonly reported as $10^3 \rho^2(E0)$. Databases of $\rho^2(E0)$ values between 0^+ states across the chart of the nuclides are available [32].

The transition probability for an $E0$ transition, $\lambda(E0)$, can be written as

$$\lambda(E0) = \lambda_{IC}(E0) + \lambda_{\pi}(E0) = \frac{\ln 2}{T_{1/2}(E0)} = \rho^2(E0) \times [\Omega_{IC}(E0) + \Omega_{\pi}(E0)], \quad (2.39)$$

where $\lambda_{IC}(E0)$ and $\lambda_{\pi}(E0)$ are the partial transition probabilities for internal conversion and internal pair production, respectively. $\rho^2(E0)$ is the electric monopole transition strength. The quantities $\Omega_{IC}(E0)$ and $\Omega_{\pi}(E0)$ are the “electronic factors” [33] for internal conversion and pair production, respectively, and $T_{1/2}(E0)$ is the partial half-life of the $E0$ transition.

Electronic factors depend on the atomic number of the nucleus and the transition energy but are independent of nuclear properties. Tabulations of the electronic factors can be found in the BrIcc database [34].

In the limits of a simple two-level mixing model, $\rho^2(E0)$ can be related to the difference in deformation between the two 0^+ states. In this approach, each of the 0^+ states is described as a linear combination of two different configurations of nucleons each with a 0^+ spin and parity but with a different intrinsic quadrupole moment. In the two-level mixing model the two 0^+ states $|0_i^+\rangle$ and $|0_f^+\rangle$ can be expressed as

$$|0_i^+\rangle = \cos(\theta)|0_s^+\rangle - \sin(\theta)|0_d^+\rangle \quad (2.40)$$

and

$$|0_f^+\rangle = \sin(\theta)|0_s^+\rangle + \cos(\theta)|0_d^+\rangle, \quad (2.41)$$

where θ is the mixing angle, and $|0_s^+\rangle$ and $|0_d^+\rangle$ are two different configurations of nucleons associated with spherical and deformed shapes, respectively [31]. In the limit of maximal mixing $\sin(\theta) = \cos(\theta) = 1/\sqrt{2}$. In this model, Eq. (2.37) can be written as

$$\rho^2(E0) = \left(\frac{1}{eR^2} [[\cos^2(\theta) - \sin^2(\theta)]\langle 0_d^+ | \hat{T}(E0) | 0_s^+ \rangle + \cos(\theta)\sin(\theta)(\langle 0_s^+ | \hat{T}(E0) | 0_s^+ \rangle - \langle 0_d^+ | \hat{T}(E0) | 0_d^+ \rangle)] \right)^2. \quad (2.42)$$

In Eq. (2.42), if no mixing occurs the second term is zero, since $\cos(0)\sin(0) = 0$ and the matrix element $\langle 0_d^+ | \hat{T}(E0) | 0_s^+ \rangle$ from the first term will be small due to the small radial overlap of the spherical and deformed configuration wavefunctions. Therefore, $\rho^2(E0)$ becomes very small in the absence of mixing.

On the other hand, in the case of maximal mixing the first term becomes zero, since

$\sin^2(\theta) = \cos^2(\theta)$, leaving

$$\rho^2(E0) \approx \left[\cos(\theta)\sin(\theta)(\langle 0_s^+ | \hat{T}(E0) | 0_s^+ \rangle - \langle 0_d^+ | \hat{T}(E0) | 0_d^+ \rangle) \right]^2. \quad (2.43)$$

Using Eqs. (2.43) and (2.38), $\rho^2(E0)$ can be expressed as a difference in mean-square charge radii, $\Delta\langle r^2 \rangle$, using

$$\rho^2(E0) = \frac{Z^2}{e^2 R^4} \cos^2(\theta)\sin^2(\theta) \left[\Delta\langle r^2 \rangle \right]^2. \quad (2.44)$$

The larger the difference in the $\langle r^2 \rangle$ the larger the value of $\rho^2(E0)$.

While maximal mixing is an useful approximation, the mixing angle, θ , can be deduced from electric quadrupole ($E2$) transition probabilities [35]. The $E2$ transition between the 2^+ and 0^+ states involves only the deformed admixture to each wavefunction, and as such, it follows from Eqs. (2.40) and (2.41) that

$$B(E2; 2^+ \rightarrow 0_i^+) = B(E2; 2_d \rightarrow 0_d)\cos^2(\theta) \quad (2.45)$$

and

$$B(E2; 2^+ \rightarrow 0_f^+) = B(E2; 2_d \rightarrow 0_d)\sin^2(\theta). \quad (2.46)$$

Therefore, within the two-level mixing model

$$\tan^2(\theta) = \frac{B(E2; 2^+ \rightarrow 0_f^+)}{B(E2; 2^+ \rightarrow 0_i^+)}, \quad (2.47)$$

such that the mixing between two 0^+ states can be deduced entirely from spectroscopic information [35], but the $2^+ \rightarrow 0^+$ transitions must be accessible.

Chapter 3

Experimental Description

In this chapter, two complimentary experiments performed at the National Superconducting Cyclotron Laboratory (NSCL) are described. The first experiment was e14039, for which the primary goals were the first observation of the $2_1^+ \rightarrow 0_2^+$ transition in ^{68}Ni , and a search for the 0_2^+ state in ^{70}Ni . The second experiment, e14057, was performed to measure level lifetimes of excited states, particularly the 0_3^+ state, in ^{68}Ni . The combined results of these two experiments yield a comprehensive investigation of shape coexistence in ^{68}Ni and ^{70}Ni and provide extensive knowledge about the low-energy level structure of ^{68}Ni and neighboring nuclei.

This chapter is divided into several sections. Section 3.1 explains the beam production and delivery techniques at the National Superconducting Laboratory (NSCL). The experimental end stations used for e14039 and e14057 are presented in sections 3.2 and 3.3, respectively. Section 3.4 describes the NSCL Digital Acquisition System (DDAS) used to instrument all detectors. Detailed descriptions of all detector systems including the necessary calibration and analysis techniques are presented in Sections 3.5 through 3.8.

3.1 Isotope Production, Identification, and Delivery at the National Superconducting Cyclotron Laboratory (NSCL)

The National Superconducting Cyclotron Laboratory (NSCL) produces exotic isotopes through projectile fragmentation. A schematic representation of the Coupled Cyclotron Facility (CCF) at NSCL is shown in Fig. 3.1. A stable primary ion beam is produced and accelerated by the coupled cyclotrons [36] to an energy of order of 100 MeV/nucleon. The primary beam is then impinged on a stationary stable target, typically Be, creating a wide variety of both stable and radioactive nuclei.

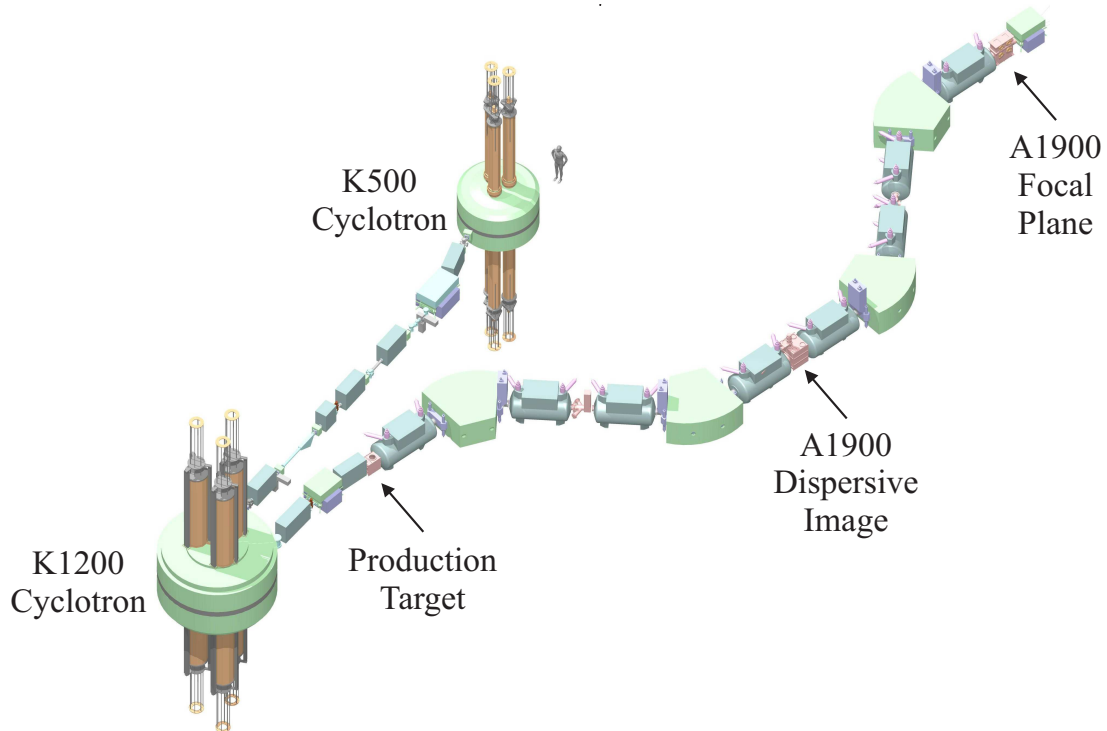


Figure 3.1: Schematic representation of the Coupled Cyclotron Facility (CCF) [36] and A1900 fragment separator [37] at NSCL

Isotopes of interest, produced in the fragmentation reaction, are selected for transmission

to the experimental end station by the A1900 fragment separator [37] based on their magnetic rigidity, $B\rho$, defined as the ratio of momentum, p , to atomic charge, q . Due to the kinematics of fragmentation reactions, products entering the A1900 all possess nearly the same velocity, slightly below that of the primary beam velocity [24], which means separation by $B\rho$ selects species with similar mass to charge ratio. To enhance selectivity, a wedge-shaped degrader was placed at the dispersive image of the A1900 fragment separator. Energy loss through the degrader is proportional to the square of the atomic number of the ion, Z^2 , so that ions with different numbers of protons experience different energy loss. Following the degrader, ions with similar mass-to-charge ratios but different Z will have different momenta and a second $B\rho$ selection, coupled with slits located at the A1900 focal plane, is used to remove unwanted fragments. Slits located at each intermediate image position of the A1900 serve to control the overall momentum acceptance, $\Delta p/p$, which has a maximum value of 5%.

Identification of ions produced by the CCF is performed using standard ΔE -TOF techniques. These techniques involve measuring the energy loss (ΔE) of ions traveling through one or more silicon PIN detectors along with the Time-Of-Flight (TOF) between a scintillator in the A1900 fragment separator and the first Si PIN detector at experimental end station. The TOF is proportional to A/q while (ΔE) is proportional to Z^2 such that isotopic information can be obtained by plotting ΔE vs. TOF. Each of the two experiments employed three silicon PIN detectors upstream of the central implantation detector for particle identification.

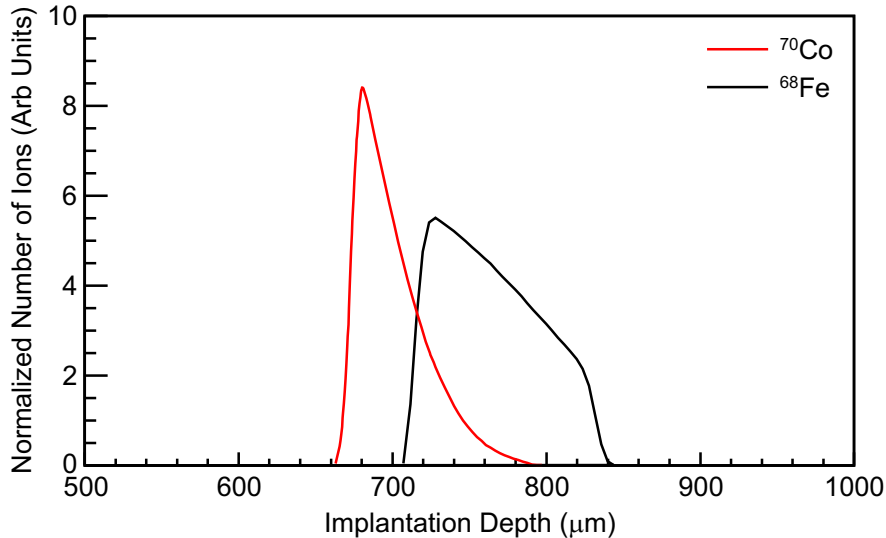


Figure 3.2: Normalized implantation depth distributions for ^{68}Fe and ^{70}Co ions deposited inside the GeDSSD crystal during e14039.

3.2 NSCL e14039 Experimental Setup

The setup for NSCL experiment e14039 consisted of the Germanium Double Sided Strip Detector (GeDSSD), described in Section 3.5, surrounded by sixteen detectors from the Segmented Germanium Array (SeGA), described in Section 3.7. The SeGA detectors were arranged into two concentric rings of eight detectors surrounding the GeDSSD, with the face of each detector in close proximity (~ 1 cm) to the side of the GeDSSD cryostat. Approximately 1 m upstream of the GeDSSD was a set of three silicon PIN detectors with thicknesses of 996, 488, and 503 μm .

Ions of interest were created by fragmenting a ^{76}Ge primary beam at 130 MeV/A on a 282 $\mu\text{g}/\text{cm}^2$ ^9Be target. The beam delivered to the experimental end station passed through the silicon PIN detectors, a thin kapton window, one to two cm of air, and the cryostat of the GeDSSD. Ions were implanted into the 1-cm thick GeDSSD crystal to a depth of roughly 750 microns. The depth distributions of the implanted ^{68}Fe and ^{70}Co ions inside the GeDSSD crystal, as calculated using LISE++ [38], are presented in Fig. 3.2. LISE++ calculations

were performed using the A1900 magnet settings (Segment 1 and 2 $B\rho = 4.16$ Tm, Segment 3 and 4 $B\rho = 3.92$ Tm) and knowledge of the materials upstream of the detector.

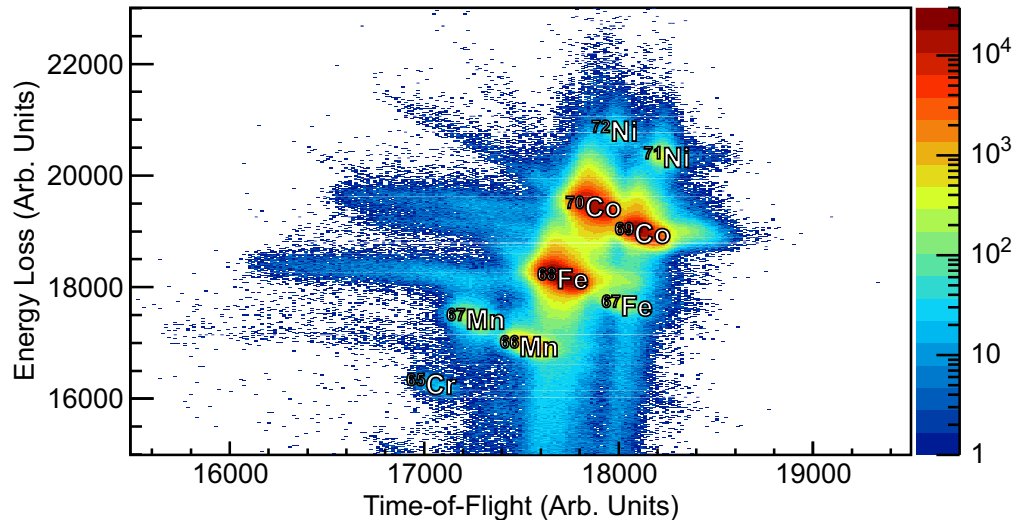


Figure 3.3: Particle identification plot for ions deposited in the GeDSSD crystal during e14039. The data shown were obtained from the energy loss information provided by the first PIN detector and the TOF measured between the extended focal plane scintillator in the A1900 and the first PIN detector. As a condition on the plot, the GeDSSD had to record coincident implant energy deposition in at least one front and one back strip.

Using the techniques discussed in Section 3.1, the particle identification plot for e14039, obtained from the energy loss information provided by the first PIN detector and the TOF measured between the extended focal plane scintillator in the A1900 and the first PIN detector at the experimental end station, was created, and is shown in Fig. 3.3. Energy from the implanted ion must be recorded on both the front and back strips of the planar GeDSSD for the ion to be recorded in the particle identification plot in Fig. 3.3.

Graphical cuts were made on each isotope spot in Fig. 3.3 and integrated to provide the quantity of each isotope deposited inside the GeDSSD crystal during e14039, shown in Table 3.1.

Table 3.1: Number of ions of each isotope implanted into the GeDSSD crystal over the nine days of beamtime during e14039.

Isotope	Number of Implants
^{65}Cr	$3.67(19) \times 10^3$
^{66}Mn	$2.84(14) \times 10^4$
^{67}Mn	$5.75(29) \times 10^4$
^{67}Fe	$5.55(28) \times 10^4$
^{68}Fe	$6.10(30) \times 10^6$
^{69}Co	$3.21(16) \times 10^6$
^{70}Co	$3.93(20) \times 10^6$
^{71}Ni	$3.91(19) \times 10^4$
^{72}Ni	$1.30(6) \times 10^4$

3.3 NSCL e14057 Experimental Setup

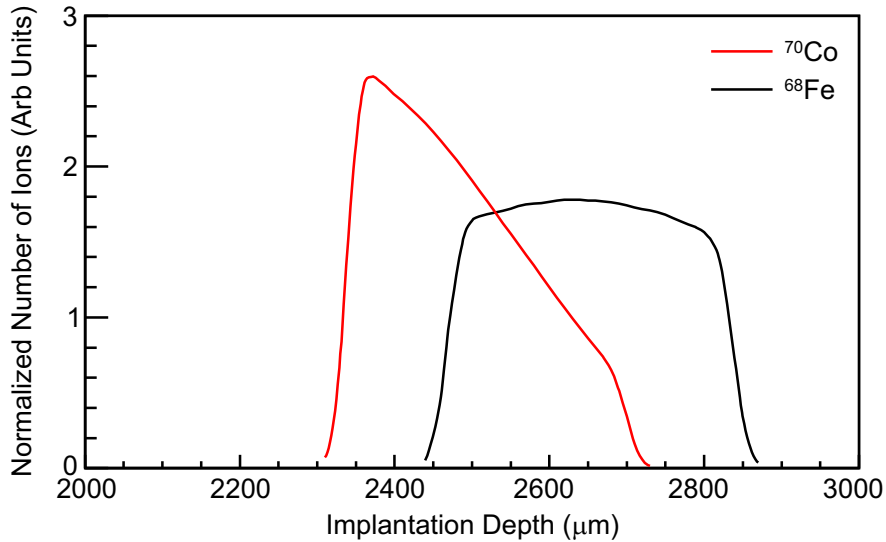


Figure 3.4: Normalized implantation depth distributions for ^{68}Fe and ^{70}Co ions deposited inside the segmented plastic scintillator during e14057.

In NSCL experiment e14057, a segmented plastic scintillator coupled to a position-sensitive photomultiplier tube (PSPMT), described in Section 3.6, was used as the central implantation detector in place of the GeDSSD to improve the intrinsic time resolution for detection of β -decay electrons. This implantation detector assembly was placed into a light-tight, thin-walled, cylindrical aluminum chamber. Ten LaBr₃ detectors, described in Section

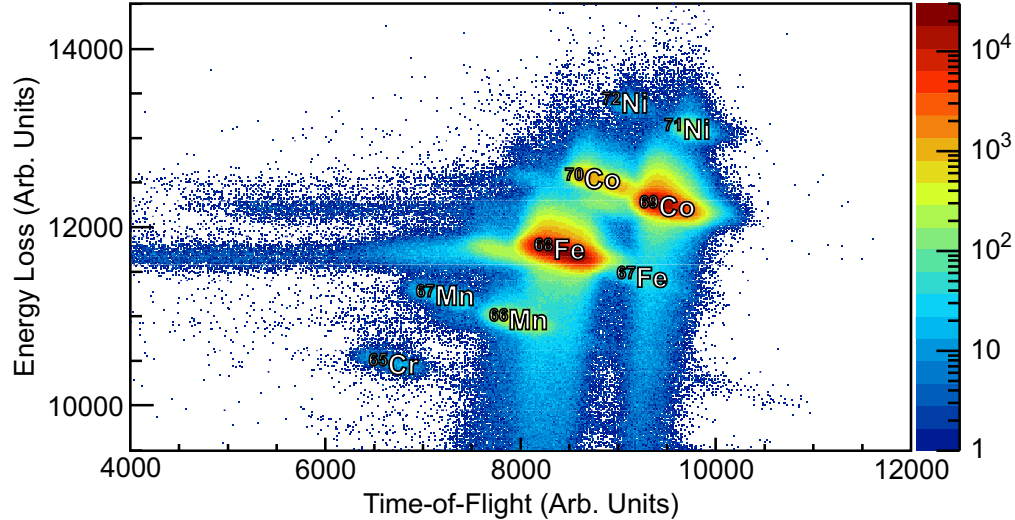


Figure 3.5: Particle identification plot for ions deposited in the segmented plastic scintillator during e14057. The data shown were obtained from the energy loss information provided by the first PIN detector and the TOF measured between the scintillator at the dispersive image of the A1900 and the first PIN detector. As a condition on the plot, the segmented plastic scintillator had to record implant energy deposition.

3.8, were positioned radially surrounding the chamber with the face of each LaBr₃ detector located ~ 1 mm away from the outside of the chamber. The LaBr₃ detectors were arranged into two rings, one with eight detectors centered on the segmented plastic scintillator, and one with the remaining two detectors located slightly downstream of the segmented plastic scintillator.

The aluminum chamber, with its enclosed detectors, and the frame holding the surrounding ten LaBr₃ detectors were designed such that sixteen SeGA detectors could be utilized in the same configuration as e14039. The three PIN detectors used in e14039 were placed in the same location ~ 1 m upstream of the segmented plastic scintillator.

Ions of interest were created by fragmenting a ^{76}Ge primary beam at 130 MeV/A on a $282 \mu\text{g}/\text{cm}^2$ ^9Be target. The beam delivered to the experimental end station passed through the silicon PIN detectors followed by a thin kapton window before entering the aluminum chamber. The chamber was at atmospheric pressure meaning the beam encountered ~ 10

Table 3.2: Number of ions of each isotope implanted into the segmented plastic scintillator over the six days of beamtime during e14057.

Isotope	Number of Implants
^{65}Cr	$4.59(24) \times 10^3$
^{66}Mn	$1.32(6) \times 10^5$
^{67}Mn	$1.41(7) \times 10^4$
^{67}Fe	$2.55(13) \times 10^4$
^{68}Fe	$7.94(40) \times 10^6$
^{69}Co	$4.22(21) \times 10^6$
^{70}Co	$4.65(23) \times 10^5$
^{71}Ni	$3.65(18) \times 10^4$
^{72}Ni	$5.81(30) \times 10^3$

cm of air before passing through the silicon DSSD and depositing into the segmented plastic scintillator. Ions were implanted to a depth of roughly 2500 microns into the 1-cm thick plastic scintillator. The depth distributions of the implanted ^{68}Fe and ^{70}Co ions inside the GeDSSD crystal, as calculated using LISE++ [38], are presented in Fig. 3.4. LISE++ calculations were performed using the A1900 magnet settings (Segment 1 and 2 $B\rho = 4.16$ Tm, Segment 3 and 4 $B\rho = 3.86$ Tm) and knowledge of the materials upstream of the detector.

Using the techniques discussed in Section 3.1, the particle identification plot for e14057, obtained from the energy loss information provided by the first PIN detector and the TOF measured between a scintillator located at dispersive image of the A1900 and the first PIN detector, was created, and is shown in Fig. 3.5. Energy from the implanted ion must be recorded in the segmented plastic scintillator for the ion to be recorded in the particle identification plot in Fig. 3.5.

Graphical cuts were made on each isotope in Fig. 3.5 and integrated to provide the number of ions of each isotope deposited inside the segmented plastic scintillator during e14057, shown in Table 3.2.

3.4 NSCL Digital Data Acquisition System (DDAS)

In both experiments, the NSCL Digital Data Acquisition System (DDAS) [39] was used to instrument all detectors and the system’s capabilities played a critical role in accomplishing the experimental objectives. DDAS is a modular system comprised of 16-channel, FPGA-programmable modules, existing in three varieties: 12-bit, 100 Mega-Sample Per Second (MSPS), 14-bit, 250 MSPS, and 12-bit, 500 MSPS. Each module type has two hardware gain settings. The (low-, hi-) gain settings have dynamic ranges of (0.5 V, 1.2 V), (1 V, 2 V), and (1 V, 4 V) for the 100-, 250-, and 500-MSPS modules, respectively. DDAS modules of any variety can coexist in the same crate with up to 13 modules per crate, and up to 8 crates can be synchronized together.

There are several benefits of DDAS, realized simultaneously, over analog electronics, including lower-energy thresholds, unique triggering conditions, large dynamic range from digital filtering, nearly zero acquisition dead time, and the ability to record the detector signal as a function of time (referred to as “trace capture”).

3.4.1 Triggering

Triggering in the modules is performed using a leading-edge trigger on the response of a symmetric trapezoidal filter algorithm, which is referred to as the “trigger filter”. The trigger-filter response, TF , is calculated from the digitized detector signal, Tr , using Eq. (3.1) by taking the difference of two summing regions, both of length L , and separated by a gap G .

$$TF[i] = \sum_{i=t-L+1}^t Tr[i] - \sum_{i=t-2L-G+1}^{t-L-G} Tr[i] \quad (3.1)$$

The response of the trigger-filter algorithm, shown in dark red, when applied to a digitized signal from the GeDSSD, shown in black, is presented in Fig. 3.6. Superimposed is a black dashed line representing the user-defined trigger-filter threshold.

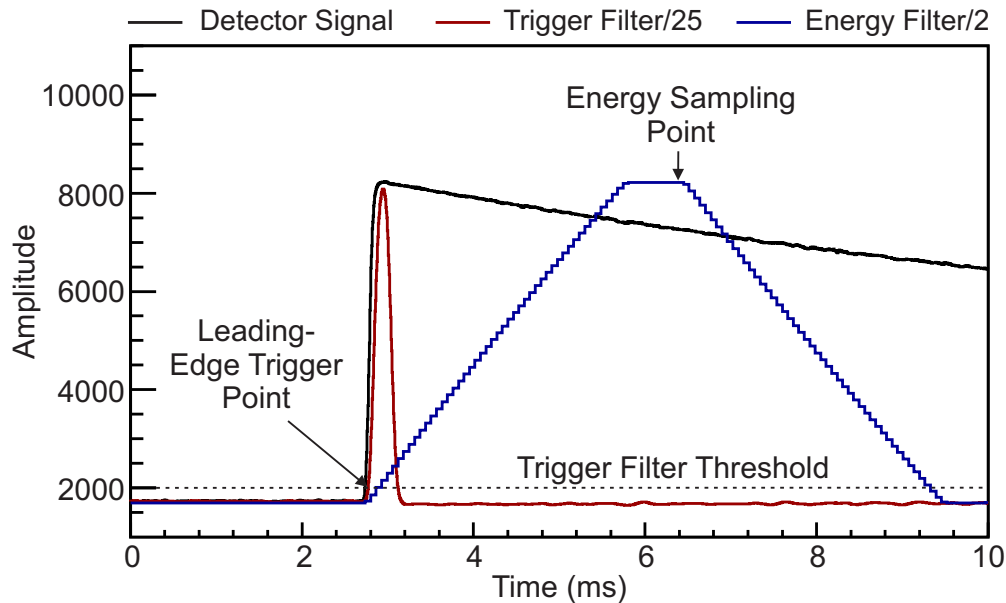


Figure 3.6: Example of DDAS digital filtering algorithms. A sample detector signal acquired from the planar GeDSSD by a 14-bit 250 MSPS is shown in black. The response of the DDAS trigger-filter algorithm is shown in dark red along with the user-defined trigger filter threshold illustrated as a black dashed line. Shown in dark blue is the response of the DDAS energy filter algorithm. Key points in time related to triggering and energy extraction are labeled.

When the amplitude of the trigger filter crosses the user-defined threshold, the system triggers, and, upon validation of the trigger, records the event. In leading-edge triggering, the time associated with each event will have a native precision of 10 ns, 8 ns, and 10 ns for the 100 MSPS, 250 MSPS, and 500 MSPS modules, respectively. These values differ from the naive prediction of the digitizer’s clock period due to parallel processing necessitated by FPGA bandwidth limitations.

Trigger validation can be configured in a variety of ways to suit the needs of the experiment. The least complicated method is a free-running channel-by-channel mode, where all

events with a trigger-filter response above threshold are validated without any additional requirements. DDAS can also require an external validation, where an external gate, of user-defined length and delay, is presented to the module and defines a window of time in which triggers can be validated.

3.4.2 Energy Extraction

Energy extraction in DDAS is accomplished by employing a second, simultaneous, symmetric, trapezoidal-filter algorithm that is referred to as the “energy filter”. The response of the energy filter, EF , is given by Eq. (3.2) and formulated in Ref. [40]. In contrast with the trigger filter, the energy filter corrects for the exponential decay of the preamplifier, yielding a trapezoidal-shaped response. The energy filter is described by:

$$EF[i] = a_0 \left[\sum_{i=t-L+1}^t Tr[i] \right] + a_g \left[\sum_{i=t-L-G+1}^{t-L} Tr[i] \right] + a_1 \left[\sum_{i=t-2L-G+1}^{t-L-G} Tr[i] \right] - kB, \quad (3.2)$$

where

$$a_0 = \frac{(b_1)^L}{(b_1)^L - 1}, \quad (3.3)$$

$$a_g = 1, \quad (3.4)$$

and

$$a_1 = -\frac{1}{(b_1)^L - 1}, \quad (3.5)$$

with

$$b_1 = \text{Exp} \left[\frac{-\Delta t}{\tau} \right]. \quad (3.6)$$

In Eqs. (3.2) through (3.5), the digitized detector waveform, or trace, is denoted as Tr while the characteristic length and gap of the energy filter are L and G , respectively. The coefficients a_0 , a_g , and a_1 that multiply the running sums in Eq. (3.2) are functions of L and a parameter b_1 , defined in Eq. (3.6), which depends on the sampling period, Δt ,

and the preamplifier decay constant τ . The background is accounted for in the response of the algorithm by subtracting off the baseline value, B , multiplied by a constant, k , which depends on the values of a_0 , a_g , and a_1 .

The response of the energy filter is shown in dark blue in Fig. 3.6. The rise time and length of the flat top are fixed by L and G , respectively, and the amplitude of the trapezoidal response is proportional to the amplitude of the detector signal. When DDAS triggers, denoted by the “Leading-Edge Trigger Point” in Fig. 3.6, the system waits a period of time, defined as $2L + G - 1$, to sample the response of the energy filter, shown as the “Energy Sampling Point” in Fig. 3.6. The amplitude of the energy filter at the “Energy Sampling Point” is recorded as the extracted energy. This method samples the energy filter in the “flat-top” region where there is minimal variation, yielding enhanced energy resolution.

3.4.3 Fast Timing Capabilities of DDAS

In addition to extracting high-resolution energy information from detector signals, DDAS can be used to perform simultaneous, high-resolution, timing measurements. A digital constant fraction discriminator (CFD) is used to extract time information with precision greater than the ADC clock period. The digital CFD employed in DDAS is formulated in Ref. [41] and described by Eq. (3.7).

$$CFD[i] = f * \left[\sum_{i=k}^{k-L} Tr[i] - \sum_{i=k-2L+G}^{k-L-G} Tr[i] \right] - \left[\sum_{i=k-D-L}^{k-D} Tr[i] - \sum_{i=k-D-2L-G}^{k-D-L-G} Tr[i] \right] \quad (3.7)$$

In Eq. (3.7), the CFD is characterized by four parameters. There are two running sums both characterized by a length, L , separated by a gap, G . The CFD fraction is f and the

CFD delay is D .

The response of the digital CFD algorithm, shown in red, to a LaBr₃ detector signal, shown in black, acquired using a 500-MSPS module, is presented in Figure 3.7. At the present time, the 500-MSPS module firmware fixes the CFD parameters to be $f = 1$, $D = 5$, $L = 5$, and $G = 1$. These values were chosen by the manufacturer to optimize the algorithm for fast scintillator detectors. Details of a method designed to optimize the timing properties of the digital CFD in the 100- and 250-MSPS modules can be found in Ref. [42].

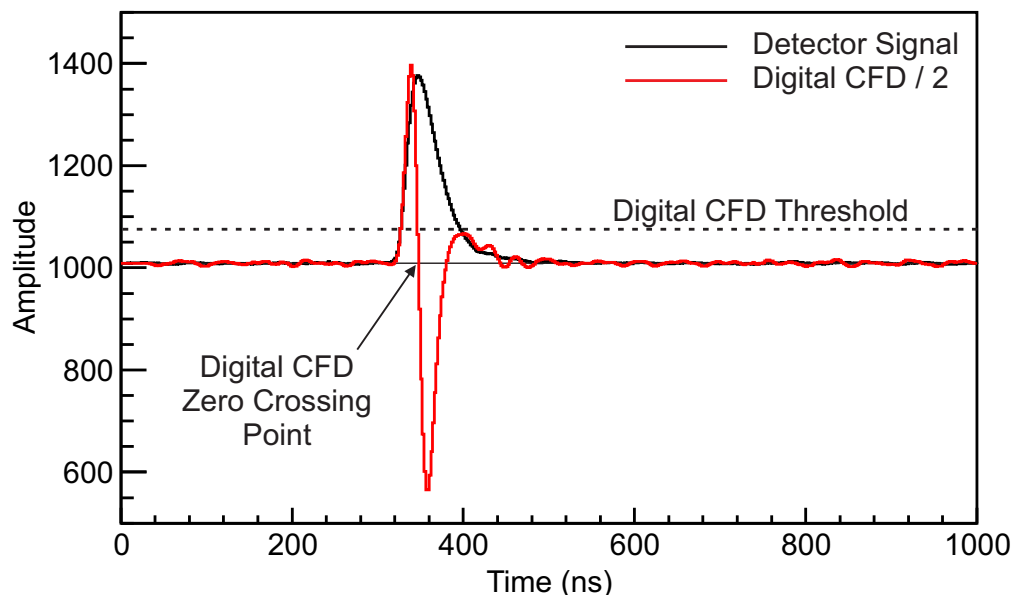


Figure 3.7: Example of the DDAS digital constant fraction discriminator (CFD) algorithm. A sample detector signal acquired from a LaBr₃ detector by a 12-bit 500 MSPS is shown in black. The response of the DDAS CFD algorithm is shown in red along with the user-defined CFD threshold illustrated as a black dashed line. Key points in time related to precision time extraction are labeled.

The CFD time is extracted from the CFD response, shown in red in Fig. 3.7, using a linear interpolation across the points directly before and after the CFD zero crossing point. If the CFD response either does not cross the CFD threshold or does not zero cross within 32 ADC clock periods (64 ns in the present example) of crossing the CFD threshold, a 0 value is reported for the CFD time. The CFD algorithms employed by DDAS result in a nearly

negligible contribution to the detector system time resolution, provided signal amplitudes occupy $>10\%$ of the ADC dynamic range. Figure 3.8 shows the DDAS time resolution for simulated LaBr_3 detector type signals, generated by a Agilent 33522A arbitrary waveform generator, as a function of input signal amplitude. Further details can be found in Ref. [42].

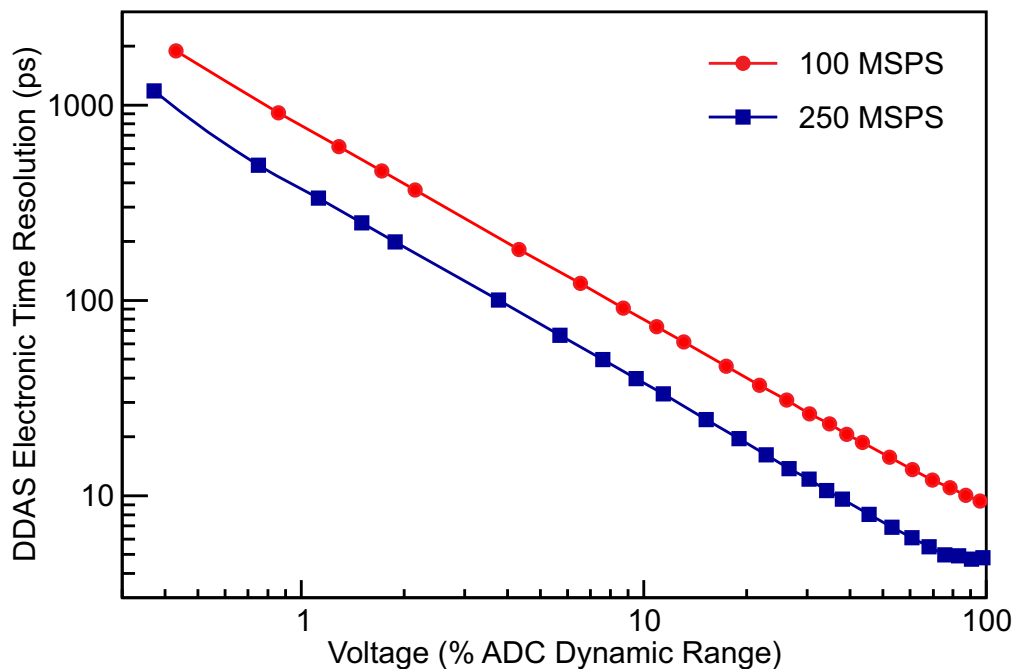


Figure 3.8: DDAS Electronics time resolution for LaBr_3 detector type signals, generated by a Agilent 33522A arbitrary waveform generator, as a function of input signal amplitude relative to the dynamic range of the ADC. For signal amplitudes occupying $>10\%$ of the ADC dynamic range the electronics contribution to the detector system time resolution is essentially negligible.

The improvement in electronics time resolution one can obtain both from faster digitizers and larger signal amplitudes is demonstrated in Fig. 3.8. The electronics contribution adds in quadrature with the detector contribution. In general, the best time resolution is achieved by the fastest digitizer.

3.5 Planar Germanium Double-Sided Strip Detector (GeDSSD)

A planar germanium double sided strip detector (GeDSSD) served as the central implantation detector for e14039. The GeDSSD is comprised of a 1-cm thick by 9-cm diameter Ge crystal that is electrically segmented into sixteen 5-mm strips on the front and sixteen orthogonal 5-mm strips on the back. The crystal is contained in a stainless steel cryostat with 0.1143-mm thick aluminum windows on both faces and mechanically cooled to a temperature of 66 K by a Stirling cooler. Each strip of the GeDSSD is instrumented with two preamplifiers. The low-gain preamplifier has a 0 to 30 GeV dynamic range, suitable for detecting ions implanted into the crystal, while the high-gain preamplifier has a 0 to 15 MeV dynamic range capable of detecting β -decay electrons and γ -rays. Additional details about the GeDSSD can be found in Ref. [43].

3.5.1 Instrumentation and Triggering Conditions

The high-gain preamplifiers of the GeDSSD were instrumented with 14-bit 250-MSPS modules, while the low-gain preamplifiers were instrumented with 12-bit 100-MSPS modules. The low-gain strips were not required for high-resolution spectroscopy or sophisticated pulse-shape analysis routines and the implementation of lower frequency digitizers reduced the overall data rate.

The GeDSSD was operated in a “free running” acquisition mode. In this mode, DDAS records data for each strip every time the trigger filter crosses an user-set threshold. Trace capture was enabled for both the front and back of the GeDSSD, for both the high- and low-gain electronics, and the trace length was set to 6 μ s with a 2 μ s delay for all channels.

3.5.2 Event Localization and Correlation

As mentioned above, the GeDSSD has two sets of orthogonal strips, one set either side of the crystal, which yields an effective grid of $256 \times 5 \times 5 \times 10 \text{ mm}^3$ pixels. Both high-gain and low-gain events are localized in the GeDSSD by identifying the intersection of the strips with the most energy deposited on each side of the detector. β decays, along with any coincident radiation detected in ancillary detectors, are correlated to previously implanted ions by locating the most recent ion implantation within the same pixel or range of pixels. The coincidence window was set in software to $10 \mu\text{s}$.

The spatial distribution of implanted ions for e14039 is shown Fig. 3.9 as a two-dimensional histogram of the low-gain maximum strip on the front vs. the low-gain maximum strip on the back for all low gain events recorded during e14039.

Immediately obvious in Fig. 3.9 is a region of the detector where there are missing events. The profile of the distribution along either strip axis is expected to be a smooth, roughly Gaussian, shape with no jagged features like what is seen the Fig. 3.9. The region of the GeDSSD where there are missing events is the same region where the beam has been implanted at various intensities and depths for several experiments. Therefore, a likely explanation for this behavior is severe charge trapping due to damage of the crystal.

The same behavior is observed for the decay events. Figure 3.10 presents the same two-dimensional histogram shown in Fig. 3.9, but for the high-gain strips.

In Fig. 3.10, the charge-trapping region of the detector is less obvious until one projects the two-dimensional histogram onto the front- and back-strip axes. The high-gain behavior is slightly different than the low-gain behavior. Heavy ions deposit all of their energy in a very localized region of the detector while the β -decay electrons, on average, travel much

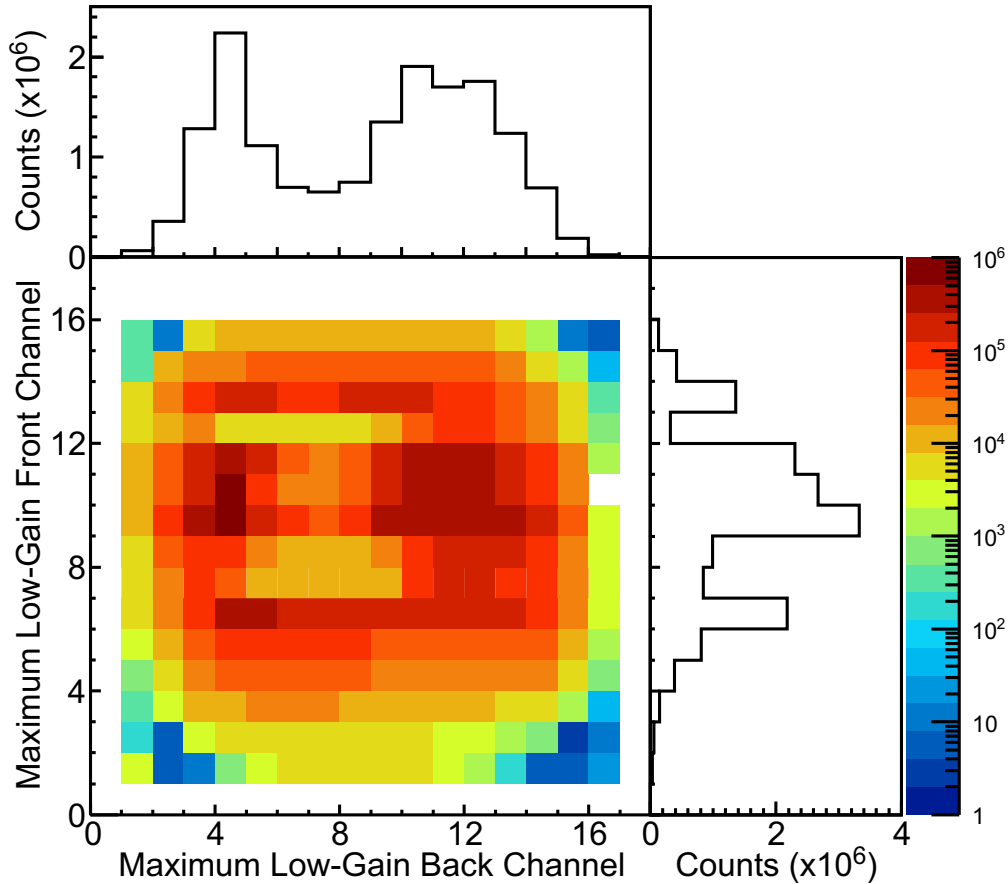


Figure 3.9: Two-dimensional histogram showing the maximum low-gain front channel vs. the maximum low-gain back channel for all low-gain events in e14039. Projections onto the front- and back-strip axes are shown to the right and above the two-dimensional histogram, respectively. There is a clear region of missing events due to charge trapping as a result of crystal damage.

further in very erratic trajectories depositing energy across all depths of the damaged region.

As a result, some electrons will deposit energy across a range of depths, some of which are not damaged, and are recorded. Several attempts were made during the analysis to locate the missing implanted ions, but no method was successful in recovering the data. In these attempts the number of events with a front(back) energy but no back(front) energy were examined. A relatively large number of these were observed suggesting that often one side or the other records no charge. Ultimately, this problem did not significantly impact the analysis, but did increase the number of spurious correlations and reduce the overall statistics

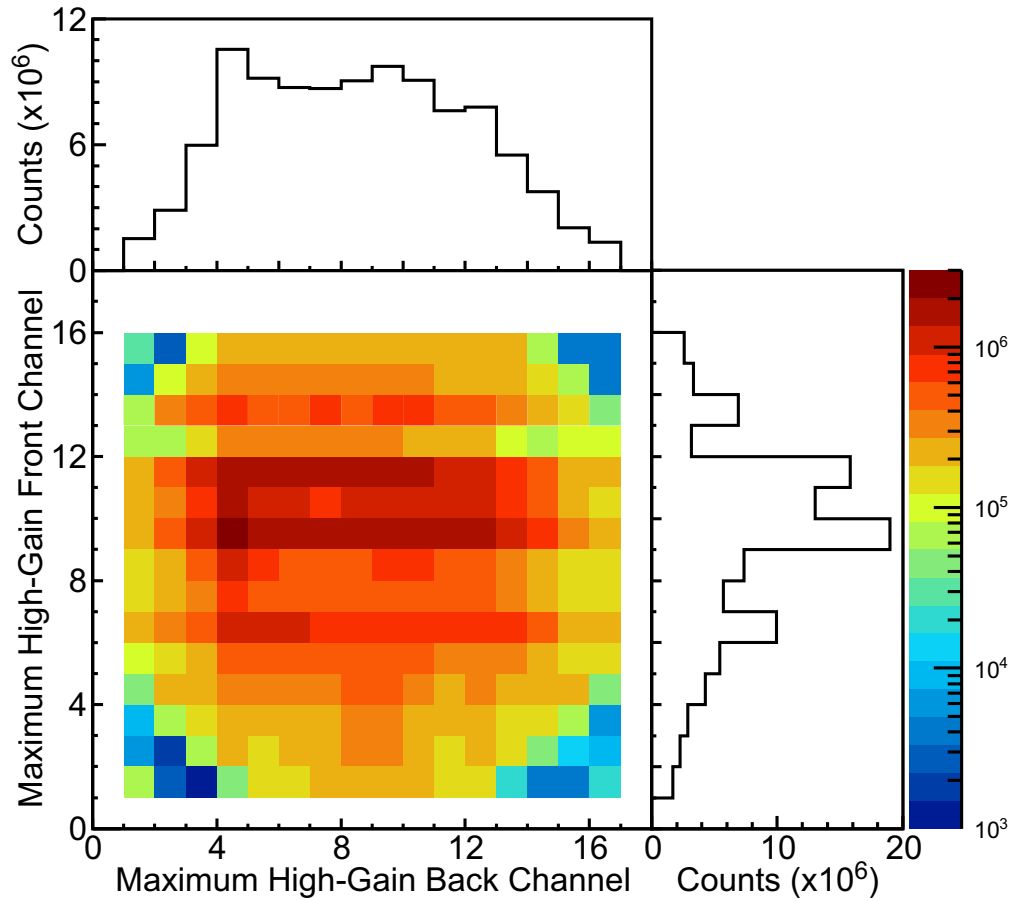


Figure 3.10: Two-dimensional histogram showing the maximum high-gain front channel vs. the maximum high-gain back channel for all high-gain events in e14039. Projections onto the front- and back-strip axes are shown to the right and above the two-dimensional histogram, respectively. The region of missing events due to charge trapping as a result of crystal damage is less evident due to the fact that the electrons and γ rays can travel outside the localized damaged region and can deposit energy across the depth of the detector.

in the β -gated and correlated spectra.

3.5.3 Crosstalk Calibration

The preamplifier channels of the GeDSSD exhibit electronic crosstalk. Crosstalk manifests itself as small amplitude signals induced on the neighboring channels of a strip that has charge deposition. In an energy spectrum, this results in low-energy peaks that are artifacts, and thus must be calibrated out. Electronic crosstalk is roughly symmetric on either side of the strip that collects the real charge from the event. Figure 3.11 shows an example of electronic crosstalk across three strips observed when measuring a ^{137}Cs source.

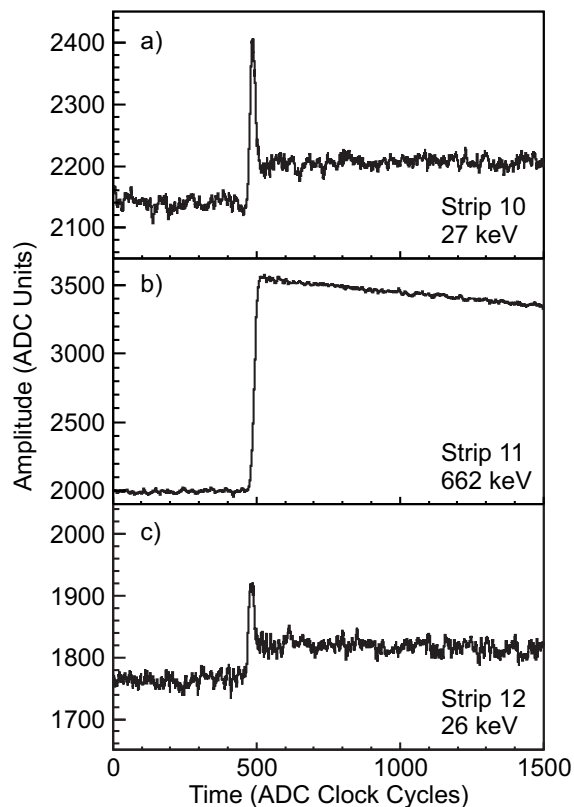


Figure 3.11: Representative crosstalk example for the GeDSSD showing (b) a full energy deposition of a 662-keV γ ray in strip 11. Panels (a) and (c) show induced signals in strips 10 and 12 respectively. These induced signals yield low-energy peaks in the GeDSSD strip energy spectra and must be calibrated out.

The crosstalk correction was determined before the experiment using a ^{137}Cs source by examining the ratio of signal amplitudes in coincident adjacent strips for events where

at least three consecutive strips fired and a 662-keV photopeak event was detected in the central strip of the group of three. Figure 3.12 presents a representative sample of crosstalk calibrations using strip 10 on the back of the GeDSSD. Figures 3.12a and 3.12b show the ratio of the signal induced on strips 9 and 11, respectively, by the signal present on strip 10.

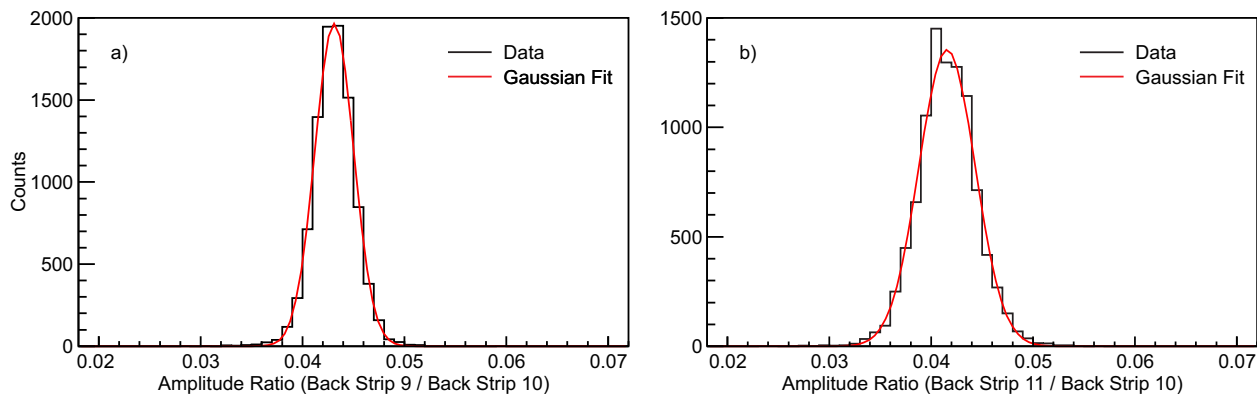


Figure 3.12: Representative sample of crosstalk calibrations using strip 10 on the back of the GeDSSD. Panels (a) and (b) show the ratio of the signal induced on strips 9 and 11, respectively, by a signal present on strip 10.

The centroid of the Gaussian fit in Figs. 3.12a and 3.12b, multiplied by the amplitude of any signal on strip 10, is the crosstalk correction and the amount that must be subtracted from a signal on strips 9 and 11, respectively. This calibration is performed for each strip in the detector for both the front and back. Table 3.3 presents the summary of the crosstalk corrections for the GeDSSD used in all subsequent analysis.

The results of the crosstalk correction for strip 10 is shown in Fig. 3.13. The uncorrected spectrum is shown in Fig. 3.13a with an inset showing the low-energy region where crosstalk peaks induced by adjacent strips are present. Figure 3.13b shows the results of the crosstalk calibration with an inset expanding the same low-energy region as in Fig. 3.13a. The crosstalk peaks have been removed and the $K\alpha$ x-rays around 32 keV are clearly observed.

Table 3.3: Ratios of induced signals in the GeDSSD by strip n on adjacent strips $(n + 1)$ or $(n - 1)$. When multiplied by the signal amplitude of strip n these values correct the amplitude of the signal present on strips $n + 1$ or $n - 1$.

Strip	Front $(n+1)/n$	Front $(n-1)/n$	Back $(n+1)/n$	Back $(n-1)/n$
1	0.0215	-	0.0261618	-
2	0.0288	0.0215	0.0335	0.0267
3	0.0321	0.0290	0.0357	0.0328
4	0.0396	0.0321	0.0404	0.0344
5	0.0708	0.0382	0.0470	0.0426
6	0.0718	0.0698	0.0378	0.0427
7	0.0710	0.0717	0.0390	0.0386
8	0.0680	0.0691	0.0387	0.0373
9	0.0552	0.0702	0.0467	0.0450
10	0.0387	0.0571	0.0416	0.0431
11	0.0408	0.0401	0.0417	0.0423
12	0.0359	0.0401	0.0420	0.0413
13	0.0328	0.0353	0.0397	0.0415
14	0.0273	0.0331	0.0316	0.0401
15	0.0215	0.0275	0.0266	0.0336
16	-	0.0226	-	0.0254

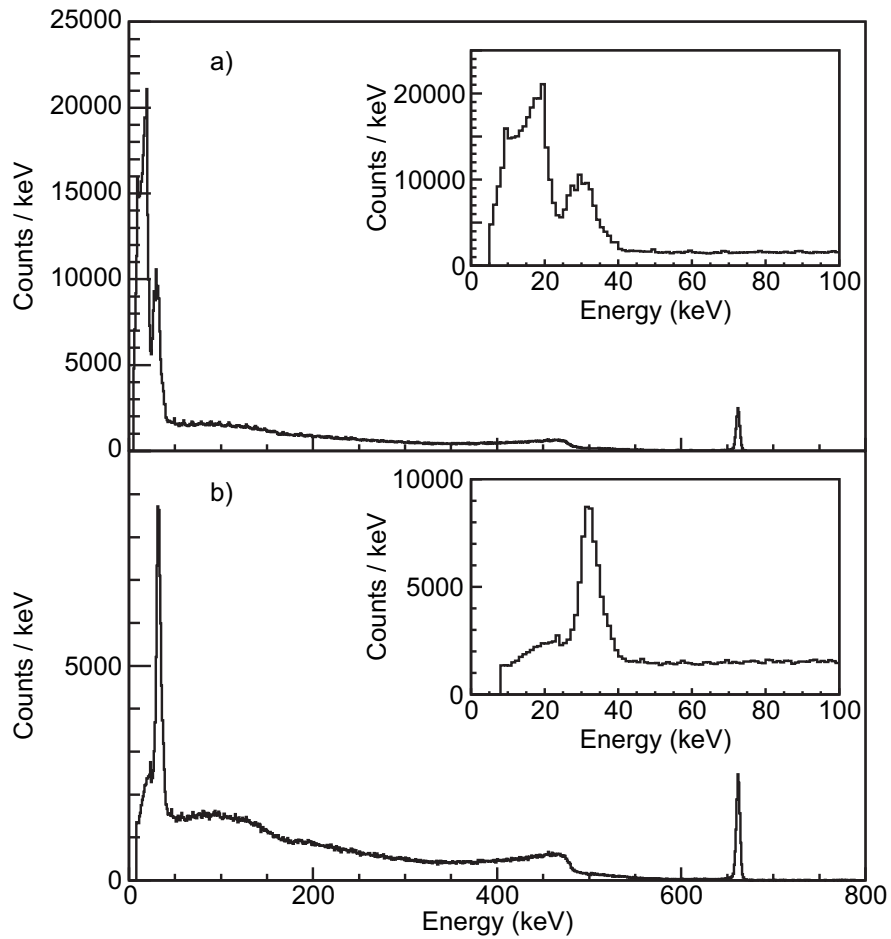


Figure 3.13: Results of the crosstalk calibration for a representative strip of the back of the GeDSSD. The uncorrected and corrected spectra for ^{137}Cs are shown in (a) and (b), respectively. For each spectrum an inset expands the low energy region and demonstrates the existence and subsequent removal of the crosstalk induced peaks.

3.5.4 Energy Calibration

Several methods were used throughout the analysis to extract the energy of events in the GeDSSD. These include the DDAS energy filter, described in Section 3.4.2, as well as pulse amplitude, pulse area, and pulse fitting, discussed later in Section 3.5.5. In all cases the energy calibration procedures were identical.

The uncalibrated, crosstalk corrected, energy spectra for the back strips of the GeDSSD acquired using a ^{137}Cs source are shown in Fig. 3.14.

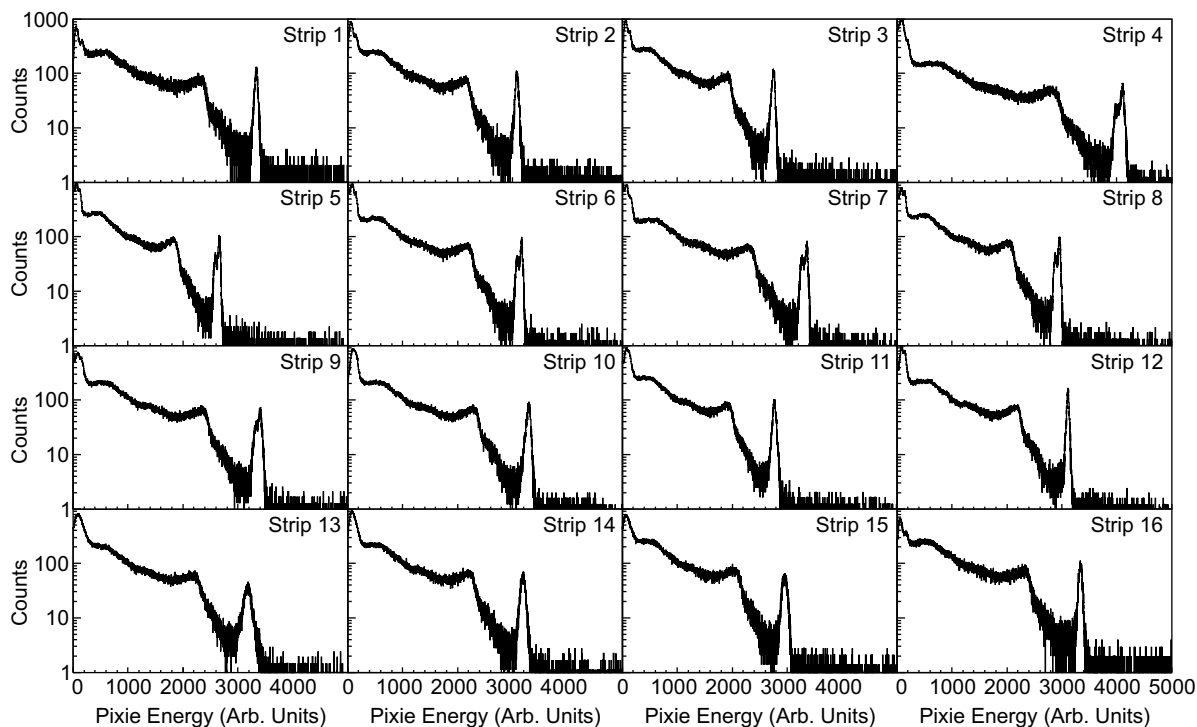


Figure 3.14: Uncalibrated, crosstalk corrected, energy spectra for all 16 back strips of the GeDSSD for a ^{137}Cs source. Strips 4 through 9 clearly exhibit multiple peaks which result from differences in charge collection along the damaged regions of those strips. Energies were obtained from the DDAS digital filter.

In Fig. 3.14, strips 4 through 9 exhibit multiple peaks for a monoenergetic source. These strips have been bombarded with heavy ions at the highest rates during all experiments for which the GeDSSD was used. The energy spectra for back strip 7 at different positions,

based on the location of the coincident signal on the front of the GeDSSD, are shown in Fig. 3.15. Based on these energy spectra a simple strip-by-strip energy calibration would be insufficient. Instead, the energy calibration for the GeDSSD was done individually for each of the 256 effective pixels for both the front and back of the GeDSSD, and is referred to as the two-dimensional energy calibration.

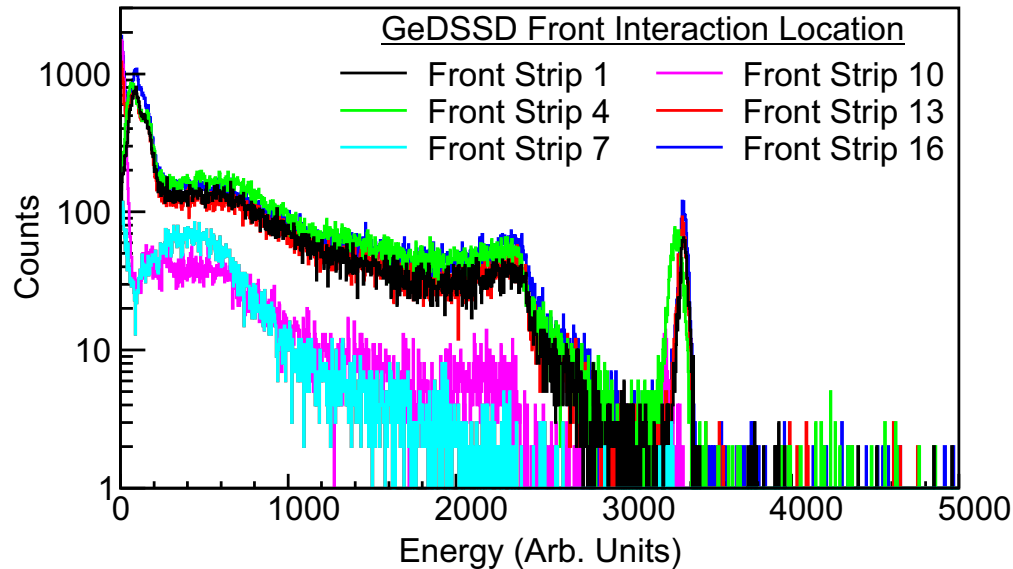


Figure 3.15: Energy spectra of GeDSSD back strip 7 taken with a ^{137}Cs source and histogrammed by interaction location from the front of the GeDSSD. The black, green, cyan, magenta, red, and blue spectra correspond to positions along the length of back strip 7 based on the coincident signal in front strips 1, 4, 7, 10, 13, and 16, respectively. The location of the 662-keV photopeak is identical for strips 1, 13, and 16 but is lower in energy for strip 4. Events occurring in back strip 7 localized to strips 7 and 10 on the front do not display a photopeak.

The two-dimensional energy calibration is a linear one point calibration with a fixed 0-keV offset for each of the 256 effective pixels. Data was recorded with a ^{137}Cs source and the energy spectra for each effective pixel, for both the front and back of the GeDSSD, were created. The centroid of the 662-keV photopeak is then extracted for each pixel, and the ratio of 662.6-keV to the extracted centroid provides the slope for the energy calibration of each pixel. For pixels that do not provide a 662-keV photopeak, the energy calibration

was performed using the Compton edge. The application of the two-dimensional energy calibration to the data shown in Fig. 3.14 is presented in Fig. 3.16. The two-dimensional energy calibration removes the multi-peaking present in Fig. 3.14 and all strips give the same photopeak energy for ^{137}Cs .

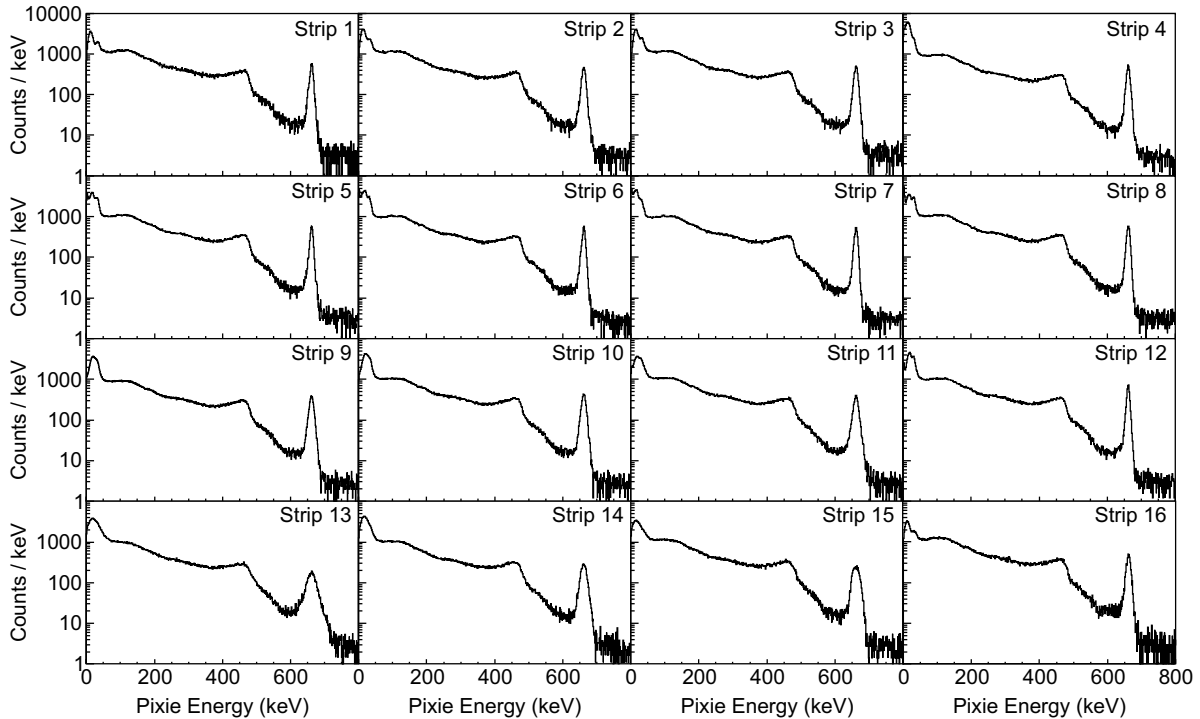


Figure 3.16: Calibrated, crosstalk corrected, energy spectra for all 16 back strips of the GeDSSD for a ^{137}Cs source.

3.5.5 Pulse Shape Analysis

A pulse-shape fitting algorithm was employed to analyze GeDSSD signals to search for the $0_2^+ \rightarrow 0_1^+$ $E0$ transition from the decay of the 0_2^+ state in ^{68}Ni . A schematic level scheme for ^{68}Ni , depicting the first two states, is presented in Fig. 3.17. Populated in the β decay of ^{68}Co , the 0_2^+ state has been studied extensively, and three half-life measurements have yielded values of 270(5) ns [44], 268(12) ns [18], and 235(23) ns [21].

Due to the high electron detection efficiency of the planar GeDSSD and the ~ 270 ns

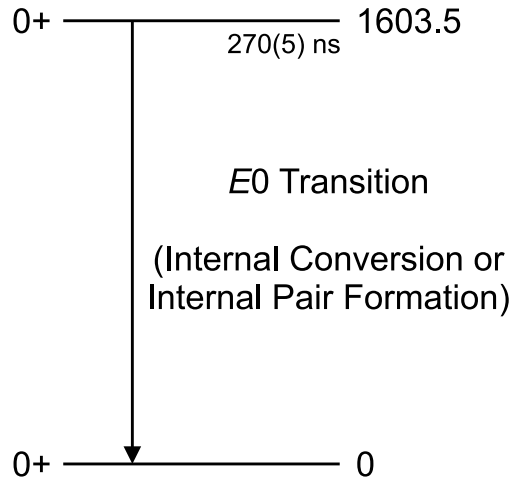


Figure 3.17: Selected level scheme for ^{68}Ni showing the first two levels and the $E0$ transition that connects them.

half-life of the 0_2^+ state in ^{68}Ni , its decay leaves a characteristic “double-pulse” signature in the GeDSSD. An example of a double pulse recorded in the GeDSSD during e14039 is shown in Fig. 3.18.

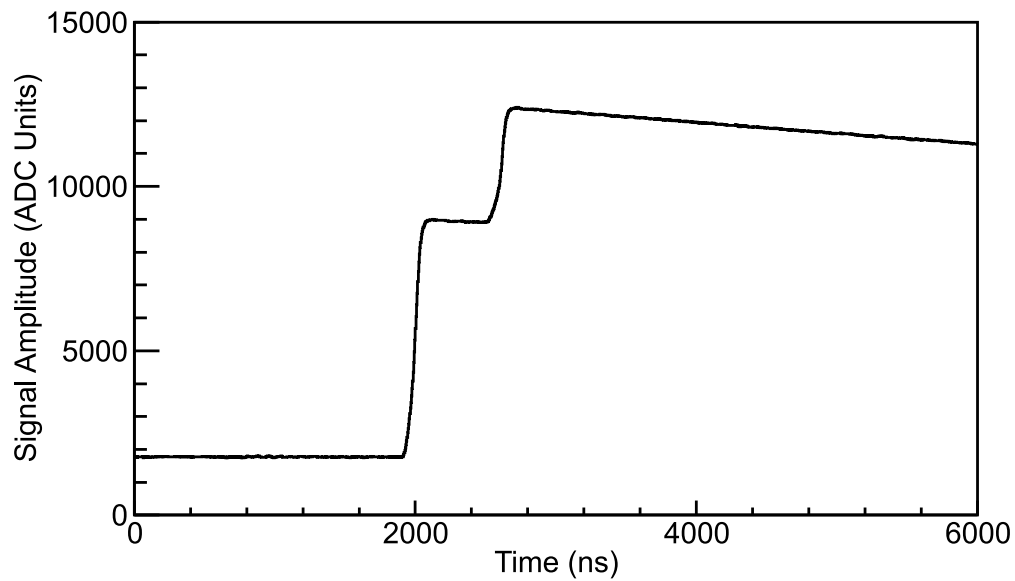


Figure 3.18: Example double-pulse signal recorded in the GeDSSD during e14039.

The double-pulse signal shape is well understood. The first constituent pulse is the electron from the β decay of ^{68}Co , which directly or indirectly populates the 0_2^+ state in ^{68}Ni . Some time later, a second electron event due to the decay of the 0_2^+ state is recorded,

which produces the second rise of the double-pulse signal. Since the decay time of the preamplifier ($\approx 30\mu\text{s}$) is long compared to the half-life of the 0_2^+ state, the pulses pile up on one another. Offline pulse-shape analysis of this double-pulse signal is required to extract the amplitudes of each pulse as well as the time difference between them. The techniques described herein are very similar to those of Ref. [18], adapted from Ref. [45].

Before fitting commenced, traces were checked for overflows, underflows, transients, and noise, all of which would preclude a good fit result. These preliminary checks reduced the number signals to be fitted and thus the amount of analysis time required. An overflowed or underflowed trace is simply one for which the amplitude of the detector signal extends above or below, respectively, the dynamic range of the ADC at some point in the trace window.

Transients were identified using the trigger filter algorithm, described in Section 3.4.1, set to a 40 ns length with a 0 ns gap. The response of the trigger filter to various types of signals detected in the planar GeDSSD is shown in Fig. 3.19.

The relatively long ($\tau \approx 30 \mu\text{s}$) decay time of the GeDSSD preamplifiers results in a near step like pulse on the 10's of ns time scale of the trigger filter. Therefore normal single-pulse signals give a single triangular shaped response, shown in Figs. 3.19a and 3.19b. A positive(negative) transient signal leads to a trigger filter response which rapidly increases(decreases) then abruptly crosses zero, further decreasing(increasing) before returning to baseline. Examples of negative and positive transients are shown in Figs. 3.19c and 3.19d, respectively. The trigger-filter response was compared to the root mean square of the baseline of the detector signal. If the trigger-filter response dropped below a factor of ten of the baseline RMS, the signal was rejected as a transient. Some transients do make it through this initial filter, but were rejected later in the fitting procedure.

Additionally, if the signal had a large baseline RMS (> 20 ADC Units) the signal was

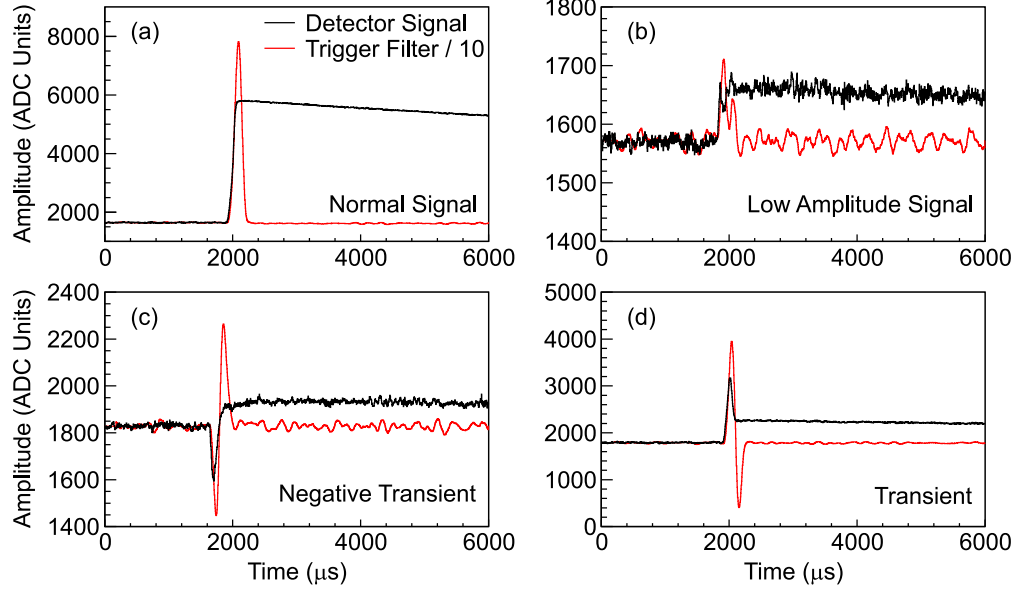


Figure 3.19: Response of the trigger filter algorithm used for transient rejection in the analysis to (a) large-amplitude single pulse, (b) low-amplitude single pulse, (c) negative transient, and (d) positive transient GeDSSD signals. Detector signals are shown in black while the trigger filter responses are shown in red. Trigger filter responses have been reduced by a factor of ten and the baseline of the signal has been added.

rejected as well. Typically, such signals have strange shapes or sloping baselines and would fail the fitting procedure if allowed to pass. Upon passing all checks, traces continued on to pulse fitting.

The first iteration of the trace fitting procedure attempted to fit all detector signals with the response of the detector to a single energy deposition referred to as a “single-pulse” fit. A sample GeDSSD signal associated with a single energy deposition is shown in Fig. 3.20.

A template single pulse was created for each of the 256 effective GeDSSD pixels from the average of 1000 signals like that of Fig. 3.20. In each fit, the height and relative time offset were free parameters. The χ^2 from the fit divided by amplitude of the trace, denoted from here on out as χ_n^2 , was used to assess the quality of the fit. The distribution of χ_n^2 values, obtained from the single-pulse fits to all GeDSSD signals, is presented in Fig. 3.21.

There are three distinct regions of normalized χ^2 values in Fig. 3.21. The first peak

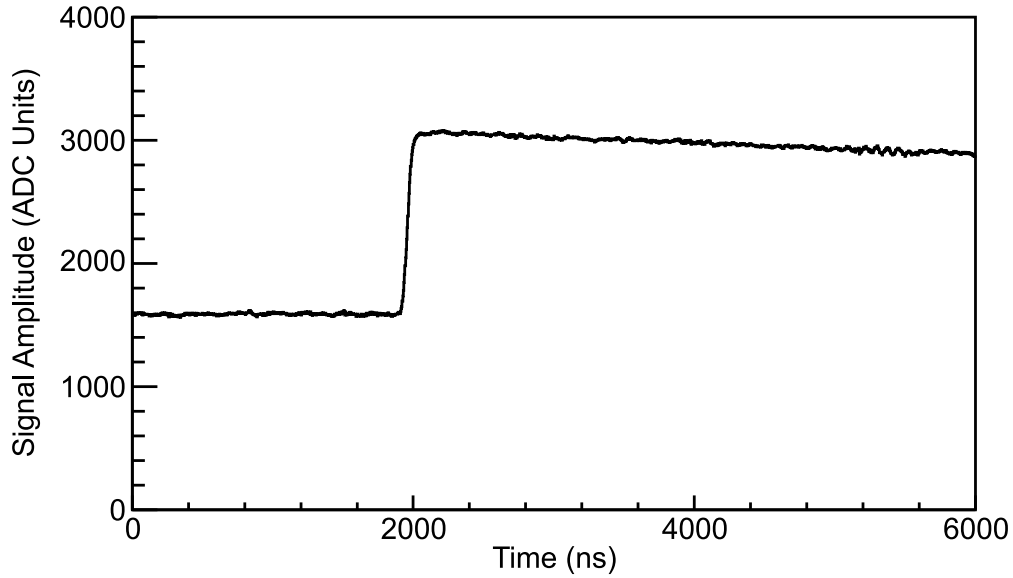


Figure 3.20: Sample response of the GeDSSD to a single event recorded using a ^{137}Cs source.

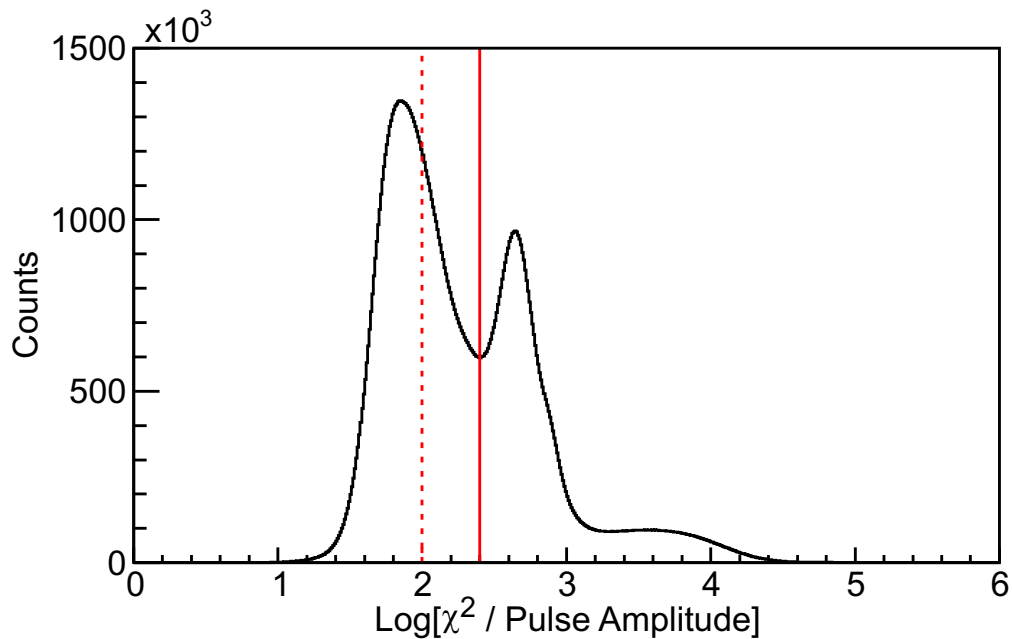


Figure 3.21: Distribution of χ^2 divided by signal amplitude (χ_n^2) for the fit of high-gain GeDSSD signals with a single detector pulse. All fits above the red dashed line are fit with the linear combination of two single detector pulses while all fits below the red solid line are considered good single-pulse events.

around 100 is from good fits of single-pulse detector signals. The second peak is from low-amplitude signals, some of which are transients that made it through the transient rejection algorithm. The third peak are double-pulse signal events. Example fits from each region are

shown in Fig. 3.22.

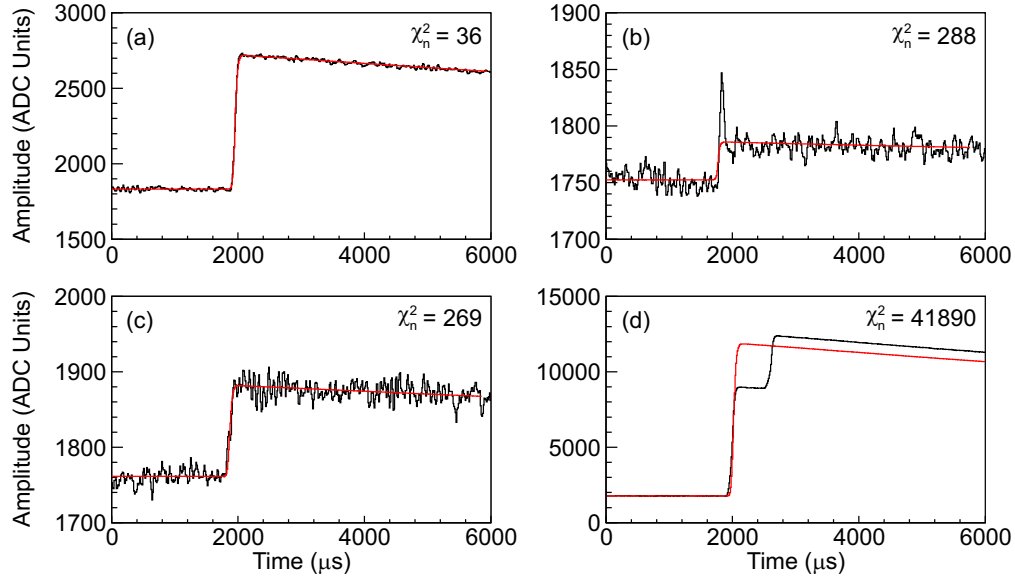


Figure 3.22: Single-pulse fit results for a variety of different signal types in the GeDSSD. (a) Good fit of a single pulse by a single-pulse fit. (b) Fit of a transient with a single pulse. (c) Fit of a low amplitude signal with a single-pulse fit. (d) Fit of a double-pulse event with a single pulse. Detector signals are shown in black while the fits are shown in red. The χ_n^2 is labeled on each fit.

The energies of all GeDSSD events that have a single-pulse fit χ_n^2 of less than 250 are histogrammed to generate the energy spectrum for all single radioactive decays recorded in the planar GeDSSD during e14039, shown in Fig. 3.23.

The spectrum of single radioactive decay energies in the GeDSSD is dominated by β -decay electrons coming from the decay of unstable nuclei implanted within the detector. Since β decay is a three-body process, the electron energy distribution is continuous with a maximum energy up to the Q-value, which is between 500 keV and 12.5 MeV for nuclei decaying inside the GeDSSD. There is also a contribution from low-energy γ rays and Compton scattering. The peaks labeled in Fig. 3.23 originate from known sources and are further discussed in Appendix A

GeDSSD events that yielded a χ_n^2 greater than 100 for the single-pulse fit, denoted by

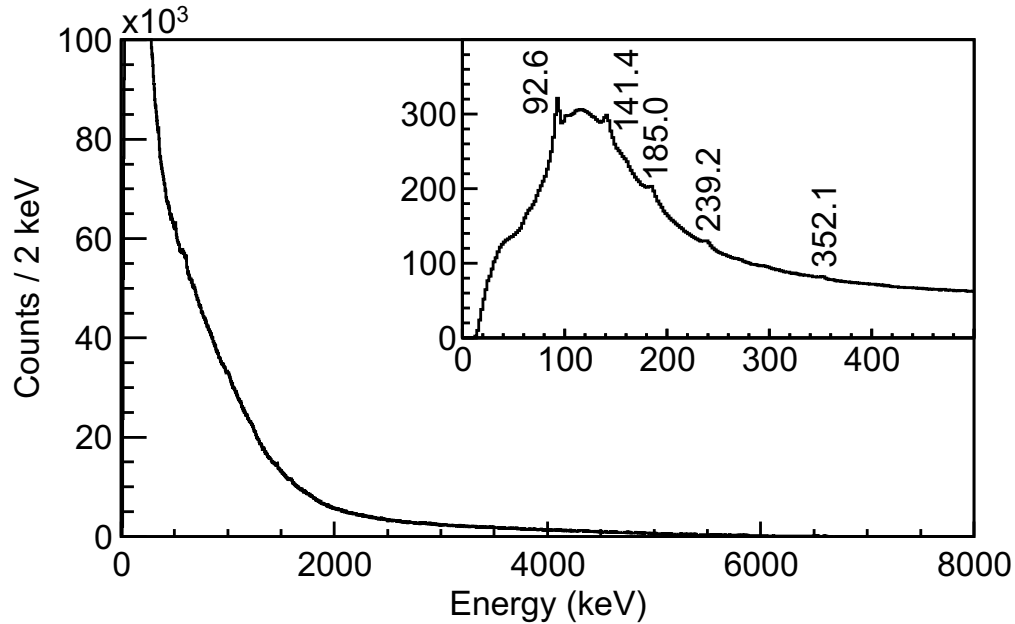


Figure 3.23: Energy spectrum obtained from the fit of GeDSSD signals by a single template detector signal where $\chi_n^2 < 250$. Most of the counts are from the continuous electron energy distributions from β decay and from Compton-scattered γ rays. The peak at 92.6-keV is from the decay of the 93.3-keV $1/2^-$ state in ^{67}Zn and 141.4-keV transition comes from the decay of the 242.6-keV isomeric state in ^{70}Cu . The 185.0-keV, 239.2-keV, and 352.1-keV are room background lines from ^{226}Ra , ^{212}Pb , and ^{214}Pb , respectively.

the red dashed line in Fig. 3.21, continued on to the double-pulse fitting procedure. In this approach, a linear combination of two single detector pulses, offset by some amount of time, is attempted. The amplitudes and time offsets of each pulse were free parameters in the fit. The resulting distribution of χ_n^2 values, obtained in the double-pulse analysis, is shown in Fig. 3.24.

The χ_n^2 distribution is broad and relatively featureless, such that further analysis was required. The signals of interest in the GeDSSD originating from the $0_2^+ \rightarrow 0_1^+$ $E0$ transition in ^{68}Ni should have second pulse energies of roughly 581 and 1603 keV for the internal pair formation and internal conversion decay processes, respectively. From examination of the χ_n^2 distribution vs. the extracted energy of the second pulse, shown in Fig. 3.25, the limit on the acceptable χ_n^2 values was determined. A value of 600 (2.78 in log scale) was chosen

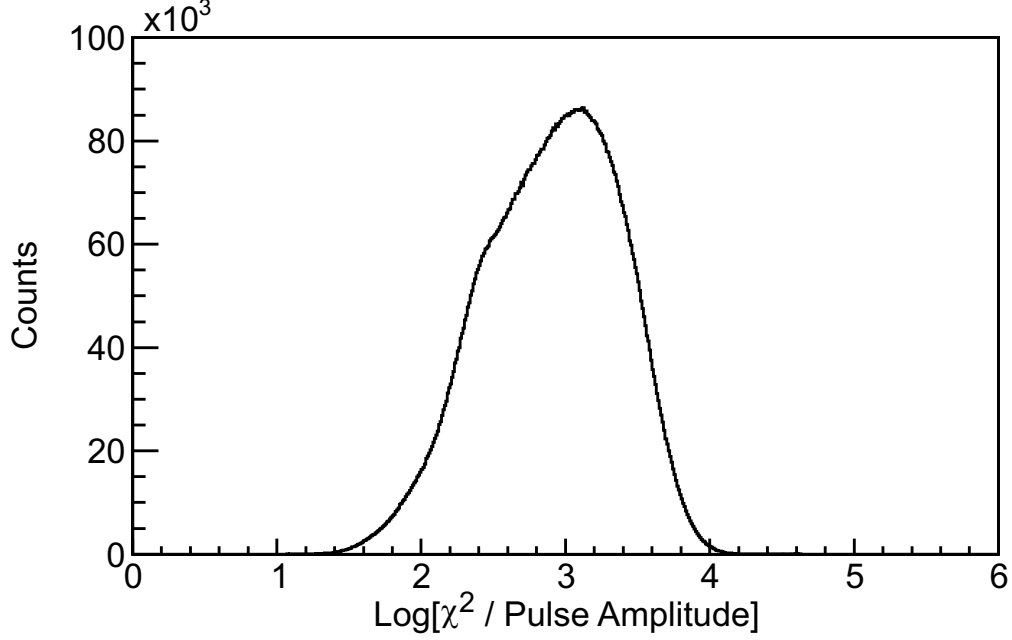


Figure 3.24: Plot of double-pulse χ_n^2 obtained from the fits of GeDSSD signals using a linear combination of two single detector pulses.

as the upper limit on χ_n^2 , shown as a red line in Fig. 3.25. Traces with double-pulse fit χ_n^2 values above the red line have poor shapes, often from ballistic deficit, and, as such are poorly fit. Below the red line a high percentage of the fits are good double-pulse fits and peaks corresponding to known transition energies are present.

After examination of several additional recorded detector traces, three more χ_n^2 cuts using specific regions on the trace were made to remove additional poor quality double-pulse fits not eliminated by the χ_n^2 cut. The first of these is the χ_{nT}^2 , which looks along the tail of the pulse from 4440 ns to 5040 ns. The second, denoted as χ_{nLE}^2 examines the leading edge of the pulse from 1920 to 2160 ns. The third, labeled χ_{nLEL}^2 is a slightly delayed longer time region on the leading edge from 2040 ns to 2400 ns. Example traces, overlaid with their double-pulse fit, and labeled with associated χ^2 values, are shown in Fig. 3.26.

The χ_{nT}^2 , χ_{nLE}^2 , and χ_{nLEL}^2 distributions obtained from the analysis are presented in Figs. 3.27a, 3.27b, and 3.27c, respectively. In Fig. 3.27d the single-pulse fit χ_n^2 divided

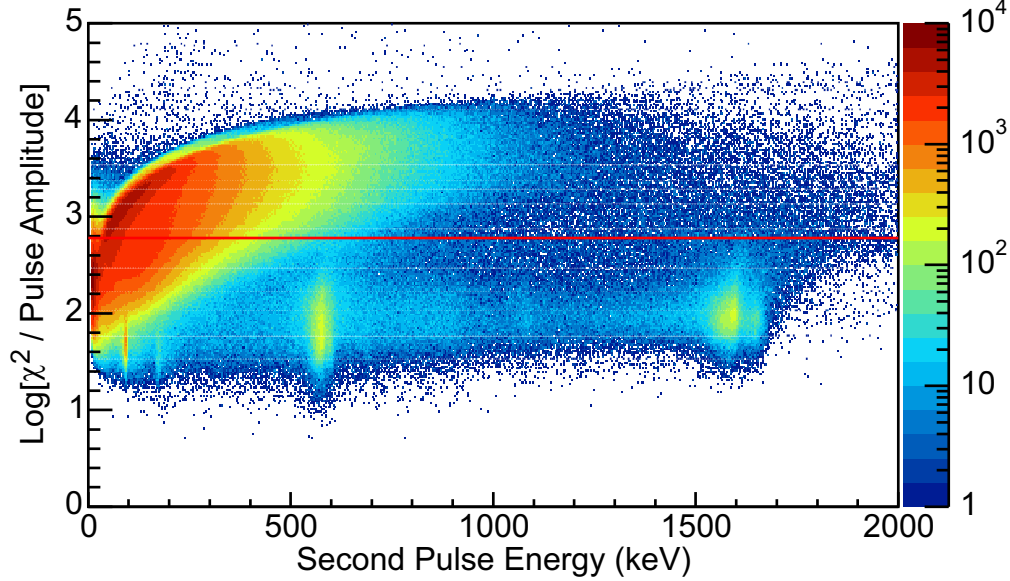


Figure 3.25: Plot of χ_n^2 vs. energy of the second pulse for the GeDSSD obtained from the double-pulse fitting method.

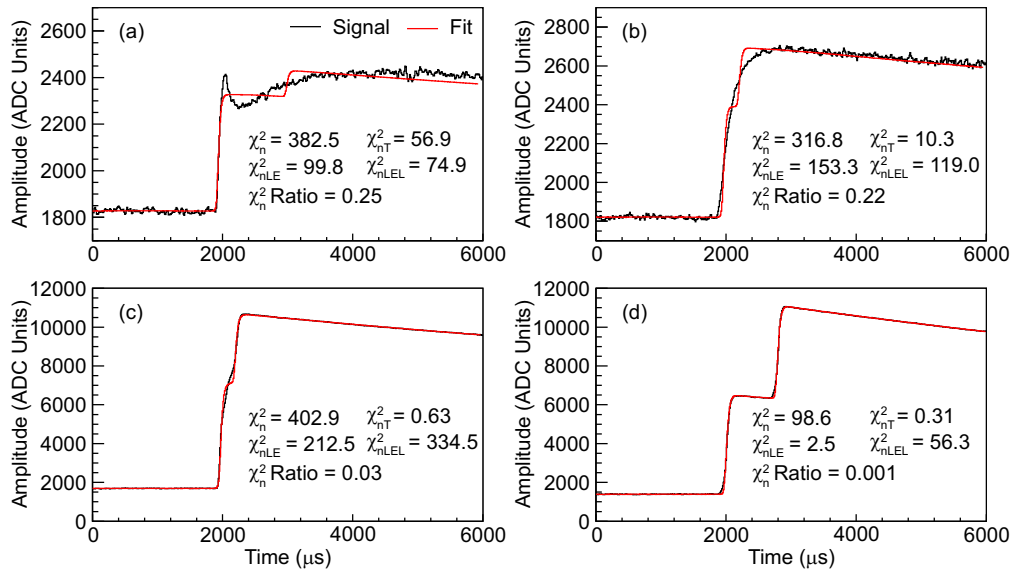


Figure 3.26: Panels (a) through (c) display GeDSSD signals, shown in black, with the double-pulse fit, shown in red, overlaid for three signal types that fail the double-pulse fit but pass the χ_n^2 test. The values obtained from the various χ^2 metrics used for this analysis, described in the text, are labeled on each panel. One or more of the additional χ^2 cuts reject each signal in (a) through (c). A good double-pulse fit is shown in (d) with the same set of χ^2 metrics as (a) through (c). The fit in (d) passes all metrics. In all panels the signals are shown in black while the best double-pulse fit to each signal is shown in red.

by double-pulse fit χ_n^2 as a function of the extracted energy of the second pulse from the double-pulse fit is shown. Cuts placed on each distribution, shown as red lines on Fig. 3.27, were motivated by examination of several fits to poor-quality traces of the type presented in Figs. 3.26a through 3.26c as well as fits to real double-pulse traces like that of Fig. 3.26d.

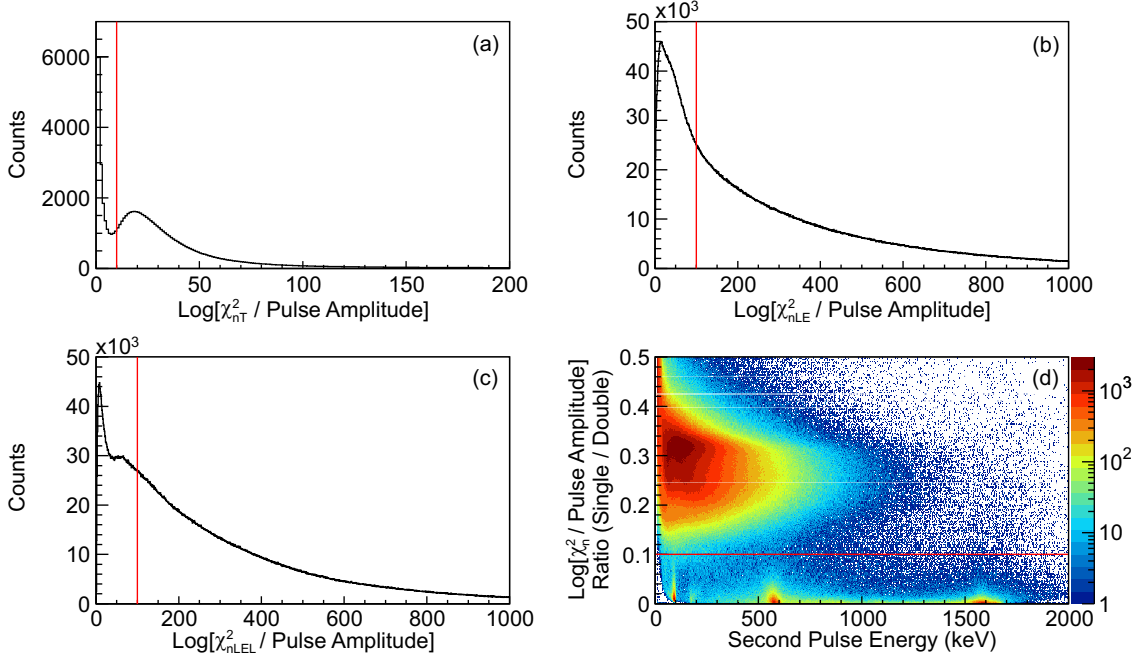


Figure 3.27: (a) Distribution of χ_{nT}^2 values. (b) Distribution of χ_{nLE}^2 values. (c) Distribution of χ_{nLEL}^2 values. The red vertical lines in (a) through (c) represent the upper limit of acceptability for each respective χ^2 value, with acceptable values being below the red line in each case. (d) Plot of the ratio (single-pulse fit / double-pulse fit) of χ_n^2 vs. energy of the second pulse obtained from the double-pulse fitting method. Values below the red horizontal line are acceptable double-pulse events.

After all double-pulse signals were fitted, applying the selected χ^2 cuts, the spectra shown in Figs. 3.28a and 3.28b were obtained for the energy of the first and second rises, respectively.

The energy spectra from the first rise of the double-pulse signals, shown in Fig. 3.28a, is dominated by the β -decay electron energy distribution. However, two peaks are observed at 100.2 and 308.3 keV both coincident with the 92.6-keV second rise energy, exclusively.

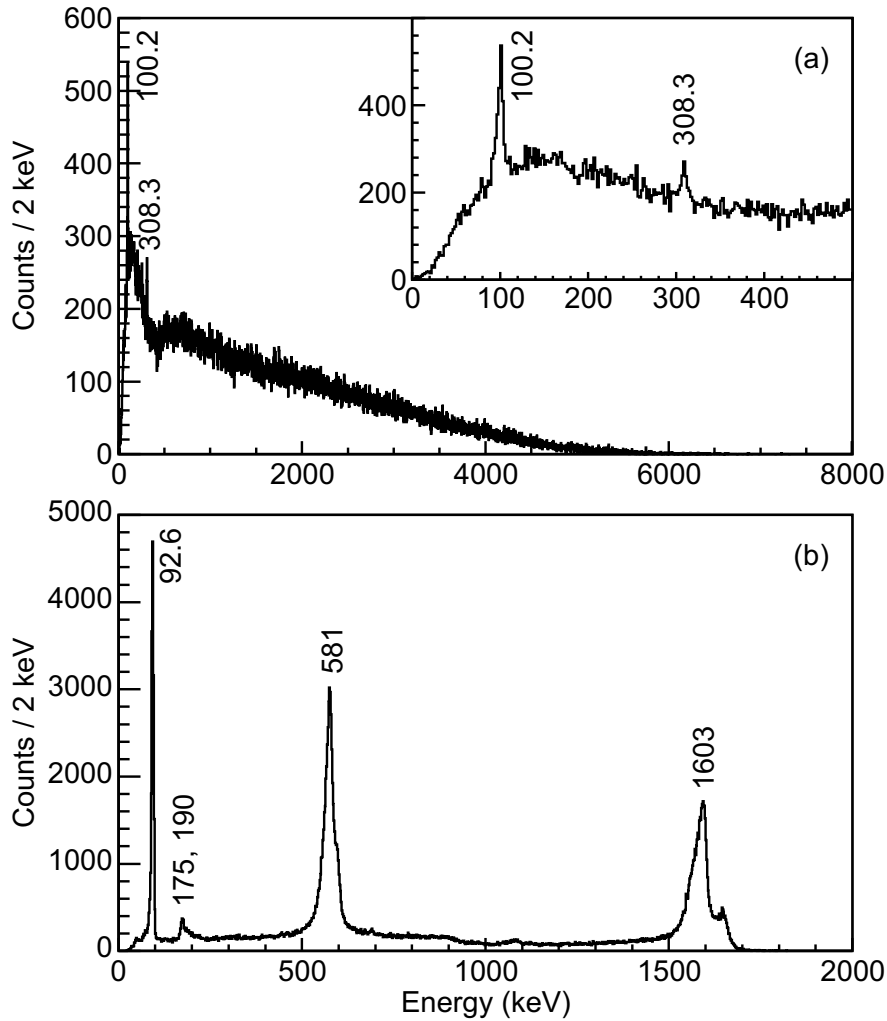


Figure 3.28: Energy spectrum displaying the energy of the (a) first and (b) second rise of the double-pulse signals. The energies were obtained from the amplitudes of the constituent pulses of double-pulse fits satisfying the χ^2 criteria, and were calibrated using the techniques described in Section 3.5.4.

These are discussed further in Appendix A.

The two largest peaks in Fig. 3.28b, located at 581 keV and 1603 keV, are from the pair-production and internal conversion decay modes of the 0_2^+ state in ^{68}Ni . The γ rays coincident with these two second pulse energies are presented and analyzed in detail in the next chapter. The features present, to some degree, above the 581-keV peak and, to a greater extent, above the 1603-keV peak are from differences in individual strips. Figure 3.29 presents the energy of the second rise of the double pulses on the x axis for each back

strip of the GeDSSD on the y axis.

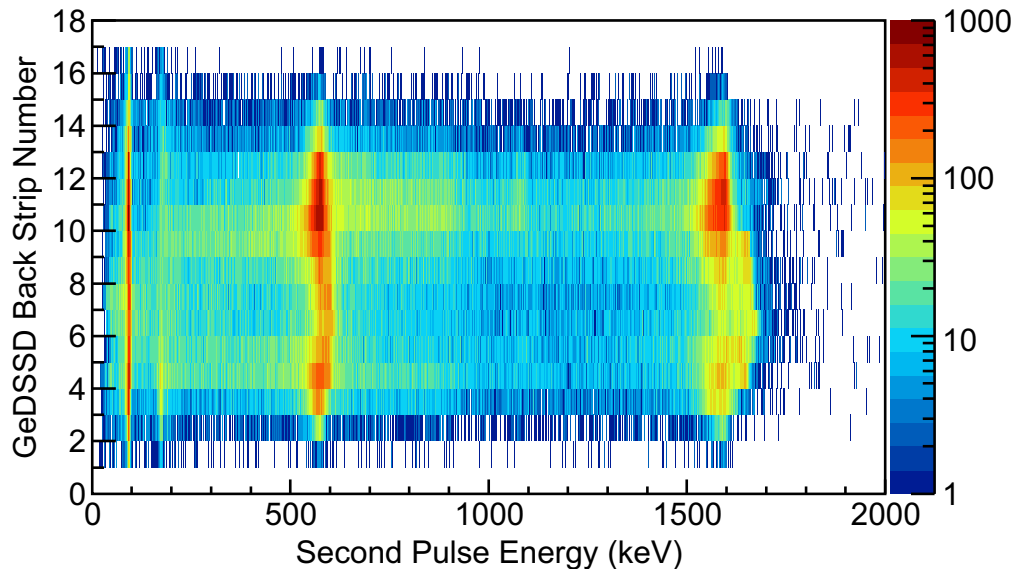


Figure 3.29: Plot of the energy of the second rise of the double pulses on the x axis for each back strip of the GeDSSD on the y axis.

Over the ten day experiment, damage to the detector crystal from heavy ion implantation resulted in a change to the two-dimensional energy calibration in the strips exposed to beam. Therefore, the calibration used for this analysis, generated after the experiment using the techniques described in Section 3.5.4, performs poorly for data early in the experiment and the energy spectra exhibit double-peaking in the region where ions were implanted at a high rate. Data taken later in the experiment fall into one peak, with degraded resolution, and the centroid is relatively uniform across the different GeDSSD strips. However, since the purpose of the double-pulse detection algorithm in this analysis is to provide a sensitive tag for the $0_2^+ \rightarrow 0_1^+$ $E0$ transition in ^{68}Ni , no attempt was made to more precisely calibrate the GeDSSD.

3.6 Segmented Plastic Scintillator and Position-Sensitive Photo-Multiplier Tube (PSPMT)

The segmented plastic scintillator, made of ELJEN EJ-204, was $52 \times 52 \times 10 \text{ mm}^3$ in size and optically segmented into 256 $3.25 \times 3.25 \times 10 \text{ mm}^3$ pixels. The scintillator was coupled to a Hamamatsu H8500 series multi-anode Position-Sensitive Photo-Multiplier Tube (PSPMT) with 64 true pixels. The output of the PSPMT was 65 channels, where one channel was the common dynode signal and the remaining 64 were the individual anode readouts. Additional information about the construction and characterization of this detector can be found in Ref. [46]. The remainder of this section describes in detail the instrumentation and operation of the PSPMT.

3.6.1 Instrumentation and Triggering Conditions

The dynode of the PSPMT was instrumented by the 12-bit, 500-MSPS module, while each of the 64 anode signals were read out by the 14-bit, 250-MSPS modules with one channel dedicated to each anode. The faster digitizer employed for the dynode signal maximizes the time-resolving capabilities of the system. The anode signals are used for position localization of events in the PSPMT rather than timing and, as such, the increased bit depth of the 14-bit digitizer is ideal for this application.

Trace capture was enabled in DDAS for the dynode and all anode signals. The dynode traces were $2 \mu\text{s}$ long with a 400 ns delay and anode traces were 500 ns long with a 160 ns delay.

The acquisition for the dynode signal was left in a “free-running” mode, where data were recorded each time the dynode triggered based on the algorithms described in Section 3.4.1.

The digital CFD, discussed in Section 3.4.3, was employed to extract precision timing below the native clock period of the digitizer.

The anode signals were collected using an external validation trigger mode where, upon triggering, they still required the presence of an external input signal, generated when the dynode triggers, to record data. The CFD algorithm was also enabled for the anode signals.

3.6.2 Event Localization and Correlation

The location of both implant and decay events inside the plastic scintillator was determined using a “center-of-gravity” algorithm [46], presented in Eqs. (3.8) and (3.9). One can think of the grid of pixels as rows (i) and columns (j) such that the energy of each of the 64 pixels can be labeled as E_{ij} where i and j run from 1 to 8.

$$ActiveRow = \frac{2}{E_T} \sum_{i=1}^{64} i * E_{ij} \quad (3.8)$$

$$ActiveColumn = \frac{2}{E_T} \sum_{j=1}^{64} j * E_{ij} \quad (3.9)$$

The response of the PSPMT to a single implantation event is shown in Fig. 3.30. Each of the 64 digitized PSPMT anode signals are shown in a box in Fig. 3.30. The height of each box is 16384 ADC units (1 V full scale range) and the width is 500 ns. The energy of each signal was obtained from the area under the pulse, determined offline using pulse-shape analysis.

The results of the center-of-gravity algorithm return a non-integer value for the active row and column of the event for the 8×8 grid of pixels. These values were multiplied by two and truncated to give a 16×16 pixel field.

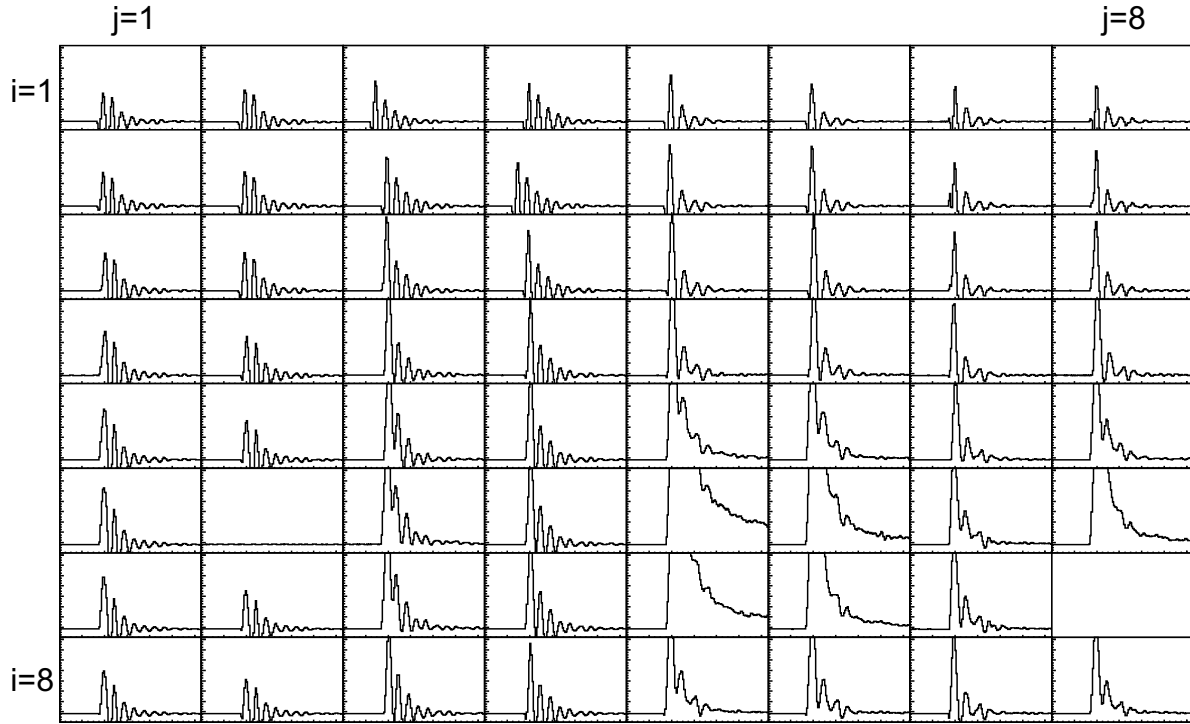


Figure 3.30: Response of the PSPMT to a single ion implantation event in the segmented plastic scintillator. Each box shows the digitized detector signal from a pixel of the PSPMT. The height of each box is 16384 ADC units (1 V full scale range) and the width is 500 ns

Unlike the GeDSSD described in, Section 3.5, the PSPMT does not have two gain ranges for detecting \sim GeV implanted ions and subsequent \sim MeV β -decay electrons. Therefore, the smaller gain range (1.0 V) was chosen to maintain sensitivity to low-energy electrons, but as a consequence the implant pixel and those surrounding are overflowed, as depicted in Fig. 3.30. These overflows are the reason for using the pulse areas instead of the amplitudes, since the former retains some proportionality to the energy, while the later does not. Additionally, all pixels in Fig. 3.30 exhibit a ringing behavior during an implant. The area of the ringing pulses was often very small compared to the area of signals central to the implant location, and therefore the ringing pulses little effect on the center-of-gravity algorithm.

The identification of an implant was based on the presence of the ΔE and TOF signals, in the Si PIN detectors and TACs, respectively, within the same event. Implantation events

must coincide with PIN detector signals as well as a time-to-amplitude converter signal, while decay events cannot have either in coincidence. The coincidence window was set to 10 μs .

The location distribution of implanted ions for e14057 is shown Fig. 3.31 as a two-dimensional histogram of the active row vs. active column in the PSPMT for all implantation events recorded during e14057. Projections onto the active-row and active-column axes are shown to the right and above the two-dimensional histogram, respectively. The same two-dimensional active row vs. active column histogram for all decay events recorded during e14057 is presented in Fig. 3.32.

With the position information extracted and identification of events complete, the correlation techniques used for the PSPMT were identical to that of the GeDSSD, detailed in Section 3.5.2, where the β decays, along with any coincident radiation detected in ancillary γ -ray detector arrays, were correlated to previously-implanted ions by locating the most recent ion implantation within the same pixel or range of pixels. The analysis presented in Chapter 4 utilized a nine-pixel field, consisting of the central pixel, identified as the location of the event, along with the immediate 8 neighboring pixels for the PSPMT.

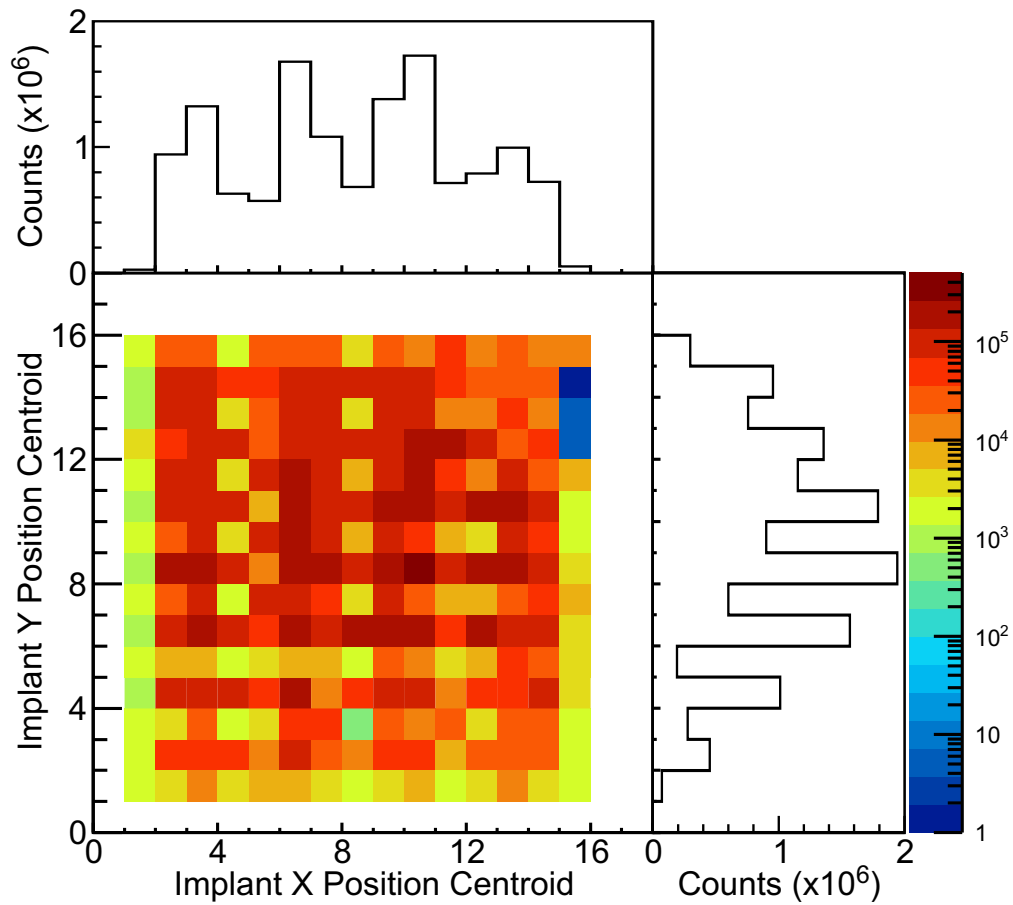


Figure 3.31: Two-dimensional histogram showing the active row vs. active column in the PSPMT, determined in the center of gravity algorithm, for all implantation events recorded in e14057. Projections onto the active-row and active-column axes are shown to the right and above the two-dimensional histogram, respectively.

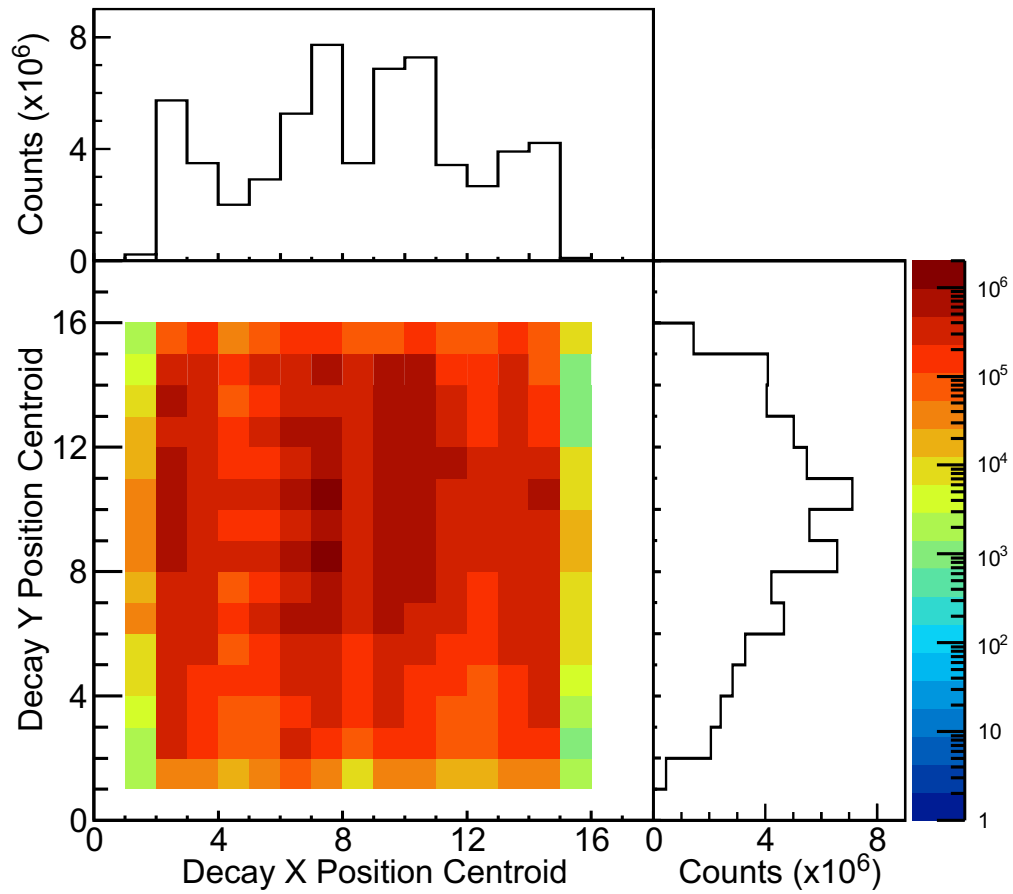


Figure 3.32: Two-dimensional histogram showing the active row vs. active column in the PSPMT, determined in the center of gravity algorithm, for all decay events recorded in e14057. Projections onto the active-row and active-column axes are shown to the right and above the two-dimensional histogram, respectively.

3.6.3 Pulse Shape Analysis

The PSPMT, like the GeDSSD, is sensitive to the characteristic double-pulse signature from the internal conversion and internal pair formation decays following the decay of implanted nuclei. An example double-pulse event recorded in the PSPMT is shown in Fig. 3.33a.

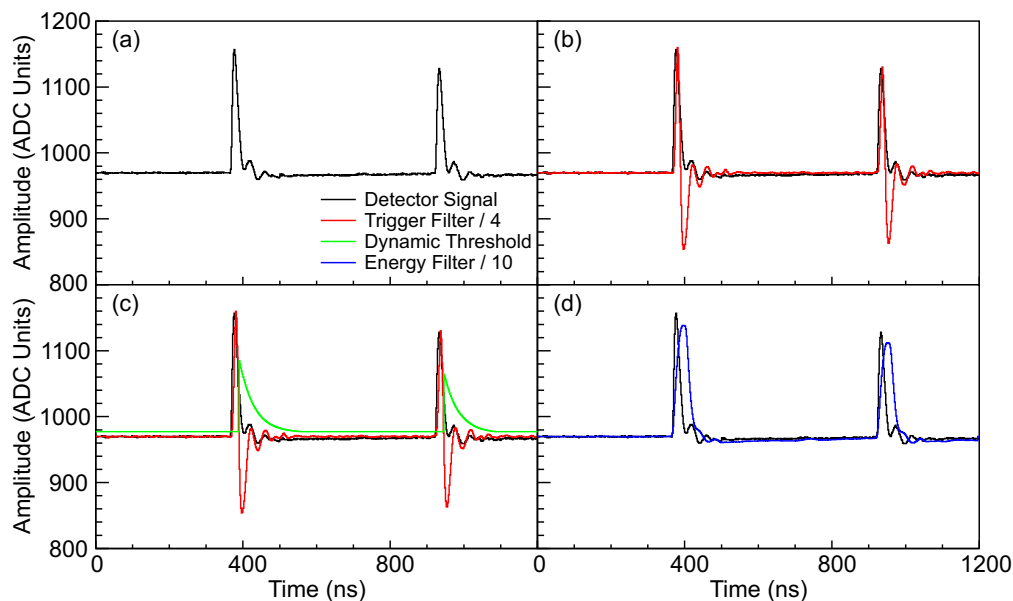


Figure 3.33: (a) Sample double-pulse event recorded during e14057. (b) Same double-pulse event as in (a) shown in black with an overlay of the scaled trigger filter algorithm shown in red. The zero crossing points of the trigger filter algorithm are used to identify subsequent triggers and extract timing information. (c) Overlay of the dynamic threshold, shown in green, discussed in the text. (d) Scaled response of the energy filter algorithm used to extract the energy of each pulse.

Double-pulse events were identified using a short timescale (Length = 10 ns, Gap = 0 ns) trigger-filter algorithm, described in Section 3.4.1. The application of this algorithm to the double-pulse signal shown in Fig. 3.33a is shown in red in Figs. 3.33b and 3.33c. The characteristic zero-crossing behavior associated with each detector pulse was used to identify multiple signals falling in a single trace window.

The PSPMT exhibits ringing behavior following each signal, shown in Fig. 3.33. A constant threshold would have to be placed high ($\approx 25\%$ of the original signal height) in

amplitude to prevent the ringing from triggering the double-pulse search algorithm. As such, a time- and amplitude-dependent threshold was developed and used to search for the second constituent pulse in a double-pulse event. The amplitude of the ringing is dependent upon the preceding pulse amplitude as well as the time difference between that first pulse and the subsequent ring. The ratio of the amplitude of each ring divided by the corresponding pulse height as a function of time difference between the pulse and subsequent ring is presented in Fig. 3.34. The amplitudes were taken from the trigger filter algorithm 6 ns before the zero crossing time (ZCT) of the trigger filter and the time difference was calculated from the difference between the two ZCT values. The ringing behavior manifests itself as bright regions in the bottom left corner in Fig. 3.34. A function of the form $A_n/A_0 = \text{Exp}(B + Cx) + D$, shown as the solid red line, was defined as the time-dependent or “dynamic” threshold. When multiplied by the height of the corresponding pulse, A_0 , the threshold was calculated as a function of time following the pulse. Events below threshold were categorized as ringing events, while events above were identified as potential double-pulse events in the PSPMT.

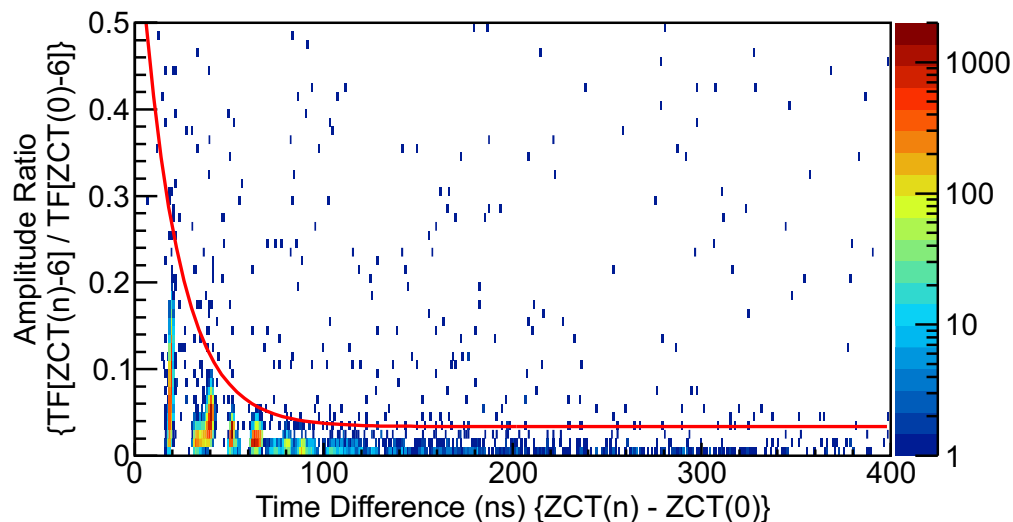


Figure 3.34: Creation of a “dynamic” threshold to mitigate subsequent triggering from the ringing of the scintillator during the double-pulse search. The red line is the threshold and all events below threshold are considered as ringing events while events above are from potential double-pulse events in the PSPMT.

The application of the dynamic threshold is shown in Fig. 3.33c as the green line. Before the arrival of the first pulse, the threshold is a constant value above baseline. After the arrival of the first pulse the threshold immediately rises and then decays back to the constant offset above baseline. Some time later, a second pulse is recorded above threshold and the dynamic threshold adjusts to a high value and again decays back to the constant value above baseline. This method allows for as low of a threshold as possible while mitigating contamination from ringing.

The energy of each pulse in a double-pulse event is obtained using the energy filter algorithm described in Section 3.4.2. The scaled response of the energy filter algorithm is shown in blue in Fig. 3.33d. The flat top region of the filter following each pulse is the recorded energy of each pulse. Figure 3.35 shows the distribution of second pulse energies from e14057.

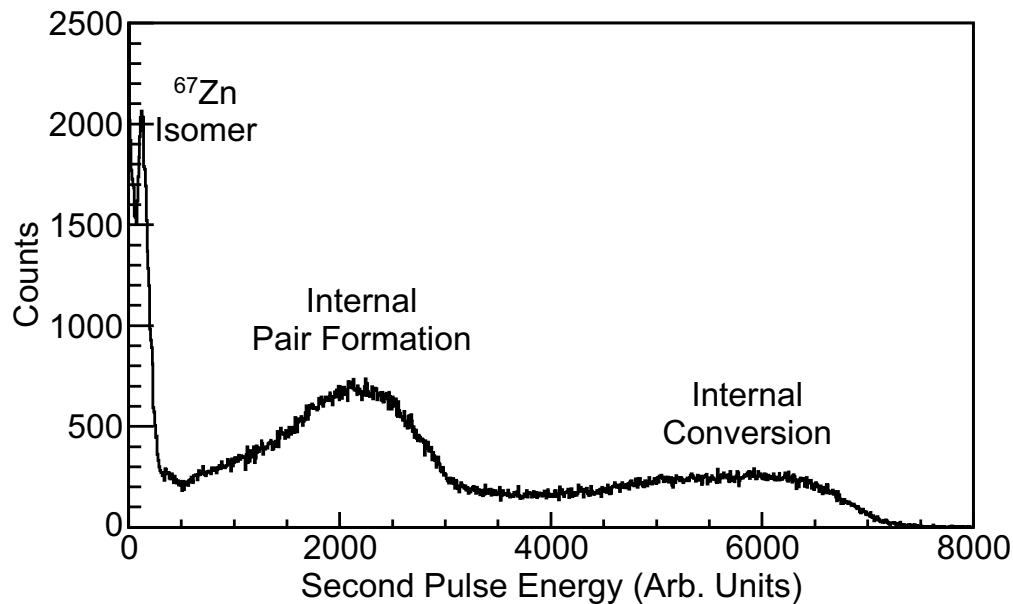


Figure 3.35: Energy spectrum displaying the energy of the second constituent pulse of the double-pulse signals recorded in e14057.

The same features present in the second-pulse energy spectrum from e14039, shown

in Fig. 3.28b, are present in Fig. 3.35. The energy resolution of the plastic scintillator was expected to be far worse than that of the GeDSSD and experiment bears this out. The peaks corresponding to the internal pair formation and internal conversion processes of the $0_2^+ \rightarrow 0_1^+$ $E0$ transition in ^{68}Ni are broad features. At the low energy region of the spectrum the ^{67}Zn isomer is also visible. However, the double-pulse technique with the plastic scintillator is primarily useful as a selective identification of the $0_2^+ \rightarrow 0_1^+$ $E0$ transition in ^{68}Ni .

3.7 Segmented Germanium Array (SeGA)

The Segmented Germanium Array (SeGA) [47] was used for the detection of prompt, isomeric, and β -delayed γ rays for both experiments e14039 and e14057. In both experiments, SeGA was used in a “beta-SeGA” configuration, which consists of two concentric rings of 8 detectors each placed at a radial distance of 8.65 cm from the center of the implantation detector. To allow placement of the GeDSSD during e14039 and the LaBr₃ array during e14057, a spacer was added to expand the distance between the detector faces to 11.5 cm.

3.7.1 SeGA Instrumentation and Triggering Conditions

In both experiments, the central contact of each of the sixteen SeGA detectors was instrumented by the 14-bit, 250-MSPS digitizers. The 32 individual segment signals from the SeGA Ge crystals were not instrumented. The SeGA central contacts were left in a free-running triggering mode where, upon energy deposition above threshold, data was collected. Traces were not recorded for SeGA.

3.7.2 SeGA Energy Calibrations

SeGA was calibrated roughly every three hours throughout the experiment using room background lines. The SeGA energy calibration is linear and performed using four background lines with energies of 351.932(2) keV from ^{214}Pb decay [48], 609.320(5) from ^{214}Bi decay [48], 1460.822(6) from ^{40}K decay [49], and 2614.51(1) keV from ^{208}Tl decay [50]. The energy calibration residuals for each of the 16 detectors for a representative run taken during e14039 are presented in Fig. 3.36. The residuals for all 16 detectors combined are shown in Fig. 3.37a for that same run, while Fig. 3.37b shows the residuals for all 16 detectors for all runs over the duration of e14039.

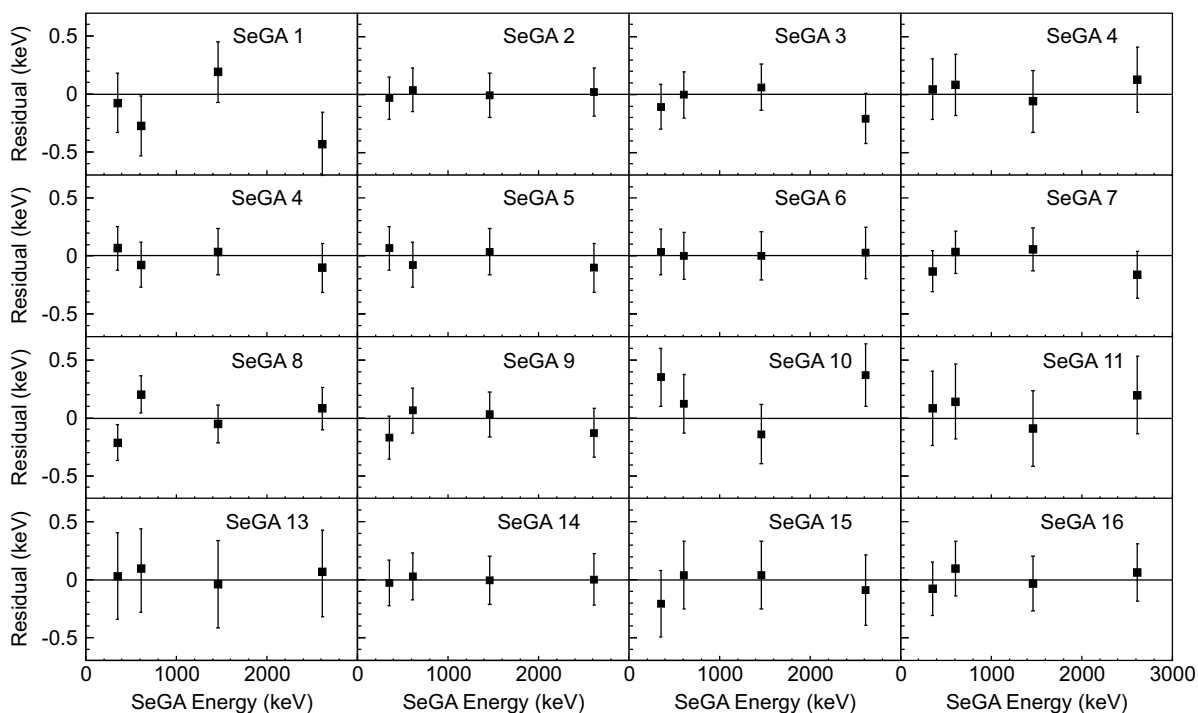


Figure 3.36: SeGA energy calibration residuals for each of the 16 individual detectors from a representative run taken during experiment e14039.

The residuals obtained from the data from all detectors in all runs are below 0.1 keV and are distributed randomly, suggesting no systematic or energy-dependent problems with the calibration procedure. Based on these calibration residuals, a 0.2-keV uncertainty was

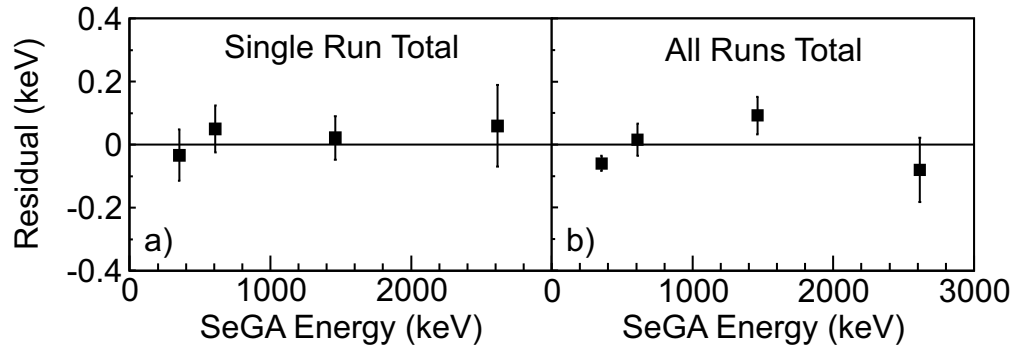


Figure 3.37: (a) SeGA energy calibration residuals for all 16 detectors combined over the same representative run used in Fig. 3.36. (b) SeGA energy calibration residuals for all 16 detectors combined for all runs over the duration of e14039.

ascribed to all γ -ray energies deduced from SeGA data collected in e14039.

The same γ -ray energy calibration procedure was used for e14057, yielding similar results.

A similar 0.2-keV energy calibration uncertainty was applied to γ -rays detected in SeGA in e14057.

3.7.3 SeGA Absolute Efficiency Calibrations

Extraction of both relative and absolute γ -ray intensities requires an absolute efficiency calibration be performed on SeGA. The use of thick implantation detectors such as the planar GeDSSD and segmented plastic scintillator prohibit the placement of NIST calibrated sources at the implant position. Therefore, data was taken with a NIST-calibrated multi-component standard reference material (SRM) comprised of ^{125}Sb , ^{154}Eu , and ^{155}Eu located in well-defined locations across the experimental setup and used to benchmark a GEANT4 simulation.

The first test of the simulation was matching SeGA alone in the standard “beta SeGA” configuration. The SRM was placed in a well-defined location between the two rings of SeGA detectors and data were collected for two hours. Twelve lines from the SRM, ranging

from 42.8 keV to 1596.5 keV, were fitted and efficiencies were calculated and corrected for detector dead time. With DDAS, dead time is minimal ($< 2\%$ for this application) but was included regardless. The dead-time correction was calculated from the live-time data from the internal scalers, which keep track of the ratio of accepted triggers to total triggers for each channel of DDAS.

In addition to corrections for dead-time, summing corrections are required for multi-line sources where γ rays of interest are part of, or parallel to, a γ -ray cascade. The treatment of summing corrections was prescribed in the SRM datasheet provided by NIST. The summing corrections applied to the efficiency calibrations using the SRM are shown in Table 3.4. The magnitude of these corrections was below 5 % relative for all γ -ray energies.

After application of dead-time and summing corrections, the GEANT4 simulation was run using one million monoenergetic, isotropically-emitted, γ rays for each of the 12 lines from the SRM and the result of the simulation was compared to experiment. The best way to visualize this comparison is a plot of the ratio of the simulated to deduced efficiency as a function of γ -ray energy. If the simulation were perfect, the ratio would be one. Results are shown in Fig. 3.38.

The agreement between simulation and experiment demonstrates that the simulation can model SeGA. However, the simulation must match the SRM efficiency data taken with the full compliment of detectors for both e14039 and e14057. For e14039, the transmission of γ rays through the planar GeDSSD indicates whether or not the GeDSSD is being effectively modeled by the simulation. For this measurement, data were collected with the SRM source positioned downstream of the planar GeDSSD in a well-defined location. The simulation was modified to re-position SeGA and include the planar GeDSSD and one million monoenergetic, isotropically-emitted, γ rays were simulated for each of the 12 lines from the SRM.

Table 3.4: Summing corrections used for absolute efficiency calibration with SRM source. Total efficiencies at a given energy E are denoted as [E] while photo-peak efficiencies are denoted as {E}. The corrected efficiency is obtained by dividing the experimental efficiency by the value of the summing correction.

Energy (keV)	Summing Corrections
42.8	1.0
86.6	1.0
105.3	1.0
123.1	$1.0 - 0.072[248.0] - 0.055\{591.7\} - 0.019[692.4] - 0.120[723.3] - 0.049\{756.9\} - 0.130[873.2] - 0.201[1004.8] - 0.010[1246.2] - 0.401[1274.4] - 0.021[1596.5]$
248.0	$1.0 - 0.287[42.8] - 0.455\{123.1\} - 0.072[444.4] - 0.022\{582.0\} - 0.134\{591.7\} - 0.015[612.2] - 0.043[625.2] - 0.022[676.6] - 0.039[723.3] - 0.613\{756.9\} - 0.059[892.7] - 0.022[904.1] - 0.130[1246.2]$
591.7	$1.0 - 0.297[42.8] - 0.455\{123.1\} - 0.178[248.0] - 0.196[756.9] - 0.800[1004.8]$
723.3	$1.0 - 0.154[42.8] - 0.243[123.1] - 0.013[248.0] - 0.014[625.2] - 0.518[873.2] - 0.465[996.4]$
873.2	$(1.0 + 0.024\{248.0\}\{625.2\}/\{873.2\}) \times (1.0 - 0.282[42.8] - 0.455[123.1] - 0.894[723.3])$
996.4	$(1.0 - 0.894[723.3]) \times (1.0 + 0.507\{123.1\})\{873.2\}/\{996.4\}$
1004.8	$(1.0 + 0.221\{248.0\})\{756.9\}/\{1004.8\} \times (1.0 - 0.282[42.8] - 0.455[123.1] - 0.217[591.7])$
1274.4	$(1.0 + 0.014\{692.4\})\{582.0\}/\{1274.4\} (1.0 - 0.281[42.8] - 0.455[123.1])$
1596.5	$(1.0 - 0.281[42.8] - 0.455[123.1]) \times (1.0 + 5.568\{873.2\}\{723.3\}/\{1596.5\} + 2.094\{1004.8\}\{591.7\}/\{1596.5\} + 0.052\{1118.5\}\{478.3\}/\{1596.5\} + 0.275\{692.4\}\{904.1\}/\{1596.5\})$

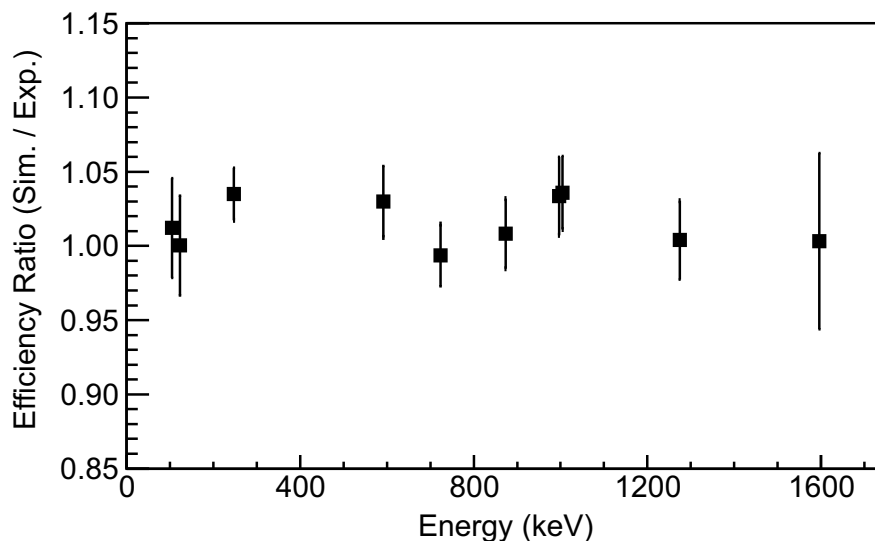


Figure 3.38: Efficiency ratios (Simulation/Experiment) for γ rays of the SRM source with SeGA in the “beta-SeGA” configuration.

During the analysis of the data, dead time and summing corrections were performed in the same manner described above for the “beta-SeGA” configuration efficiency verification. The simulated efficiency was then compared to the deduced efficiency using the ratios of simulated efficiency to experimental efficiency at each measured energy. Results are shown in Fig. 3.39.

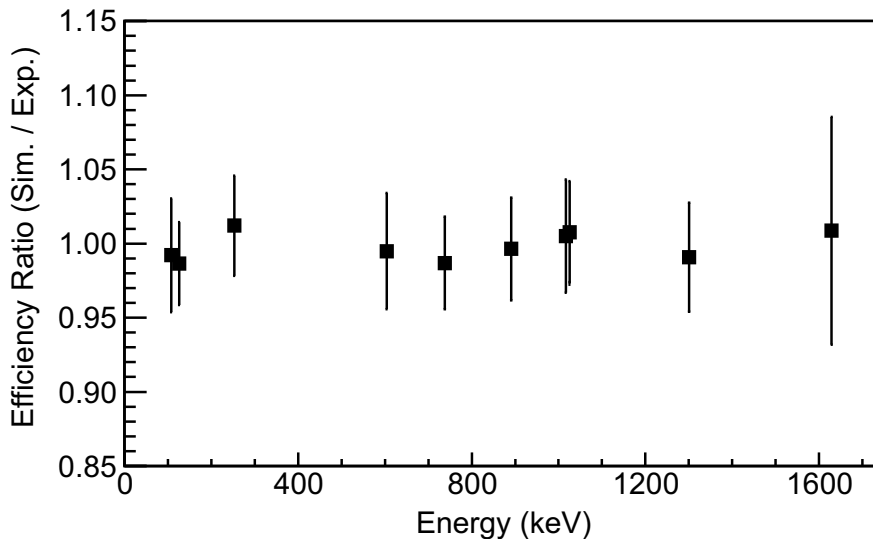


Figure 3.39: Efficiency ratios (Simulation/Experiment) for γ rays of the SRM source placed downstream of the planar GeDSSD with SeGA in the final e14039 experimental configuration.

The agreement between simulation and experiment is excellent, suggesting that all detectors used in the experiment are being correctly modeled in the simulation. The same benchmarking procedure was used for the e14057 simulation to investigate the ability of the simulation to model the PSPMT, silicon DSSD, and beam pipe. Similar to the e14039 results, the agreement between the simulation and collected data, shown in Fig. 3.40, is excellent.

The validated simulations were used to obtain the absolute γ -ray efficiencies for the respective experimental detector geometries. The beam is defined as traveling in the $+z$ direction, the x and y profile of the beam was approximated as a two-dimensional Gaussian

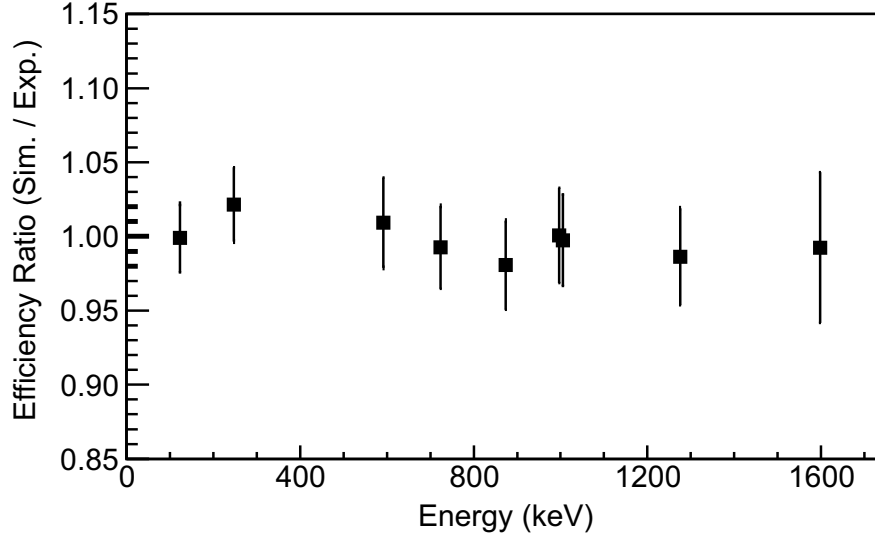


Figure 3.40: Efficiency ratios (Simulation/Experiment) for γ rays of the SRM source placed upstream of the segmented plastic scintillator with SeGA in the final e14057 experimental configuration.

with widths determined from the x and y profile of the implant distributions shown in Figs. 3.9 and 3.31 for e14039 and e14057, respectively. Ion depth distributions were taken from Fig. 3.2 for e14039 and from Fig. 3.4 for e14057. The efficiency simulation was run for one million monoenergetic isotropically-emitted gamma rays for 12 different energies spanning an energy range of 50 to 8000 keV for each isotope in each experiment. The simulated γ -ray detection efficiencies for γ -rays that would be recorded in SeGA emanating from implanted $A = 68$ nuclei during e14039 (black squares) and e14057 (red circles) is shown in Fig. 3.41.

The simulation results in Fig. 3.41 are plotted on log-log scale to facilitate easy fitting of a sixth order polynomial used for interpolation. The γ -ray detection efficiency in SeGA for $A = 68$ nuclei in e14039 can be calculated using a function of the form

$$\text{Eff}[E_\gamma](\%) = 100 \times 10^{[a(x)^6 + b(x)^5 + c(x)^4 + d(x)^3 + e(x)^2 + f(x) + g]}, \quad (3.10)$$

where $x = \log_{10}(E_\gamma)$ and E_γ is the γ -ray energy in keV. The values used for parameters a

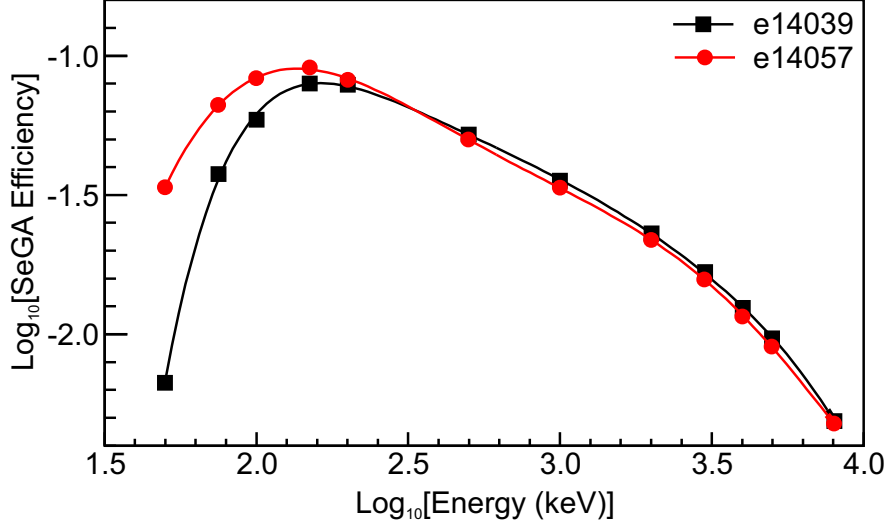


Figure 3.41: Simulated SeGA γ -ray detection efficiencies for $A=68$ nuclei in experiments e14039 (black squares) and e14057 (red circles). The depth of ions in were taken from Figs. 3.2 and 3.4 for e14039 and e14057, respectively, while the implant x and y distributions are from Figs. 3.9 and 3.31 for e14039 and e14057, respectively. Symbols represent simulation results while lines are sixth-order polynomial fits to the simulation results used for interpolation.

through g are presented in Table 3.5 for both e14039 and e14057.

Table 3.5: Values used in Eq. 3.10 to parameterize the γ -ray detection efficiency of SeGA for e14039 and 14057.

Parameter	Value in e14039	Value in e14057
a	-0.2272838	0.09806254
b	4.2325952	-1.49857809
c	-32.8120350	8.88693213
d	135.3245904	-25.1129315
e	-312.9024203	31.55816037
f	383.9575499	-7.70484349
g	-196.0154575	- 11.50983194

A 5 % uncertainty was assigned to all efficiencies uniformly across energy for both experiments based on the comparison of the SRM data with simulation in Figs. 3.39 and 3.40. Since the implant distributions for $A = 68$ and $A = 70$ nuclei are similar, the simulated γ -ray detection efficiencies in SeGA are also similar differing within the ascribed 5 % error.

3.8 Lanthanum Bromide Array

The PSPMT was surrounded with an array of ten Saint Gobain BrillanCe[®] 380 Lanthanum Bromide (LaBr₃) detectors arranged as described in Section 3.3. The crystals of each detector were cylindrical with a diameter of 38 mm and a length of 38 mm, and each crystal was coupled to a Hamamatsu R6231 photomultiplier tube (PMT).

3.8.1 Instrumentation and Triggering Conditions

All ten LaBr₃ detectors in the array were instrumented using the 12-bit, 500-MSPS digitizers. They were operated in a “free-running” trigger mode described in Section 3.4.1. Trace capture was enabled and traces were 2 μ s long with a 400 ns delay. The digital CFD, discussed in Section 3.4.3, was employed to extract precision timing below the native 2 ns clock period of the digitizer.

3.8.2 LaBr₃ Energy Calibrations

Energy calibrations for the LaBr₃ detectors were performed approximately every 12 to 15 hours throughout the experiment. However, the poor energy resolution of LaBr₃ compared to Ge, coupled with the large internal activity from ¹³⁸La, precludes using the same room background lines from the SeGA calibration procedure. Instead, the energy calibration was performed using five well-known γ rays from the decay of various implanted isotopes. The 161.8(2)-keV and 184.3(2)-keV transitions in ⁶⁸Co, the 594.3(2)-keV transition in ⁶⁹Ni, the 1077.4(2)-keV transition in ⁶⁸Zn, and the 2032.9(2)-keV transition in ⁶⁸Ni were used to calibrate the LaBr₃ detectors. The energy calibration fit function was a second-order polynomial, and data from six sequential runs were grouped together for the fit. Figure 3.42

shows the LaBr₃ energy calibration residuals for a representative group of six runs.

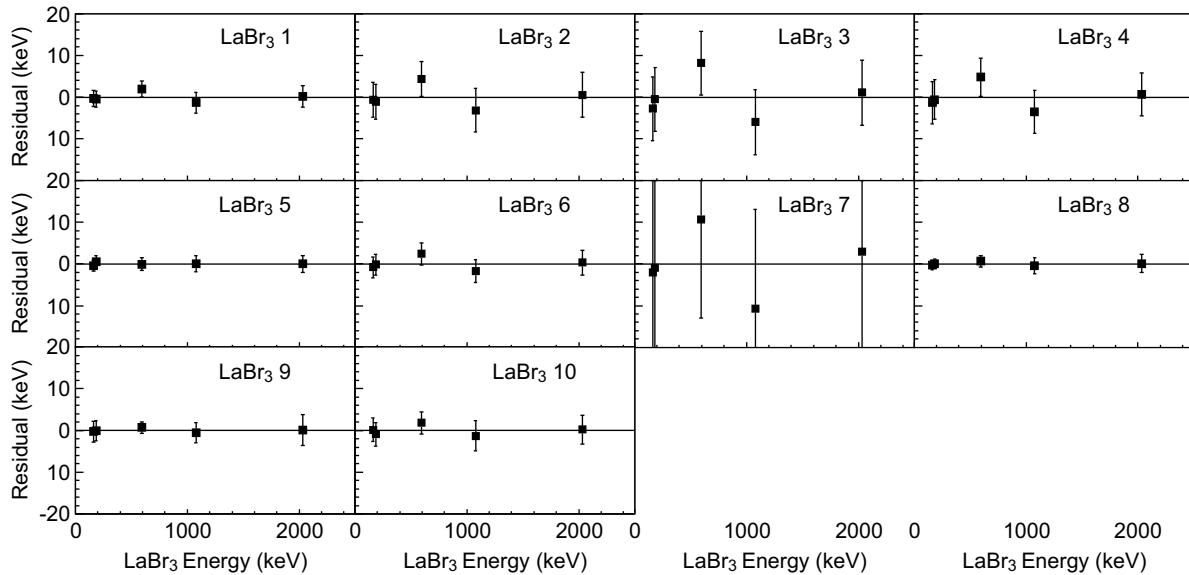


Figure 3.42: Energy calibration residuals for the individual ten LaBr₃ detectors over a representative group of six runs during e14057.

Most of the residuals are below 5 keV. Detector 7 had a very nonlinear calibration, yielding larger residuals and error bars. The residuals from a fit of the energy spectrum of all 10 detectors combined over the same group of six runs are shown in Fig. 3.43a. The residuals for all 10 detectors for all runs over the duration of e14057 combined are presented in Fig. 3.43b shows

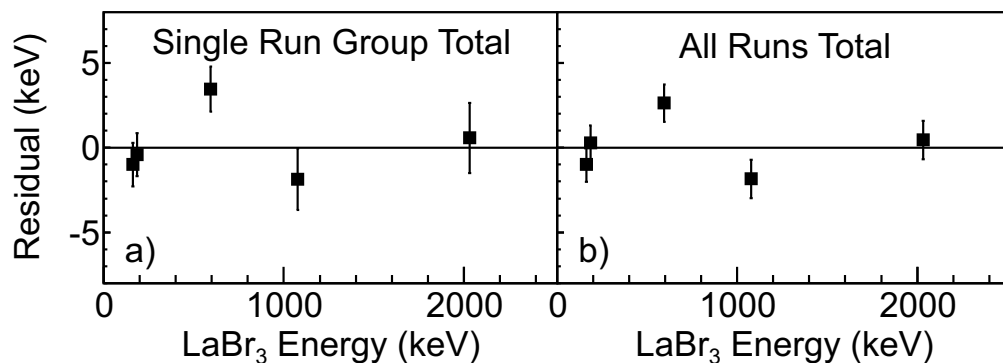


Figure 3.43: (a) LaBr₃ energy calibration residuals for all 10 detectors combined over the same representative group of runs used in Fig. 3.42. (b) SeGA energy calibration residuals for all 16 detectors combined for all runs over the duration of e14039.

Based on these calibration residuals, a 5-keV uncertainty was ascribed to all γ -ray energies measured in LaBr₃ in e14057.

3.8.3 Absolute LaBr₃ Efficiency Calibrations

Like the energy calibrations, the LaBr₃ detector efficiency calibrations were also performed relative to SeGA. The same five 161.8(2)-, 184.3(2)-, 594.3(2)-, 1077.4(2)-, and 2032.9(2)-keV transitions used in the energy calibration and an additional 1259.0-keV transition from ⁷⁰Ni were used. The ratio of peak areas (LaBr₃ / SeGA) for these six γ rays, plotted as a function of γ -ray energy, is shown in Fig. 3.44.

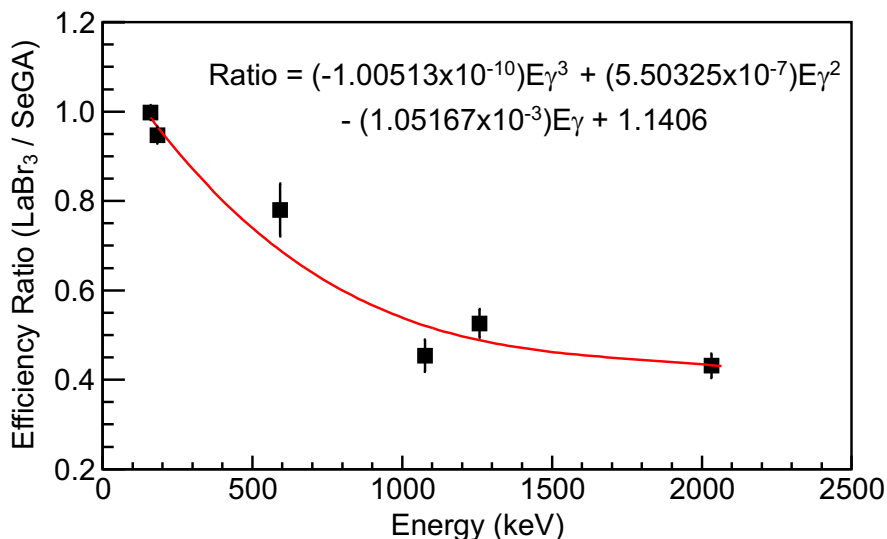


Figure 3.44: Ratio of γ -ray efficiencies (LaBr₃ / SeGA) as a function of energy.

A third-order polynomial fit to these ratios was used to interpolate between the 161- to 2033-keV energy region. The interpolated ratio at a given energy multiplied by the simulated SeGA efficiency at that energy was used for the LaBr₃ efficiency.

3.9 Level Lifetime Measurement Techniques

Level lifetime measurements in this work were performed using the $\beta\gamma$ lifetime measurement technique. The $\beta\gamma$ lifetime measurement technique involves measuring the time difference between the detection of the β decay and the γ ray emitted by the decay of an isomeric state populated by the β decay.

In the present work, β decays were detected in the segmented plastic scintillator, described in Section 3.6, and γ rays were detected in the LaBr₃ detectors. Both detector systems have intrinsic time resolutions of hundreds of ps and thus the techniques described herein are sensitive to half lives of 100 ps to hundreds of ns.

The distribution of time-differences between γ rays and their preceding β decays is a convolution of the Gaussian detector responses with the exponential decay of the isomeric state. The detector timing response is energy dependent, in both the segmented plastic scintillator and LaBr₃ detectors.

Typically thin (~ 3 mm) scintillators are chosen to mitigate the energy dependence in the time and energy response [35]. However, in the present work a thick (10 mm) plastic scintillator was used to enhance β -decay electron detection. The thick scintillator amplifies the energy dependence in the time response and introduces an additional dependence on the depth of interaction within the scintillator [51]. The next two sections describe the techniques developed to properly calibrate the time-response of the detection system.

3.9.1 Time Walk Corrections

The first step in the analysis of $\beta\gamma$ timing experiments involves correcting the time response of each detector for the pulse-amplitude dependent time walk. Though the deployment of a

digital Constant Fraction Discriminator (CFD) [41] minimizes the time walk, it still persists at the hundreds of picoseconds level across the dynamic range and must be removed.

The walk correction technique made use of a ^{60}Co source, which β decays mainly (99.9 % branch) to the 2505.7-keV state in ^{60}Ni . This state then yields a cascade of two γ rays with energies of 1173.2 and 1332.5 keV. The 0.9 ps half-life of the intermediate 1332.5-keV state in ^{60}Ni is below the sensitivity of the $\beta\gamma$ techniques in the present work and can be considered as prompt.

Data were collected with the full experimental array and the time-difference between the LaBr_3 detectors and the plastic scintillator dynode was calculated for each event and stored with the LaBr_3 and plastic scintillator energy in ten, three-dimensional histograms; one for each LaBr_3 detector.

A preliminary time-difference correction was applied to the time differences uniformly across the LaBr_3 and plastic scintillator dynode dynamic ranges to account for differences in cable lengths and digitizer synchronization for each LaBr_3 detector. An artificial time-difference offset of 1000 ns was introduced to avoid negative time differences.

Next, the plastic scintillator time response was calibrated. In this process, a two-dimensional projection of each three-dimensional histogram described above was taken over the 1173.2- and 1332.5-keV γ photopeak energy region in each LaBr_3 detector. This provides a region in the LaBr_3 detectors with low time walk variability, high statistics, and good time resolution for investigating the dynode time walk.

Each projection showed the dynode amplitude vs. time difference between each LaBr_3 detector and the dynode. The sum of all ten two-dimensional histograms is presented in Fig. 3.45a.

For each dynode amplitude bin in Fig. 3.45a, the centroid of the projection onto the

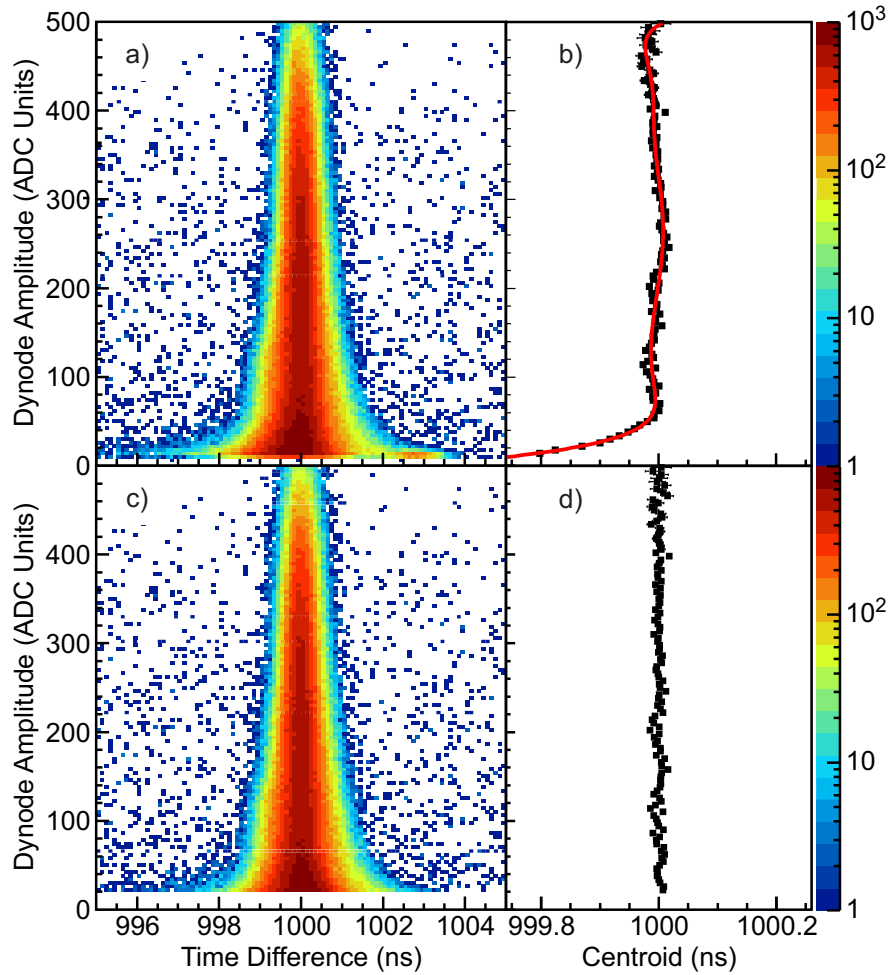


Figure 3.45: (a) Two-dimensional histogram of the dynode signal amplitude plotted against the LaBr₃ - PSMP T dynode time difference for a single LaBr₃ detector gated on either the 1173.2- or 1332.5-keV γ photopeak in that detector. (b) Plot of centroid position, extracted from fitting the projection of each bin in a) onto the time-difference axis. A high-order polynomial, shown in red, was used for interpolation between the data to extract the time walk as a function of dynode signal amplitude.

time-difference axis, obtained from a Gaussian fit, is displayed in Fig. 3.45b. These centroid values were fitted with a high-order polynomial, shown as a red line in Fig. 3.45b, to extract the walk correction as a function of the dynode signal amplitude.

The result of the dynode walk correction is shown in Figs. 3.45c and 3.45d. The corrected two-dimensional dynode amplitude vs. time-difference spectrum is shown in the former, while the dynode walk-corrected time-difference centroid values for each bin of Fig. 3.45c is

presented in the latter. The walk correction is valid for dynode-amplitude ranges of 20 to 500 ADC units. The resulting centroid values are all within 10 ps of the 1000 ns offset.

The next step focused on correcting the individual LaBr_3 detector responses. To obtain the time walk as a function of LaBr_3 detector energy, each bin of the dynode walk-corrected two-dimensional LaBr_3 energy vs. time-difference histogram, shown in Fig. 3.46a for one of the ten LaBr_3 detectors, was projected onto the time-difference axis and fitted with a Gaussian. Specific regions corresponding to the Compton edges and backscatter peaks of both the 1173.2- and 1332.5-keV photopeaks were removed from the spectrum shown in Fig. 3.46a due to anomalous behavior observed in the time response over these regions.

The centroid position extracted from the fit of the projection of each LaBr_3 detector energy bin shown in Fig. 3.46a is presented in Fig. 3.46b. These centroid values were fitted with a high-order polynomial, shown as a red line in Fig. 3.46b, to extract the walk correction as a function of LaBr_3 energy.

The result of the LaBr_3 walk correction is shown in Figs. 3.46c and 3.46d. The walk correction is valid for LaBr_3 energy ranges of 30 to 1400 keV and the resulting centroid values are all within 50 ps of the 1000 ns offset across the entire dynode dynamic range.

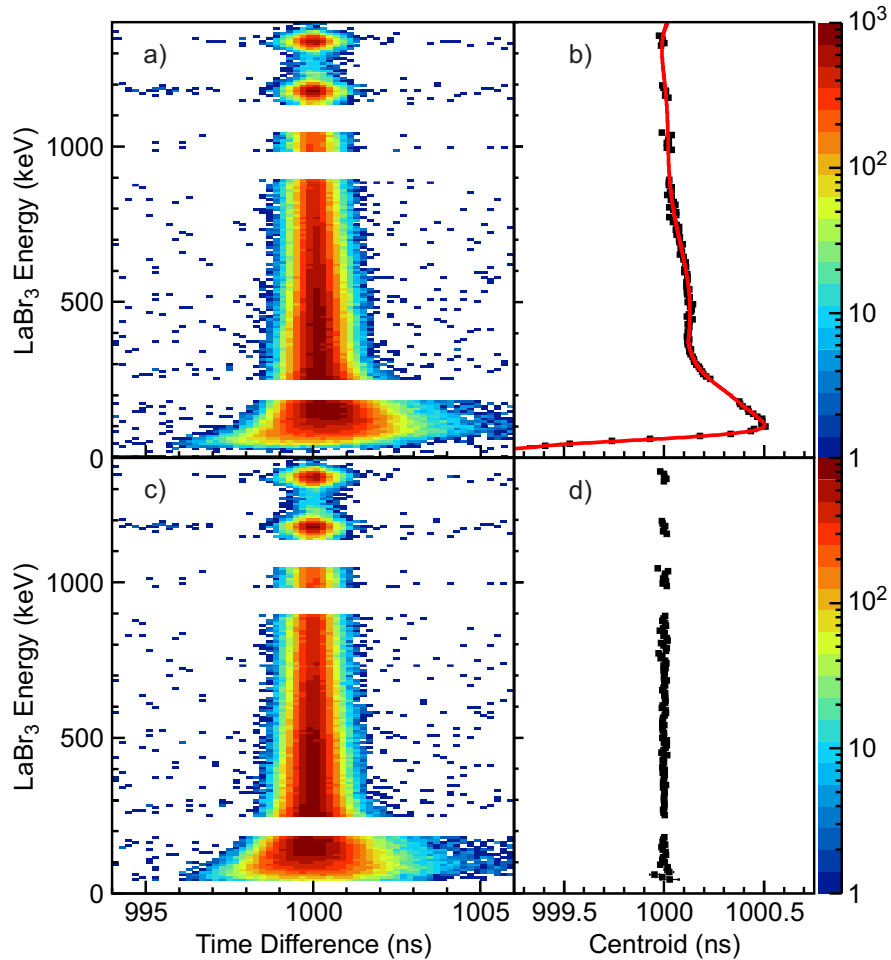


Figure 3.46: (a) Two-dimensional histogram of the LaBr₃ energy plotted against the LaBr₃ - PSMPD dynode time difference for a single LaBr₃ detector gated on dynode amplitudes between 20 and 500 ADC units. (b) Plot of centroid position for each LaBr₃ energy bin, extracted from fitting the projection of each bin in (a) onto the time-difference axis. A high order polynomial, shown in red, was used extract the time walk as a function of LaBr₃ energy.

3.9.2 Depth of Interaction Corrections

With the walk correction process complete, attention focused on accounting for the difference in plastic scintillator time resolution between the external source data and the internal decay data due to depth of interaction (DOI) effects. The lifetime extraction technique, presented later in this section, utilized the ⁶⁰Co source data to model the detector response. Therefore, an understanding of the difference in detector responses between the experimental and source

data is required. DOI effects are studied heavily in the medical imaging community and can alter time resolutions significantly [51].

To quantify the DOI effects in the present system, the decay of the 1077.4-keV state in ^{68}Zn was studied. Populated by the β decay of ^{68}Cu , this state in ^{68}Zn decays to the ground state with a half-life of 1.61 ps [22]. The 1.61 ps half-life is below the sensitivity of $\beta\gamma$ timing methods presented here and therefore was considered prompt.

The LaBr_3 energy spectrum for all ten detectors, gated on dynode amplitudes of >60 and <500 ADC units, in the region around 1077.4 keV is shown in Fig. 3.47. The peak region spans from 1064 to 1094 keV (solid red lines) while a background region was chosen from 1110 to 1140 keV (dashed red lines).

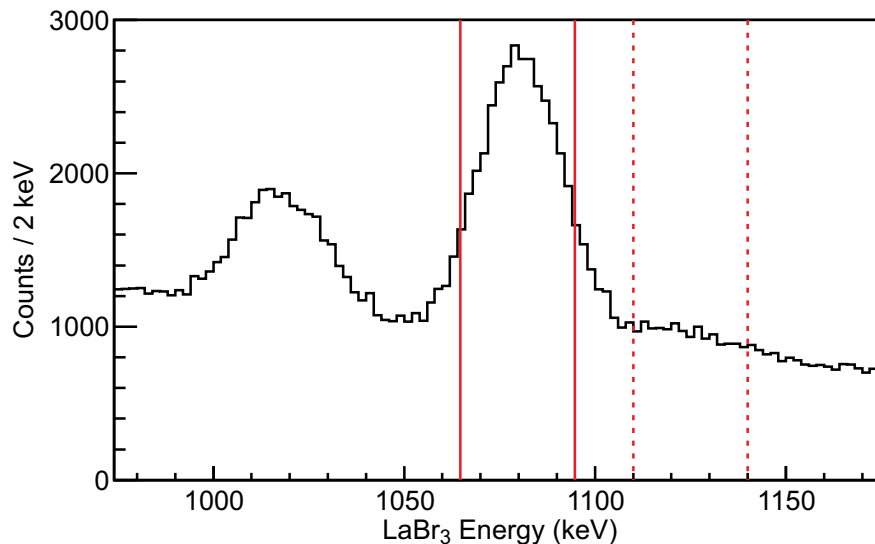


Figure 3.47: (a) LaBr_3 energy spectrum for all ten detectors, gated on dynode amplitudes of >60 and <500 ADC units, in the region around 1077.4 keV. The peak and background regions used for this analysis are denoted with red solid and red dashed lines, respectively.

The same peak and background regions were used to gate the two-dimensional dynode signal amplitude vs. time-difference spectrum for both the experimental and source data. In the case of the experimental data, the background-gated two-dimensional spectrum was scaled to match the background counts in the peak region and subtracted from the two-dimensional

spectrum in the peak region. This removes any response from potentially non-prompt contributions from Compton scattering of higher-energy transitions. The background-subtracted two-dimensional dynode signal amplitude vs. time-difference spectrum for the experimental data in the peak region shown in Fig. 3.47 is shown in Fig. 3.48a. The two-dimensional spectrum for the source data over the same LaBr₃ energy region as Fig. 3.48a is shown in Fig. 3.48b.

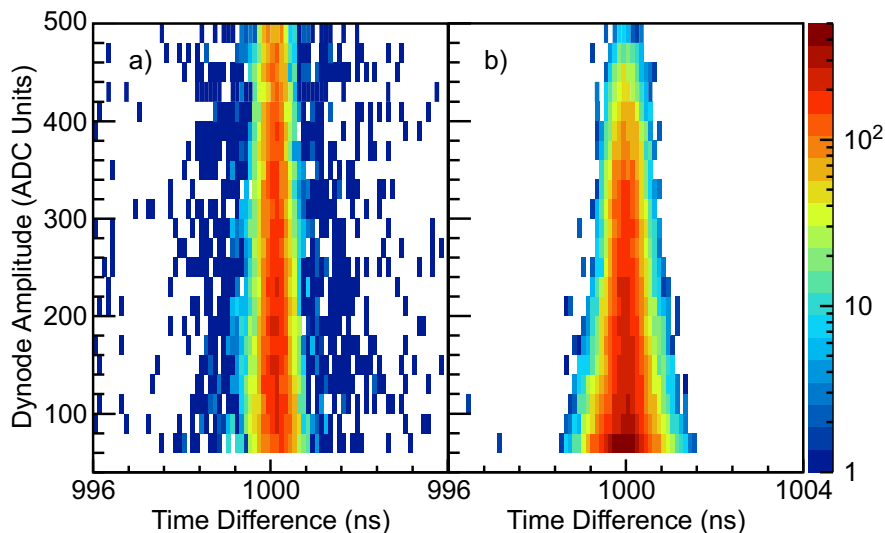


Figure 3.48: (a) Background-subtracted two-dimensional dynode signal amplitude vs. time-difference spectrum for the 1077.4-keV peak in the experimental data. (b) The two-dimensional dynode signal amplitude vs. time-difference spectrum for the ⁶⁰Co source measurements for the same energy gate as a).

The time resolution as a function of dynode signal amplitude was determined for both the experimental and source data by projecting each bin of the two-dimensional spectra shown in Figs. 3.48a and 3.48b, respectively, onto the time-difference axis and fitting a Gaussian function to each projection. The σ values (in ns) obtained from these projection fits are shown as a function of dynode signal amplitude in Fig. 3.49a. The data for the experimental time response are shown as black squares while the source results are shown as blue circles. Each of the two response curves were fitted with a power law, which is drawn

in its respective color in Fig. 3.49a.

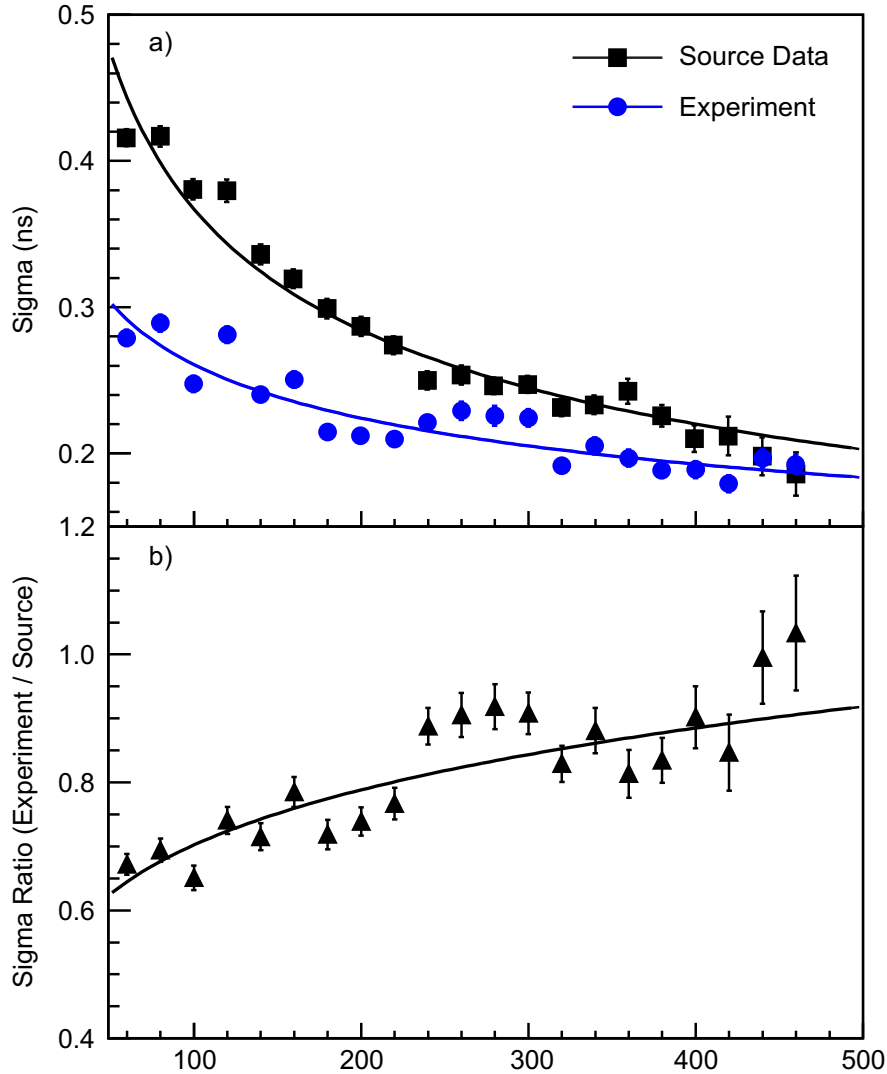


Figure 3.49: (a) Sigma (in ns) as a function of dynode signal amplitude shown in blue circles for the experimental data and as black squares for the source data presented in Figs. 3.48a and 3.48b, respectively. (b) The ratio (experiment/source) of sigma values from a) as a function of dynode signal amplitude. The fit to the data represents the DOI correction for the time resolution.

The ratio of the experimental data to the source data as a function of dynode signal amplitude is shown in Fig. 3.49b. The distribution of ratios was fitted with a power law, which is drawn as a solid black line in 3.49b. The fit to the ratios represents the dynode-amplitude-dependent correction factor that must multiply the sigma value for the source

data in the method described in the next section.

3.9.3 New Analysis Method for $\beta\gamma$ Lifetime Techniques

As demonstrated in the previous sections, the use of a thick plastic scintillator introduces a host of features that must be accounted for in the analysis for $\beta\gamma$ lifetime measurements. The amplitude dependence of the plastic scintillator response removes the ability to accurately fit the lifetime data with the convolution of a single Gaussian response and an exponential decay curve. Instead, the convolution of a continuum of Gaussian response functions with an exponential decay weighted by the number of counts at each energy in the continuum must be employed. In reality, the continuous distributions are discretized into bins and the technique to describe the detector system time response, $R(t, t_0, \tau, E_p, E_\gamma)$, can be summarized by Eq. (3.11).

$$R(t, t_0, \tau, E_p, E_\gamma) = sB(t) + \sum_{i=1}^n \sum_{E_p=E_0}^{E_F} \quad (3.11)$$

$$L_{i, E_p, E_\gamma} P_{E_p, E_\gamma} [f(t, t_0, i, E_p, E_\gamma) \otimes g(t, t_0, \tau)]$$

with

$$f(t, t_0, i, E_p, E_\gamma) = \text{Exp} \left[-\frac{1}{2} \left(\frac{(t - t_0)}{D(E_p) \sigma_i(E_p, E_\gamma)} \right)^2 \right]$$

and

$$g(t, t_0, \tau) = \text{Exp} \left[-\frac{(t - t_0)}{\tau} \right]$$

In Eq. (3.11), $B(t)$ represents the background underneath the peak. Typically $B(t)$ is sampled from nearby regions with minimal spectral interference. In most cases, $B(t)$ is roughly constant over the energy range one needs to sample and the background scale factor, s , is close to one.

The Gaussian response function, $f(t, t_0, i, E_p, E_\gamma)$, is characterized by a centroid t_0 and a time response width $\sigma_i(E_p, E_\gamma)$. The value of $\sigma_i(E_p, E_\gamma)$ for a particular LaBr₃ detector, i , depends on the photopeak energy, E_γ , and the plastic scintillator energy, E_p , has to be determined for each lifetime measurement. The DOI correction is represented by $D(E_p)$. The walk corrections presented above have removed the energy and detector dependencies from t_0 .

The exponential decay of the excited state, $g(t, t_0, \tau)$, depends only on the centroid, t_0 , and the lifetime, τ , of the decaying state. In Eq. (3.11), $g(t, t_0, \tau)$ is convolved with the detector response, $f(t, t_0, i, E_p, E_\gamma)$, for each LaBr₃ detector, i , and plastic scintillator dynode amplitude, E_p , at a specific photopeak energy E_γ . The resulting convolution is scaled by the relative contribution of each LaBr₃ detector, denoted as L_{i, E_p, E_γ} , and the dynode amplitude distribution, P_{E_p, E_γ} , to create the total convolution.

The linear combination of convolution functions describes the shape of the time distribution for the decay of a particular state of interest. That distribution function is sampled many times using Monte Carlo methods and the results are histogrammed. The resulting histogram is scaled to the number of counts in the peak over the region of interest, added to the scaled background, $sB(t)$, and compared with the experimental data. A χ^2 minimization is performed using trial lifetimes and the result is obtained from the fit of a χ^2 distribution.

3.9.4 Demonstration of the Technique on a Prompt Transition

Throughout the remainder of this section the new lifetime technique is demonstrated on three different excited states, all with known lifetimes. The first of these states is the 1077.4-keV state in ^{68}Zn , which was used to obtain the DOI correction. This is a simple case because, with a prompt decay, there is no convolution and only the energy-dependent Gaussian detector response remains. In particular, this test probes our ability to reproduce the time spectrum with no free parameters.

The LaBr₃ energy vs. time difference and vs. dynode amplitude are shown in Figs. 3.50a and 3.50b, respectively, for the same LaBr₃ energy range as in Fig. 3.47. The same 1064- to 1094-keV peak and 1110- to 1140-keV background regions, illustrated in Fig. 3.47, were used here and are once again depicted by red solid and dashed lines, respectively.

Figures 3.50c and 3.50e are the projection of Fig. 3.50a onto the time-difference axis for the peak and background regions, respectively. Figure 3.50c represents the total time-difference spectrum, while Fig. 3.50e is the unscaled background, which is $B(t)$ from Eq. (3.11). The scale factor, s , was obtained by fitting the one-dimensional LaBr₃ energy spectrum and comparing the integrated counts in the peak over the region of interest with both the total number of counts in the peak region and in the background region. For this case, $s = 1.05$.

Figures 3.50d and 3.50f are the projection of Fig. 3.50b onto the dynode signal amplitude axis for the peak and background regions, respectively. The data in Fig. 3.50f, scaled appropriately, are subtracted from the data in Fig. 3.50d. This provides the final dynode amplitude distribution, shown in Fig. 3.51, for the counts under the peak in the region of interest and also corresponds to P_{E_p, E_γ} from Eq. (3.11).

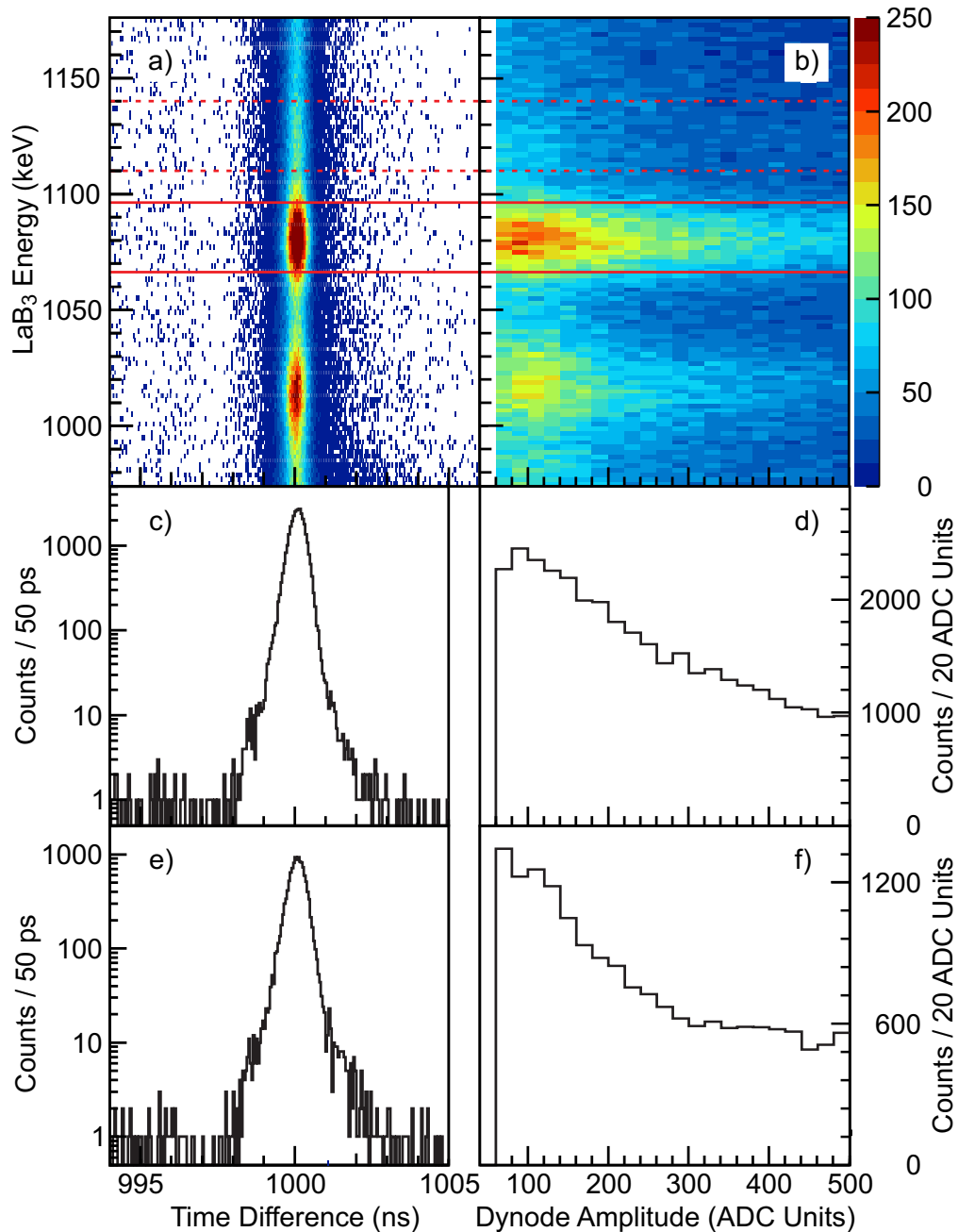


Figure 3.50: (a) LaBr₃ energy vs. time difference and (b) vs. LaBr₃ energy dynode amplitude, respectively, for the same LaBr₃ energy range as in Fig. 3.47. The same 1064- to 1094-keV peak and 1110- to 1140-keV background regions illustrated in Fig. 3.47 are shown again by red solid and dashed lines, respectively. Panels (c) and (d) show the projections of a) and b) onto the time-difference and dynode amplitude axes respectively, for the peak region between the solid red lines. Panels (e) and (f) show the projections of (a) and (b) onto the time-difference and dynode amplitude axes respectively, for the background region between the dashed red lines.

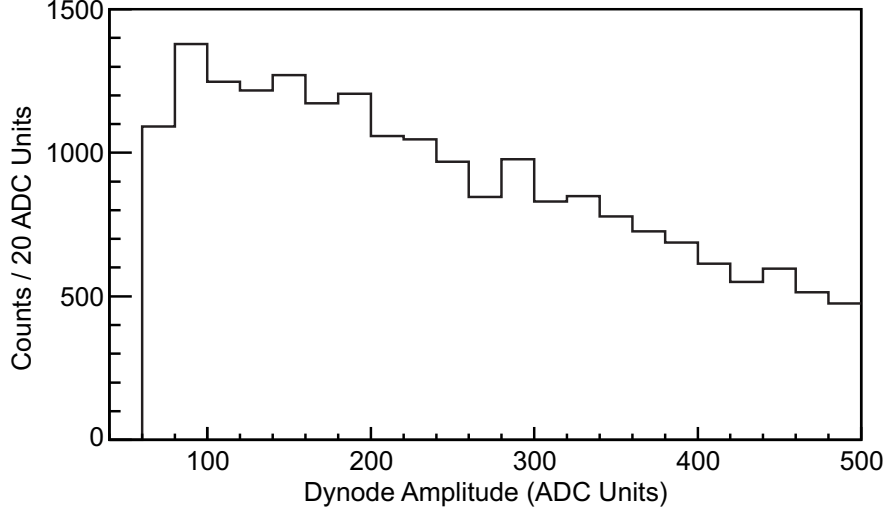


Figure 3.51: Dynode signal amplitude distribution for the LaBr_3 - dynode coincidences between 1064 and 1094 keV. This distribution is obtained by subtracting the data in Fig. 3.50f, scaled by s , from Fig. 3.50d. The counts at each dynode energy, E_p , at this specific γ energy, E_γ , are P_{E_p, E_γ} from Eq. (3.11).

The values of L_{i, E_p, E_γ} were obtained from the individual LaBr_3 $\beta\gamma$ coincidence spectra. The counts for each detector for the background energy region, scaled by s , are subtracted from the counts of each respective detector in the peak energy region.

Sigma values, $\sigma_i(E_p, E_\gamma)$, were obtained from the ^{60}Co source data as a function of dynode signal amplitude, E_p for the specific LaBr_3 energy region, E_γ in the same method described above to obtain the plots shown in Fig. 3.49a. The DOI correction, $D(E_p)$, shown in Fig. 3.49b, was then applied. With this, all quantities needed to fit the data have been extracted and the results of the procedure for the 1077.4-keV state in ^{68}Zn are shown in Fig. 3.52.

In Fig. 3.52, the total time-difference spectrum for the 1064- to 1094-keV LaBr_3 energy region is shown in black. This is the same spectrum that is shown in Fig. 3.50c. The scaled background time-difference spectrum over the 1110- to 1140-keV LaBr_3 energy region is shown in blue. The total fit of the detector response for the counts under the peak is

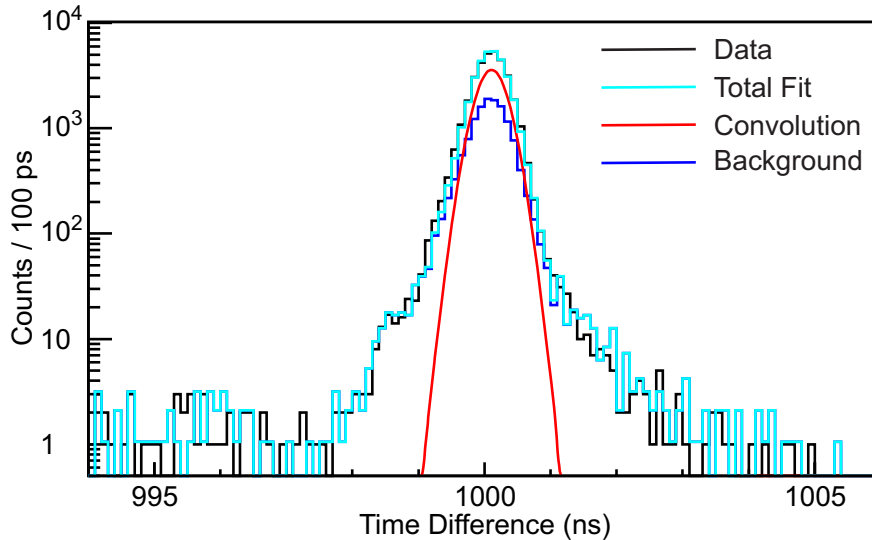


Figure 3.52: Results of the fitting technique for the 1077.4-keV state in ^{68}Zn . The total time-difference spectrum for the 1064- to 1094-keV LaBr_3 energy region, also shown in Fig. 3.50c, is shown in black. The scaled background time-difference spectrum over the 1110- to 1140-keV LaBr_3 energy region is shown in blue, while the total fit of the detector response for the counts under the peak is shown in red and the total fit is shown in cyan.

shown in red and the total fit is shown in cyan.

This test demonstrates the ability to completely describe the time response of the detector system. The stochastic background is accounted for by the scaled background contribution and the method takes into account the various higher-order amplitude dependent detector response effects to reproduce the experimental spectrum to a high degree.

3.9.5 Benchmarking the Technique on a Two Excited States with Known Lifetimes

With the lifetime-extraction technique demonstrated for a prompt transition, efforts focused towards deducing lifetimes of excited states with known lifetimes. The first of these was the 915.3-keV state in ^{69}Ni . This state has a previously measured half-life of 120(34) ps and there is strong, direct feeding following the β decay of ^{69}Co [52]. The state is depopulated

exclusively by a 594.3-keV γ ray.

The LaBr₃ spectrum coincident with counts in the dynode between 60 and 500 ADC units in the region around 594.3-keV is shown in Fig. 3.53. The peak and background energy regions of interest are denoted with solid and dashed red lines, respectively.

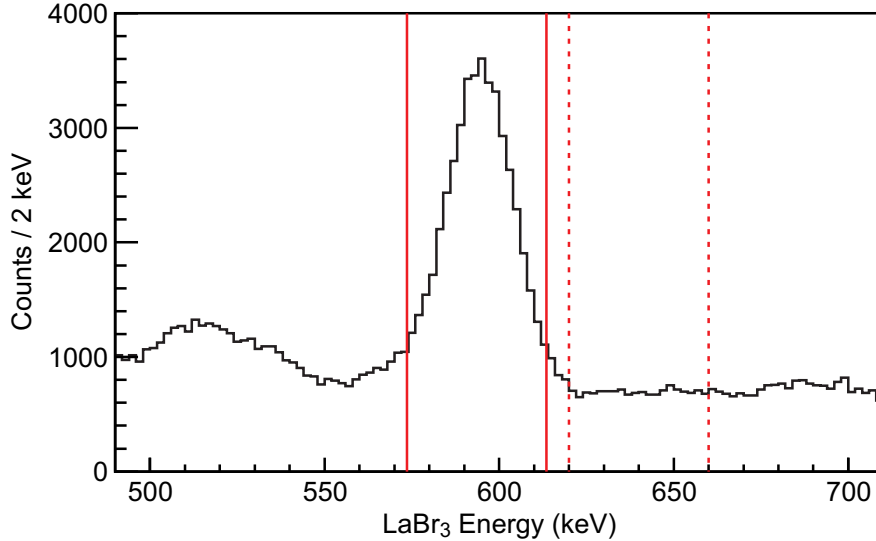


Figure 3.53: LaBr₃ energy spectrum for all ten detectors, gated on dynode amplitudes of >60 and <500 ADC units, in the region around 594.3 keV. The peak and background regions used for the analysis are denoted with red solid and red dashed lines, respectively.

The same procedure used for the ^{68}Zn analysis for obtaining the peak- and background-gated time-difference and dynode distribution spectra, analogous to those in Fig. 3.50, was used here. From those results the along with the calculated background scale factor, s , the dynode amplitude distribution for the counts in the peak, analogous to Fig. 3.51, was obtained.

The total detector response function described in Eq. (3.11) was constructed for fourteen trial half-lives and the χ^2 between $R(t, t_0, \tau, E_\gamma, E_p)$ and the experimental data was calculated for each trial half-life. The distribution of χ^2 values as black squares for the set of trial half-lives is shown in Fig. 3.54. A second order polynomial, presented in (3.12), was used to

fit the χ^2 distribution and is shown as a solid red line in Fig. 3.54.

$$\chi^2 = a\tau^2 + b\tau + c \quad (3.12)$$

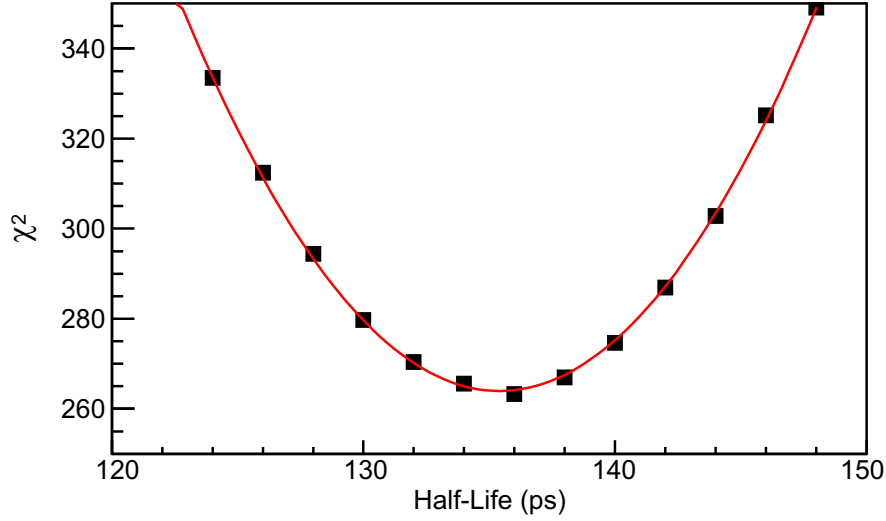


Figure 3.54: Distribution of χ^2 values obtained from a comparison of the total fit, $R(t, t_0, \tau, E_\gamma, E_p)$, and the experimental data, shown as cyan and black in Fig. 3.55, respectively, for fourteen half-life values equally distributed about the minimum. The distribution is fit with a second order polynomial shown in red. The location of the minimum represents the half-life of the state and the second derivative of the fit is the error on that value. A half-life of 135(26) ps is obtained for the 915.3-keV state in ^{69}Ni which agrees with the previously measured value of 120(34) ps [53].

The fit was used to extract the half-life and its error from the χ^2 distribution using Eq. (3.13) and Eq. (3.14), respectively [54].

$$\tau = -\frac{b}{2a} \quad (3.13)$$

$$\sigma_\tau^2 = 2 \left(\frac{\delta^2 \chi^2}{\delta \tau^2} \right)^{-1} \quad (3.14)$$

A value of 135(26) ps was obtained for the 915.3-keV state in ^{69}Ni , which agrees with the previously measured value of 120(34) ps [53]. The statistical error was determined from

the half-life values one χ^2 unit from the minimum. Systematic errors were investigated by varying quantities such as the ratio of counts in the peak to counts in the background, the centroid of the underlying Gaussian component of the convolution, and the magnitude of the DOI correction. All errors were added in quadrature. The best fit result for the 915.3-keV state in ^{69}Ni is presented in Fig. 3.55.

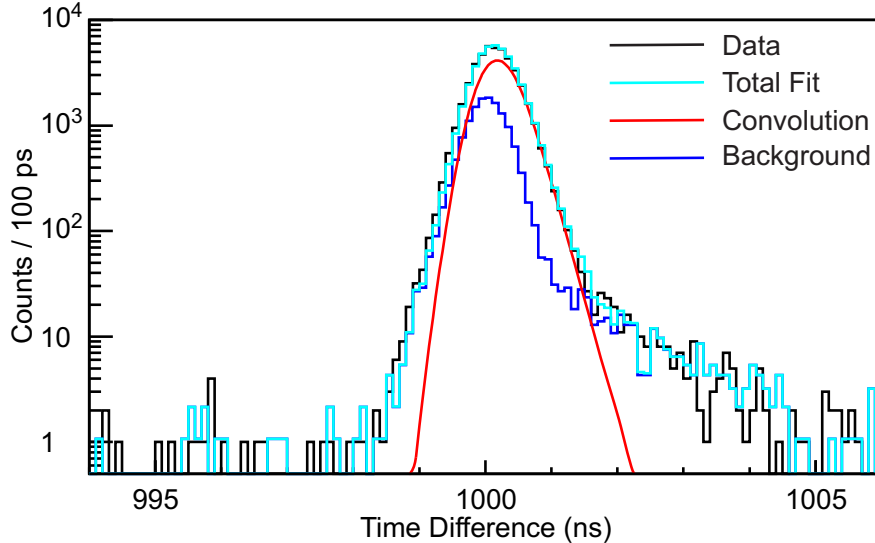


Figure 3.55: Results of the fitting technique for the 915.3-keV state in ^{69}Ni . The total time-difference spectrum for the 574- to 614-keV LaBr_3 energy region is shown in black. The scaled background time-difference spectrum over the 620- to 660-keV LaBr_3 energy region is shown in blue, while the total fit of the detector response for the counts under the peak is shown in red and the total fit is shown in cyan.

The total time-difference spectrum for the 574- to 614-keV LaBr_3 energy region is shown in black. The scaled background time-difference spectrum over the 620- to 660-keV LaBr_3 energy region is shown in blue, while the best fit convolution for the counts under the peak is shown in red and the resulting total best-fit to the data is shown in cyan. Once again, the technique does a good job of reproducing all the features of the data.

The second state used to benchmark the technique is the 2677-keV state in ^{70}Ni . This state has a previously measured half-life of 1.05(3) ns [53]. The LaBr_3 spectrum coincident with counts in the dynode between 60 and 500 ADC units in the region around 448.5-keV

is shown in Fig. 3.56. The peak and background energy regions of interest are denoted with solid and dashed red lines, respectively. For this region, the background must be sampled below the peak to avoid any contamination from the 478-keV transition in ^{68}Ni .

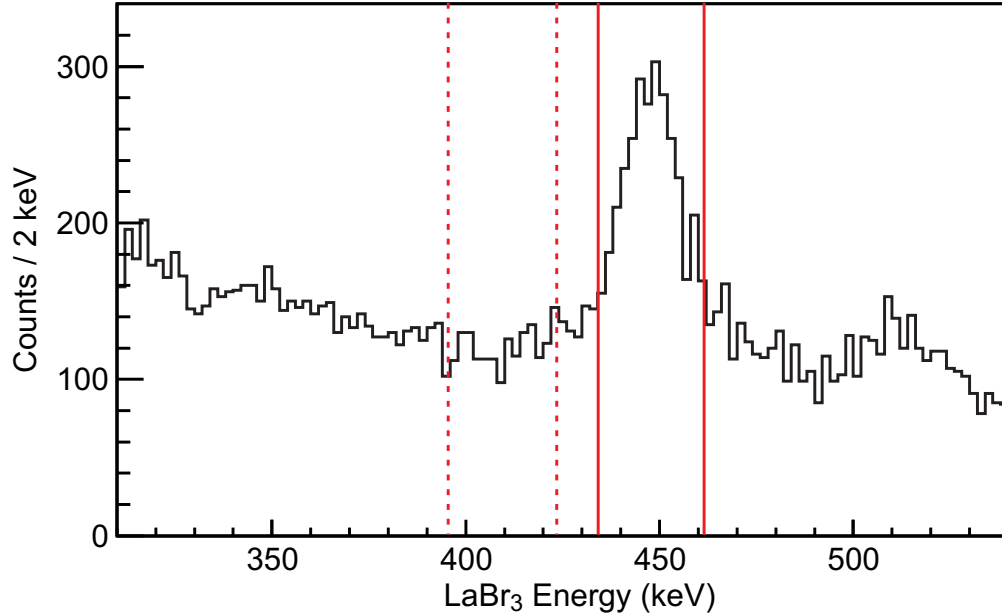


Figure 3.56: LaBr₃ energy spectrum for all ten detectors, gated on dynode amplitudes of >60 and <500 ADC units, in the region around 448.5 keV. The peak and background regions used for the analysis are denoted with red solid and red dashed lines, respectively.

The analysis for the 2677-keV 6_1^+ state in ^{70}Ni , which decays by emitting a 448.5-keV γ -ray, is identical to the techniques described for the 915.3-keV state in ^{69}Ni . The resulting χ^2 distribution for the fourteen trial half lives distributed evenly about the minimum is presented in Fig. 3.57. The same fitting procedure for the χ^2 distribution using the Eq. (3.12) was carried out and the result is shown as a solid red line in Fig. 3.57.

From the fit of the χ^2 distribution in Fig. 3.57 and Eqs. (3.13) and (3.14), a value of 1.04(6) ns was obtained for the half-life of the 2677-keV state in ^{70}Ni . The statistical error was determined from the half-life values one χ^2 unit from the minimum. Systematic errors were investigated by varying quantities such as the ratio of counts in the peak to counts in the background, the centroid of the underlying Gaussian component of the convolution, and

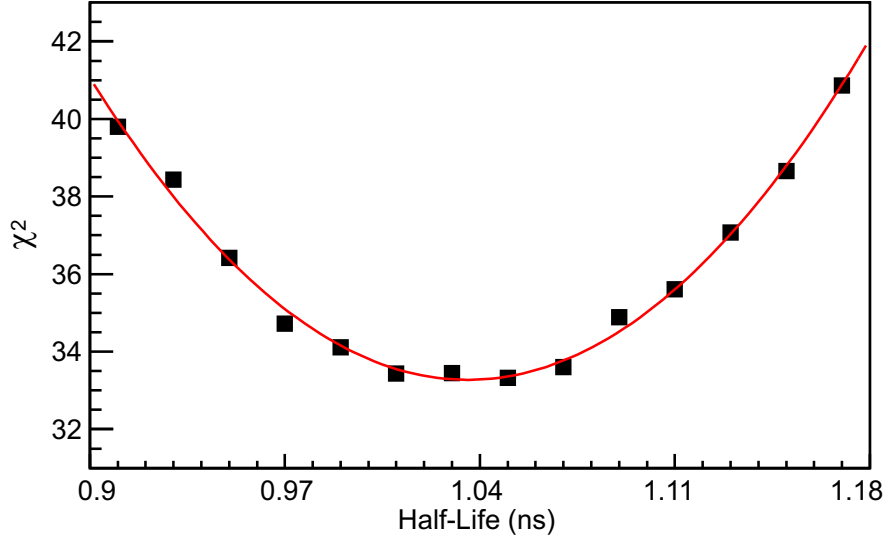


Figure 3.57: Distribution of χ^2 values obtained from a comparison of the total fit and the experimental data, shown as cyan and black in Fig. 3.55, respectively, for fourteen half-life values equally distributed about the minimum. The distribution is fit with a second order polynomial shown in red resulting in a lifetime of 1.04(6) ns for the 2677-keV state in ^{70}Ni .

the magnitude of the DOI correction. All errors were added in quadrature. The result agrees very well with the previously measured value of 1.05(3) ns [53]. The best fit result for the 2677-keV state in ^{70}Ni is presented in Fig. 3.58.

The total time-difference spectrum for the 434- to 462-keV LaBr_3 energy region is shown in black. The scaled background time-difference spectrum over the 396- to 424-keV LaBr_3 energy region is shown in blue, while the best fit convolution for the counts under the peak is shown in red and the resulting total best-fit to the data is shown in cyan. Once again, the technique does a good job of reproducing all the features of the data.

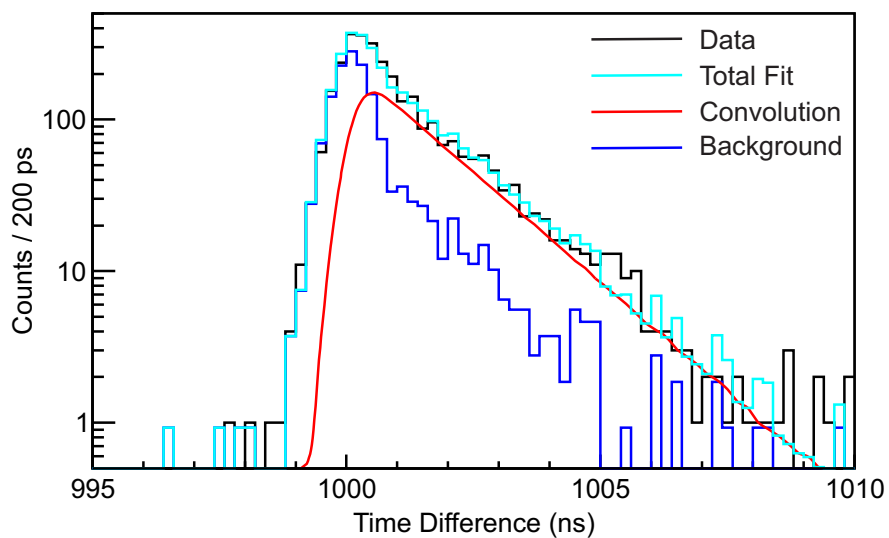


Figure 3.58: Results of the fitting technique for the 2677-keV state in ^{70}Ni . The total time-difference spectrum for the 396- to 424-keV LaBr_3 energy region is shown in black. The scaled background time-difference spectrum over the 434- to 462-keV LaBr_3 energy region is shown in blue, while the total fit of the detector response for the counts under the peak is shown in red and the total fit is shown in cyan.

Chapter 4

Experimental Results

In this chapter, the full analysis of the decays of $^{68,70}\text{Co}$ is presented. Each section begins by summarizing the results of prior experimental investigations and concludes with the decay schemes obtained from the present work. All spectra and relevant analyses, required to obtain the final results, are presented and described in detail.

4.1 Decay of ^{68}Co

4.1.1 Decay of the Long-Lived ^{68}Co Isomer

The low-energy level scheme of ^{68}Ni was studied following the β -decay of the low-spin isomer of ^{68}Co [12], selectively populated through the β decay of ^{68}Fe . Several prior experiments focused on ^{68}Ni have been performed, and as such, a fair amount was previously known about the low-energy level scheme of ^{68}Ni . More specifically, the characterization of the three low-lying 0^+ states has been of paramount importance for understanding the evolution of nuclear structure in the region. The most recent work, described in Ref. [21], studied the decay of the low-spin isomer of ^{68}Co into ^{68}Ni and yielded the decay scheme shown in Fig. 4.1.

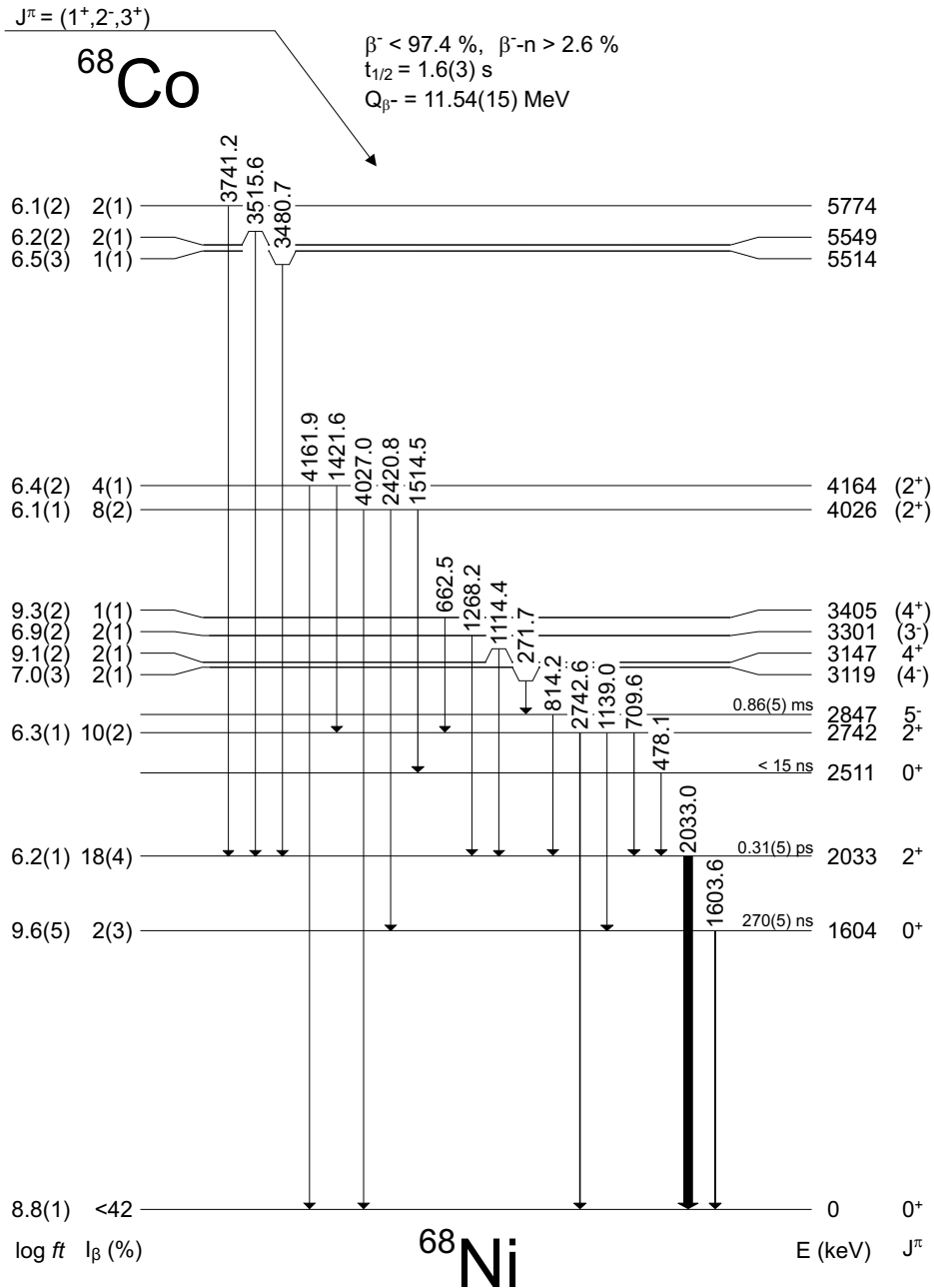


Figure 4.1: Decay scheme, adapted from Ref. [21], for the decay of the low-spin ^{68}Co isomer populating states in ^{68}Ni representing the extent of knowledge prior to the present work. Other low-energy levels in ^{68}Ni , not shown here, are known from reaction studies and decay spectroscopy of the high-spin ^{68}Co isomer. Three spin and parity assignments of $(1^+, 2^-, 3^+)$ have been proposed for the low-spin ^{68}Co isomer by Refs. [12, 21, 55]. The 1.6(3)s half-life comes from Ref. [12], as does the <15 ns limit on the half-life of the 2511-keV 0_3^+ state. A β -delayed neutron branch of >2.6 % was reported by Ref. [21]. The β -decay Q -value was taken from Ref. [56]. All log ft values and β -decay feeding intensities were taken from Ref. [21]. The half-lives of 270(5) ns for the 1604-keV 0_2^+ state, 0.31(5) ps for the 2033-keV 2_1^+ , and 0.86(5) ms for the 2847-keV 5^- state were taken from Ref. [22].

The decay scheme in Fig. 4.1 represents the extent of existing knowledge of the low-energy level scheme of ^{68}Ni populated by the decay of the long-lived, low-spin ^{68}Co isomer prior to the present work.

The first excited state in ^{68}Ni is the 0_2^+ state, originally placed at 1770(30) keV, and was discovered using the $^{70}\text{Zn}(^{14}\text{C}, ^{16}\text{O})^{68}\text{Ni}$ transfer reaction and assigned a 0^+ spin and parity from angular distributions [17]. A subsequent experiment deduced a half-life of 270(5) ns for the 0_2^+ [44]. More recently, the work of Ref. [18] utilized the same methods described in Section 3.5.5 to directly observe the $0_2^+ \rightarrow 0_1^+$ $E0$ transition in the planar GeDSSD. The results of Ref. [18] adjusted the energy of the 0_2^+ state to 1605(3) keV and yielded a half-life of 268(12) ns for the 0_2^+ state. The placement of the 1139-keV transition was moved to feeding the 0_2^+ state [18] from the 2742-keV 2^+ state [12, 20]. A second γ ray with an energy of 2420-keV was also identified and placed feeding the 0_2^+ state [18] from a state at 4026-keV [12].

The adjusted energy of the 0_2^+ state in ^{68}Ni and placement of the 1139-keV γ ray and were confirmed in subsequent experiments using complimentary deep inelastic scattering and two-neutron knockout reactions [19]. The most recent work of Ref. [21] was also able to directly detect the $(0_2^+ \rightarrow 0_1^+)$ $E0$ transition using coincidence technique between two plastic scintillators, where the electron from the β decay of ^{68}Co was recorded in one scintillator followed a short time later by detection of the electron from the discrete $E0$ transition in the other. The 0_2^+ state was placed at 1603.6(8) keV and from a fit of the histogram of time differences between the two plastic scintillators, accounting for both spurious coincidences and scattered β -decay electrons, a half-life of 235(23) ns was obtained [21].

The two most recent decay spectroscopy measurements [18, 21] searched for the expected 430-keV $(2_1^+ \rightarrow 0_2^+)$ transition, but only limits on the $(2_1^+ \rightarrow 0_2^+)$ branch were established

as $<1\%$ and $<0.7\%$, respectively. Lacking a measurement of transition strength, the work of Ref. [18] assumed maximal mixing between spherical and deformed configurations in a two-level mixing model and obtained a difference in mean-square charge radii of 0.15 fm^2 between the 0_1^+ and 0_2^+ states and a value of $|102\text{ efm}^2|$ for the intrinsic quadrupole moment of the 0_2^+ state. When compared to the -95 efm^2 predicted by the Monte Carlo Shell Model (MCSM), these results provided the first indication of shape coexistence in ^{68}Ni .

The 2511-keV 0_3^+ state was observed in the work of Ref. [12] and subsequent angular correlation measurements confirmed the 0^+ spin and parity assignment [20]. Until the present work, only a limit of $<15\text{ ns}$ was placed on the half-life of the 0_3^+ state [12]. The work of Ref. [12] placed a limit of $<50\%$ for the $0_3^+ \rightarrow 0_1^+$ $E0$ transition branch. Subsequent measurements placed a limit of $<4\%$ for the sum of the $0_3^+ \rightarrow 0_1^+$ and $0_3^+ \rightarrow 0_2^+$ $E0$ transitions branch.

The remainder of this section describes the analysis of ^{68}Co β decay populated by the β decay of ^{68}Fe . ^{68}Co has two β -decaying isomeric states, with tentative spin and parity assignments of $(1^+, 2^-, 3^+)$ [12, 21, 55] and (7^-) [12] and measured half-lives of $1600(300)\text{ ms}$ [12] and $200(2)\text{ ms}$ [22], respectively. The (1^+) spin and parity assignment is adopted for the long-lived, low-spin ^{68}Co isomer for the remainder of this chapter and the reasons for this choice are discussed in Section. 5.2. The ground-state spin and parity of ^{68}Fe is 0^+ [22], and thus, based on the β -decay selection rules discussed in Section 2.1, β decay predominately populates positive-parity low-spin ($J = 0,1$) states in ^{68}Co with little population of the (7^-) isomer ^{68}Co isomer. Previous β -decay studies [12] suggest that the only the β decay of the low-spin ^{68}Co isomer leads to population of the 0_2^+ state in ^{68}Ni .

Ions of ^{68}Fe were implanted into the GeDSSD, described in Section 3.5, and the segmented plastic scintillator, described in Section 3.6 during experiments e14039 and e14057,

respectively. Subsequent β decays were correlated to ^{68}Fe ions using the techniques described in Section 3.5.2 and Section 3.6.2 for the GeDSSD and segmented plastic scintillator, respectively, using a 4000 ms correlation window.

The β -delayed γ -rays recorded within 4000 ms of a ^{68}Fe ion implantation are shown in Fig.4.2. Transitions identified as belonging to ^{68}Ni are labeled with an energy, while all other transitions from the decay of both beam contaminants and daughter, granddaughter, etc. nuclei are denoted with symbols. The two peaks at 1460 and 2614 keV, denoted with two asterisks, are the strong background γ rays from the decay of ^{40}K [49] and ^{208}Tl [50], respectively.

/FloatBarrier

A list of all observed transitions placed in ^{68}Ni , their absolute intensities, and the initial and final states between which the transition occurs is presented in Table 4.1. Absolute intensities were calculated by dividing the number of counts in each peak, obtained from a Gaussian fit plus a linear background component, corrected for γ -ray efficiency, by the number of ^{68}Co decays listed in Table 4.7 and discussed in Section 4.1.2.5.

/FloatBarrier

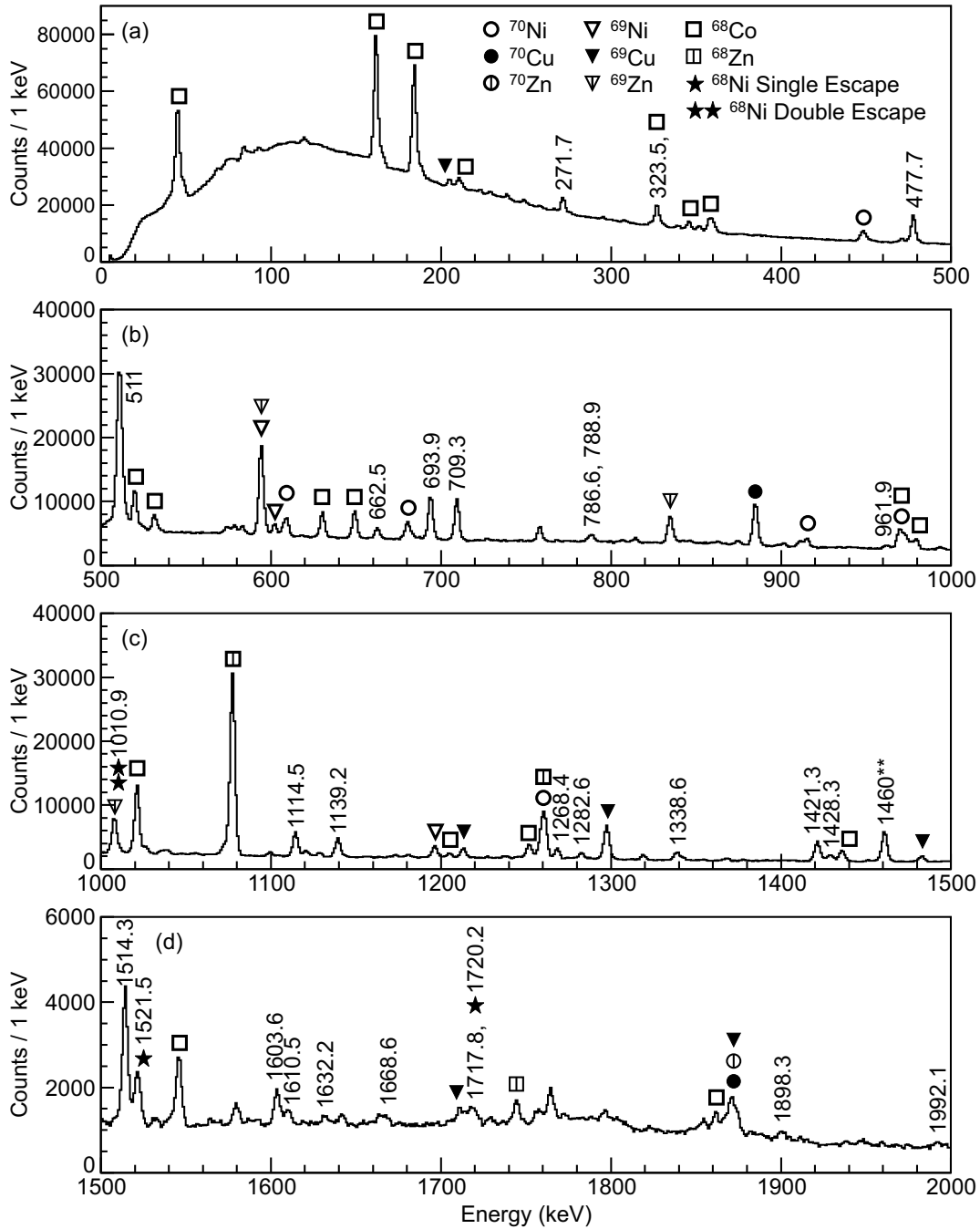


Figure 4.2: β -delayed γ -ray spectrum recorded in SeGA within 4000 ms of an implanted ^{68}Fe ion. Transitions identified in the subsequent analysis as affiliated with the decay of ^{68}Ni are labeled with their energy while contaminating transitions, resulting from spurious correlations of the decay of other implanted nuclei, are denoted with symbols. The peaks at 1460 and 2614 keV are known background γ -rays from the decay of ^{40}K [49] and ^{208}Tl [50], respectively. The inset in (e) shows the full height of the 2032.9-keV peak truncated in the spectrum displayed in (e).

Figure 4.2: (cont'd)

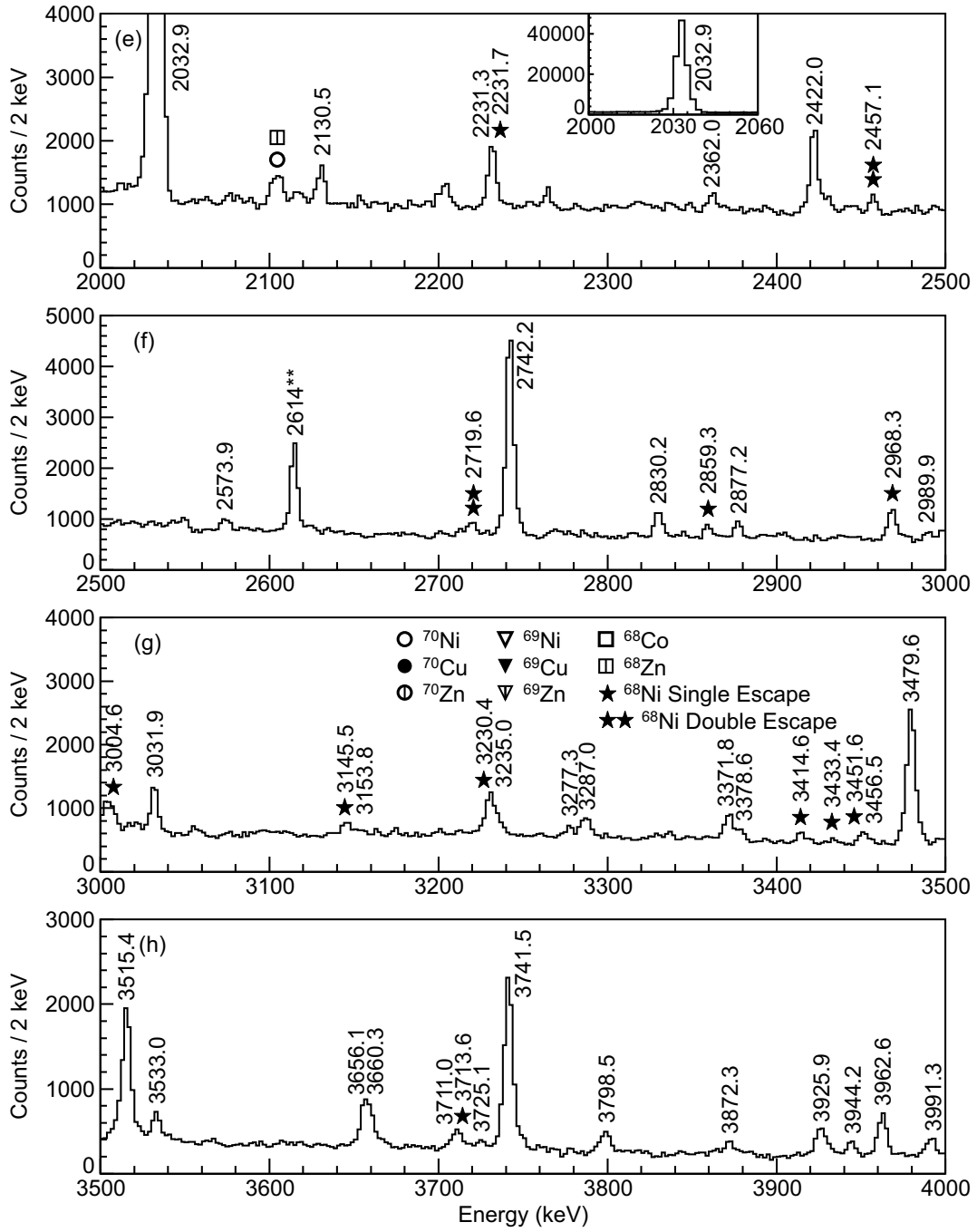


Figure 4.2: (cont'd)

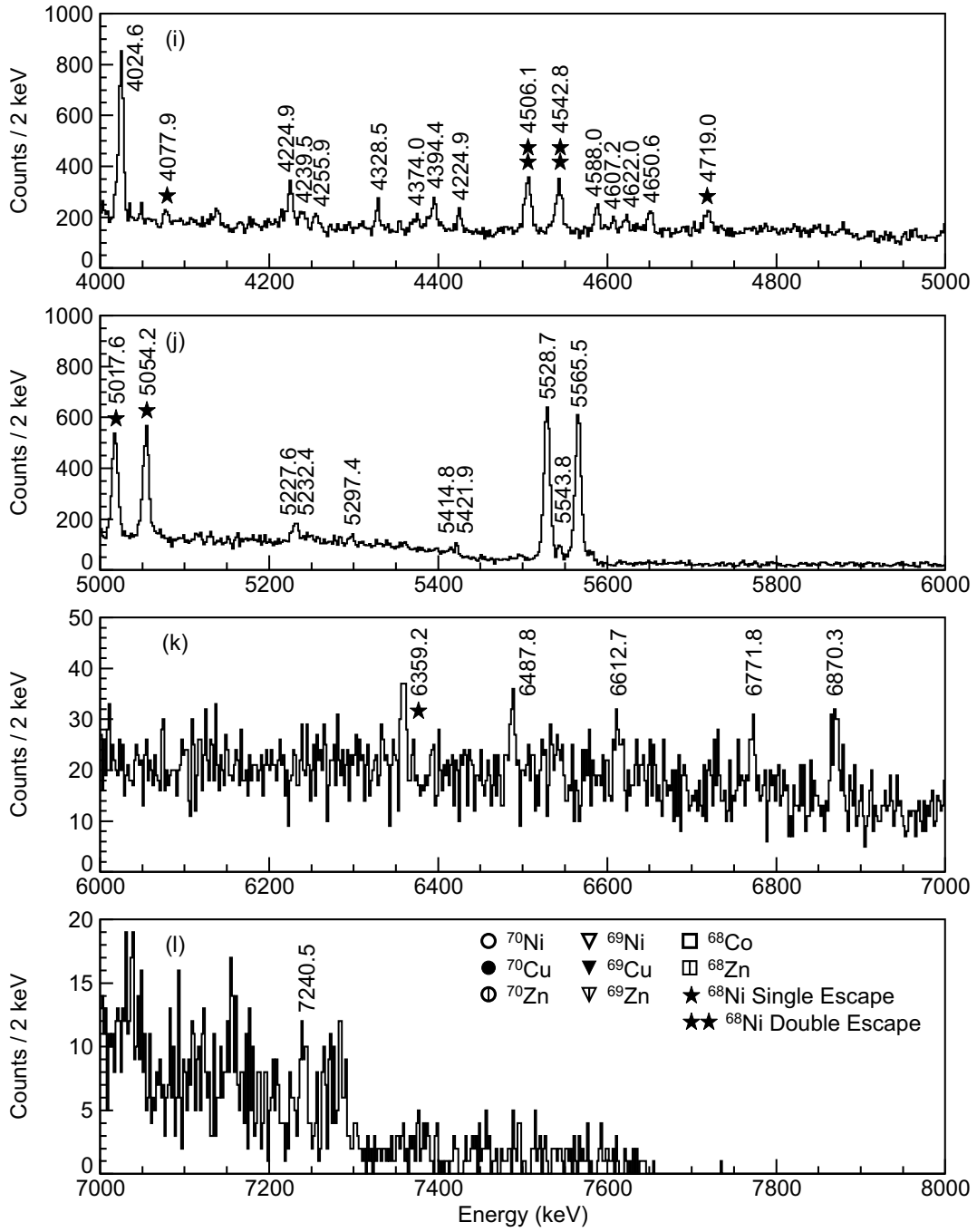


Table 4.1: Energies and absolute intensities of the γ -ray transitions placed in ^{68}Ni following the β decay of the long-lived, low-spin, ^{68}Co isomer selectively populated by the β decay of ^{68}Fe . The energies of the initial and final states for each transition are also listed.

E_γ (keV)	$I_\gamma^{absolute}$ (%)	Initial State (keV)	Final State (keV)
258.3(2)	0.26(8)	3406	3147
271.7(2)	2.26(22)	3119	2847
323.5(3)	0.39(10)	3442	3119
429.8(3) ^b	0.06(1)	2033	1603
477.7(2)	6.18(56)	2511	2033
662.5(2)	1.31(11)	3405	2742
693.9(2) ^a	5.53(50)		
709.3(2)	5.10(47)	2742	2033
786.6(5)	0.35(13)	2819	2033
788.9(3)	0.87(22)	2822	2033
862.8(4)	0.27(8)	2896	2033
961.9(2)	0.54(8)	4109	3147
1104.2(5)	0.12(5)	4405	3301
1114.5(2)	4.22(39)	3147	2033
1139.2(2)	3.34(25)	2742	1603
1268.4(2)	1.68(17)	3301	2033
1282.6(2)	1.05(10)	4025	2742
1338.6(2)	1.61(36)	3371	2033
1344.0(8) ^b	0.22(8)	5690	4346
1366.4(4) ^b	0.40(17)	5530	4164
1400.3(3) ^b	0.70(22)	5564	4164
1421.3(2)	4.43(33)	4164	2742
1428.3(3)	0.44(10)	5774	4346
1514.3(2)	4.75(44)	4025	2511
1540.7(4) ^b	0.18(5)	4283	2742
1554.9(7) ^b	0.39(17)	7067	5512
1579.2(3) ^b	0.24(11)	5744	4164
1603.6(2)	1.29(11)	4346	2742
1610.5(3)	0.73(13)	5774	4164
1631.2(3)	0.16(4)	4373	2742
1641.3(3) ^b	0.04(1)	5774	4133
1668.6(3)	0.24(6)	5694	4025
1705.3(7) ^b	0.10(4)	4448	2742

^a Transition belongs to ^{67}Ni populated by ^{68}Co β -delayed neutron emission

^b Transition observed only in coincidence spectra

^c Transition placed without coincidences based on energy differences between known levels

Table 4.1: (cont'd)

E_γ (keV)	$I_\gamma^{absolute}$ (%)	Initial State (keV)	Final State (keV)
1713.3(5) ^b	0.29(8)	4456	2742
1716.0(5) ^b	1.03(40)	3750	2033
1717.8(4)	0.27(12)	5743	4025
1898.3(5) ^b	0.69(33)	3931	2033
1992.1(5)	0.27(8)	4025	2033
2032.9(2)	51.4(46)	2033	0
2130.5(2)	0.86(11)	4163	2033
2231.3(8) ^b	0.63(30)	4264	2033
2362.0(4)	0.36(7)	4395	2033
2422.0(2)	1.90(15)	4025	1603
2529.8(3) ^b	0.23(4)	4133	1603
2573.9(4)	0.41(8)	4607	2033
2728.3(4) ^b	0.13(8)	4761	2033
2742.2(2)	6.65(61)	2742	0
2830.2(2)	0.86(11)	5978	3147
2844.6(3) ^b	0.21(3)	4448	1603
2947.1(6) ^b	0.36(10)	5689	2742
2989.9(5)	0.24(6)	6361	3371
3002.6(8) ^b	0.13(9)	6407	3405
3020.3(6) ^c	0.52(11)	5531	2511
3031.9(2)	1.34(12)	5774	2742
3054.9(5) ^b	0.21(5)	5565	2511
3092.8(5) ^b	0.13(7)	6498	3405
3095.3(12) ^b	0.18(6)	6467	3371
3218.4(11) ^b	0.09(6)	7242	4025
3235.9(6) ^b	0.43(12)	5977	2742
3265.2(5) ^b	0.14(7)	5776	2511
3277.3(10)	0.12(4)	4880	1603
3290.9(9) ^b	1.42(47)	5324	2033
3358.2(6) ^b	0.18(11)	6506	3147
3371.8(2)	0.91(12)	3372	0
3378.6(5)	0.37(10)	5412	2033
3455.0(8) ^b	0.030(22)	5489	2033

^b Transition observed only in coincidence spectra

^c Transition placed without coincidences based on energy differences between known levels

Table 4.1: (cont'd)

E_γ (keV)	$I_\gamma^{absolute}$ (%)	Initial State (keV)	Final State (keV)
3479.6(2)	5.13(48)	5512	2033
3496.5(6) ^b	0.12(04)	5529	2033
3508.8(7) ^b	0.32(14)	6656	3147
3515.4(2)	3.59(34)	5548	2033
3533.0(3)	0.477(77)	5566	2033
3608.5(10) ^b	0.42(13)	5641	2033
3656.1(3)	1.16(28)	5689	2033
3660.3(3)	0.71(19)	5693	2033
3711.0(3)	0.49(11)	5744	2033
3741.5(2)	5.17(48)	5774	2033
3872.3(3)	0.49(11)	5905	2033
3925.9(2)	1.036(91)	5529	1603
3944.2(2)	0.378(66)	5977	2033
3962.6(2)	1.34(11)	5566	1603
4024.6(2)	1.92(19)	4025	0
4198.7(13) ^b	0.10(6)	6941	2742
4224.9(3)	0.55(10)	6258	2033
4239.5(6)	0.224(39)	5843	1604
4255.9(7)	0.264(78)	6289	2033
4328.5(3)	0.221(60)	6361	2033
4374.0(9)	0.219(69)	6407	2033
4394.4(5)	0.54(11)	4394	0
4424.9(4)	0.211(56)	6458	2033
4500.1(3) ^b	0.110(42)	7242	2742
4588.0(3)	0.358(69)	6621	2033
4607.2(5)	0.144(52)	6640	2033
5227.6(8)	0.148(61)	7260	2033
5337.7(10) ^b	0.022(11)	6941	1603
5395.8(8) ^b	0.060(18)	6999	1603
5528.7(1)	3.52(34)	5529	0
5565.5(1)	3.36(32)	5566	0
5639.8(8) ^b	0.016(8)	7242	1603
5978.0(6) ^b	0.008(4)	7581	1603
6178.6(14) ^b	0.016(8)	7782	1603
7240.5(10)	0.064(22)	7241	0

^b Transition observed only in coincidence spectra

^c Transition placed without coincidences based on energy differences between known levels

The placement of γ rays listed in Table 4.1 was done using $\beta\gamma\gamma$ coincidences. Of particular interest for investigating shape coexistence is the $\beta\gamma\gamma$ coincidence spectrum gated on the 1514.3-keV γ ray, shown in Fig. 4.3, which is known to feed the 2511-keV 0_3^+ state [12]. If the 0_3^+ state were to decay by a 2511-keV $E0$ transition, it would proceed predominately by internal pair-formation with a 92.1 % branch [34]. The 511-keV γ rays emitted from the positron annihilation would be present in the $\beta\gamma\gamma$ -ray spectrum, shown in Fig. 4.3, coincident with the 1514.3-keV feeding transition.

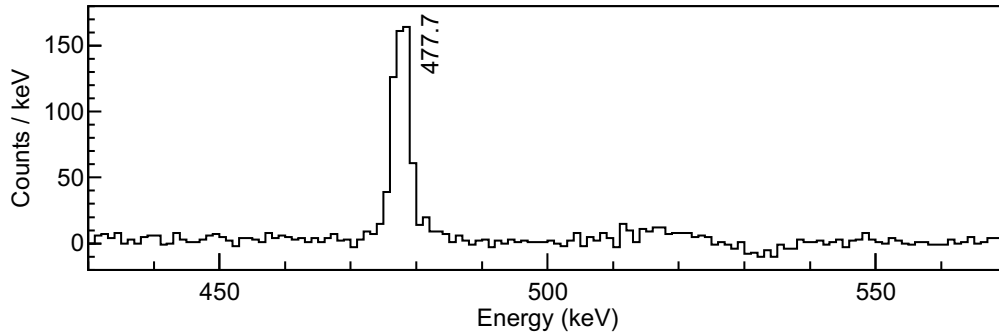


Figure 4.3: Background-subtracted $\beta\gamma\gamma$ coincidence spectra gated on the 1514.3-keV (2^+) \rightarrow 0_3^+ transition in ^{68}Ni focusing around the 511-keV region. The background was taken below the 1514.3-keV peak to avoid the 1521.5-keV single escape peak from the 2032.9-keV γ ray. The upper range of the gate was also reduced by a couple of keV to avoid including the low-energy tail of the 1521.5-keV escape peak.

The strong 477.7-keV $0_3^+ \rightarrow 2_1^+$ transition is observed in Fig. 4.3, as expected. No clear evidence of a 511-keV γ ray is present and analysis of the spectrum in Fig. 4.3 places a limit of $<1.7\%$ $0_3^+ \rightarrow 0_1^+$ $E0$ transition branch. Additional coincidences with the 1514.3-keV γ ray, outside the range of Fig. 4.3, are shown in Fig. B.3q in Appendix B. Appendix B also contains several other $\beta\gamma\gamma$ coincidence spectra, and a summary of all observed $\beta\gamma\gamma$ coincidences is presented in Table. 4.2.

/FloatBarrier

In Sections 3.5.5 and 3.6.3, the techniques for detecting the $0_2^+ \rightarrow 0_1^+$ $E0$ transition in

Table 4.2: Summary of observed γ -ray coincidences following the β decay of the long-lived, low-spin, ^{68}Co isomer populated by the β decay of ^{68}Fe .

E_γ (keV)	Coincident E_γ (keV)
258.3(2)	1114.5, 2032.9
271.7(1)	323.5,
323.5(2)	271.7
477.7(1)	477.7, 511, 1514.3, 2032.9, 3054.9, 3265.2
662.5(1)	511, 709.3, 1139.2, 2032.9, 2742.2, 3002.6, 3092.8
709.3(1)	511, 662.5, 1282.6, 1421.3, 1428.3, 1603.6, 1610.5, 2032.9, 3031.9
786.6(4)	2032.9
788.9(2)	2032.9
862.8(3)	2032.9
961.9(1)	1114.5, 2032.9
1104.2(5)	1268.4, 2032.9
1114.5(1)	511, 969.1, 2032.9, 2830.2, 3358.2, 3508.8
1139.2(1)	511, 662.5, 1282.6, 1421.3, 1428.3, 1603.6, 1610.5
1268.4(1)	1104.2, 2032.9
1282.6(1)	709.3, 1139.2, 2032.9, 2742.2
1338.6(1)	2032.9, 3095.3
1344.0(7)	1603.6
1421.3(1)	511, 709.3, 1139.2, 1610.5, 2032.9, 2742.2
1428.3(1)	1603.6, 2032.9
1514.3(1)	477.7, 1668.6, 1717.8, 2032.9
1554.9(7)	3479.6
1603.6(1)	511, 709.3, 1139.2, 1344.0, 1428.3, 2032.9, 2742.2
1610.5(2)	511, 709.3, 1421.3, 2032.9, 2742.2
1668.6(2)	477.7, 511, 1282.6, 1514.3, 2032.9, 2422.0
1716.7(5)	2032.9
1717.8(3)	477.7, 511, 1282.6, 1514.3, 2032.9
1898.3(5)	2032.9
1992.1(5)	2032.9
2032.9(1)	477.7, 511, 662.5, 709.3, 786.6, 788.9, 862.8, 961.9, 1104.2, 1114.5, 1268.4, 1338.6, 1421.3, 1514.3, 1603.6, 1610.5, 1716.0, 1898.3, 1992.1, 2130.5, 2231.3, 2362.0, 2728.3, 3031.9, 3290.9, 3378.6, 3456.5, 3479.6, 3515.4, 3533.0, 3656.1, 3660.3, 3711.0, 3741.5, 3944.2, 4224.9, 4588.0, 5227.5
2130.5(1)	2032.9
2231.3(8)	2032.9
2362.0(3)	2032.9
2422.0(1)	511, 1668.6, 1717.8
2573.9(3)	2032.9

Table 4.2: (cont'd)

E_γ (keV)	Coincident E_γ (keV)
2728.3(3)	2032.9
2742.2(1)	511, 662.5, 1282.6, 1421.3, 1428.3, 1603.6, 1610.5, 3031.9
2830.2(1)	1114.5, 2032.9
2989.9(4)	1338.6, 2032.9, 3371.8
3002.6(8)	662.5
3031.9(1)	511, 709.3, 1139.2, 2032.9, 2742.2
3054.9(5)	477.7
3092.8(5)	662.5
3095.3(12)	1338.6, 2032.9
3265.2(5)	477.7
3290.9(9)	2032.9
3358.2(6)	1114.5
3371.8(2)	2989.9, 3095.3
3378.6(4)	2032.9
3455.0(7)	2032.9
3479.6(1)	1554.9, 2032.9
3496.5(6)	2032.9
3508.8(6)	1114.5
3515.4(1)	2032.9
3533.0(2)	2032.9
3608.5(10)	2032.9
3656.1(3)	2032.9
3660.3(3)	2032.9
3711.0(3)	2032.9
3741.5(1)	2032.9
3872.3(3)	2032.9
3925.9(1)	511
3944.2(2)	2032.9
3962.6(1)	511
4224.9(3)	2032.9
4239.5(6)	511
4255.9(7)	2032.9
4328.5(2)	2032.9
4374.0(9)	2032.9
4424.9(3)	2032.9
4588.0(3)	2032.9
5227.6(7)	2032.9

the GeDSSD and PSPMT were described. These techniques provide a clean gate to isolate transitions in ^{68}Ni feeding the 0_2^+ state either directly or indirectly.

The γ rays coincident with the decay of the 0_2^+ state in ^{68}Ni are shown in Fig. 4.4. The spectrum shown in Fig. 4.4 is gated on the energy of the second pulse to remove contamination from other double-pulse events. These gates were from 400 to 2000 keV and 400 to 8000 ADC units for second pulse energy spectra shown in Figs. 3.18 and 3.33 recorded during e14039 and e14057, respectively.

Besides the strong 511-keV coincidence, predominately from the pair-production decay mode of the $E0$ transition, the two strongest coincidences are with the 1139.2- and 2422.0-keV γ rays. These two transitions are known to feed the 1603.3-keV 0_2^+ state directly [18,19,21]. The ratio of counts observed in coincidence with the $0_2^+ \rightarrow 0_1^+$ $E0$ transition to counts observed in β -gated γ -ray singles for those two transitions was used to determine the double-pulse-detection efficiency. Several additional transitions, many of which are too weak to be seen in β -gated γ -ray singles, are observed in coincidence with the $0_2^+ \rightarrow 0_1^+$ $E0$ transition.

A list of the transitions observed coincident with the $0_2^+ \rightarrow 0_1^+$ $E0$ transition and placed in the ^{68}Ni level scheme is presented in Table 4.3. Also listed are their absolute intensities, and the initial and final states between which the transition occurs. The absolute intensities of γ rays coincident with the $0_2^+ \rightarrow 0_1^+$ $E0$ transition, listed in Table. 4.3, were obtained using the number of counts recorded in coincidence with the $0_2^+ \rightarrow 0_1^+$ $E0$ transition, the double pulse detection efficiency, the branching ratios for each state through the $0_2^+ \rightarrow 0_1^+$ $E0$ transition, and the number of ^{68}Co decays listed in Table 4.7 presented in Section 4.1.2.5.

Branching ratios must be taken into consideration for transitions that do not directly feed the 0_2^+ in order to reconcile the β -delayed singles and double-pulse-gated β -delayed γ -ray spectra. Each state above the 0_2^+ state can potentially decay via one or more additional γ -ray cascades. When multiple cascades exist, the β -delayed γ -ray singles spectrum will contain the counts from other cascades, while the double-pulse-gated β -delayed γ -ray spectrum will

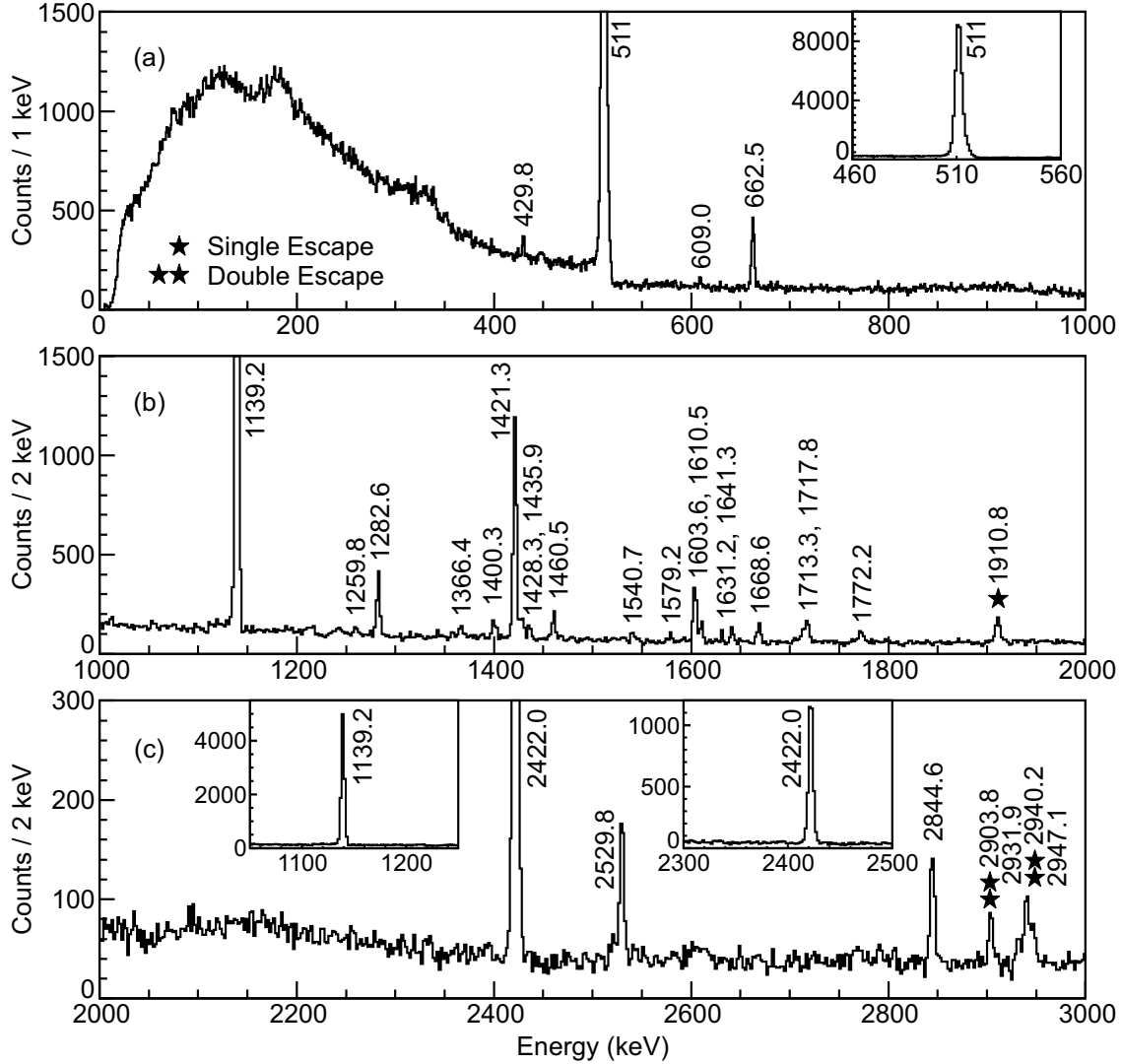
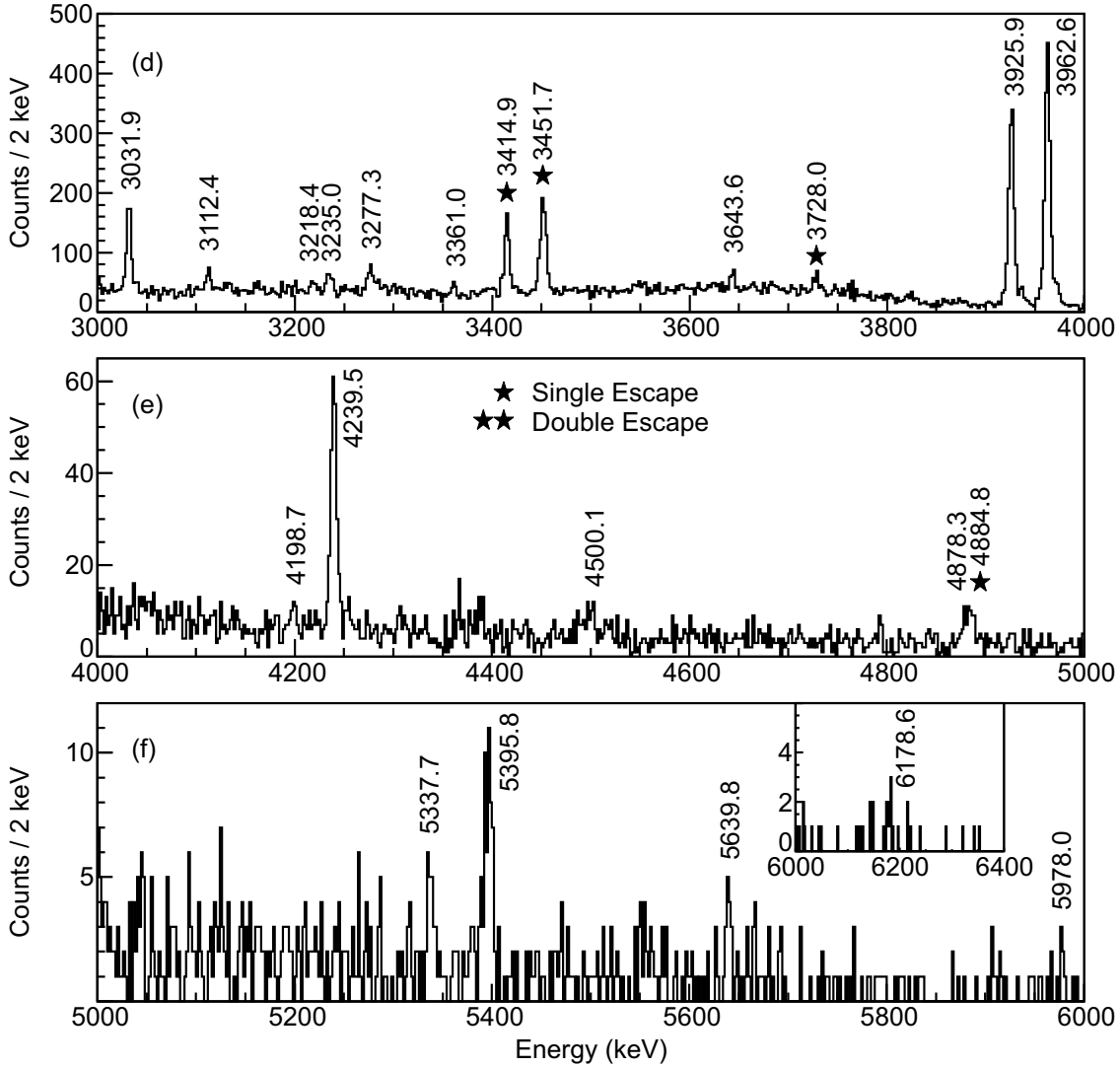


Figure 4.4: Spectrum of γ rays recorded in coincidence with the detection of the $0_2^+ \rightarrow 0_1^+$ $E0$ transition in ^{68}Ni . The inset in (a) shows the full height of the 511-keV peak truncated in (a). The left and right insets in (c) show the full heights of the 1139.2- and 2422.0-keV peaks truncated in panels (b) and (c), respectively. The inset in (f) shows the 6000- to 6400-keV region of the same spectrum presented in (a) through (f). In all cases transitions are labeled with their energies and, when applicable, single and double-escape peaks are denoted with one or two stars, respectively, in addition to the energy of the peak.

not and thus the extracted intensity in the latter would be systematically low. Branching ratios are determined from the ratio of the double-pulse efficiency corrected number of counts in the double-pulse-gated γ -ray spectra divided by the number of counts in β -gated γ -ray singles for transitions placed in the ^{68}Ni level scheme common to both spectra (denoted with

Figure 4.4: (cont'd)



a “C” in Table 4.3). A weighted average of these ratios was performed for each excited state to obtain the branching-ratio correction for transitions placed feeding that state.

Once corrected for the double-pulse-detection efficiency and the branching ratio, the number of counts for each transition was divided by the number of ^{68}Co decays obtained in Section 4.1.2.5 to give the absolute γ -ray intensities listed in Table 4.3.

Several transitions in Table 4.3, denoted with a “C”, were identified in β -delayed γ -ray singles and placed using $\beta\gamma\gamma$ coincidences. Any placement made on energy differences

between known levels (given the coincidence with the $0_2^+ \rightarrow 0_1^+$ $E0$ transition) is labeled with a “*b*”.

Transitions not conclusively placed in the ^{68}Ni level scheme can not be corrected for the branching ratios in the manner described above and instead only relative intensities can be displayed. A list of unplaced transitions coincident with the $0_2^+ \rightarrow 0_1^+$ $E0$ transition and their intensities relative to the 1139.2-keV transition is presented in Table 4.4.

Perhaps the most interesting of the transitions listed in Table 4.3 is the 429.8-keV $2_1^+ \rightarrow 0_2^+$ transition, observed here for the first time. Based on the absolute intensities of the 429.8-keV and 2032.9-keV transitions, a branch of 0.12(3) % was obtained for the 429.8-keV $2_1^+ \rightarrow 0_2^+$ transition.

The double-pulse-gated γ -ray spectrum in Fig. 4.4 can also be used to place limits on the $0_3^+ \rightarrow 0_2^+$ $E0$ transition branching ratio. Given the short half-life of 0.57(5) ns for the 2511-keV 0_3^+ state, obtained in Section 4.1.2.7, the $0_3^+ \rightarrow 0_2^+$ $E0$ transition would essentially be prompt, with the β decay in the double-pulse analysis and appear as one first rise in double-pulse events. The same spectrum presented in Fig. 4.4 focused on the 1514.3-keV region is shown in Fig. 4.5.

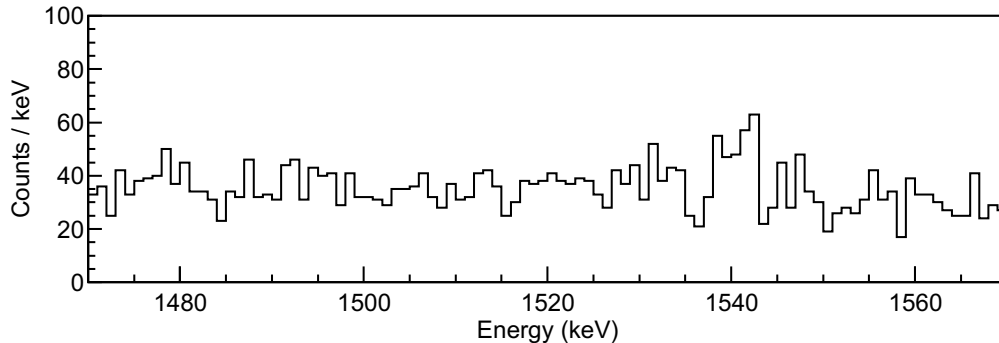


Figure 4.5: Spectrum of γ rays recorded in coincidence with the detection of the $0_2^+ \rightarrow 0_1^+$ $E0$ transition in ^{68}Ni focused in on the 1514.3-keV region.

The lack of the 1514.3-keV transition, which feeds the 2511-keV state, in coincidence with the $0_2^+ \rightarrow 0_1^+$ $E0$ transition means that only limits can be placed on the $0_3^+ \rightarrow 0_2^+$ $E0$ transition branch. Based on the counts in the 1514.3-keV region of Fig. 4.5, a limit of <0.18 % was deduced for the $0_3^+ \rightarrow 0_2^+$ $E0$ transition branch.

The level of statistics present in this work allows examination of $\beta\gamma\gamma$ -double-pulse coincidences for several of the transitions observed in Fig. 4.4. These coincidence spectra are presented in Appendix B. A summary of all $\beta\gamma\gamma$ -double-pulse coincidences is presented in Table 4.5.

Using the absolute γ -ray intensities from Tables 4.1 and 4.3 and the coincidence relationships described above, summarized in Tables 4.2 and 4.5, the decay scheme for the long-lived, low-spin, ^{68}Co isomer was constructed and is presented in Fig. 4.6. The β -decay Q-value used for this analysis is 11.54(15) MeV and was taken from Ref. [56]. The Fermi integral was calculated using Eq. (2.12) and the partial half-life for β decay to each state was calculated using Eq. (2.10). It is currently unknown which ^{68}Co isomer is the ground state and the energy difference between the two isomers is also unknown. As such, there is some additional uncertainty on the Q-value and thus the $\log ft$ values. The decay scheme for the long-lived, low-spin, ^{68}Co isomer is presented in Fig. 4.6.

Some of the transitions identified in Fig.4.2 were unable to be conclusively placed in the ^{68}Ni level scheme, and are presented in Table 4.6 along with their absolute intensities.

Table 4.3: Energies and absolute intensities of γ -ray transitions placed ^{68}Ni , detected in coincidence with the $0_2^+ \rightarrow 0_1^+$ $E0$ transition, following the β decay of the long-lived, low-spin, ^{68}Co isomer. The energies of the initial and final states between which each transition occurs are also listed.

E_γ (keV)	$I_\gamma^{absolute}$ (%)	Initial State (keV)	Final State (keV)
429.8(2) ^b	0.060(15)	2033	1603
662.5(1) ^c	1.34(11)	3405	2742
1139.2(1) ^c	3.34(25)	2742	1603
1282.6(1) ^c	1.05(10)	4025	2742
1366.4(4) ^b	0.40(17)	5530	4164
1400.3(3) ^b	0.70(22)	5565	4164
1421.3(0) ^c	4.43(33)	4164	2742
1428.3(2) ^c	0.44(10)	5774	4346
1540.7(4)	0.176(49)	4283	2742
1579.2(3)	0.24(11)	5743	4164
1603.6(1) ^c	1.29(11)	4346	2742
1610.5(2) ^c	0.73(13)	5774	4164
1631.2(2)	0.168(46)	4373	2742
1641.3(3)	0.041(11)	5774	4133
1668.6(2) ^c	0.243(97)	5694	4025
1705.3(6) ^b	0.096(41)	4448	2742
1713.3(5)	0.294(84)	4456	2742
1717.8(3) ^c	0.27(12)	5743	4025
2422.0(1) ^c	1.90(15)	4025	1603
2529.8(2)	0.228(37)	4133	1603
2844.6(2) ^b	0.205(33)	4448	1603
2947.1(6) ^b	0.36(11)	5689	2742
3031.9(2) ^c	1.34(12)	5775	2742
3218.4(10)	0.089(56)	7242	4025
3235.0(6) ^b	0.38(11)	5977	2742
3277.3(10) ^c	0.12(4)	4880	1603
3925.9(1) ^c	1.05(14)	5529	1603
3962.6(1) ^c	1.37(18)	5566	1603
4198.7(13) ^b	0.103(62)	6941	2742
4239.5(3) ^c	0.208(36)	5843	1603
4500.1(3) ^b	0.110(42)	7242	2742
5337.7(10) ^b	0.022(11)	6941	1603
5395.8(8)	0.060(18)	6999	1603
5639.8(8) ^b	0.016(8)	7242	1603
5978.0(6)	0.008(4)	7581	1603
6178.6(14)	0.016(8)	7782	1603

^b Transition placed in ^{68}Ni without additional coincidences using only energy differences

^c Transition also observed in β -gated γ -ray singles

Table 4.4: Energies and relative intensities ($I_\gamma^{1139.2} = 100\%$) of unplaced γ -ray transitions coincident with the $0_2^+ \rightarrow 0_1^+$ $E0$ transition, following the β decay of the long-lived, low-spin, ^{68}Co isomer.

E_γ (keV)	$I_\gamma^{1139.2=100\%}$ (%)
609.0(2)	0.93(32)
1259.8(6)	1.10(49)
1435.9(3)	1.25(42)
1460.5(2)	3.27(69)
1772.2(4)	2.53(74)
2931.9(6)	1.54(49)
3112.4(5)	2.37(78)
3361.0(6)	1.27(53)
3643.6(6)	1.83(65)
4878.3(17)	0.55(28)
5001.2(10)	0.36(26)

Table 4.5: Summary of $\beta\gamma\gamma$ -double-pulse coincidences in ^{68}Ni following the decay of the long-lived, low-spin, ^{68}Co isomer.

E_γ (keV)	Coincident E_γ (keV)
662.5	511, 1139.2, 845.4, 969.6, 1259.1, 1392.9
1139.2	511, 662.5, 1282.6, 1421.3, 1428.3, 1603.6, 1610.5, 3031.9
1282.6	511, 1139.2
1421.3	511, 1139.2
1428.3	511, 1139.2, 1603.6
1540.7	511, 1139.2
1579.2	511, 1139.2, 1421.3
1603.6	511, 1139.2, 1428.3
1610.5	511, 1139.2, 1421.3
1631.2	511, 1139.2
1641.6	2529.8
1668.6	511, 2422.0
1713.3	511, 1139.2
1717.8	511, 2422.0
2422.0	511, 1668.6, 1717.8
2529.8	511, 1641.3
3031.9	511, 1139.2

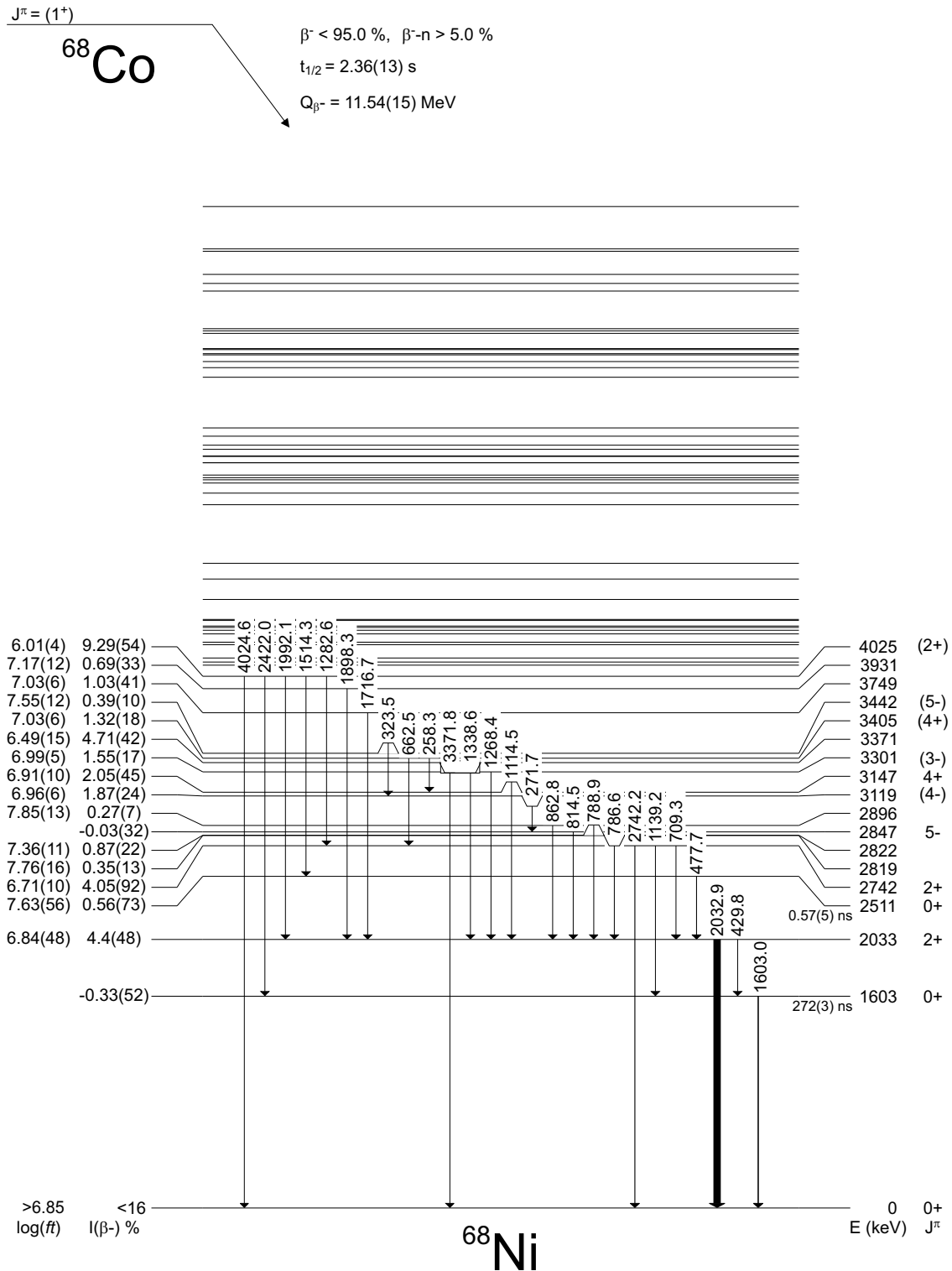


Figure 4.6: Decay scheme for the long-lived, low-spin, ^{68}Co isomer populated through the β decay of ^{68}Fe . States in ^{68}Ni are labeled with an energy in keV and the spin in parity (if known) on the right. On the left, β -decay branching ratios and $\log_{10} ft$ values are shown. β -decay Q-value taken from Ref. [56]. The 0.31(5) ps half-life of the 2033-keV 2_1^+ state is taken from the evaluation in Ref. [22].

Figure 4.6: (cont'd)

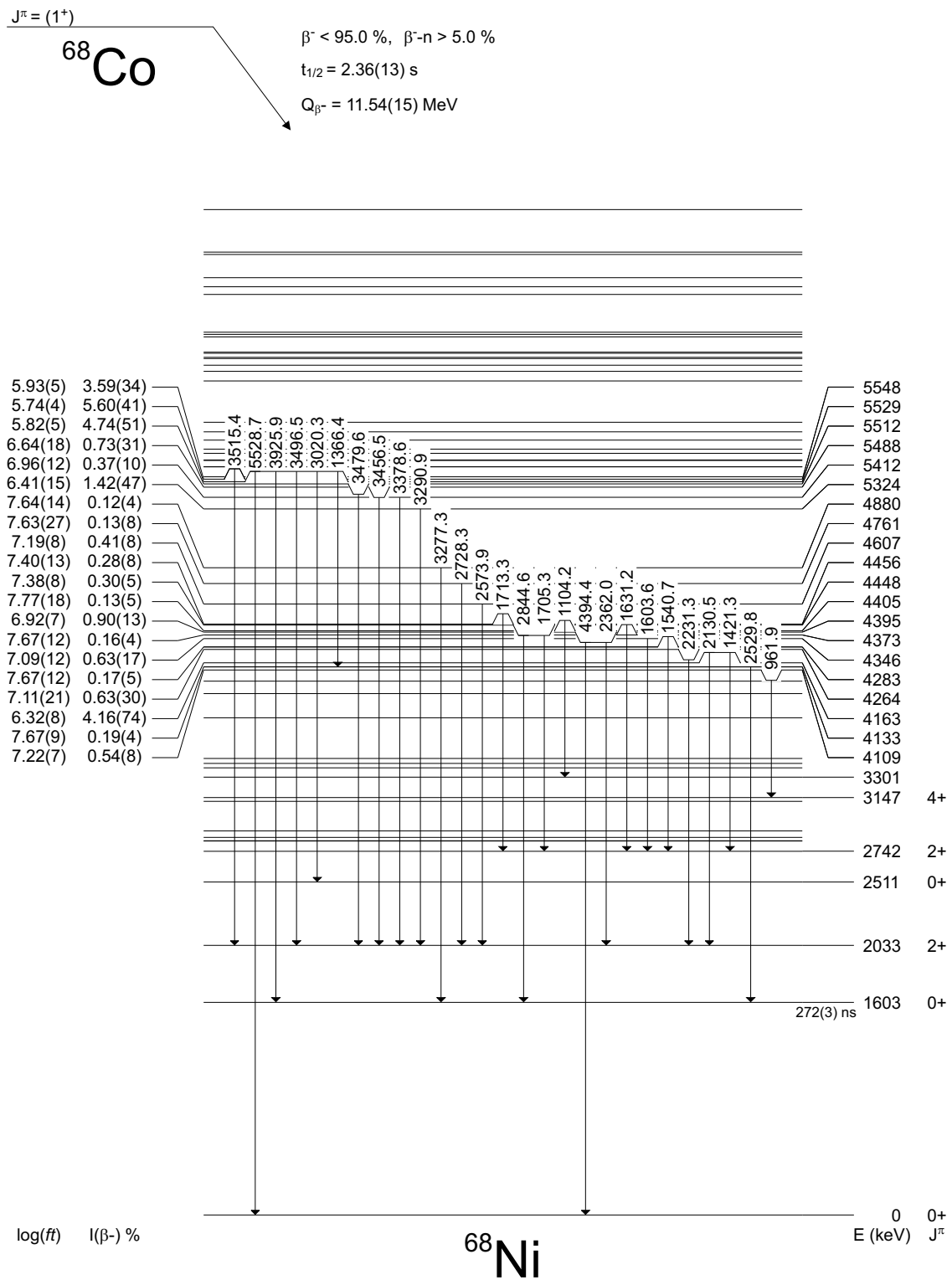


Figure 4.6: (cont'd)

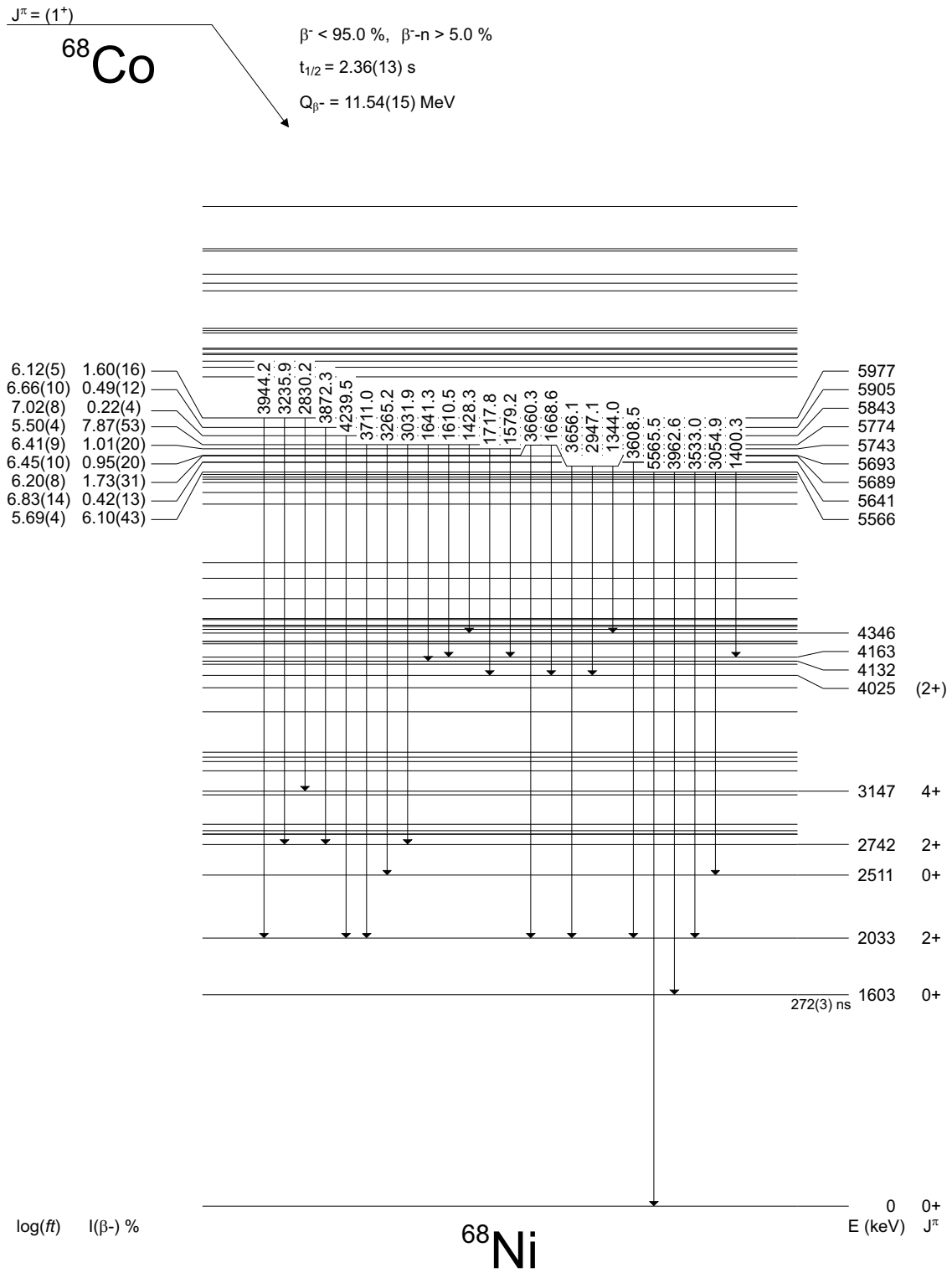


Figure 4.6: (cont'd)

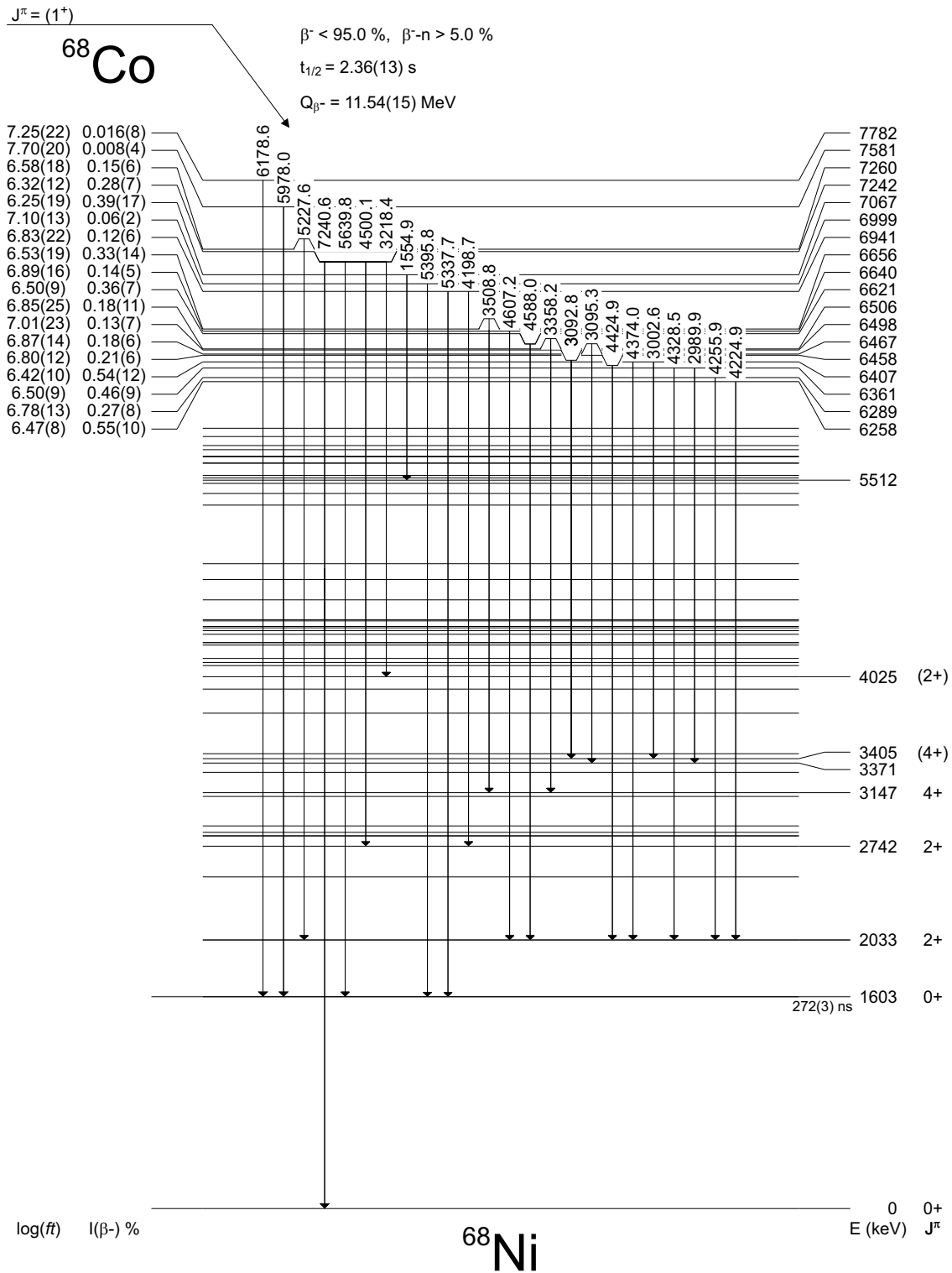


Table 4.6: Summary of unplaced γ rays potentially affiliated with the decay of the long-lived, low-spin, ^{68}Co isomer.

E_γ (keV)	$I_\gamma^{absolute}$ (%)
1367.6(2)	0.57(9)
1377.7(2)	0.25(7)
2877.2(2)	0.56(8)
3153.8(11)	0.16(6)
3287.0(3)	0.84(12)
3667.3(5)	0.17(6)
3725.1(6)	0.16(7)
3798.5(3)	0.76(10)
3991.3(2)	0.62(9)
4622.0(6)	0.21(7)
4650.6(4)	0.31(6)
5232.4(5)	0.29(8)
5297.4(9)	0.11(5)
5414.8(11)	0.11(7)
5421.9(3)	0.11(7)
5543.8(3)	0.26(5)
6487.8(9)	0.09(4)
6612.7(9)	0.10(3)
6771.8(13)	0.10(3)
6870.3(9)	0.17(5)

4.1.2 Half-Life Measurements

In addition to adding several new transitions and levels to the ^{68}Ni level scheme, half-life measurements of β -decaying states in ^{68}Fe and ^{68}Co as well as excited 0^+ states in ^{68}Ni were performed. The remainder of this section presents the half-life measurements carried out in the present work and the techniques required to perform them.

4.1.2.1 Assessing Spurious Correlations

The correlation algorithms described in Sections 3.5.2 and 3.6.2 attempt to associate β -decay electrons, as well as coincident γ rays, with their respective implanted ions. This was done by searching for the most recent ion implantation in the same spatial region of the detector as the detected β -decay electron. However, these methods are not perfect and two common failure modes exist.

In the first failure mode, a second ion implants into the same spatial region as the first before the decay of the first ion. The decay is incorrectly attributed to the second ion and the time difference between the β decay and second implanted ion, referred to as the decay time, is not representative of the decay of the second implanted ion. The second failure mode occurs when the β -decay electron traverses pixel boundaries. If the majority of the β -decay electron energy is deposited in an adjacent pixel, the β -decay electron may be associated with an incorrect ion in that adjacent pixel. The extracted decay time is again random. Correlations due to these failure modes are referred to as spurious correlations. The quantity and decay-time distribution of spurious decays depends on the ion implantation rate per pixel, the size of the correlation field, and the β -decay half-lives.

In e14039 the average implant rate for all ions was 40 Hz giving an average time between implants of ≈ 2 s in the illuminated pixels. In e14057 the average implant rate was 30

Hz giving an average time between implants of ≈ 3 s in each illuminated pixel. Half-lives of the nuclei of interest are several hundred ms to several seconds. As a result spurious correlations were significant in both experiments. The nine pixel correlation field used in e14057 to compensate for the poor position resolution effectively reduces the time between implants to ≈ 300 ms and significantly increases spurious correlations.

The distribution of decay times for a given isotope is called a decay curve. Decay curves are often fit with the Bateman equations, described in Section 2.1, to deduce half-lives and the number of decays recorded from a particular isotope. However, decay curves may contain contributions from spurious correlations that must be included in the fit. Therefore, to accurately perform the fit, assessment of the spurious-correlation component is crucial.

A technique to determine the time structure and quantity of spurious correlations was developed in Ref. [57]. The method involves running the full analysis backwards through time, which isolates the spurious correlations. Decay curves generated for each isotope in the backwards-time analysis are then used as spurious-correlation component in the decay curve for each respective isotope in the forwards-time analysis. Application of this technique removes the would-be free parameters due to spurious correlations from the decay curve, leaving the number of decaying nuclei and their half-lives as free parameters in the fit.

4.1.2.2 “Exclusion Technique” for Correlations

This section describes a new correlation technique referred to as the “exclusion technique”. This technique was developed to combat the effects of the relatively high implantation rate (average ~ 2 implants per pixel per second) and long daughter and granddaughter half-lives (~ 1 ’s to 10 ’s of seconds) of the decaying nuclei. Standard correlation techniques described in Sections 3.5.2 and 3.6.2 result in a systematic skewing of half-lives to shorter values. Figure

4.7 illustrates this effect for the decay of ^{68}Fe .

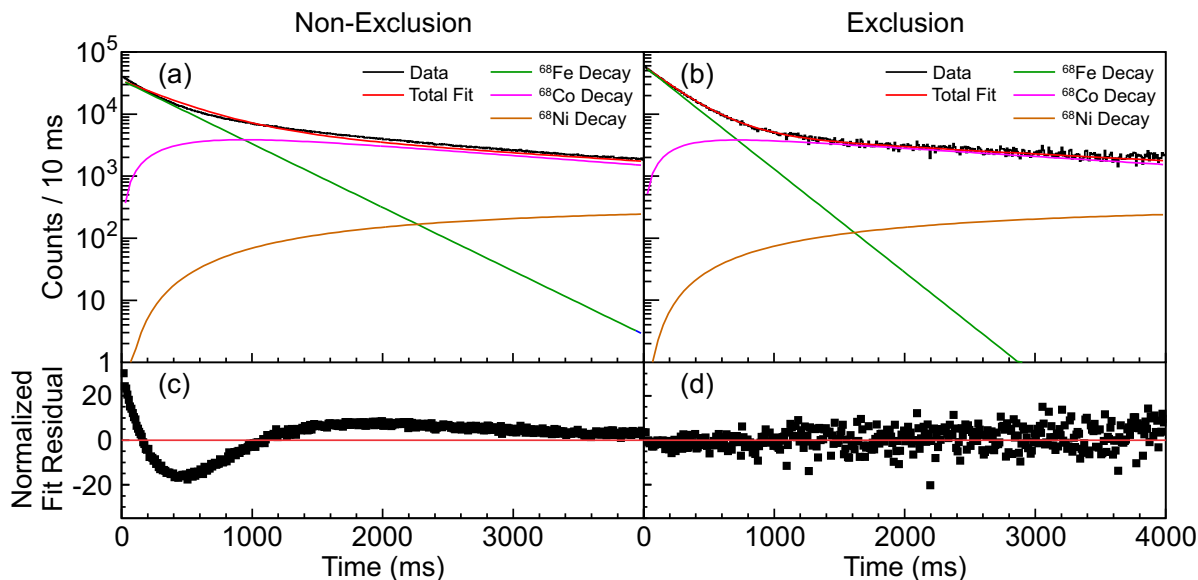


Figure 4.7: Motivation for the development of the exclusion technique. Two decay curves for ^{68}Fe are shown in black in (a) and (b) obtained from the analysis using the non-exclusion and exclusion correlation techniques, respectively. The decay curves have had their spurious-correlation component, determined using the techniques in Section 4.1.2.1, subtracted out and were normalized to have equivalent integral numbers of counts. For each decay curve a total fit (red) was performed comprised of ^{68}Fe parent (green), ^{68}Co daughter (magenta), and ^{68}Ni granddaughter (orange) decays. The half-life of ^{68}Ni was fixed to the literature value of 29 s [22]. Fit residuals, normalized to the bin error, are shown in (c) and (d) for the total fit compared to the data in (a) and (b), for the non-exclusion and exclusion decay curve fits, respectively.

Two decay curves for ^{68}Fe obtained from the non-exclusion and exclusion correlation techniques are shown in black in Figs. 4.7a and 4.7b, respectively. The spurious-correlation component, determined using the methods presented in Section 4.1.2.1, was subtracted from each and the resulting decay curves were normalized to have equivalent numbers of counts. Each decay curve was fit with the Bateman equations comprised of ^{68}Fe parent (green), ^{68}Co daughter (magenta), and ^{68}Ni granddaughter (orange) components. The half-life of ^{68}Ni was fixed to the literature value of 29 s [22]. Fit residuals, normalized to the bin error, are shown in (c) and (d) for the non-exclusion and exclusion decay curve fits, respectively.

The decay curve in Fig. 4.7a, generated from the non-exclusion technique, was not able

to be fit by the Bateman equations using the fixed 29 s half-life of ^{68}Ni [22]. Only when the ^{68}Ni half-life was reduced by an order of magnitude did the fit become reasonable. If all parameters are left free the non-exclusion technique yields values of 180(5), 800(30), and 2100(200) ms for the half-lives of ^{68}Fe , ^{68}Co , and ^{68}Ni respectively. While the ^{68}Fe half-life does agree with the evaluated value of 188(4) ms [22], the ^{68}Co half-life is discrepant with the 1600(300) ms from Ref. [12].

The decay curve in Fig. 4.7b was fit well using the Bateman equations and the fixed 29 s half-life of ^{68}Ni [22]. Values of 180(4) and 2300(110) ms are obtained for the half-lives of ^{68}Fe and ^{68}Co , respectively. The ^{68}Fe half-life remains unchanged, but the ^{68}Co half-life is significantly larger. Though also discrepant with Ref. [12] this result agrees well the half-life obtained in Sec. 4.1.2.4. The exclusion technique is shown schematically in Fig. 4.8a.

In Fig. 4.8 the time structure of implantations (black vertical lines), parent decays (red vertical lines), and daughter decay (blue vertical lines) for two implanted ions is shown. Solid and dashed lines are used to distinguish events affiliated with each different ion. Horizontal brackets represent the correlations and time proceeds forward left to right. In Fig. 4.8a the exclusion window of time is a crosshatched rectangle above the correlations.

The techniques described in Sections 3.5.2 and 3.6.2 are shown schematically in Fig. 4.8b, where decays are correlated with the most recent ion within the correlation window out to a time difference less than or equal to the correlation window. The decay of the first implant is shown as a solid red vertical line while the time of arrival of the first ion is the black vertical line. This first decay would be correlated and have the same results using in either method.

A short time after the first decay a second ion implants in the same spatial location and is denoted with a dashed black vertical line in Fig. 4.8. In the non-exclusion technique, all subsequent decay events would correlate with this most recent implant. However, in the

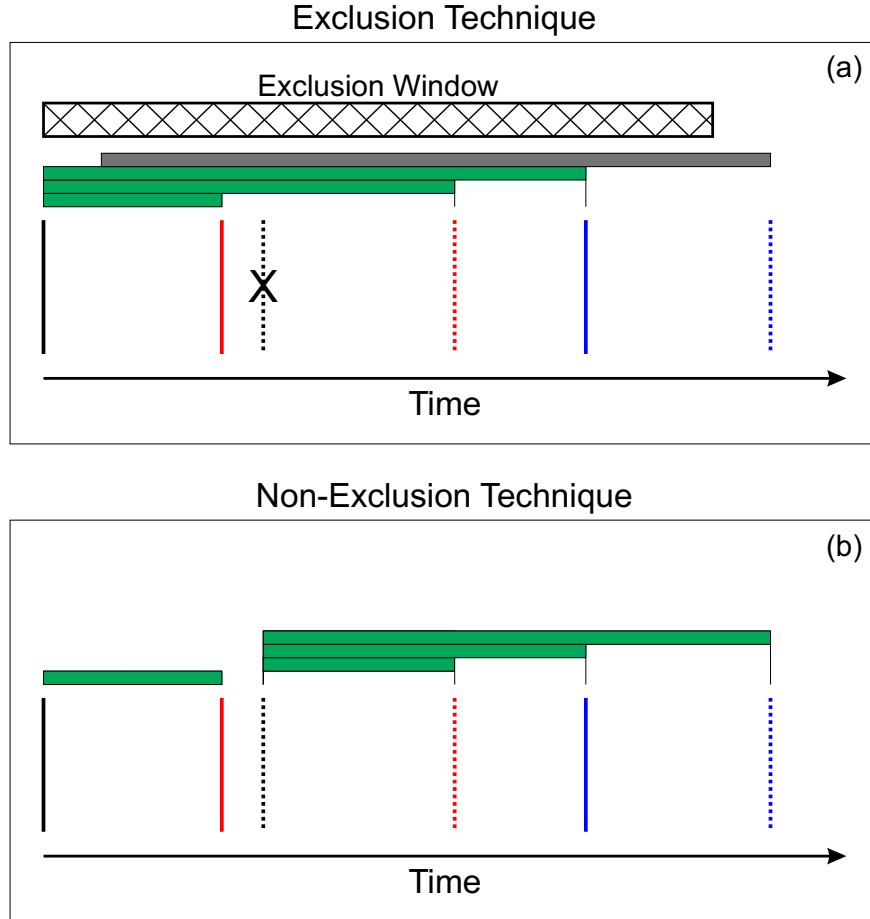


Figure 4.8: Schematic view of the exclusion technique highlighting the differences with the non-exclusion correlation techniques. The time structure of implantations (black vertical lines), parent decays (red vertical lines), and daughter decay (blue vertical lines) for two implanted ions is shown. Solid and dashed lines are used to distinguish events affiliated with each different ion. Horizontal green bars represent the correlations and a gray horizontal bar represents a decay event that is outside the correlation window. In (a) the exclusion window of time is a crosshatched rectangle above the correlations. Implants removed from the analysis by the exclusion technique are labeled with an “X”. Time proceeds forward left to right indicated by the black arrow at the bottom of each panel.

exclusion technique this second implantation falls within the exclusion window, which is the same length as the correlation window, and the implantation is ignored.

When the second implanted ion decays, denoted by the dashed red vertical line, the non-exclusion technique gets the correlation correct and records the correct time difference. The exclusion technique the decay contributes to the spurious-correlation component. Spurious

correlations are present in both techniques, but the exclusion technique increases their frequency. However, using the techniques in Section 4.1.2.1, their contribution in a decay-curve can be easily separated from the real correlations.

The purpose of the exclusion technique becomes apparent when examining the decay of the daughter of the first implanted ion shown as a solid blue vertical line. In the non-exclusion analysis the decay is correlated, incorrectly, to the second implanted ion. If the second implanted ion is the same isotope as the first, an incorrect, shorter, time difference is recorded thereby skewing extracted half-lives to smaller values. In the exclusion analysis the decay of the daughter of the first implanted ion is correctly correlated and no skewing of extracted half-lives occurs.

Finally in this example, the decay of the daughter of the second implanted ion, shown as a dashed blue vertical line, is correctly correlated in the non-exclusion analysis, but is outside the correlation window in the exclusion analysis. If it were in the correlation window for the exclusion analysis it would contribute to the spurious correlation component.

The impact of spurious correlations to the time-difference distributions depends on the overall implantation rate per pixel, the size of the correlation field, and the half-lives of the nuclei of interest. For e14039 and e14057 the exclusion technique is one possible approach needed to extract accurate values for the half-lives of the β -decaying nuclei.

4.1.2.3 Half-Life of ^{68}Fe

The half-life of ^{68}Fe was extracted by gating the decay curves on the 161.8-keV and 184.3-keV transitions from the decay of two excited states in the ^{68}Co daughter [22]. The exclusion technique for correlations, described in the previous section, was employed. The decay curve vs. coincident γ -ray energy for ^{68}Fe is shown in Fig. 4.9a. The projection onto the energy

axis is presented in Fig. 4.9b.

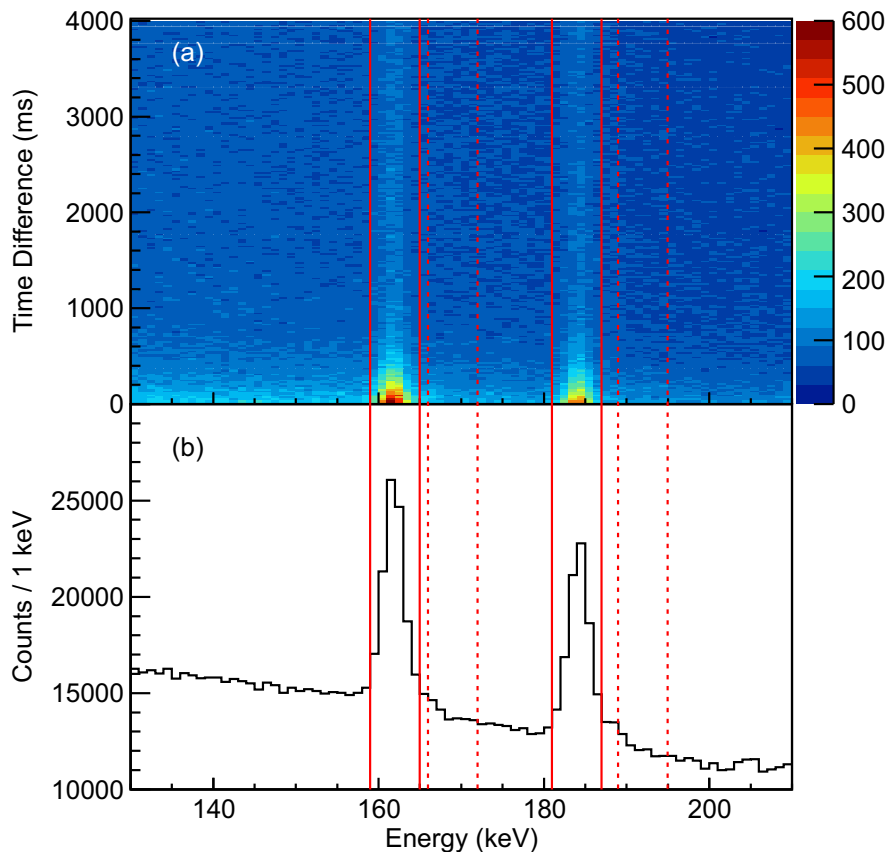


Figure 4.9: (a) Decay curve vs. coincident γ -ray energy, recorded in SeGA during e14039, for the region around the 161.8- and 184.3-keV peaks. (b) Projection of (a) onto the energy axis. Sets of solid red vertical lines and dashed vertical lines identify the peak and background regions, respectively, for each peak.

Decay curves for both the 161.8-keV and 184.3-keV peak regions (solid red lines) as well as the background regions (dashed red lines) were generated from the projection of Fig. 4.9 onto the time-difference axis. These decay curves are shown in Figures 4.10a and 4.10c for the peak regions and in Figs. 4.10b and 4.10d for the background regions. The background decay curves shown in Figs. 4.10b and 4.10d were scaled and subtracted from those in Figs. 4.10a and 4.10c, respectively. The two resulting background-subtracted time-distributions were summed together to create the decay curve shown in black in Fig. 4.11, used to extract the half-life of ^{68}Fe .

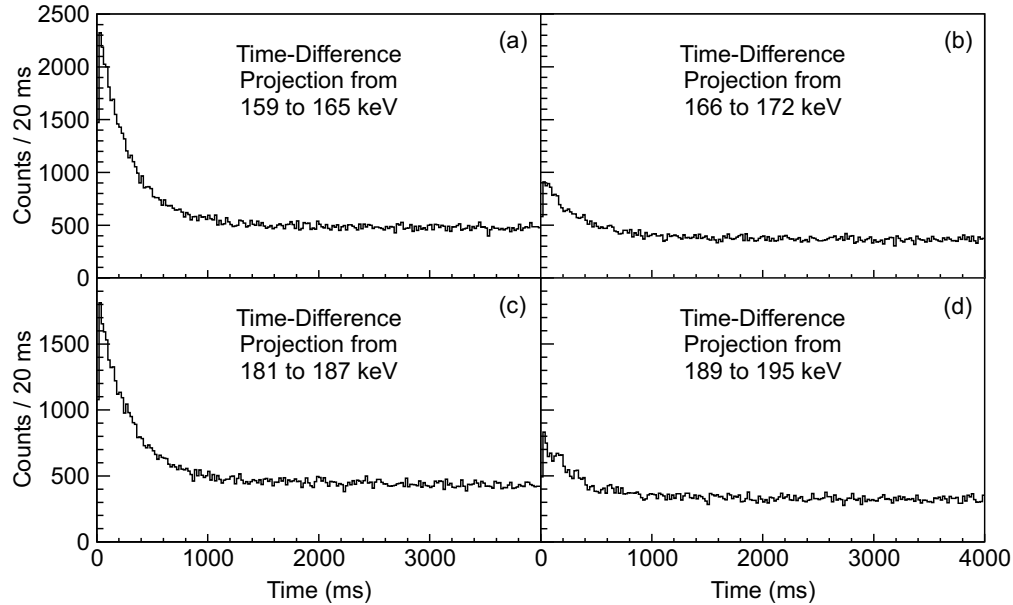


Figure 4.10: Decay curves obtained by projecting 4.27a onto the time-difference axis over the regions of (a) 159 to 165 keV, (b) 166 to 172 keV, (c) 181 to 187 keV, and (d) 185 to 195 keV. Regions shown in (a) and (c) represent the encompass the 161.8-keV and 184.3-keV peaks, respectively, while (b) and (d) are representative backgrounds to be scaled and subtracted for each respective peak.

The counts in the background-subtracted decay curve in Fig. 4.11 originate from two sources. Most are from real correlations between a ^{68}Fe implant and its subsequent β decay, and as expected, their corresponding decay curve exhibits an exponential decay with the half-life of ^{68}Fe . However, a portion of the total counts originate from spurious correlations and yield a roughly flat time-difference distribution.

The spurious-correlation component was determined using the techniques in Section 4.1.2.1. Figure 4.12a shows the two-dimensional time-difference vs. coincident γ -ray energy spectrum with the analysis run backwards in time. Figure 4.12b shows the projection of the two-dimensional spectrum shown in Fig. 4.12a onto the energy axis.

The ratio of the peak areas between Figs. 4.9b and 4.12b is the ratio of spurious correlations to total counts in the background-subtracted decay curve. The decay curve for spurious correlations was obtained by projecting the spectrum shown in Fig. 4.12a onto the

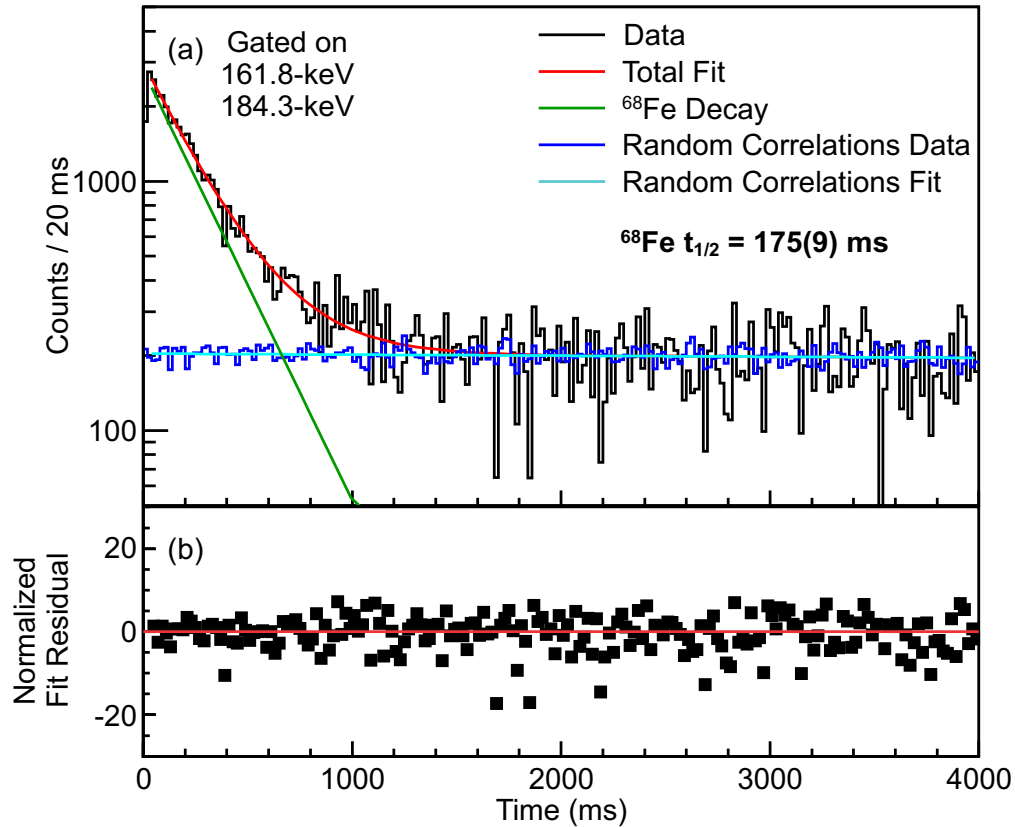


Figure 4.11: (a) Background-subtracted γ -gated decay curve for the decay of ^{68}Fe into ^{68}Co . Gates were placed on the 161.8-keV and 184.3-keV transitions in ^{68}Co and the background, scaled appropriately and subtracted, was sampled directly above each peak. The background-subtracted data are shown in black while the spurious correlation component, obtained using the techniques in Section 4.1.2.1, is shown in blue. In cyan, a fit to the spurious correlation component is shown, and was used to represent the spurious correlations in the total fit of the data shown in red. The contribution from the decay of ^{68}Fe is shown in green. The half-life of ^{68}Fe , extracted from the fit, is 175(9) ms. This compares to the evaluated value of 188(4) ms [22]. (b) Fit residuals for the total fit compared to the data in (a) normalized to the bin error in (a).

time-difference axis, and is shown in blue in Fig. 4.11. A fit to the spurious correlation data, shown in cyan in Fig. 4.11, was used in lieu of the data to provide a smoothly varying component for use in the total fit shown in red in Fig. 4.11. The total fit was a combination of the spurious correlation component and an exponential decay. The exponential decay component, from the real correlations between ^{68}Fe and its subsequent decay, extracted from the fit is shown in green. The results of the fit yield a half-life of 175(9) ms for ^{68}Fe . The

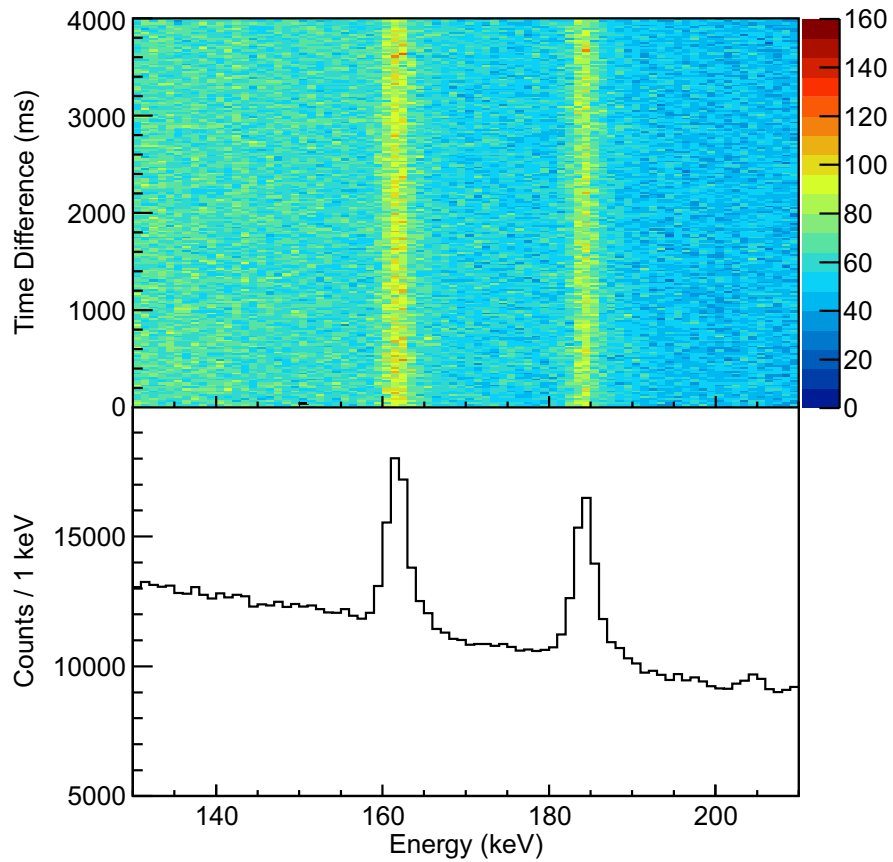


Figure 4.12: Results of the analysis run backwards in time through the data. (a) Decay curve vs. coincident γ -ray, recorded in SeGA during e14039, for the region around the 161.8- and 184.3-keV peaks. (b) Projection of (a) onto the energy axis.

evaluated value is $188(4)$ ms [22].

4.1.2.4 Half-Life of the Long-Lived ^{68}Co Isomer

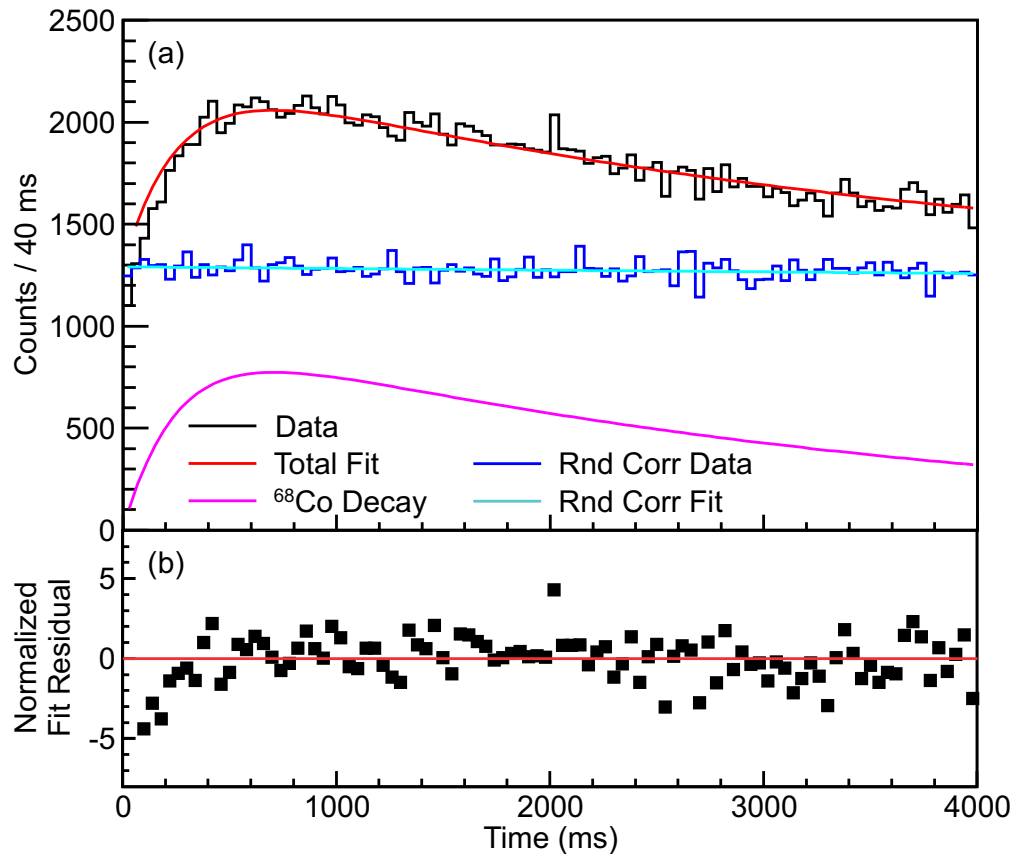


Figure 4.13: (a) Double-pulse-gated decay curve for the decay of ^{68}Co into ^{68}Ni . The data are shown in black while the spurious correlation component, obtained by running the analysis backwards in time and scaled by the fit, is shown in blue. In cyan, a fit to the spurious correlation component is shown, and was used to represent the spurious correlations in the best total fit of the data shown in red using the half-life of the minimum obtained from Fig. 4.14. The contribution from the decay of ^{68}Co is shown in magenta. (b) Fit residuals for the total fit compared to the data in (a) normalized to the bin error in (a).

The “double-pulse” analysis described above provides a clean experimental signature to gate the β -decay time spectrum permitting investigation of the half-life of the low-spin ^{68}Co β -decaying isomer. The only existing measurement of this half-life, performed in the work of Ref. [12], yielded a value of 1600(300) ms deduced from fitted β -delayed γ -ray gated decay curves.

Figure 4.13a shows the decay curve coincident with “double-pulse” events in both the

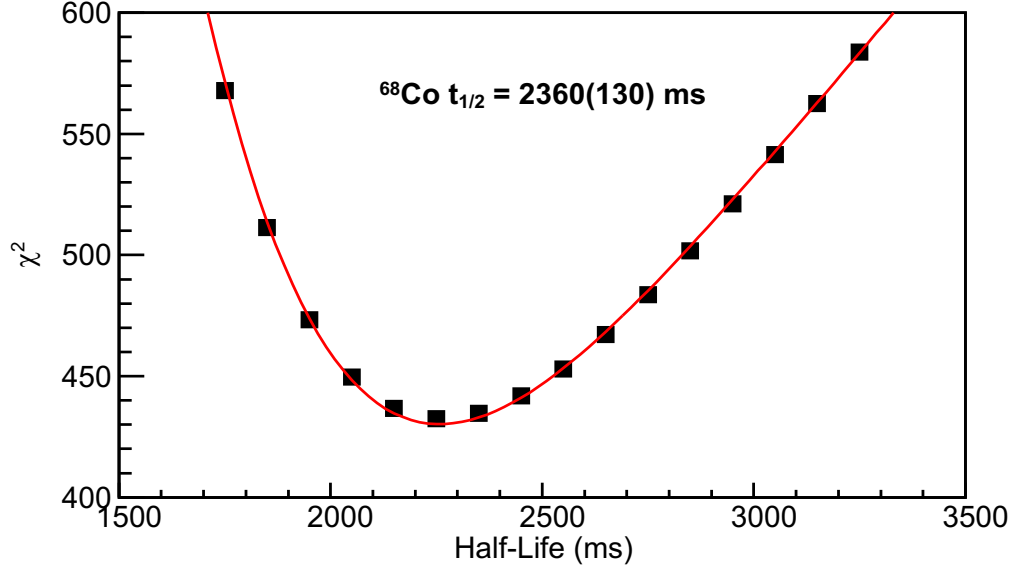


Figure 4.14: Distribution of χ^2 values as a function of ^{68}Co half-life obtained from fitting the data shown in black in Fig. 4.13 with a combination of spurious correlations and the ^{68}Co daughter grow-in, described by equation (2.21). The spurious-correlation component and half-life of ^{68}Fe were fixed leaving the ^{68}Co half-life as the only free parameter. The χ^2 distribution was fit with a fifth order polynomial, shown in red, for interpolation between points. A value of 2360(130) ms was extracted for the half-life of the ^{68}Co low-spin isomer.

GeDSSD and segmented plastic scintillator is shown in black. The spurious-correlation component, shown in blue in Fig. 4.13a, was obtained using the same backward time analysis techniques described above. A fit to the spurious correlation component used in the total fit is shown in cyan.

The total fit, shown in red in Fig. 4.13a, was comprised of two components. The first was the spurious correlation component, determined using the techniques in Section 4.1.2.1, and the second was a single growth and decay of the form of Eq. (2.21). The spurious-correlation component and half-life of ^{68}Fe were fixed leaving the ^{68}Co half-life as the only free parameter. Several fits were performed with the half-life of the long-lived low-spin ^{68}Co isomer varied in 100 ms increments. The distribution of reduced χ^2 values as a function of half-life is shown in Fig. 4.14.

A fifth-order polynomial, shown in red in Fig. 4.14, was used to fit the distribution,

shown as black squares in Fig. 4.14, and interpolate between points. The half-life is 2360 ms, obtained at the minimum of the red curve in Fig. 4.14. An initial uncertainty of ± 60 ms was obtained from the corresponding values either side of the minimum at 1 χ^2 unit up from the minimum [54]. An additional uncertainty of ± 110 ms was obtained from the change in extracted half-life when both the contribution of the spurious correlations and the half-life of ^{68}Fe were varied within their errors. The two errors were added in quadrature, and a final uncertainty of ± 130 ms was obtained.

The best fit result, corresponding to the minimum of the χ^2 distribution, is shown in magenta in Fig. 4.13a with the total best fit shown in red. Fit residuals, normalized to the error in each bin, are presented in Fig. 4.13b and remain roughly flat across most of range in time.

4.1.2.5 $A = 68$ Decay Curves

Using the newly-obtained half-lives for ^{68}Fe and ^{68}Co , the decay curves for all decay events correlated with ^{68}Fe implants were fitted for each experiment. The decay curves for the time distribution of recorded decay events following within 4000 ms of an implanted ^{68}Fe ion for e14039 and e14057 are shown in Figs. 4.15a and 4.16a, respectively. The exclusion technique, described in Section 4.1.2.2, was used in both analyses.

For the GeDSSD, the location of the ion and subsequent decay had to be in the same pixel. For the segmented plastic scintillator, the decay could be in the same pixel or any of the surrounding eight immediate neighbor pixels. The larger correlation field for the plastic scintillator was chosen due to the poor position resolution obtained from the segmented plastic scintillator and also led to a large increase in spurious correlations. In both cases a 4000 ms correlation window was chosen to provide a long time region to properly fit the

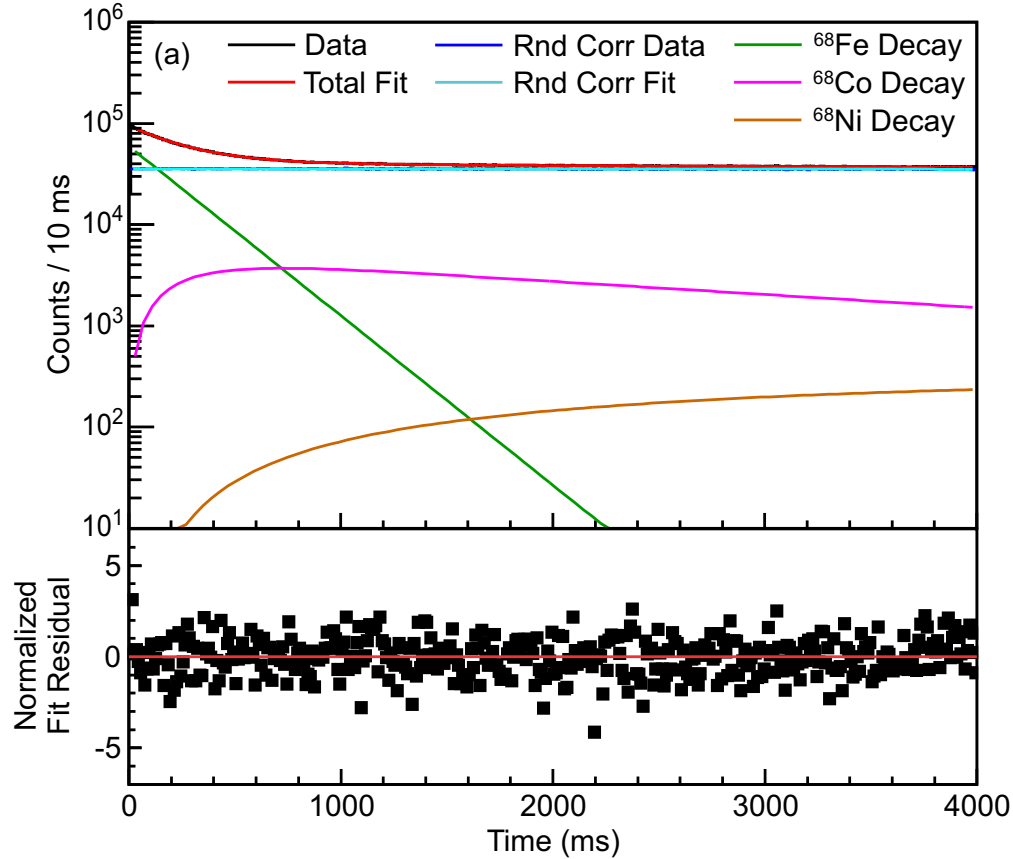


Figure 4.15: (a) Decay curve for the decay of ions of ^{68}Fe in e14039. The data are shown in black while the spurious correlation component, obtained by running the analysis backwards in time and scaled by the fit, is shown in blue. In cyan, a fit to the spurious correlation component is shown, and was used to represent the spurious correlations in the best total fit of the data shown in red using the half-life of the minimum obtained from Fig. 4.14. The contribution from the decay of ^{68}Fe , ^{68}Co , and ^{68}Ni is shown in green, magenta, and orange, respectively. The total fit is shown in red. (b) Fit residuals for the total fit compared to the data in (a) normalized to the bin error in (a).

background and to encompass nearly two half-lives of the the long-lived ^{68}Co isomer decays while not excessively removing implants in the exclusion window.

The decay curves in Figs. 4.15 and 4.16 were fitted using the Bateman equations consisting of the ^{68}Fe parent ($t_{1/2} = 175(9)$ ms) shown in green, ^{68}Co daughter ($t_{1/2} = 2330^{+790}_{-460}$ ms) shown in magenta, and the ^{68}Ni granddaughter ($t_{1/2} = 29(2)$ s [22]) shown in orange. The spurious-correlation component for each decay curve was determined using the techniques discussed in Section 4.1.2.1. In both Figs. 4.15 and 4.16 the spurious correlation

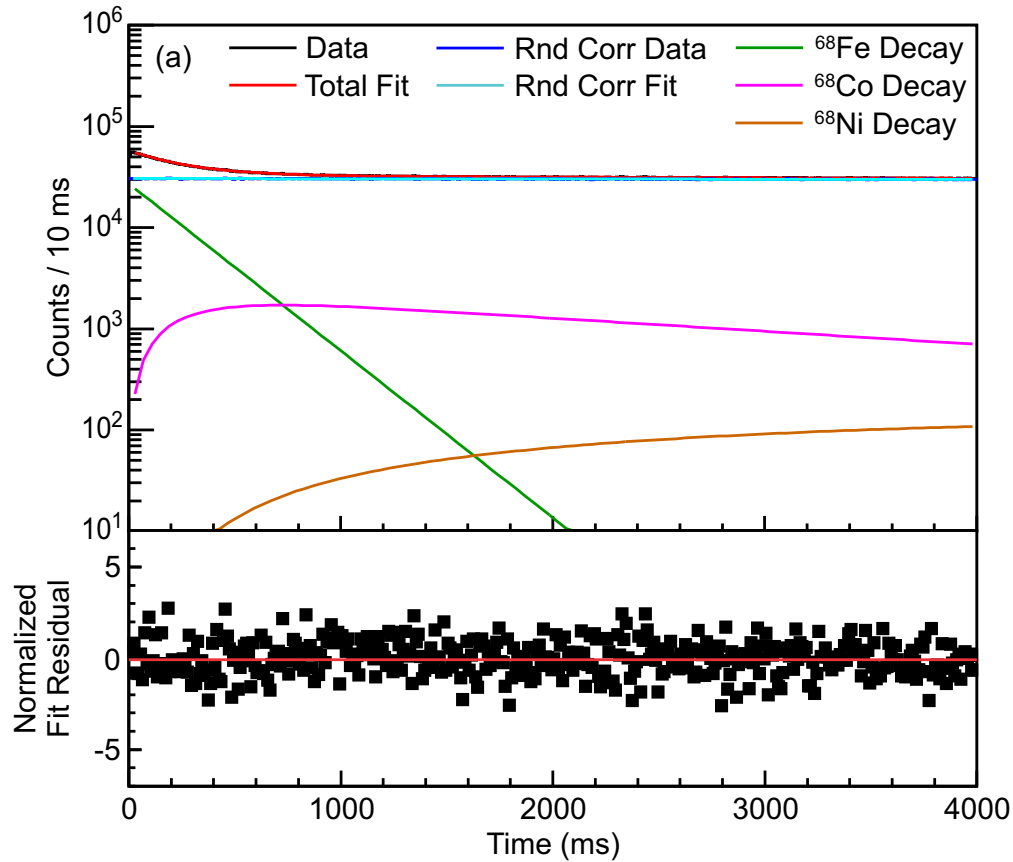


Figure 4.16: (a) Decay curve for the decay of ions of ^{68}Fe in e14057. The data are shown in black while the spurious correlation component, obtained by running the analysis backwards in time and scaled by the fit, is shown in blue. In cyan, a fit to the spurious correlation component is shown, and was used to represent the spurious correlations in the best total fit of the data shown in red using the half-life of the minimum obtained from Fig. 4.14. The contribution from the decay of ^{68}Fe , ^{68}Co , and ^{68}Ni is shown in green, magenta, and orange, respectively. The total fit is shown in red. (b) Fit residuals for the total fit compared to the data in (a) normalized to the bin error in (a).

component is shown in blue and the fit to the spurious correlation data is shown in cyan. The total fit is shown in red.

The number of correlated decays recorded for each β -decaying nucleus was obtained by integrating the Bateman equations and is required to obtain the absolute γ -ray efficiencies presented in Tables 4.1 and 4.3. However, this number must be first corrected for spurious correlations and differences between the exclusion and non-exclusion correlation techniques to be comparable with the correlated β -delayed γ -ray statistics from the non-exclusion analysis.

The number of decays extracted from the decay-curve fit is exclusively the contribution from real correlations. However, in the correlated β -delayed γ -ray spectra, shown earlier in this chapter, each peak, associated with a given isotope, has counts from both real and spurious correlations. The contribution from spurious correlations was determined by comparing peak areas of four transitions in ^{68}Ni (477.7, 709.3, 2032.9, and 2742.3 keV) in the correlated β -delayed γ -ray spectra between the forwards and backwards exclusion analyses. Peak areas in the forward time analysis are the sum of both spurious and real correlation. However, in the backwards time analysis, peak areas are exclusively the contribution of spurious correlations. The ratio of peak areas (backward/forward) represents the ratio of spurious correlations to the total. Therefore, the inverse of one minus this ratio is the spurious correlation correction.

In addition to increasing the fraction of spurious correlations, the exclusion technique, in this application, also reduces the overall quantity of correlations. The effect was quantified by comparing correlated β -delayed γ -ray spectra between the exclusion and non-exclusion techniques in the forward-time analysis. The peak areas for the same four γ -rays used above were determined using both techniques. The ratio of peak areas (non-exclusion/exclusion) is the exclusion technique correction.

The integrated number of counts for ^{68}Ni from the Bateman equations are presented in Table 4.7 along with the corrections for spurious correlations and the exclusion technique for both experiments.

Using the numbers from Table 4.7, the total number of correlated ^{68}Co decays was determined to be $9.71(37)\times 10^6$. This number was used to obtain the absolute γ -ray efficiencies and subsequently the β -decay feedings to various states in ^{68}Ni . The large differences in

Table 4.7: Decay curve integration results and correction factors for ^{68}Ni in each experiment. The “corrected” number of decays is obtained by multiplying the integrated number of counts by the spurious correlation and exclusion technique correlation factors. The corrected number of decays is then directly comparable to the non-exclusion analysis β -delayed γ -ray statistics.

	e14039	e14057
Integrated Number of ^{68}Co decays	$1.04(5)\times 10^6$	$0.48(2)\times 10^6$
Spurious Correlation Correction	2.95(4)	5.35(7)
Exclusion Technique Correction	1.24(1)	2.31(2)
Corrected Number of ^{68}Co decays	$3.79(20)\times 10^6$	$5.92(31)\times 10^6$

spurious correlation and exclusion technique correction values between the two experiments is due to the larger correlation field used for the plastic scintillator in e14057.

4.1.2.6 Half-Life of the 0_2^+ state in ^{68}Ni

The half-life of the 0_2^+ state in ^{68}Ni had been measured three times prior to the present work, and values of 270(5) ns [44], 268(12) ns [18], and 235(23) ns [21] were obtained. The present work employs the same techniques used in Ref. [18], where the half-life of the 0_2^+ state in ^{68}Ni was extracted by examining the histogram of time differences between the first and second pulses in the “double-pulse” analysis.

Based on the level scheme from this work and all prior investigations, no states with significant lifetimes are known to feed the 0_2^+ state following β decay. Therefore, on the ns time scale, the β decay of ^{68}Co , which is the first pulse observed in the recorded double-pulse signals, can be considered the time at which the 0_2^+ state is populated. The second pulse of the double-pulse signals is the decay of the 0_2^+ state. The time difference between the two pulses can be fitted as a first-order decay to extract the half-life of the 0_2^+ state.

The time-difference distributions, shown in Figs. 4.17a and 4.17b, were obtained by histogramming the time difference between the two constituent pulses of all double-pulse

signals recorded in e14057 and e14039, respectively. The same gates used in the previous sections were applied to the energy of the second pulse for time-difference spectra to remove contamination from lower energy double-pulse events discussed in Sections 3.5.5 and 3.6.3. For e14039, the gate was from 400 to 2000 keV; while in e14057, this gate was between 400 and 8000 ADC units.

In the spectrum displayed in Fig. 4.17a, the time-difference distribution covers a relatively short time-difference range due to the available length of trace before the inclusion of an external time-reference signal. The external time reference was not used in the present analysis, but restricts the range of time differences obtained from the double-pulse analysis. At short time difference, several features are present due to the detector ringing exceeding the dynamic double-pulse-detection threshold, discussed in Section 3.6.1. A single exponential decay fit over the time-difference range of 200 to 700 ns yields a half-life of 279(6) ns.

The time-difference spectrum in Fig. 4.17b spans a larger dynamic range. The effect of the finite trace window coupled with an amplitude-dependent time walk associated with the leading-edge triggering algorithm can be seen at large-time difference. The relatively slow rise time of the GeDSSD did not permit positive identification of double pulse signals with time difference less than ~ 200 ns. An exponential decay fit of the histogram in Fig. 4.17b over the same 200 to 700 ns range yielded a half-life of 271(10), and when the range was extended out to 2000 ns, the extracted half-life became 270(5) ns.

A weighted average of the results from the present two experiments gave a value of 274(4) ns for the half-life of the 0_2^+ state in ^{68}Ni . This value is in excellent agreement with the previously measured values of 270(5) ns [44] and 268(12) ns [18], but is discrepant with the value of 235(23) ns obtained in Ref. [21]. A weighted average of the present work with the values of Refs. [44] and [18] gives a value of 272(3) ns for the half-life of the 0_2^+ state in ^{68}Ni ,

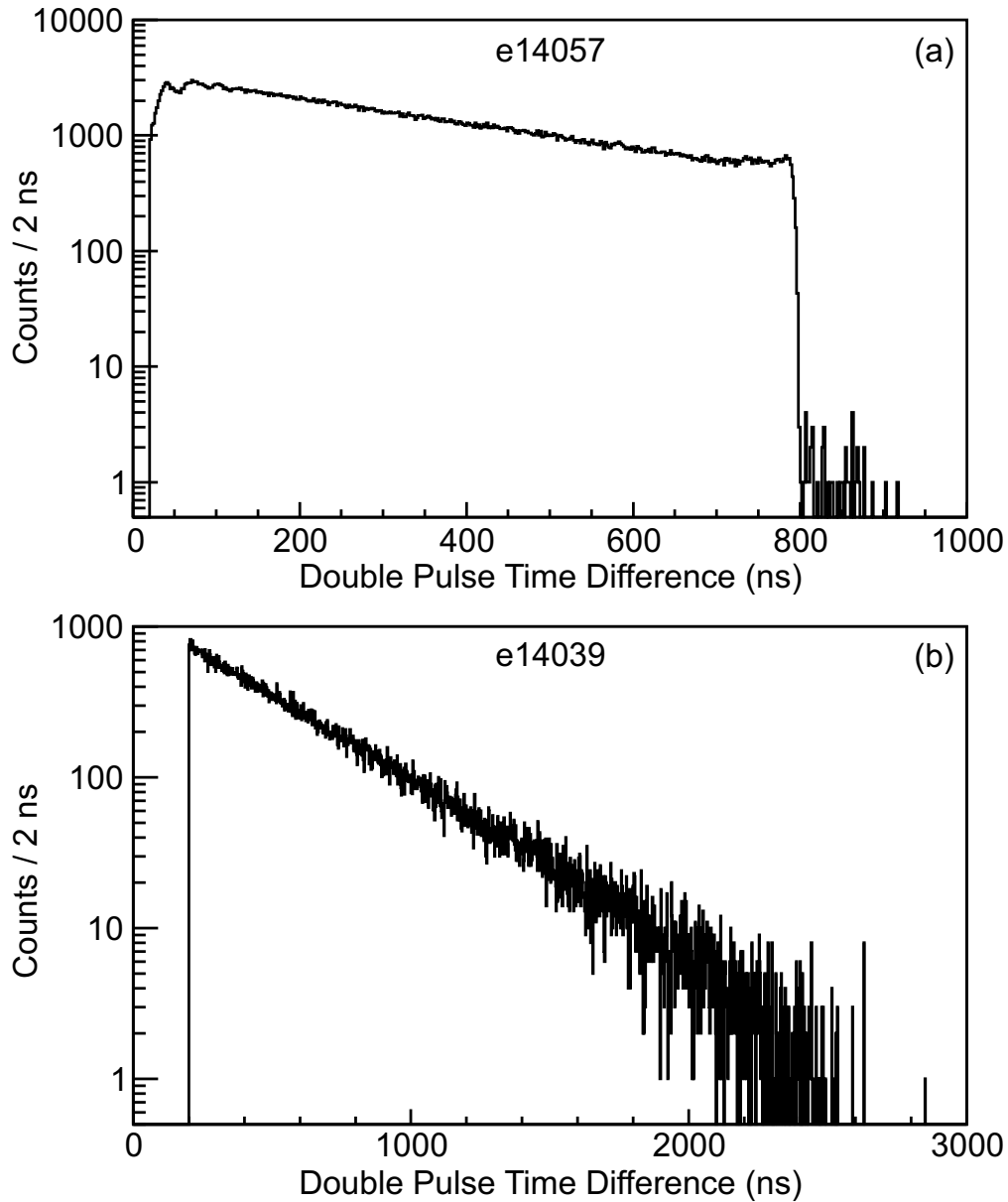


Figure 4.17: (a) and (b) Time-difference distributions between the two constituent pulses of double pulse signals recorded in e14057 and e14039, respectively. The second pulse was restricted to amplitudes between 400 and 8000 ADC units in e14057 and energies of 400 and 2000 keV for e14039. A weighted average between the two results yields a value of 274(4) ns for the half-life of the 0_2^+ state in ^{68}Ni .

displayed on the level scheme in Fig. 4.6.

4.1.2.7 Half-Life of the 0_3^+ state in ^{68}Ni

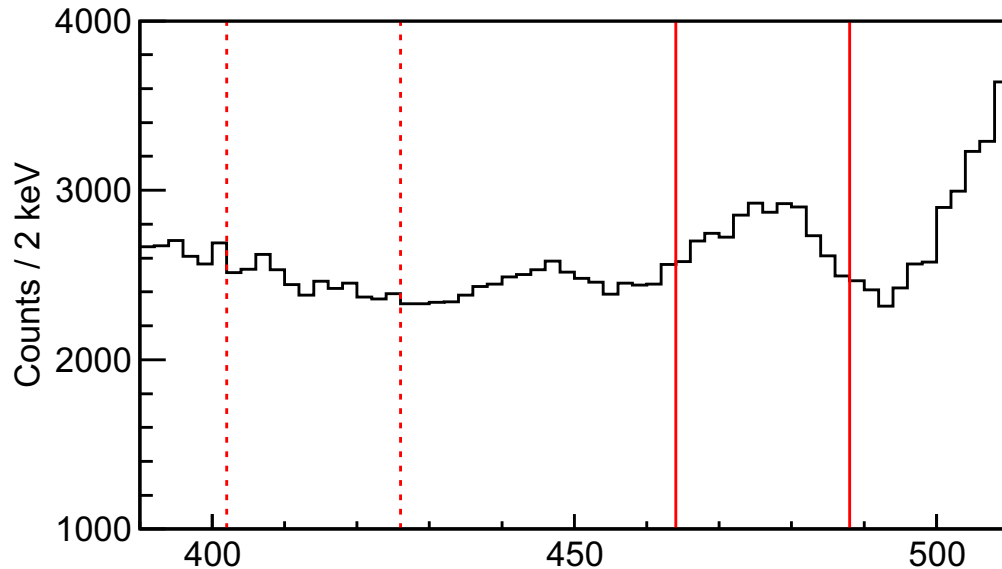


Figure 4.18: Spectrum of γ -rays recorded in the LaBr₃ detectors around the 477.7-keV peak coincident with a decay event in the segmented plastic scintillator. The set of solid red and dashed red bars represent the energy windows used for the peak and background regions of interest, respectively.

A measurement of the half-life of the 2511keV 0_3^+ state was performed using the $\beta\gamma$ timing methods presented in Section 3.9. The 477.7-keV γ ray was recorded in the LaBr₃ detectors, described in Section 3.8, coincident with the β -decay electron detected in the PSPMT, detailed in Section 3.6. The LaBr₃ energy spectrum in the region of the 477.7-keV transition is shown in Fig. 4.18.

In Fig. 4.18, the solid red and dashed red bars denote the energy windows used for the peak and background regions of interest (ROI), respectively. The peak around 448 keV in energy is from the decay of the 2677-keV 6_1^+ state in ^{70}Ni . At the top of the energy range in Fig. 4.18, the lower-energy portion of the 511-keV peak is present. These two spectral contaminants preclude placing the background region in the immediate vicinity of the 477.7-keV peak. Therefore, the region between 402 and 426 keV was chosen. The peak region of interest ranges from 464 to 488 keV.

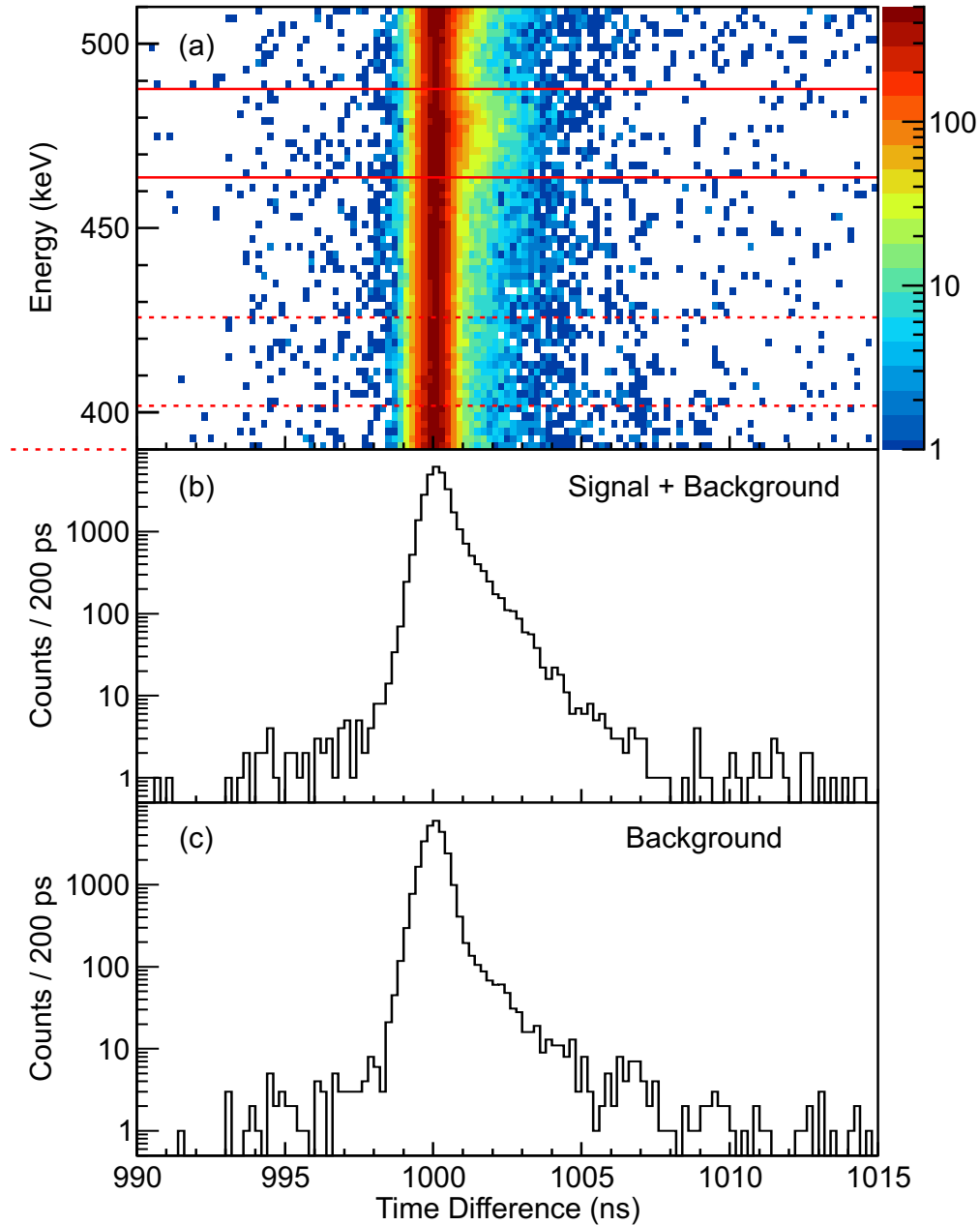


Figure 4.19: (a) Two-dimensional spectrum of γ -rays recorded in the LaBr_3 detectors coincident with a decay event in the segmented plastic scintillator vs. time difference between the LaBr_3 and segmented plastic scintillator. The solid red and dashed red bars denote the energy windows used for the peak and background regions of interest (ROI), respectively. (b) and (c) Time-difference spectra (LaBr_3 - segmented plastic scintillator) obtained by projecting the spectrum in (a) onto the time-difference axis over the regions between the solid (peak ROI) and dashed (background ROI) red lines, respectively.

The $\beta\gamma$ time-difference spectra between the LaBr_3 detectors and the segmented plastic scintillator is shown in Fig. 4.19a. The time-difference spectra (LaBr_3 - segmented plastic

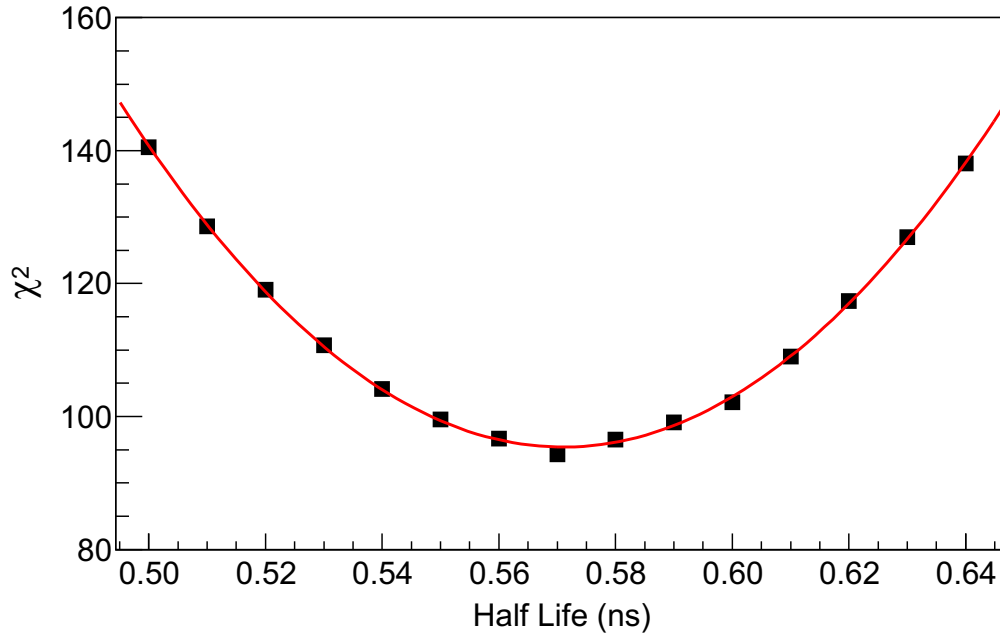


Figure 4.20: χ^2 as a function of trial half-life used in each convolution fit, shown as black squares, and quadratic fit, shown in red, for interpolation between points.

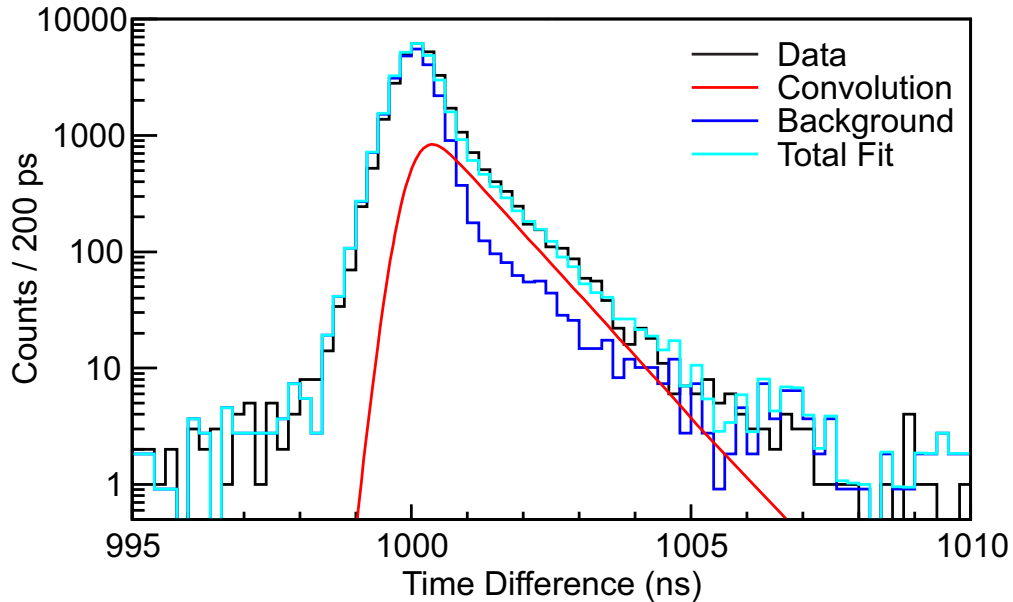


Figure 4.21: Best fit results for the lifetime of the 0_3^+ state in ^{68}Ni . In black and blue are the time-difference spectra for the peak and background ROIs shown in Figs. 4.19b and 4.19c, respectively. The convolution of the detector response with the best-fit half-life is shown in Red and the total fit of background plus convolution is shown in cyan.

scintillator), obtained by projecting the spectrum in 4.19a onto the time-difference axis over the regions between the solid (peak ROI) and dashed (background ROI) red lines, are shown

in Figures 4.19b and 4.19c, respectively. The time-difference spectra have an artificial 1000 ns offset to avoid negative time differences.

Based on the total counts in the peak, obtained from a Gaussian fit integrated over the peak ROI, and the total counts in the background ROI the background spectrum was scaled to contain the proper number of counts. Then using the techniques described in Section 3.8 a series of trial lifetimes were convolved with the measured detector response and the χ -square minimization procedure was used to extract the half-life and associated error for the 0_3^+ state in ^{68}Ni .

Figure 4.20 shows the χ^2 as a function of trial half-life used in each convolution fit. The black squares are the χ^2 values for each trial half-life and the red line is a quadratic fit for interpolation between points. The half-life was taken as the value at the minimum of the χ^2 distribution. The statistical error was determined from the half-life values one χ^2 unit from the minimum. Systematic errors were investigated by varying quantities such as the ratio of counts in the peak to counts in the background, the centroid of the underlying Gaussian component of the convolution, and the magnitude of the DOI correction. All errors were added in quadrature. A value of 0.57(5) ns was obtained for the half-life for the (0_3^+) state in ^{68}Ni .

The best fit is shown in Fig. 4.21. In Fig. 4.21, the black and blue (blue is scaled) are the time-difference spectra obtained for the peak and background ROIs from Figs. 4.19b and 4.19c, respectively. The convolution of the detector response with the best-fit 0.57-ns half-life is shown in Red. The total fit of the scaled background plus convolution is shown in cyan.

4.2 Decay of ^{70}Co

The low-energy level scheme of ^{70}Ni was investigated following the β decay of ^{70}Co . β decays in the GeDSSD were correlated to ^{70}Co ions using the techniques described in Section 3.5.2 with a 4000 ms correlation window. The γ rays correlated to the decay of ^{70}Co are shown in Fig 4.22. Transitions identified in the present analysis as belonging to ^{70}Ni are labeled with their energy while contaminating transitions, resulting from spurious correlations from the decay of other implanted nuclei, are identified with symbols.

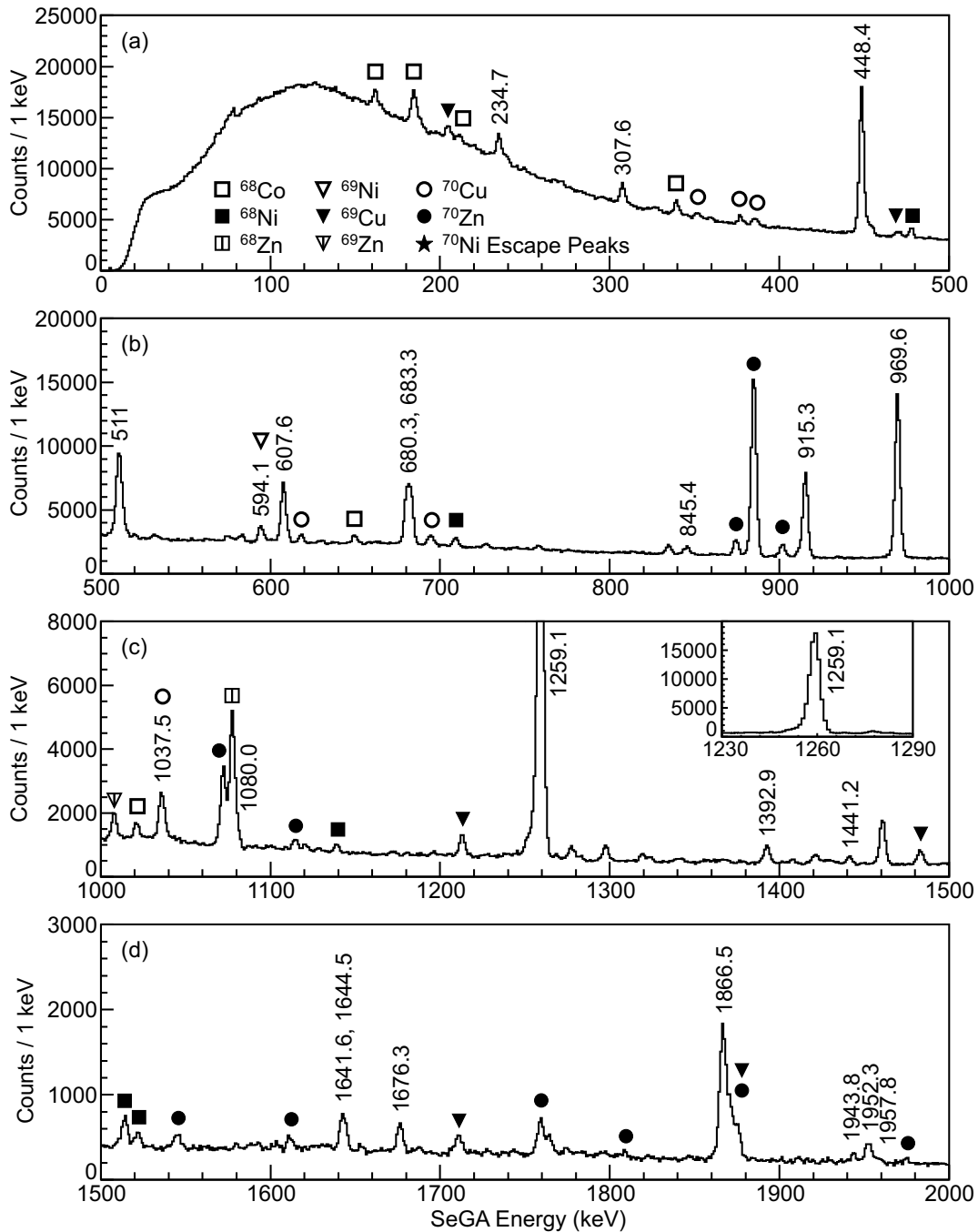


Figure 4.22: β -delayed γ -ray spectrum recorded in SeGA within 4000 ms of an implanted ^{70}Co ion. Transitions identified in the subsequent analysis as affiliated with the decay of ^{70}Ni are labeled with their energy while contaminating transitions, resulting from spurious correlations of the decay of other implanted nuclei, are denoted with symbols. The inset in (c) shows the full height of the 1259.1-keV peak cut off in spectrum shown in (c). The inset in (e) shows the full height of the 2032.9-keV peak cut off in spectrum shown in (e).

Figure 4.22: (cont'd)

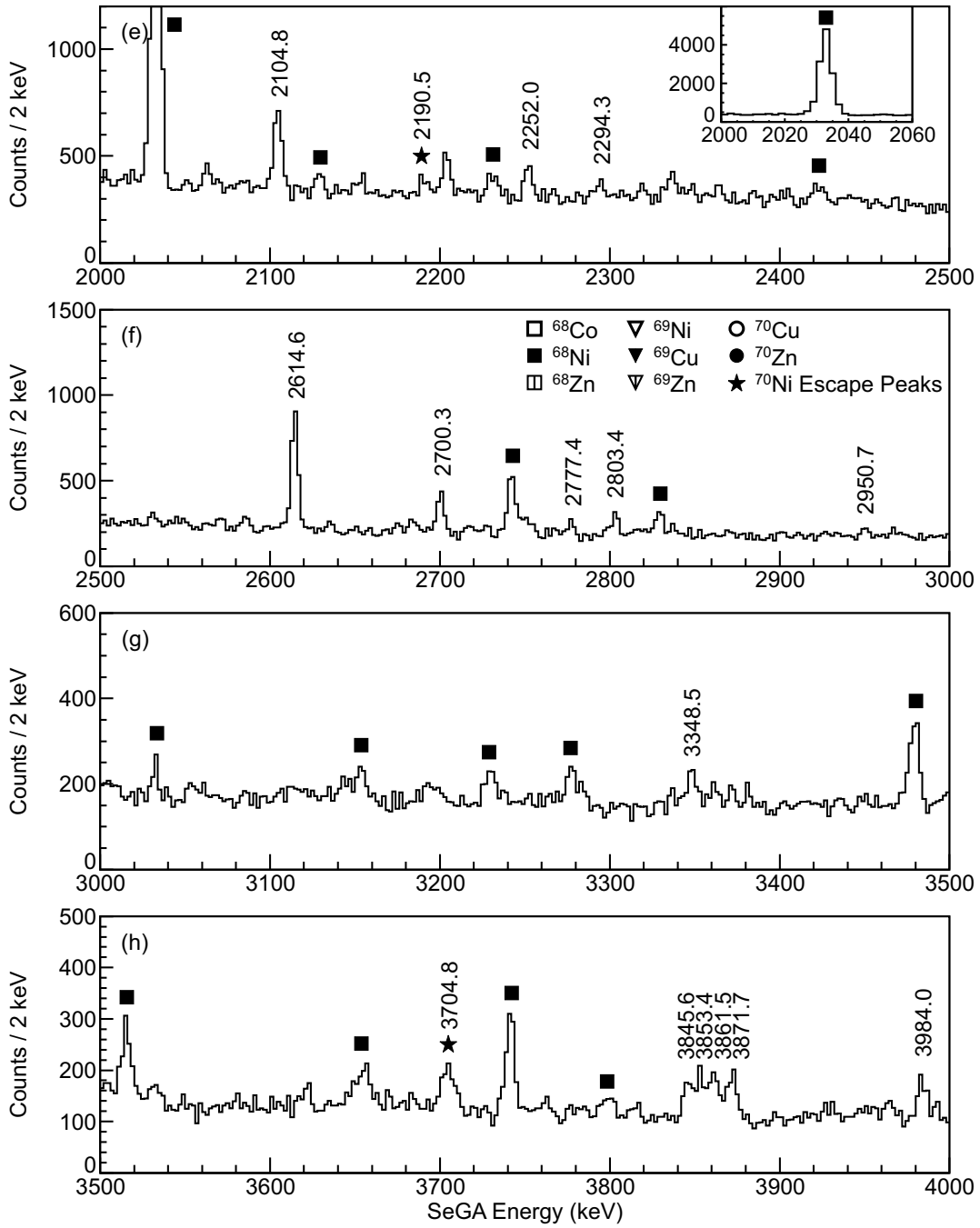
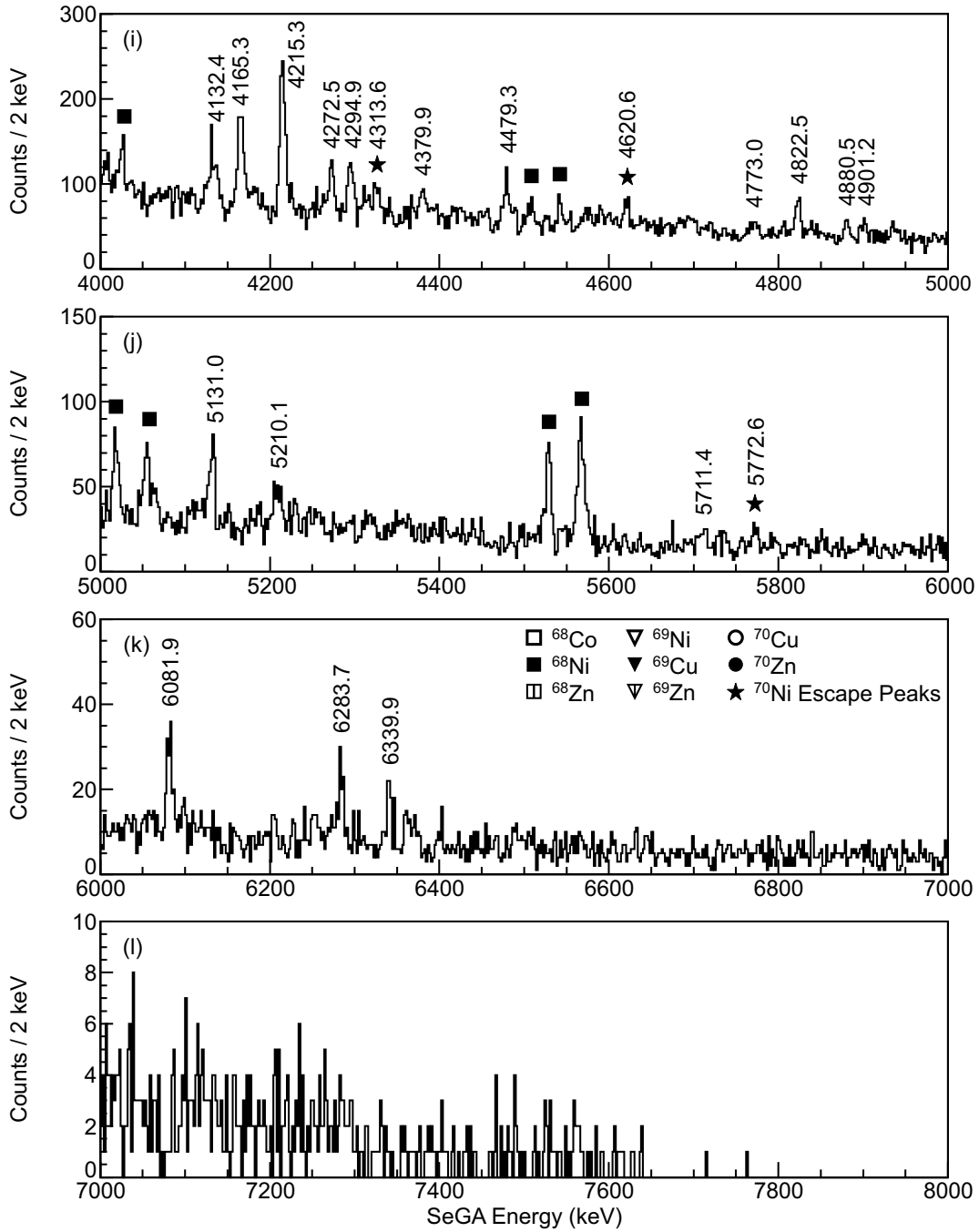


Figure 4.22: (cont'd)



4.2.1 β -Decaying Isomers in ^{70}Co

The ^{70}Co beam was delivered to the experimental end station in a mixture of two isomeric states, both observed in prior experiments. The better characterized of the two has a tentative $(6^-, 7^-)$ spin and parity assignment [12] and an evaluated half-life of 114(7) ms [58]. The second β -decaying ^{70}Co isomer has been studied once and has an assigned, tentative, (3^+) spin and parity and a measured half-life of 500(180) ms [12].

The work of Ref. [12] identified several β -delayed γ -rays unique to the decay of each isomer. The 448.5-keV transition is one such γ ray, and is observed following the decay of the short-lived, high-spin, ^{70}Co isomer exclusively. For this analysis, the exclusion technique, described in Section 4.1.2.2, was used. The ^{70}Co decay curve vs. γ -ray energy from e14039 in the region around the 448.5-keV peak is shown in Fig. 4.23a. The projection onto the energy axis is presented in Fig. 4.23b.

The decay curves shown in Figs. 4.24a and 4.24b were obtained from the projection the 448.5-keV peak region (solid red lines) and background region (dashed red lines), respectively, in Fig. 4.23 onto the time-difference axis. The background decay curve shown in Fig. 4.24b was scaled and subtracted from the decay curve in Fig. 4.24a. The background-subtracted decay-curve is shown in black in Fig. 4.25a.

The spurious-correlation component was determined using the techniques in Section 4.1.2.1. The two-dimensional time-difference vs. coincident γ -ray energy spectrum, with the analysis run backwards in time, is shown in Fig. 4.12a. The projection of the spectrum shown in Fig. 4.12a onto the energy axis is presented in Fig. 4.26b.

The ratio of the peak areas between Figs. 4.23b and 4.26b is the ratio of spurious correlations to total counts in the background-subtracted decay curve. The decay curve

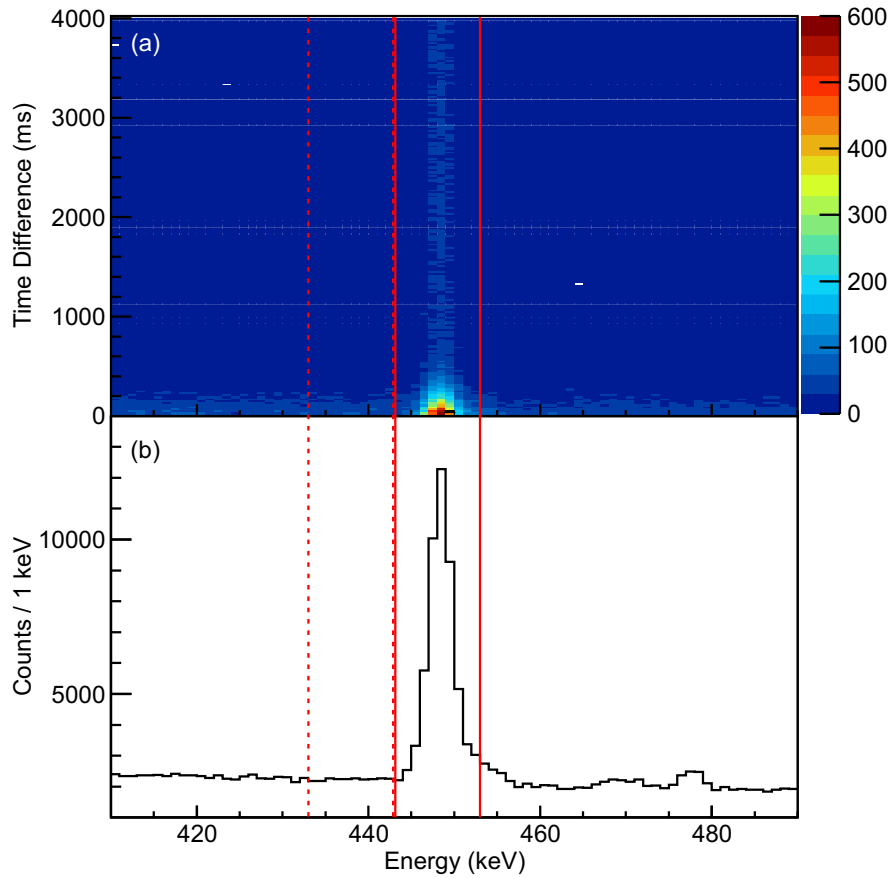


Figure 4.23: (a) Decay curve vs. coincident γ -ray energy, recorded in SeGA during e14039, for the region around the 448.5-keV peak. (b) Projection of (a) onto the energy axis. Sets of solid red vertical lines and dashed vertical lines identify the peak and background regions, respectively, for each peak.

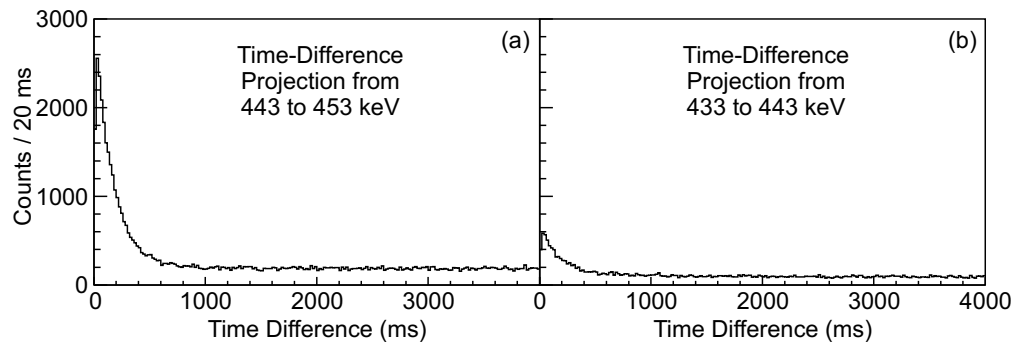


Figure 4.24: (a) and (b) Decay curves obtained by projecting 4.23a onto the time-difference axis over the regions of (a) 443 to 453 keV and (b) 433 to 443 keV. The region shown in (a) encompasses the 448.5-keV peak while (b) is a representative background to be scaled and subtracted from the peak.

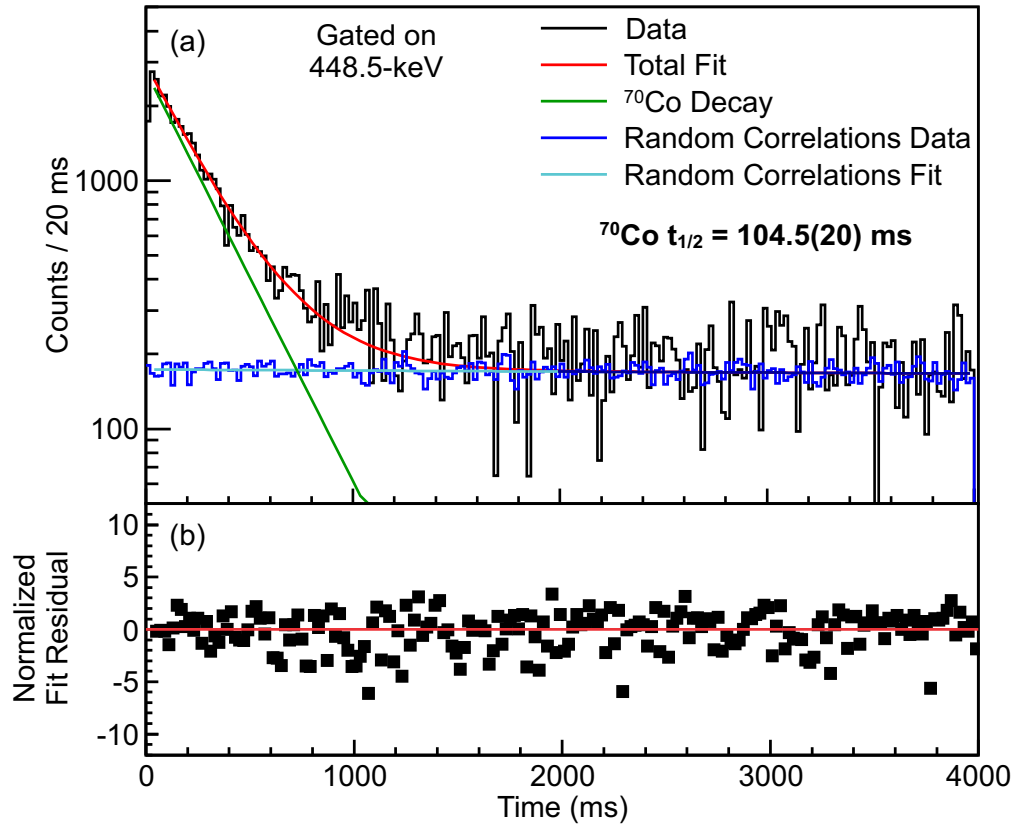


Figure 4.25: (a) Background-subtracted, γ -gated decay curve for the decay of the short-lived, high-spin, ^{70}Co isomer into ^{70}Ni . A gate was placed on the 448.5-keV transitions in ^{70}Ni to isolate the short-lived, high-spin, isomer exclusively. The background, scaled appropriately and subtracted, was sampled directly below the peak. The background-subtracted data are shown in black while the spurious correlation component, obtained using the techniques in Section 4.1.2.1, is shown in blue. In cyan, a fit to the spurious correlation component is shown, and was used to represent the spurious correlations in the total fit of the data shown in red. The correlated contribution from the decay of ^{70}Co is shown in green. The half-life of short-lived, high-spin, ^{70}Co isomer, extracted from the fit, is 104.5(20) ms which agrees with the evaluated value of 114(7) ms [58]. (b) Fit residuals, normalized to the bin error, for the total fit compared to the data in (a).

for spurious correlations events was obtained from projecting the spectrum shown in Fig. 4.26a onto the time-difference axis, and is shown in blue in Fig. 4.25. A fit to the spurious correlation data, shown in cyan in Fig. 4.25, was used in lieu of the data to provide a smoothly varying component for use in the total fit shown in red in Fig. 4.25. The total fit was a combination of the spurious correlation component and an exponential decay. The exponential decay component, from the real correlations between ^{68}Fe and its subsequent

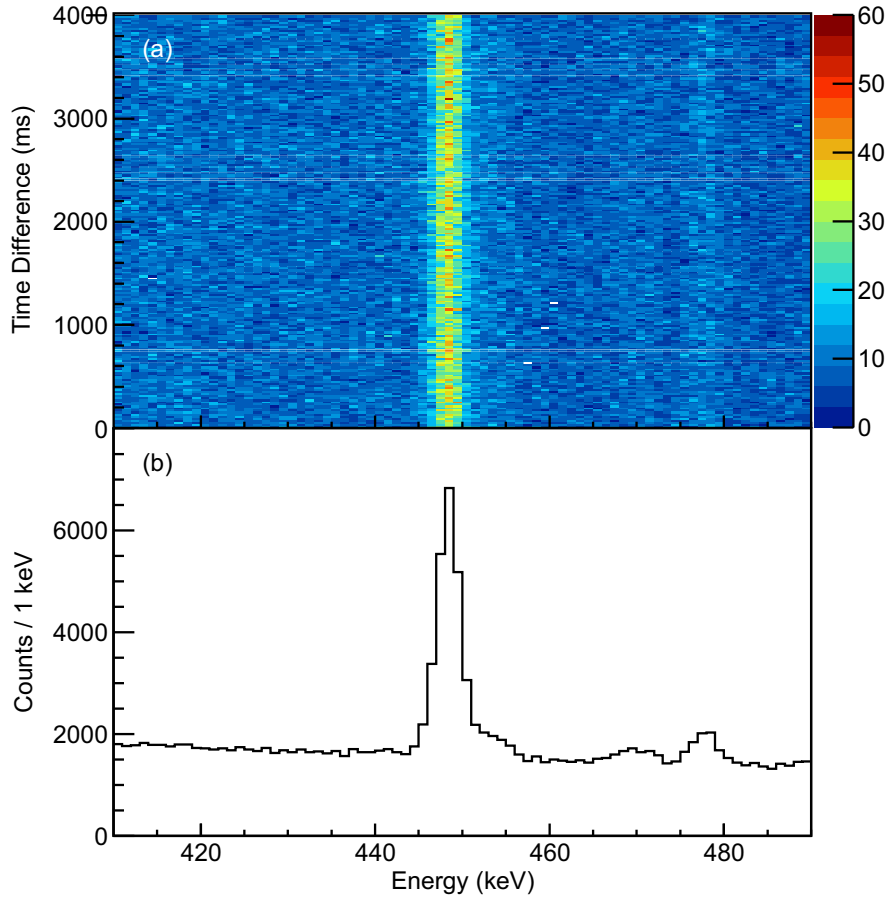


Figure 4.26: Results of the analysis run backwards in time through the data. (a) Decay curve vs. coincident γ -ray, recorded in SeGA during e14039, for the region around the 448.5-keV peak. (b) Projection of (a) onto the energy axis.

decay, extracted from the fit is shown in green. The results of the fit yielded a half-life of 104.5(20) ms for the short-lived, high-spin, ^{70}Co isomer which agrees with the evaluated value of 114(7) ms [58].

The work of Ref. [12] identified a 607.6-keV transition exclusively affiliated with the decay of the long-lived, low-spin, ^{70}Co isomer. The same analysis techniques used for the short-lived, high-spin, ^{70}Co isomer were employed again for this analysis. The ^{70}Co decay curve vs. γ -ray energy during e14039 for the region around the 607.6-keV peak is shown in Fig. 4.27a. The projection onto the energy axis is presented in Fig. 4.27b.

The decay curves shown in Figs. 4.28a and 4.28b were obtained from the projection the

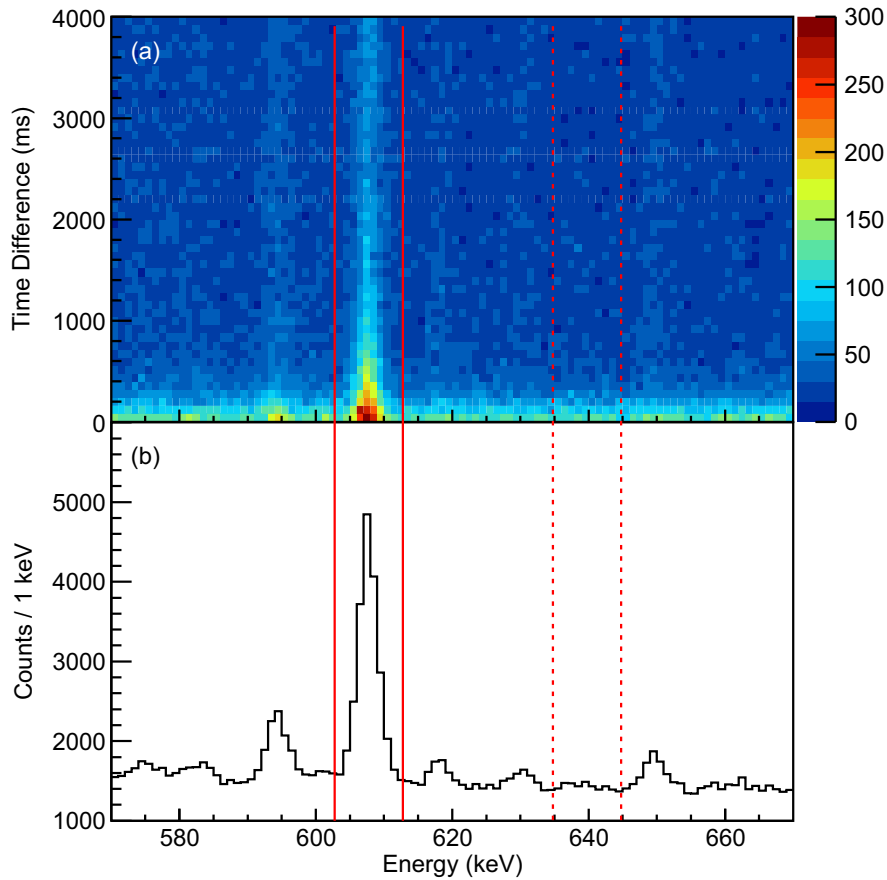


Figure 4.27: (a) Decay curve vs. coincident γ -ray energy, recorded in SeGA during e14039, for the region around the 607.6-keV peak. (b) Projection of (a) onto the energy axis. Sets of solid red vertical lines and dashed vertical lines identify the peak and background regions, respectively, for each peak.

607.5-keV peak region (solid red lines) and background region (dashed red lines), respectively, in Fig. 4.27 onto the time-difference axis. The background decay curve shown in Fig. 4.28b was scaled and subtracted from the decay curve in Fig. 4.28a. The background-subtracted decay-curve is shown in black in Fig. 4.29a.

The spurious-correlation component was determined using the techniques in Section 4.1.2.1. The two-dimensional time-difference vs. coincident γ -ray energy spectrum with the analysis run backwards in time is shown in Fig. 4.12a. The projection of the spectrum shown in Fig. 4.12a onto the energy axis is presented in Fig. 4.30b.

The ratio of the peak areas between Figs. 4.27b and 4.30b is the ratio of spurious

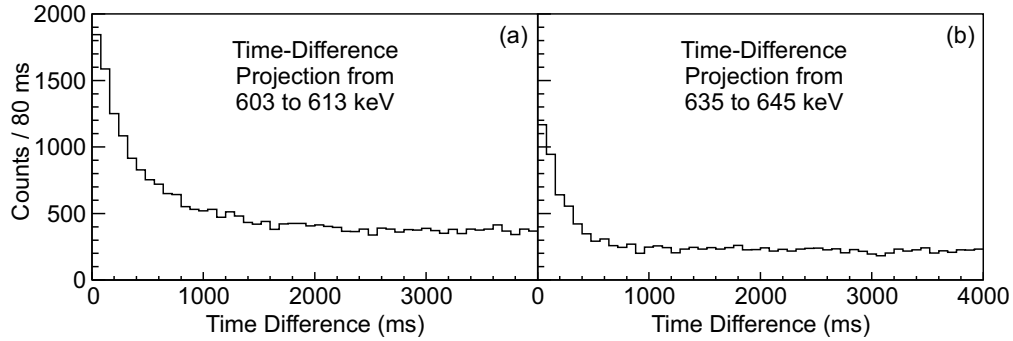


Figure 4.28: (a) and (b) Decay curves obtained by projecting 4.27a onto the time-difference axis over the regions of (a) 605 to 615 keV and (b) 635 to 645 keV. The region shown in (a) encompasses the 607.6-keV peak while (b) is a representative background to be scaled and subtracted from the peak.

correlations to total counts in the background-subtracted decay curve. The decay curve for spurious correlations events was obtained from projecting the spectrum shown in Fig. 4.30a onto the time-difference axis, and is shown in blue in Fig. 4.29. A fit to the spurious correlation data, shown in cyan in Fig. 4.29, was used in lieu of the data to provide a smoothly varying component for use in the total fit shown in red in Fig. 4.29. The total fit was a combination of the spurious correlation component and an exponential decay. The exponential decay component, from the real correlations between ^{68}Fe and its subsequent decay, extracted from the fit is shown in green. The results of the fit yield a half-life of 470(20) ms for the long-lived, low-spin, ^{70}Co isomer which agrees with the previous measured value of 500(180) ms [12].

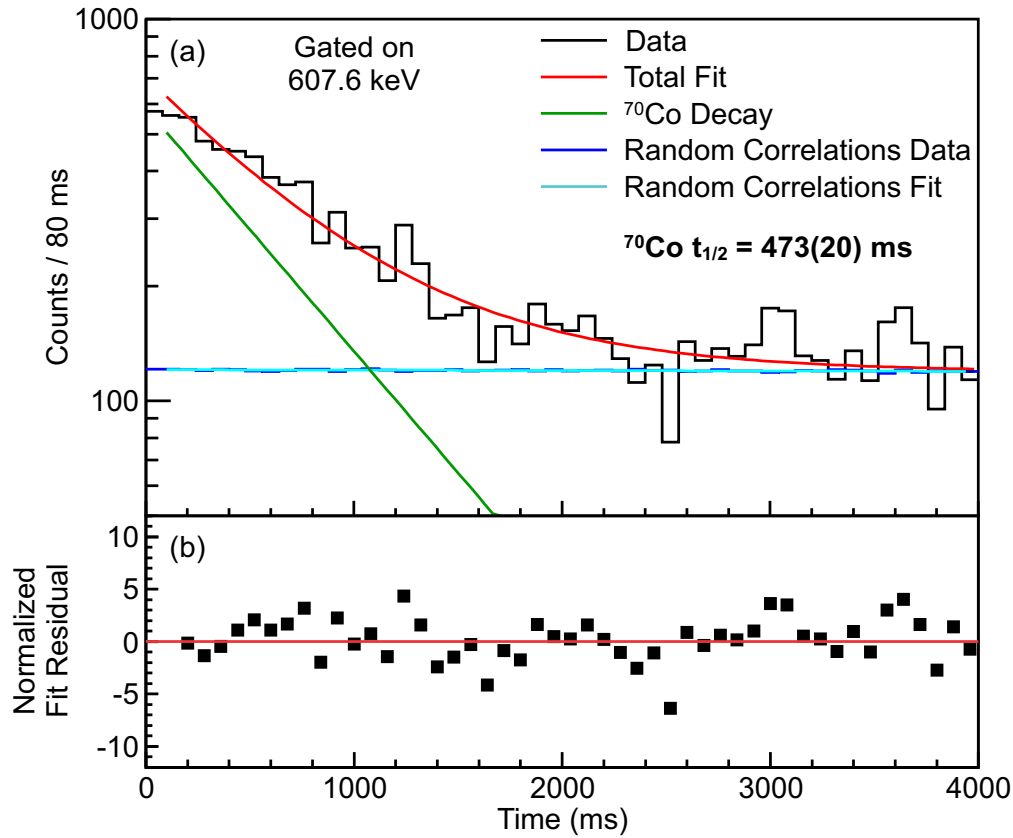


Figure 4.29: (a) Background-subtracted γ -gated decay curve for the decay of the short-lived, high-spin, ^{70}Co isomer into ^{70}Ni . A gate was placed on the 607.5-keV transitions in ^{70}Ni to isolate the short-lived, high-spin, isomer exclusively. The background, scaled appropriately and subtracted, was sampled directly below the peak. The background-subtracted data are shown in black while the spurious correlation component, obtained using the techniques in Section 4.1.2.1, is shown in blue. In cyan, a fit to the spurious correlation component is shown, and was used to represent the spurious correlations in the total fit of the data shown in red. The correlated contribution from the decay of ^{70}Co is shown in green. The half-life of short-lived, high-spin, ^{70}Co isomer, extracted from the fit, is 470(20) ms for the long-lived, low-spin, ^{70}Co isomer which is consistent with the previously measured value of 500(180) ms [12]. (b) Fit residuals, normalized to the bin error.

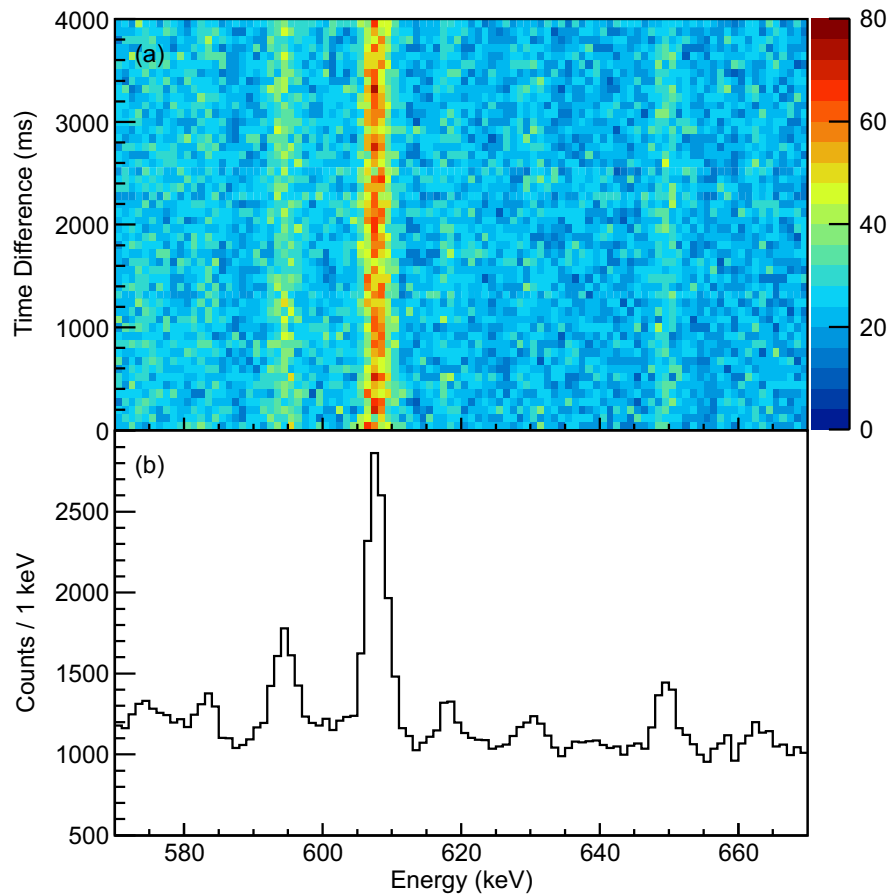


Figure 4.30: Results of the analysis run backwards in time through the data. (a) Decay curve vs. coincident γ -ray, recorded in SeGA during e14039, for the region around the 607.6-keV peak. (b) Projection of (a) onto the energy axis.

4.2.2 $A = 70$ Decay Curves

With the half-lives of the two β -decaying ^{70}Co isomers measured, the ^{70}Co decay-curve, shown in black in Fig. 4.31a, was fitted and the number of decays from each isomer extracted. The location of the ion and subsequent decay had to be in the same GeDSSD pixel for this analysis. The exclusion technique described in Section 4.1.2.2 was used again for this analysis. Both the exclusion window and correlation window were set to 4000 ms. The 4000 ms correlation window was chosen to provide a long time region to properly fit the background and to encompass nearly all the long-lived isomer decays.

The time distribution of spurious correlations was obtained running the full analysis backwards in time [57]. In Fig. 4.31a, the data (black) are fit with the sum of spurious correlations (blue) and two independent series of Bateman equations, one for each ^{70}Co isomer. Figure 4.31b shows the percent difference between the fit and the data as a function of time.

For both the short- (solid) and long-lived (dashed) isomer decays, the ^{70}Co parent, ^{70}Ni daughter, and ^{70}Cu granddaughter contributions are illustrated as green, cyan, and magenta lines, respectively. The total fit is shown as a red line. The half-lives of ^{70}Ni and ^{70}Cu were fixed to the NNDC evaluated values of 6.0 s and 6.6 s [59], respectively. The short- and long-lived ^{70}Co isomer half-lives were fixed to 104.5 ms and 470 ms, respectively.

The number of correlated decays recorded for each ^{70}Co β -decaying isomer was obtained by integrating the Bateman equations. The statistical error was obtained from the error in the fit while the systematic error was evaluated by varying all fixed half-lives within their uncertainties. The total number of correlated decays was used to obtain the absolute γ -ray efficiencies presented in Tables 4.9 and 4.11. The same techniques discussed in Section 4.1.2.5

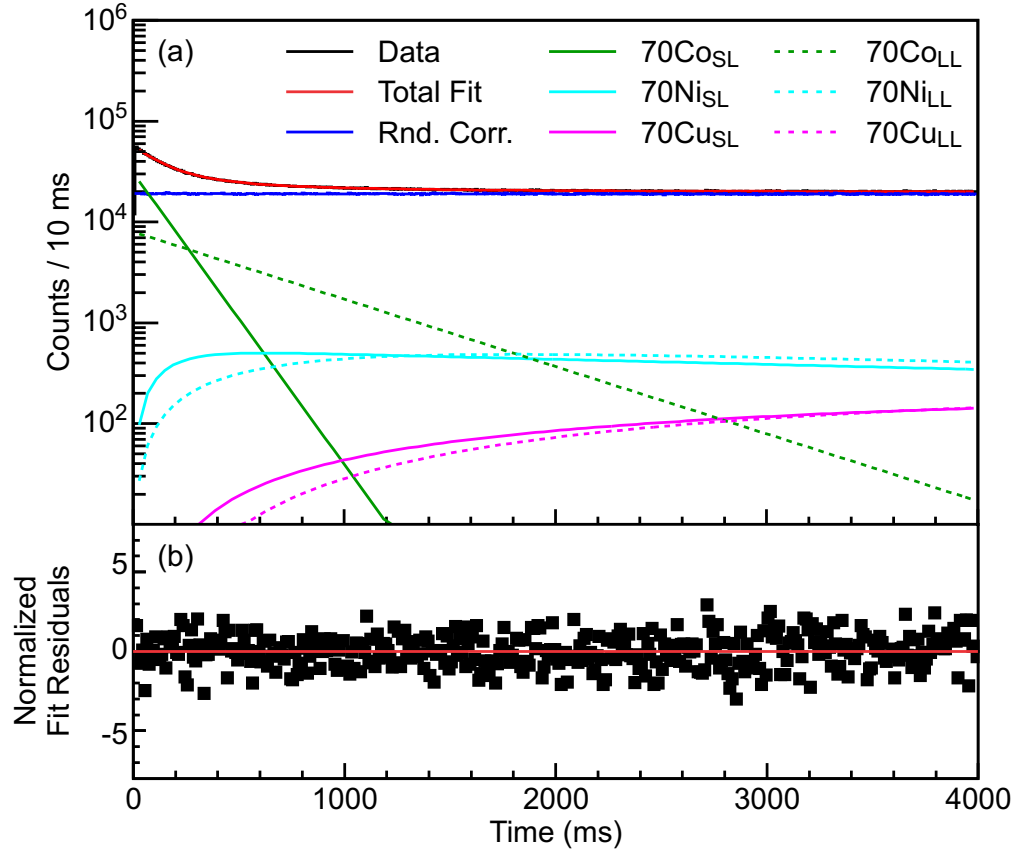


Figure 4.31: (a) Decay curve showing the time distribution of recorded decay events following within 4000 ms of an implanted ^{70}Co ion. A 4000 ms “exclusion window” was set following the implantation of each ion such that all subsequent ions within that window were ignored. The total fit is shown in red, the data are shown in black, and the time distribution of spurious correlations, obtained by running the analysis backwards in time, is shown in blue. The ^{70}Co parent, ^{70}Ni daughter, and ^{70}Cu granddaughter contributions are illustrated as green, cyan, and magenta lines, respectively. The short-lived isomer decay is shown as solid lines while the long-lived isomer decay is shown as a dashed line. The half-lives of ^{70}Ni and ^{70}Cu were fixed to the NNDC evaluated values of 6.0(3) s and 6.6(3) s [59], respectively. From the fit, the half-life of the short-lived ^{70}Co isomer was determined to be 104(4) ms while a half-life value of 450(13) ms was extracted for the long-lived ^{70}Co isomer. (b) Fit residuals normalized to the error in each bin.

were applied here to obtain the spurious correlation and exclusion technique corrections.

Table 4.8 presents the integrated number of counts for ^{68}Ni in the Bateman equations and the corrections for spurious correlations and the exclusion technique for both experiments.

The “corrected” number of decays was obtained by multiplying the integrated number of counts by the spurious correlation and exclusion technique correlation factors.

Table 4.8: Decay curve fit results and correction factors for ^{70}Ni in e14039. The “corrected” number of decays is obtained by multiplying the integrated number of counts by the spurious correlation and exclusion technique correlation factors. The corrected number of decays is then directly comparable to the non-exclusion analysis β -delayed γ -ray statistics.

	e14039
Integrated Number of Short-Lived, High-Spin, ^{70}Co Isomer Decays	$0.474(10) \times 10^6$
Integrated Number of Long-Lived, Low-Spin, ^{70}Co Isomer Decays	$0.522(14) \times 10^6$
Spurious Correlation Correction	2.06(2)
Exclusion Technique Correction	1.22(1)
Corrected Number of Short-Lived, High-Spin, ^{70}Co Isomer Decays	$0.96(2) \times 10^6$
Corrected Number of Long-Lived, Low-Spin, ^{70}Co Isomer Decays	$1.31(4) \times 10^6$

The existence of two isomers complicates the analysis required to create individual decay schemes for each β -decaying ^{70}Co isomer. The next section describes the adaptation of a technique, developed in the mid 1980s, that ultimately provides the capability to determine the contribution of each isomer flowing through any detected γ -ray transition.

4.2.3 ^{70}Co Isomer Deconvolution

In order to construct the decay schemes for both ^{70}Co isomers all β -delayed γ rays must be identified and placed. In decay spectroscopy, one typically examines $\beta\gamma\gamma$ coincidences to place transitions and identify new levels. However, in the presence of more than one β -decaying state the process is more complicated and additional techniques are needed.

One method to determine whether a particular γ ray is affiliated with the decay of an isomer is to examine the corresponding decay curve. This technique was demonstrated earlier in this chapter for the 448.5- and 607.6-keV transitions. In addition to providing half-life information, the ratio of counts in each exponential decay component can provide the contribution of each isomer to the intensity of that transition.

A prime example is the 1259.1-keV transition which has been observed to collect intensity

from the decay of both ^{70}Co isomers [12]. Figure 4.32 shows the background-subtracted decay-time distribution gated on the 1259.1-keV ($2_1^+ \rightarrow 0_1^+$) collecting transition. The procedure used to obtain the results presented in Fig. 4.32 is identical to the processes described for generating Figs. 4.25 and 4.29 and the same exclusion analysis techniques were used. The correlation and exclusion windows were set to the same 4000 ms to encompass several half-lives of the long-lived isomer.

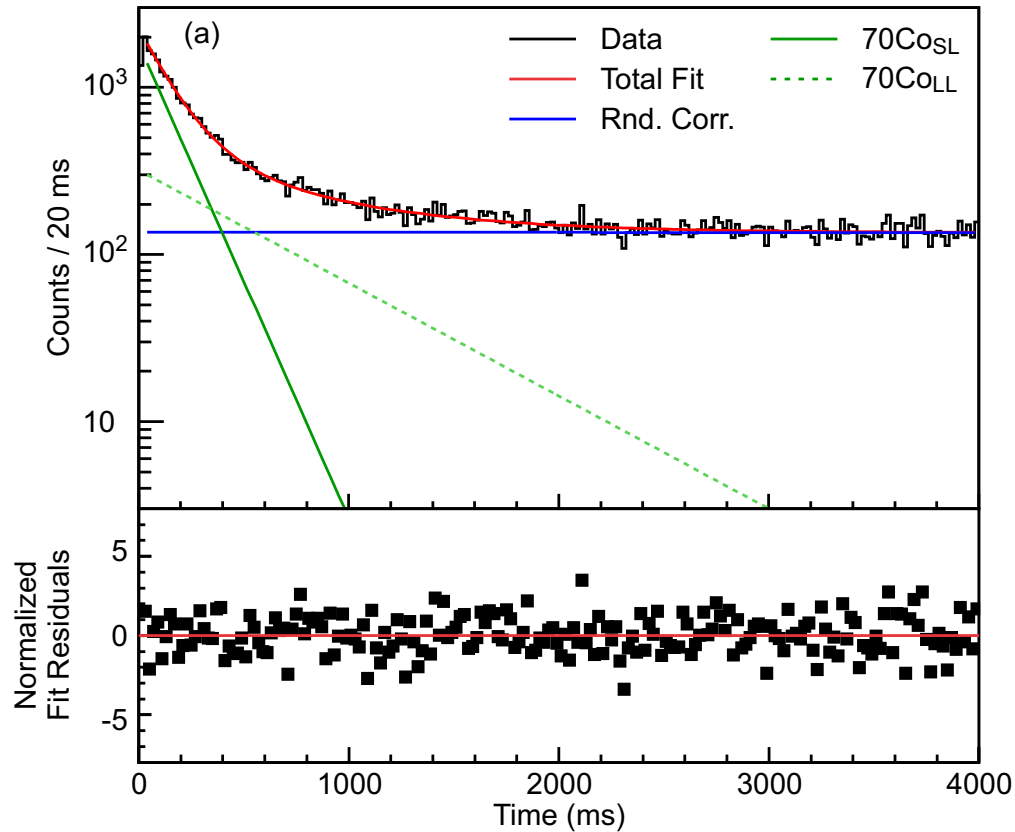


Figure 4.32: (a) Decay curve showing the time distribution of recorded decay events following within 4000 ms of an implanted ^{70}Co ion gated on the 1259.1-keV ($2_1^+ \rightarrow 0_1^+$) transition. The same 4000 ms “exclusion window” was set following the implantation of each ion such that all subsequent ions within that window were ignored. The total fit is shown in red, the data are shown in black, and the scaled time distribution of spurious correlations used in Fig. 4.31, obtained by running the analysis backwards in time, is shown in blue. The ^{70}Co parent is shown in green and the short- and long-lived isomer decays are shown as solid and dashed lines, respectively. Half-lives of 106(5) and 446(42) ms were extracted from the fit for the short- and long-lived ^{70}Co isomers, respectively. These values are consistent with the 104.5(20) and 470(20) ms determined earlier in this section. (b) Fit residuals normalized to the bin error.

In Fig. 4.32, the data (black) are fit with the sum of spurious correlations (blue) and two exponential decays, of the type given in Eq. (2.20), one for each ^{70}Co isomer, shown in green solid and dashed lines for the short- and long-lived isomers, respectively. The spurious-correlation component was fixed, but all other parameters were free. The percent difference between the fit and the data as a function of time is shown in Fig. 4.32b.

The 1259.1-keV γ -gated decay curve fit yields consistent half-lives compared to both the ^{70}Co decay curve fit as well as the 448.5- and 607.6-keV γ -gated ^{70}Co decay curve fits. The intensity contribution ratio (short-lived / long-lived) through the 1259.1-keV transition is 0.77(8). This example demonstrates the ability to perform γ -gated decay curve fits for relatively high statistics cases, but for most transitions of interest this method will not yield useful information purely due to statistics limitations. Fortunately a technique, formulated in Ref. [60], exists to transform the data of traditional decay curve, with linear time axis, to a time distribution with logarithmic time axis.

The functional form of the decay curve for parent nucleus, given originally in Eq. (2.20), is presented again in Eq. (4.1).

$$\frac{dn}{dt} = n\lambda e^{-\lambda t} \quad (4.1)$$

Then, by making the transformation $\ln(t) = \delta$, the frequency distribution from equation (4.1) becomes that of equation (4.2) [60].

$$\frac{dn}{d\delta} = n\lambda e^{\delta} e^{-\lambda e^{\delta}} \quad (4.2)$$

This method effectively “compresses” the data into a functional form, peaked at $\ln(\lambda^{-1})$, to which a more robust fit can be performed even in cases of poor statistics. In the case

of the 1259.1-keV γ -gated decay curve, the same 400 bins of data over the 4000 ms time window, shown in Fig. 4.32, are compressed into 58 bins in the transformed 1259.1-keV γ -gated decay curve, shown in Fig. 4.33. The data in Fig. 4.33 were fitted with the same components as Fig. 4.32, but of the transformed functional forms.

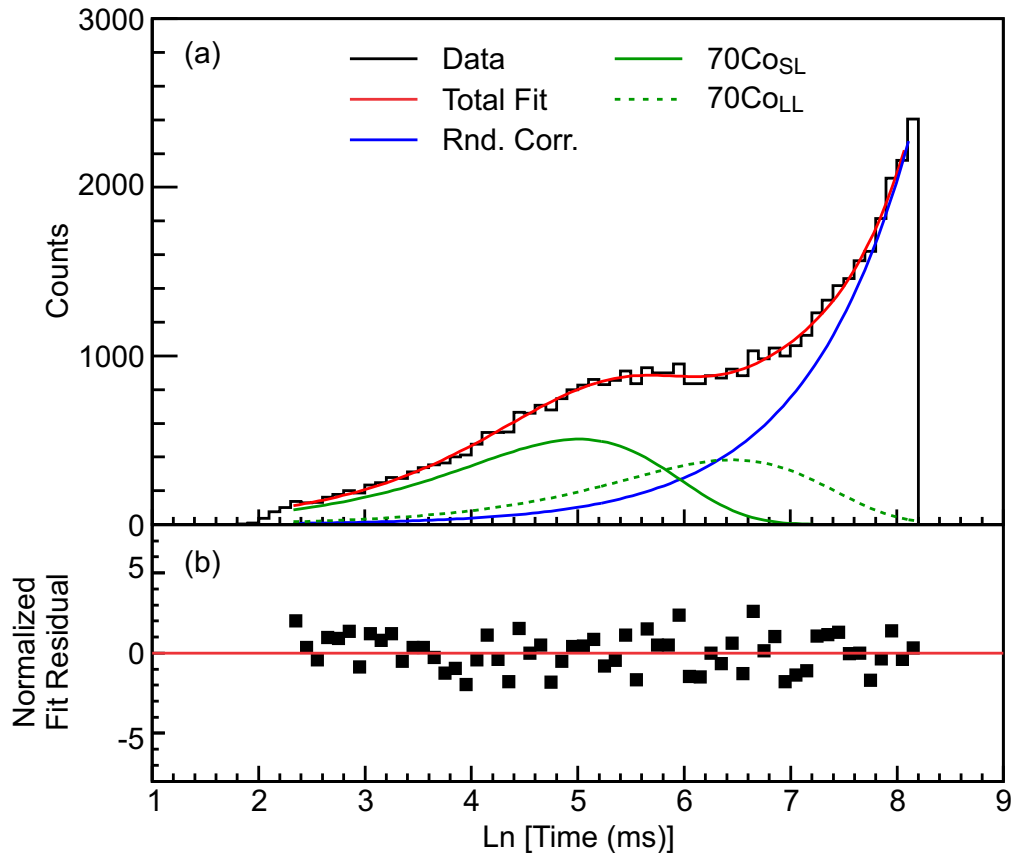


Figure 4.33: (a) Transformed decay curve showing the natural logarithm of the time distribution of recorded decay events following within 4000 ms of an implanted ^{70}Co ion gated on the 1259.0-keV ($2_1^+ \rightarrow 0_1^+$) transition. The same 4000 ms “exclusion window” was set following the implantation of each ion such that all subsequent ions within that window were ignored. The total fit is shown in red, the data are shown in black, and the scaled time distribution of spurious correlations used in Fig. 4.31, obtained by running the analysis backwards in time, is shown in blue. The ^{70}Co parent is shown in green and the short- and long-lived isomer decays are shown as solid and dashed lines, respectively. Half-lives of 104(5) and 440(50) ms for the short- and long-lived ^{70}Co isomers, respectively, were extracted from the fit. (b) Fit residuals normalized to the bin error.

The transformed, background subtracted, 1259.1-keV γ -gated decay curve fit gives short- and long-lived ^{70}Co isomer half-lives of 104(5) ms and 440(50) ms, respectively, and an inten-

sity contribution ratio (short-lived / long-lived) of 0.80(7) through the 1259.1-keV transition. The transformed decay-curve fit results are consistent with that of the traditional decay curve fit validating the technique for use with the present data.

This method can be extended to fit the time-difference distribution from the projection of each energy bin of the two-dimensional transformed time-difference (decay - implant) vs. coincident γ -ray energy spectrum. In Fig. 4.34, the natural logarithm of the time difference between β decay and ^{70}Co ion implantation is shown on the y axis histogrammed vs. coincident β -delayed γ -ray energy from 0 to 1500 keV on the x axis. The z axis represents counts per unit time difference per keV.

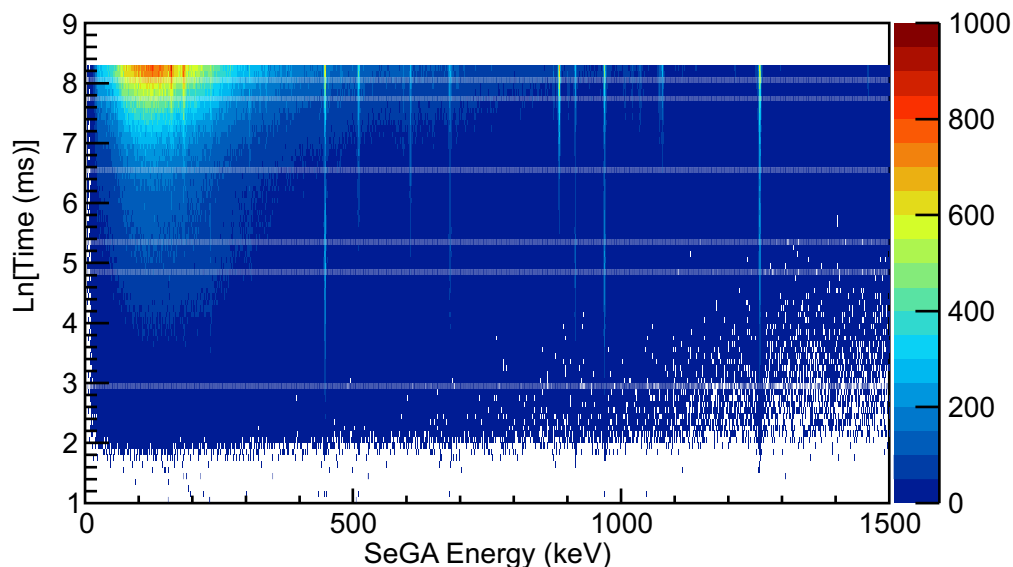


Figure 4.34: Natural logarithm of the time difference between β decay and ^{70}Co ion implantation, shown on the y axis, is histogrammed vs. coincident β -delayed γ -ray energy from 0 to 1500 keV on the x axis. The z axis is counts per unit time difference per keV.

A decay curve fit like that shown in Fig. 4.33 was performed on the projection each energy bin of Fig. 4.34 onto the logarithmic time axis. The fit was composed of transformed, short- and long-lived isomer components along with a spurious correlation component. The integrated number of counts under each fit at each energy bin is the contribution from each

component at that coincident γ -ray energy. The number of counts in each component at each energy bin were adjusted for spurious correlations using the spurious correlation correction factor of 2.06(2) presented in 4.8.

In Fig. 4.35 the results of the bin-wise decay-curve fitting described above are shown, where the short- and long-lived isomer contributions are shown as green and magenta, respectively, while the spurious correlation component is shown in blue. The sum of all components is shown in red and the total projection of the two-dimensional spectrum onto the energy axis is shown in black. The good agreement between the red and black spectra indicates no counts are lost in the deconvolution process.

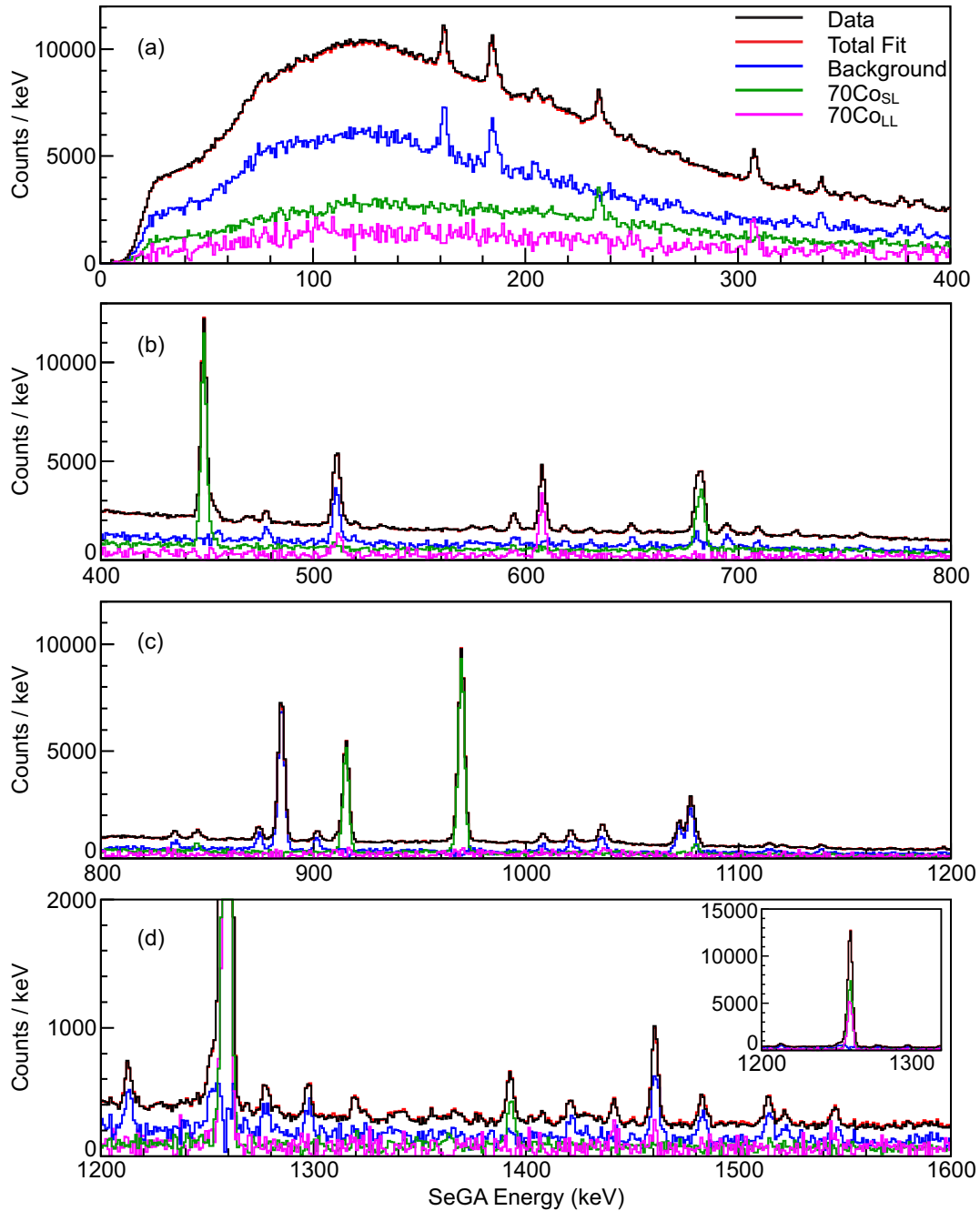


Figure 4.35: Results of fitting the projections of each energy bin onto the time axis of the two-dimensional histogram of the natural logarithm of the time difference between β decay and ^{70}Co ion implantation vs. coincident β -delayed γ -ray energy. The integral of each component is shown as a histogram. The short- and long-lived isomer contributions are shown as green and magenta, respectively, while the spurious correlation component is shown in blue. The sum of all components is shown in red and the total projection of the two-dimensional spectrum onto the energy axis is shown in black. The inset in (d) shows the full height of the 1259-keV transition cut off in (d). The inset in (e) shows the full height of the 2033-keV transition cut off in (f).

Figure 4.35: (cont'd)

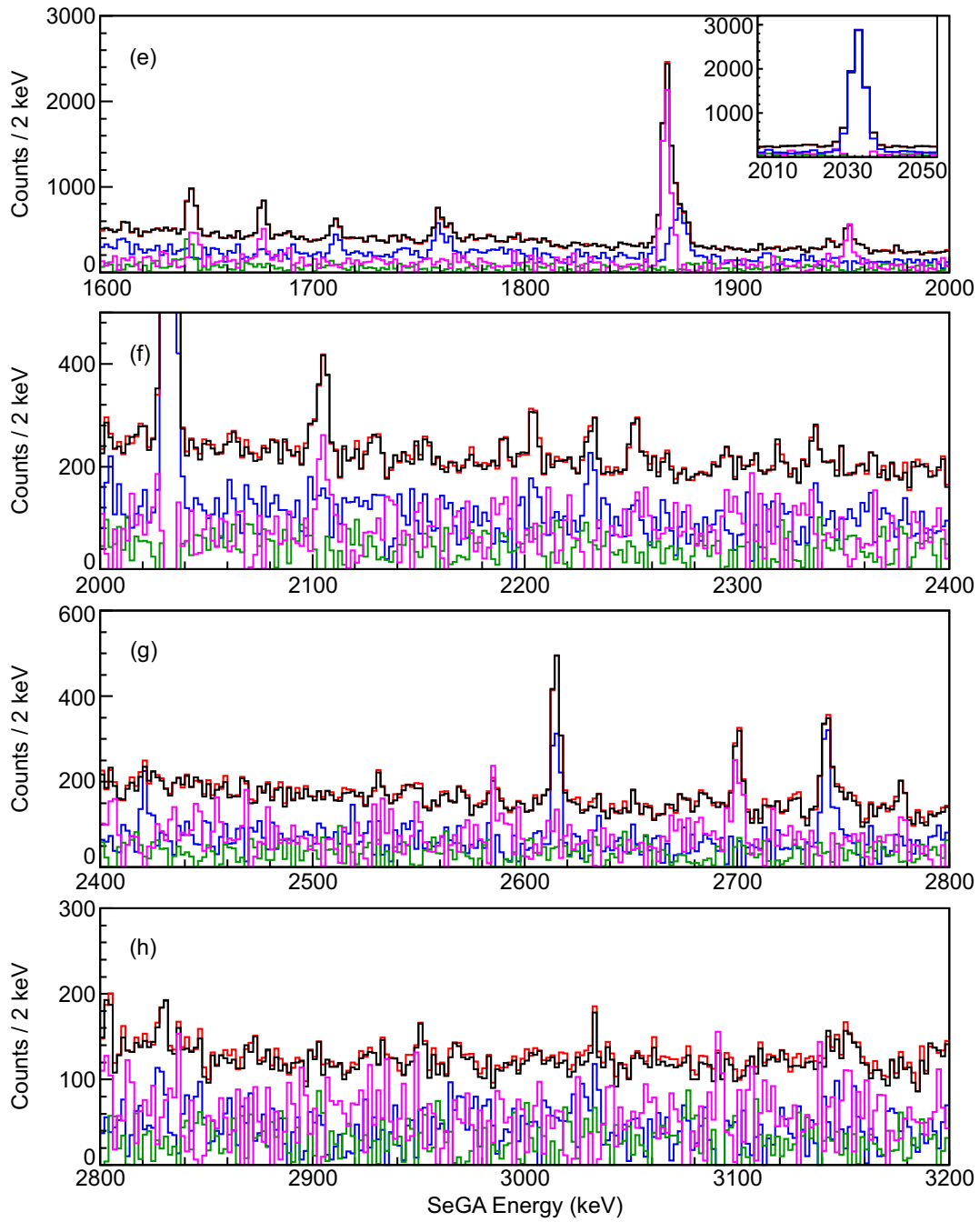
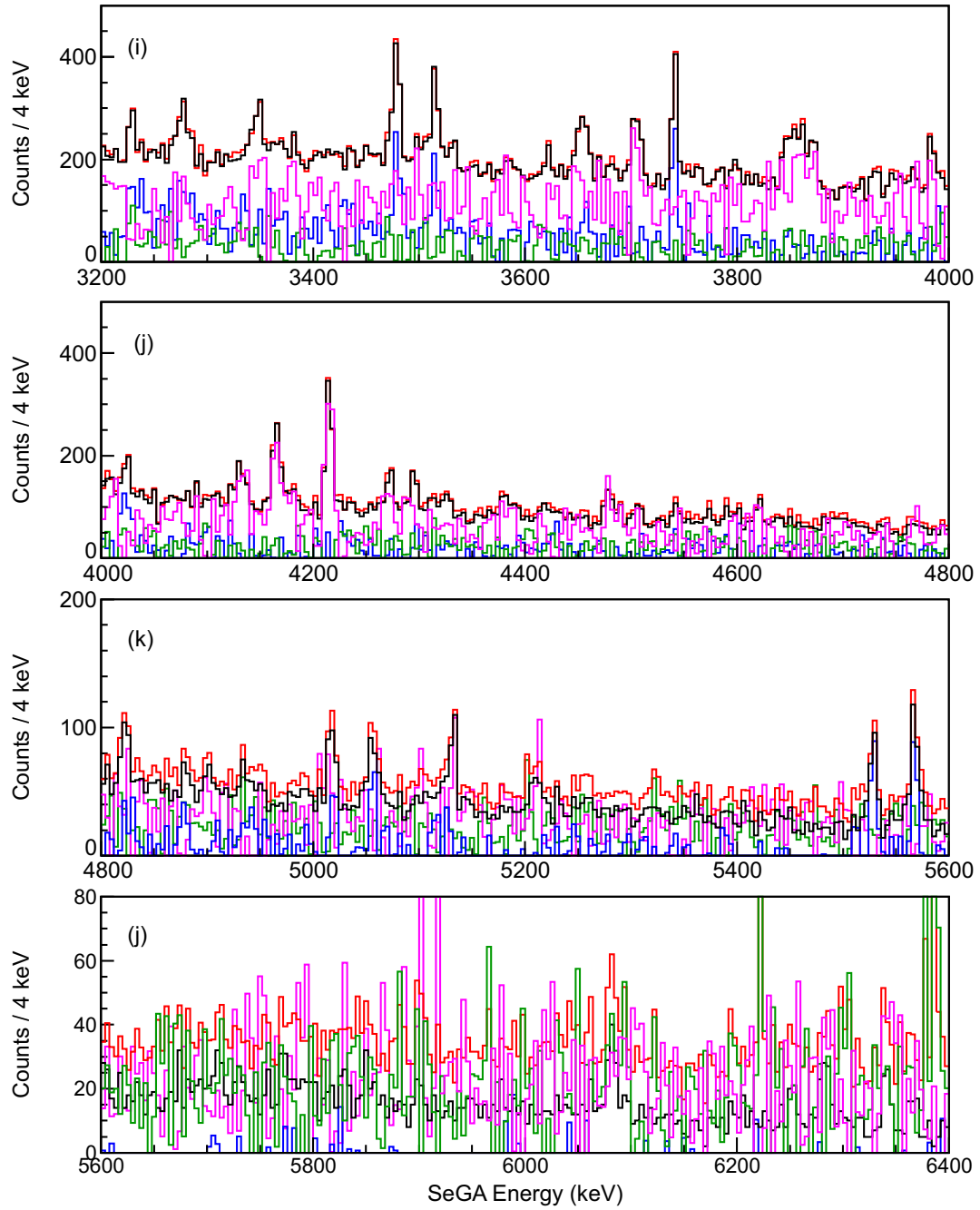


Figure 4.35: (cont'd)



4.2.4 Decay of the Short-Lived ^{70}Co Isomer

Much of the low-energy level scheme of ^{70}Ni populated by the decay of the short-lived, high-spin, ^{70}Co isomer is known. The three lowest-energy excited states of the yrast band in ^{70}Ni have measured energies of 1259 keV, 2229 keV, 2677 keV [61] with assigned spins and parities of 2^+ , 4^+ , and 6^+ , respectively [23]. These three states are connected via the 448-keV ($6_1^+ \rightarrow 4_1^+$), 970-keV ($4_1^+ \rightarrow 2_1^+$), and 1259-keV ($2_1^+ \rightarrow 0_1^+$) transitions. A fourth yrast band member, the (8^+) state at 2860 keV with a measured half-life of $0.21(5) \mu\text{s}$ [62], is also known but not populated in the present work.

The decay spectroscopy work of Ref. [12] identified a state at 3362 keV and assigned a tentative ($6^-, 7^-$) spin and parity based on comparisons with the decay of ^{68}Co . The 3362-keV state was observed to decay to the 2677-keV 6_1^+ state via a 683-keV γ ray [12]. A subsequent investigation [63] also observed the 683-keV γ -ray and confirmed the placement feeding the 2677-keV state. The work of Ref. [63] also identified a new 916-keV γ ray and assigned it to depopulate a new (5^-) state at 3146 keV.

Recent multinucleon transfer and secondary fragmentation studies [23] have identified the same 683- and 916-keV transitions in ^{70}Ni but disagree with the placement suggested by Refs. [12, 63]. This more recent work placed the 683.1-keV γ -ray feeding the 2229-keV 4_1^+ from a new state at 2912 keV with a (5^-) spin and parity and a new 234-keV transition is also observed to depopulate this 2912-keV (5^-) state feeding the 2677-keV 6_1^+ state [23]. A new state at 3758-keV, with a (7^-) spin and parity, was identified in Ref. [23] to depopulate by 1080-keV and 846-keV transitions feeding the 6_1^+ and (5^-) states, respectively. Furthermore, it was proposed that the 914.4-keV γ ray depopulates a new (6^-) state at 3592 keV feeding the 2677-keV 6_1^+ state [23].

In the present work all transitions previously observed have been identified, with the exception of the 183-keV ($8_1^+ \rightarrow 6_1^+$) transition. Three new transitions and two new levels in ^{70}Ni were found and placed to be fed exclusively by the short-lived, high-spin, ^{70}Co isomer. Table 4.9 presents a list of all γ -ray transitions observed following the decay of the short-lived, high-spin, ^{70}Co isomer, their absolute intensities, and the initial and final states between which each transition occurs. Absolute intensities were calculated by dividing the number of counts in each peak, obtained from a Gaussian fit plus a linear background component, corrected for γ -ray efficiency, by the number of short-lived, high-spin, ^{70}Co isomer decays, corrected for both spurious correlations and exclusion technique losses, listed in Table 4.8.

Table 4.9: Energies and absolute intensities of the γ -ray transitions identified in ^{70}Ni following the β decay of the short-lived, high-spin, ^{70}Co isomer. The energies of the initial and final states between which each transition occurs are also listed.

E_γ (keV)	$I_\gamma^{absolute}$ (%)	Initial State (keV)	Final State (keV)
234.7(1)	8.3(8)	2912	2677
448.4(1)	69.5(35)	2677	2229
680.3(3)	15.9(15)	3592	2912
683.3(3)	20.3(20)	2912	2229
845.4(2)	4.8(6)	3757	2912
915.3(1)	49.7(26)	3592	2677
969.6(1)	97.7(50)	2229	1259
1080.0(2)	5.5(4)	3757	2677
1259.1(1)	96.6(49)	1259	0
1392.9(1)	5.3(4)	4305	2912
1641.6(2)	3.1(4)	4319	2677

The placement of γ rays in the ^{70}Ni level scheme was accomplished using $\beta\gamma\gamma$ coincidences. Appendix C contains all $\beta\gamma\gamma$ coincidence spectra following the decay of the short-lived, high-spin, ^{70}Co isomer, and a summary of all observed coincidences is shown in Table 4.10

Using the absolute γ -ray intensities from Table 4.9, and the coincidence relationships

Table 4.10: Summary of γ -ray coincidences observed following the decay of the short-lived, high-spin, ^{70}Co isomer.

E_γ (keV)	Coincident E_γ (keV)
234.7	448.4, 680.3, 845.4, 969.6, 1259.1, 1392.9
448.4	234.7, 680.3, 845.4, 915.3, 969.6, 1080.0, 1259.1, 1641.6
680.3	234.7, 448.4, 683.3, 969.6, 1259.1
683.3	680.3, 845.4, 969.6, 1080.2, 1259.1, 1392.9
845.4	234.7, 448.4, 683.3, 969.6, 1259.1
915.3	448.4, 969.6, 1259.1
969.6	234.7, 448.4, 680.3, 683.3, 845.4, 915.3, 1080.0, 1259.1, 1392.9, 1641.6
1080.0	448.4, 969.6, 1259.1
1259.1	234.7, 448.4, 680.3, 683.3, 845.4, 915.3, 1080.0, 1259.1, 1392.9, 1641.6
1392.9	683.3, 969.6, 1259.1
1641.6	448.4, 969.6, 1259.1

described above, summarized in Table 4.10, the decay scheme for the short-lived, high-spin β -decaying ^{70}Co isomer was constructed, presented in Fig. 4.36. The β -decay Q value used for this analysis was 12.3(3) MeV, taken from Ref. [56]. It is currently unknown which ^{70}Co isomer is the ground state and the energy difference between the two isomers is also unknown. This results in some additional systematic uncertainty on the Q value and thus the $\log ft$ values.

The decay scheme presented in Fig. 4.36 is discussed in greater detail in the next chapter.

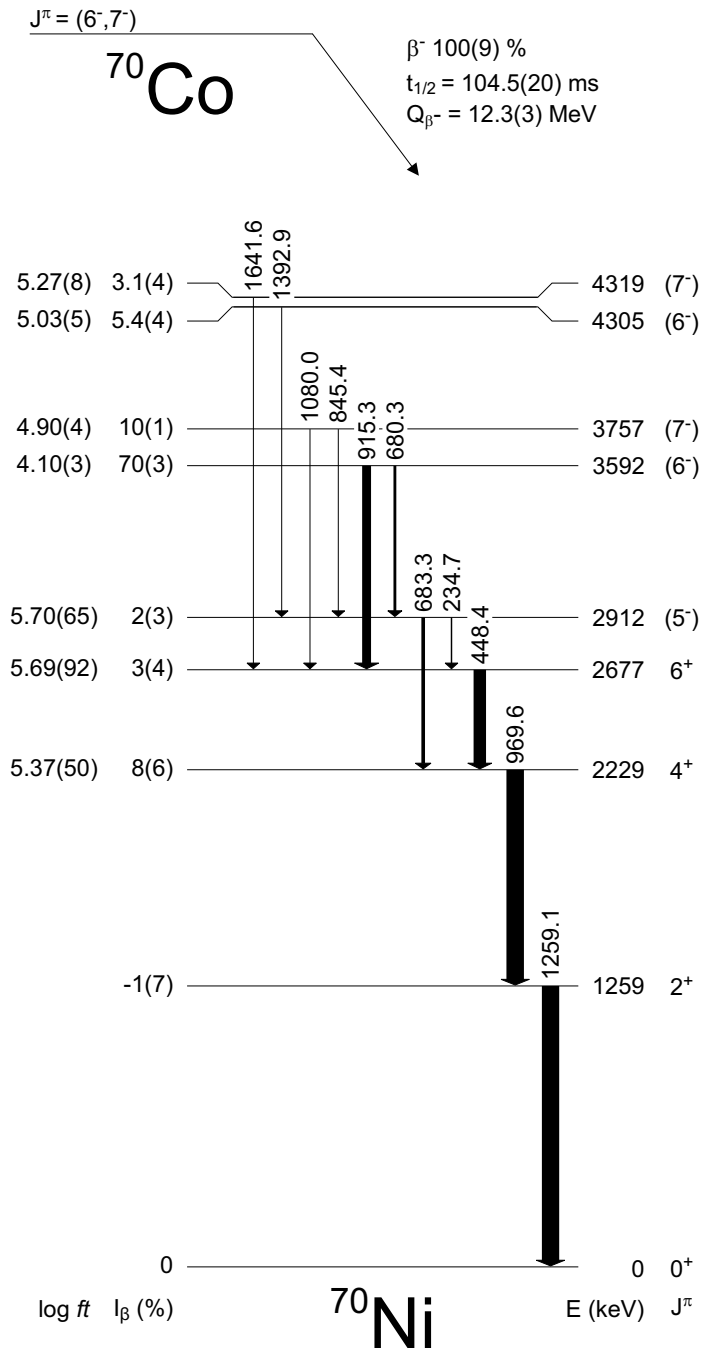


Figure 4.36: Decay scheme for the short-lived, high-spin, ^{70}Co isomer. States in ^{70}Ni are labeled with an energy in keV and the spin in parity (if known) on the right. On the left, β -decay branching ratios and $\log_{10} ft$ values are shown. Q value taken from Ref. [56].

4.2.5 Decay of the Long-Lived ^{70}Co Isomer

The first observation of the long-lived low spin isomer was made in Ref. [12]. This work added one new state in the ^{70}Ni level scheme at 1868 keV, assigned a spin and parity of 2^+ , and fed exclusively by the long-lived, low-spin, ^{70}Co isomer. A 607-keV ($2_2^+ \rightarrow 2_1^+$) transition and a 1868-keV ($2_2^+ \rightarrow 0_1^+$) transition were observed to depopulate the 1868-keV 2_2^+ state [12].

Subsequent studies confirmed the 1868-keV 2_2^+ state and the depopulating transitions from Ref. [12] and also located a tentative (4_2^+) state which decays by a 640-keV γ ray to the 1868-keV 2_2^+ state [23]. The (4_2^+) state is not observed in the current work, most likely due to β -decay selection rules. Additionally, Ref. [23] reported a new 1950-keV transition coincident exclusively with the 1259.1-keV ($2_1^+ \rightarrow 0_1^+$) transition. As such, the transition was placed depopulating a new level at 3209 keV.

The remainder of this section presents the full analysis of the decay of the long-lived, low-spin, ^{70}Co isomer. A list of all γ -ray transitions observed following the decay of the long-lived, low-spin, ^{70}Co isomer are presented in Table 4.11 along with their absolute intensities, and the initial and final states between which each transition occurs. Absolute intensities were calculated by dividing the number of counts in each peak, obtained from a Gaussian fit plus a linear background component, corrected for γ -ray efficiency, by the number of long-lived, low-spin, ^{70}Co isomer decays, corrected for both spurious correlations and exclusion technique losses, listed in Table 4.8.

Table 4.11: Energies and absolute intensities of the γ -ray transitions identified in ^{70}Ni following the β decay of the long-lived, low-spin, ^{70}Co isomer. The energies of the initial and final states between which each transition occurs are also listed.

E_γ (keV)	$I_\gamma^{absolute}$ (%)	Initial State (keV)	Final State (keV)
307.6(1)	7.1(5)	1567	1259
594.1(1) ^a	2.7(2)	-	-
607.7(1)	23.4(13)	1867	1259
1037.5(3)	2.8(3)	2296	1259
1259.1(1)	65.1(33)	1259	0
1441.2(1)	2.0(3)	2700	1259
1644.5(1)	3.0(3)	3511	1867
1676.3(1)	3.4(3)	2935	1259
1866.5(1)	18.5(10)	1867	0
1943.8(2)	1.1(1)	3511	1567
1952.3(2)	3.0(2)	3211	1259
1957.8(3) ^a	1.04(5)	-	-
2104.8(1)	2.8(4)	3364	1259
2252.0(3)	1.2(2)	3511	1259
2294.3(7)	0.6(3)	2296	0
2531.0(5)	0.6(2)	3790	1259
2614.6(1)	2.0(5)	3874	1259
2700.3(3)	2.1(3)	2700	0
2777.4(3) ^b	0.7(2)	5712	2935
2803.4(3) ^b	1.3(3)	5738	2935
2950.7(5) ^b	0.4(2)	6162	3211

^a Transition belongs to ^{69}Ni following β -delayed neutron emission

^b Transition placed in ^{70}Ni without coincidences using only energy differences

^c Transition only observed in coincidences

Table 4.11: (cont'd)

E_γ (keV)	$I_\gamma^{absolute}$ (%)	Initial State (keV)	Final State (keV)
3348.5(4) ^b	1.2(3)	6283	2935
3845.6(5)	1.3(2)	5712	1867
3853.4(5)	1.4(2)	5112	1259
3861.5(5)	1.7(2)	5728	1867
3871.7(5) ^b	1.5(2)	5738	1867
3984.0(5)	1.2(3)	5850	1867
4004.3(4) ^c	2.0(7)	5263	1259
4132.4(5)	1.5(2)	5999	1867
4165.3(3)	2.6(2)	6032	1867
4215.3(2)	4.2(4)	6082	1867
4272.5(5)	1.5(2)	6139	1867
4294.9(5) ^b	1.3(2)	6161	1867
4379.9(8)	0.8(2)	6246	1867
4479.3(5)	1.2(2)	5738	1259
4773.0(20) ^b	0.4(2)	6032	1259
4822.5(4)	1.0(2)	6082	1259
4880.5(8)	0.6(1)	6140	1259
4901.2(10)	0.6(1)	6161	1259
5711.4(10)	0.7(1)	5712	0
6081.9(5)	0.9(1)	6082	0
6283.7(7)	0.7(1)	6283	0
6339.9(8)	0.4(1)	6340	0

^a Transition belongs to ⁶⁹Ni following β -delayed neutron emission

^b Transition placed in ⁷⁰Ni without coincidences using only energy differences

^c Transition only observed in coincidences

In Table 4.11, two γ rays with energies of 594.1 keV and 1957.8 keV are listed, which belong to ^{69}Ni and are likely populated via β -delayed neutron emission. Any β -delayed neutron emission proceeding directly to the ground state would not be observed in the present work, so the sum of the absolute intensity of these two transitions provides a lower limit of 3.5 % on the magnitude of the β -delayed neutron emission branch.

The background-subtracted γ -ray spectrum coincident with the 1259.1-keV ($2_1^+ \rightarrow 0_1^+$) transition within 4000 ms of the decay of ^{70}Co is shown in Figure 4.37. In Fig. 4.38 the background-subtracted γ -ray spectra coincident with the 607.6-keV ($2_2^+ \rightarrow 2_1^+$) [panels (a) and (b)] and 1866.5-keV ($2_2^+ \rightarrow 0_1^+$) [panels (c) and (d)] transitions within 4000 ms of the decay of ^{70}Co are presented. The background was taken symmetrically on both sides of each peak. Coincidences affiliated with the long-lived, low-spin, ^{70}Co isomer are labeled with an energy while coincidences affiliated with the short-lived, high-spin, ^{70}Co isomer are denoted with black squares. Contaminating coincidences are denoted with black upside-down triangles and labeled with the offending isotope, if known.

The strong 1259.1-607.6-keV coincidence observed in Fig. 4.37a as well as in Fig. 4.38a is consistent with the previous work. Furthermore, a strong 1866.5-keV transition is observed, which is not in coincidence with the 1259.1-keV ($2_1^+ \rightarrow 0_1^+$) transition, and is, along with the 607.6-keV transition, coincident with strong transitions that are proposed to feed the 2_2^+ state. The existence and placement of the 607.6-keV and 1866.5-keV γ rays is consistent with previous work of Refs. [12, 23].

The observation of the 307.6-keV transition is new from this work. A strong 307.6-1259.1-keV coincidence is shown in Fig. 4.37. No coincidences were observed higher in the level scheme in Figs. 4.38a or 4.38c. Furthermore, no coincidences were observed in Figs. C.1b through C.1j between the 307.6-keV γ ray and transitions affiliated with the short-lived, low-

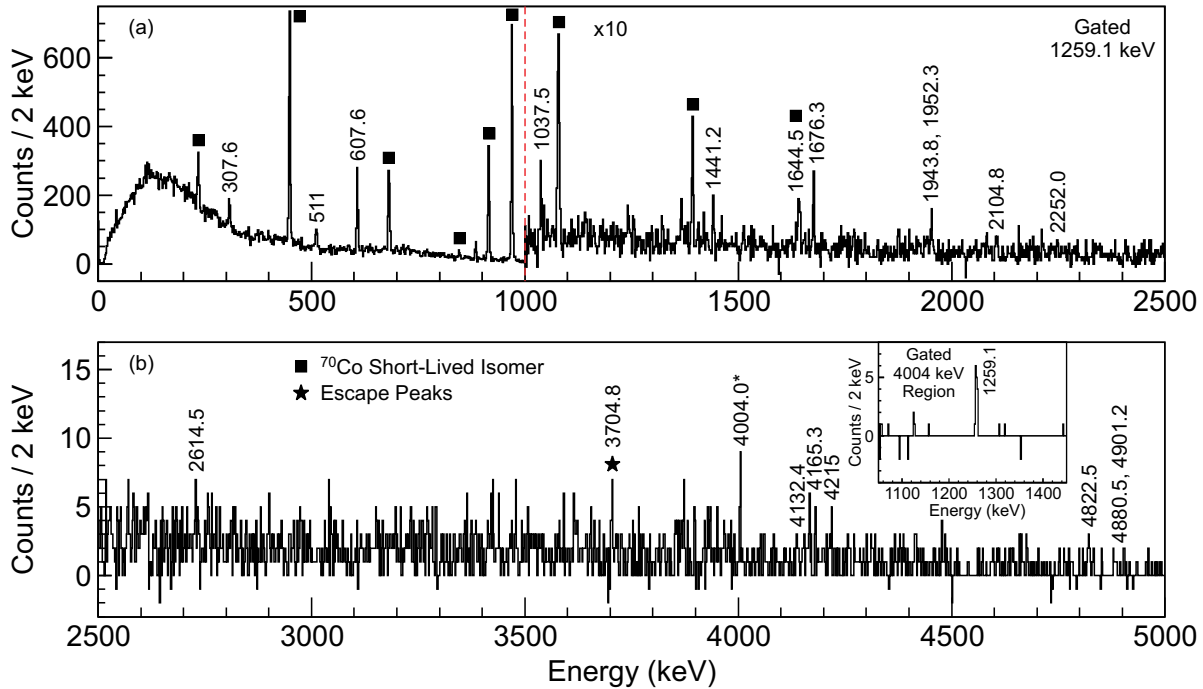


Figure 4.37: Background subtracted $\beta\gamma\gamma$ coincidence spectrum gated on the 1259.1-keV ($2_1^+ \rightarrow 0_1^+$) transition within 4000 ms of the decay of ^{70}Co from (a) 0 to 2500 keV and (b) from 2500 to 5000 keV. The background was taken symmetrically either side of the 1259.1-keV peak. Coincidences affiliated with the long-lived, low-spin, ^{70}Co isomer are labeled with an energy while coincidences affiliated with the short-lived, high-spin, ^{70}Co isomer are denoted with black squares. Escape peaks are denoted with black stars and transitions seen in coincidences but not in singles are denoted with a single asterisk.

spin, ^{70}Co isomer. The only other coincidence observed with the 307.6-keV transition is a 1943.8-keV transition. The $\beta\gamma\gamma$ coincidence spectra affiliated with the 307.6- and 1943.8-keV transitions are shown in Figs. 4.39a and 4.39b, respectively.

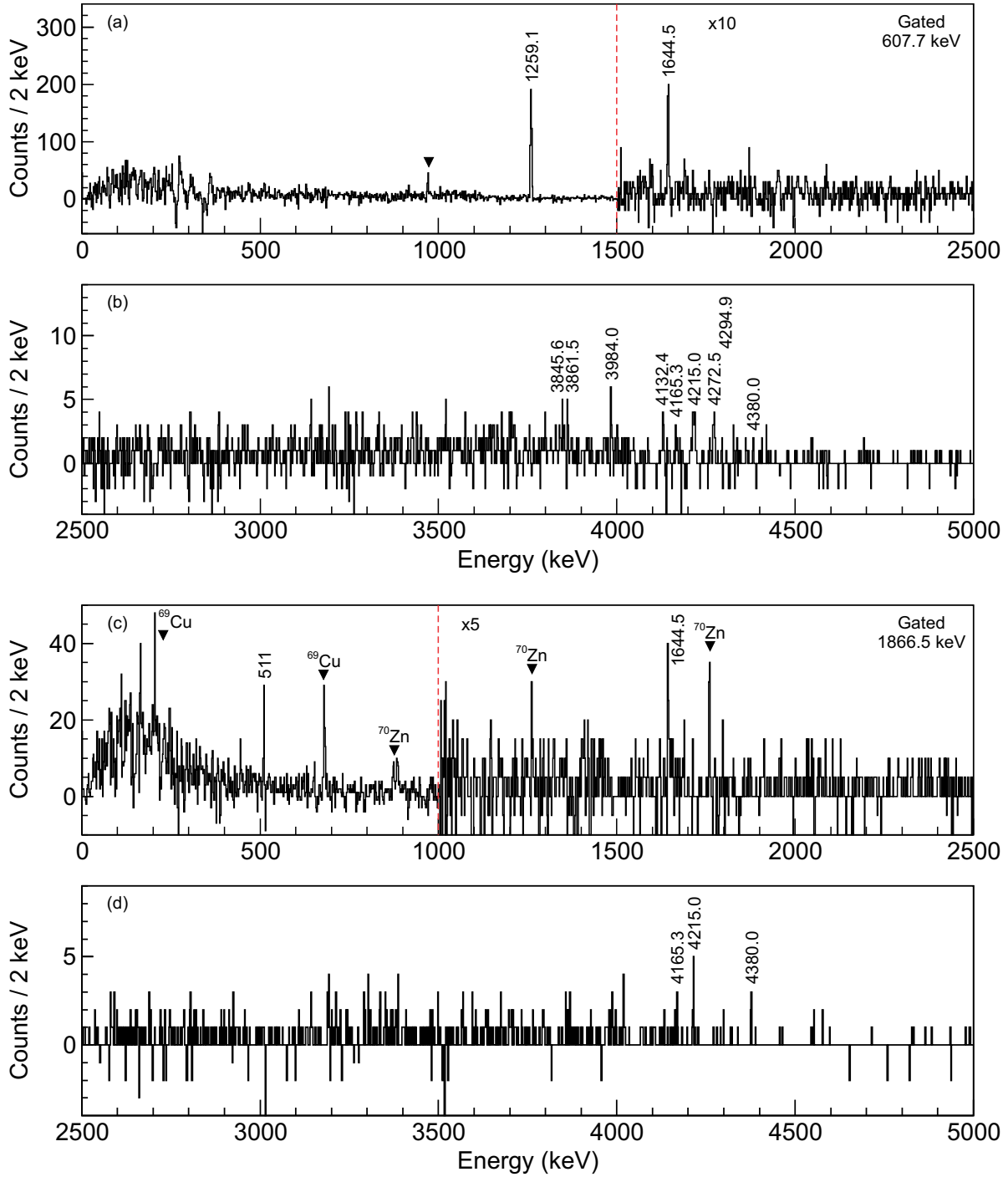


Figure 4.38: Background subtracted $\beta\gamma\gamma$ coincidence spectrum gated on the 607.6-keV ($2_2^+ \rightarrow 2_1^+$) [panels (a) and (b)] and 1866.5-keV ($2_2^+ \rightarrow 0_1^+$) [panels (c) and (d)] transitions within 4000 ms of the decay of ^{70}Co . The background was taken symmetrically either side of each peak. Coincidences affiliated with the long-lived, low-spin, ^{70}Co isomer are labeled with an energy while coincidences affiliated with the short-lived, high-spin, ^{70}Co isomer are denoted with black squares. Contaminating coincidences are denoted with black upside-down triangles and labeled with the offending isotope, if known.

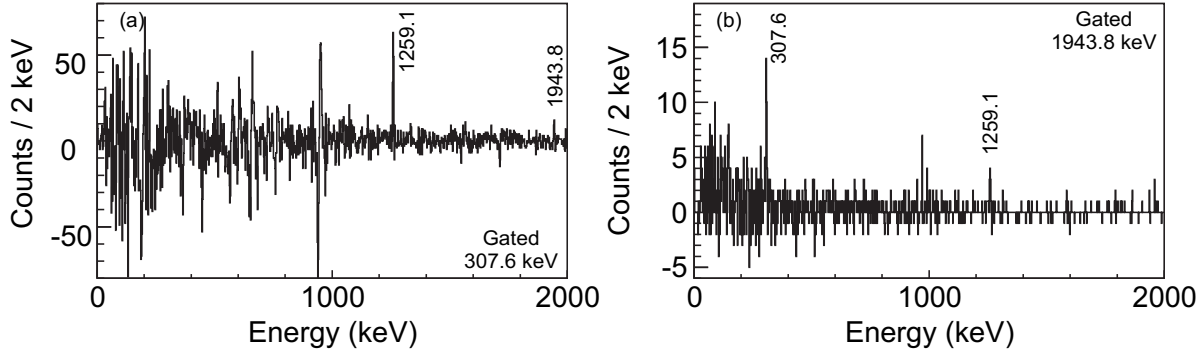


Figure 4.39: Background subtracted $\beta\gamma\gamma$ coincidence spectrum gated on the (a) 307.6-keV and (b) 1943.8-keV transitions within 4000 ms of the decay of ^{70}Co . The background was taken symmetrically either side of the 307.6-keV peak and below the 1943.8-keV peak due to closely neighboring transitions. Coincidences affiliated with the long-lived, low-spin, ^{70}Co isomer are labeled with an energy.

Based on the coincidence relationships and the ratio of γ -ray intensities, it was determined that the 1943.8-keV transition is above the 307.6-keV transition in the 1943.8-307.6-1259.1-keV γ -ray cascade, placing a new level at 1567 keV as well as a new level at 3511-keV. A search for a ground state transition out of the new 1567-keV state was unsuccessful. In Figs. 4.40a and 4.40b the region around 1567-keV in the 1943.8-keV gated $\beta\gamma\gamma$ and β -gated γ -ray singles spectra, respectively, is shown.

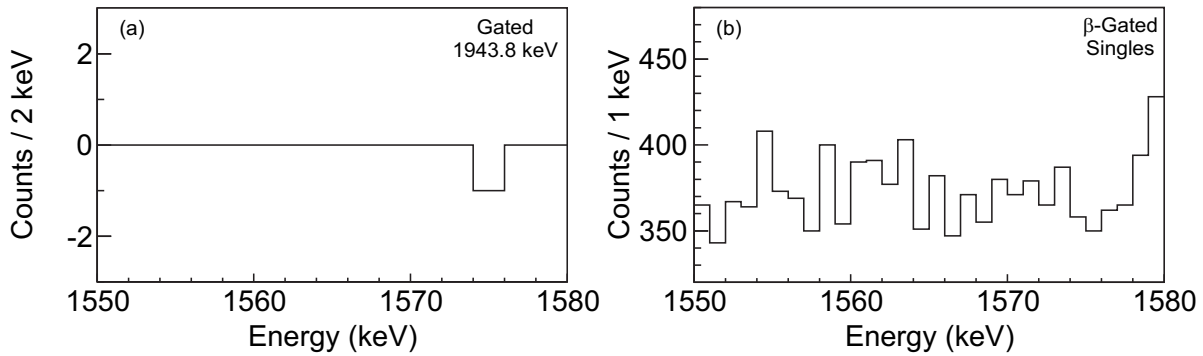


Figure 4.40: (a) Background subtracted $\beta\gamma\gamma$ coincidence spectrum gated on the 1943.8-keV transition within 4000 ms of the decay of ^{70}Co . (b) Beta-gated γ -ray singles spectrum within 4000 ms of the decay of ^{70}Co . Both spectra highlight the region around 1567 keV and no 1567-keV peak is observed in either spectrum.

Based on the lack of a ground state transition, exclusive affiliation with the decay of

the long-lived, low-spin ^{70}Co isomer, and non-observation in multinucleon transfer reactions populating yrast states [23] a tentative spin and parity of (0_2^+) is assigned to the 1567-keV state. Additional support for this assignment was provided by the good agreement between the MCSM calculations, discussed further in the next chapter, and the data.

An attempt was made to look for the $E0$ transition connecting the (0_2^+) and 0_1^+ states, but nothing was observed in the planar GeDSSD. However, the short half-life of the (0_2^+) (results presented later in this section) means that a double-pulse analysis in the GeDSSD would not be sensitive to it.

Based on the γ -ray statistics obtained here and using the BrIcc internal conversion coefficient database [34] a limit was placed on the expected $E0$ intensity. A 1567-keV $E0$ transition in ^{70}Ni would decay by 40.4 % pair production, with the rest being internal conversion. By examining the 511-keV region of the $\beta\gamma\gamma$ spectrum shown in Fig. 4.39b, a minimum of ~ 5 counts would be required to see a peak at 511 keV. Correcting for the efficiency of such a 511-keV transition, 108 γ rays of this energy would be expected to be emitted in coincidence with the 1943.8-keV feeding transition. Dividing this result by two, to account for the fact that two 511-keV γ rays are emitted per pair-production event, and considering the 40.4 % pair-production branch, approximately 133 $E0$ transitions would follow the 1943.8-keV transition. In Fig. 4.39b, there are 26(8) counts in the 1943.8-307.6-keV coincidence. When corrected for the efficiency of the detector array for a 307.6-keV γ ray, one would expect 400(150) 307-keV γ rays coincident with the 1943.8-keV transition. The ratio of the upper limit of $E0$ transitions to the total, $E0$ transitions plus 307.6-keV γ rays, gives an upper limit on the $E0$ branch of 33 % out of the 1567-keV state.

In addition to the 307.6-keV transition, several other new γ rays have been observed. The $\beta\gamma\gamma$ coincidence spectra used to place these transitions are presented in Appendix D.

A sum of all observed coincidences is shown in Table 4.12

Table 4.12: Summary of γ -ray coincidences observed following the decay of the long-lived, low-spin, ^{70}Co isomer.

E_γ (keV)	Coincident E_γ (keV)
307.6(1)	1259.1, 1943.8
607.7(1)	1259.1, 3845.6, 3861.5, 3984.0, 4132.4, 4165.3, 4215.0, 4272.5, 4294.9, 4380.0
1037.5(3)	1259.1
1259.1(1)	307.6, 607.6, 1037.5, 1441.2, 1644.5, 1676.3, 1943.8, 1952.3, 2104.8, 2252.0, 2614.5, 4132.4, 4004.0 ^c , 4132.4, 4165.3, 4215.0, 4822.5, 4880.5, 4901.2
1441.2(1)	1259.1
1644.5(1)	607.6, 1259.1, 1866.5
1676.3(1)	1259.1
1866.5(1)	1644.5, 4165.3, 4215.0, 4380.0
1943.8(2)	307.6, 1943.8
1952.3(2)	1259.1
2104.8(1)	1259.1
2252.0(3)	1259.1
2531.0(5)	1259.1
2614.6(1)	1259.1
3845.6(5)	607.6
3853.4(5)	1259.1
3861.5(5)	607.6, 1259.1, 1626 ^c , 1866.5
3984.0(5)	607.6, 1259.1, 1866.5
4004.3(4) ^c	1259.1
4132.4(5)	607.6, 1259.1, 1866.5
4165.3(3)	607.6, 1259.1, 1866.5
4215.3(2)	607.6, 1259.1, 1866.5
4272.5(5)	607.6
4379.9(8)	607.6, 1259.1, 1866.5
4479.3(5)	771.9 ^c , 1259.1
4822.5(4)	1259.1
4880.5(8)	1259.1
4901.2(10)	1259.1

^c Transition only observed in coincidences

Using the absolute γ -ray intensities from Table 4.11 and the coincidence relationships described above, summarized in Table 4.12, the decay scheme for the long-lived, low-spin, ^{70}Co isomer was constructed, and is presented in Fig. 4.36. The β -decay Q value used for this analysis was 12.3(3) MeV. taken from Ref. [56]. As stated in the short-lived isomer

analysis, it is not known which β -decaying ^{70}Co isomer is the ground state. In addition, the energy difference between the two β -decaying isomers is also unknown. As such, some additional uncertainty on the Q-value and thus the $\log ft$ values exists. The decay scheme for the long-lived, low-spin, ^{70}Co isomer is presented in Fig. 4.41.

In addition to the γ rays placed in the level scheme shown in Fig. 4.41, there were some unplaced γ rays potentially affiliated with the long-lived, low-spin, ^{70}Co isomer. The energy and absolute intensities of these unplaced transitions are listed in Table 4.13.

Table 4.13: Summary of unplaced γ rays potentially affiliated with the decay of the long-lived, low-spin, ^{70}Co isomer.

E_γ (keV)	$I_\gamma^{absolute}$ (%)
771.9(1) ^c	0.6(4)
1026.2(1) ^c	1.1(7)
2585.4(4)	0.9(2)
5131.0(4)	1.3(2)
5210.1(10)	0.7(2)

^c Transition observed exclusively in coincidences and is not conclusively affiliated with the long-lived, low-spin, ^{70}Co isomer decay

4.2.6 Half-Life of the (0_2^+) state in ^{70}Ni

A measurement of the half-life of the 1567-keV (0_2^+) state was performed using the $\beta\gamma\gamma$ timing method presented in Section 3.9. The 307.6-keV γ ray was detected in the LaBr₃ detectors, described in Section 3.8, coincident with the β -decay electron detected in the PSPMT, detailed in Section 3.6.

The β -gated ^{70}Co correlated (2000 ms correlation time) LaBr₃ energy spectrum in the region of the 307.6-keV transition is shown in Fig. 4.42a. Unfortunately, due to the small number of ^{70}Co ions delivered to the experimental end station during e14057, compared to e14039, and the relatively poor energy resolution of the LaBr₃ detectors, compared to

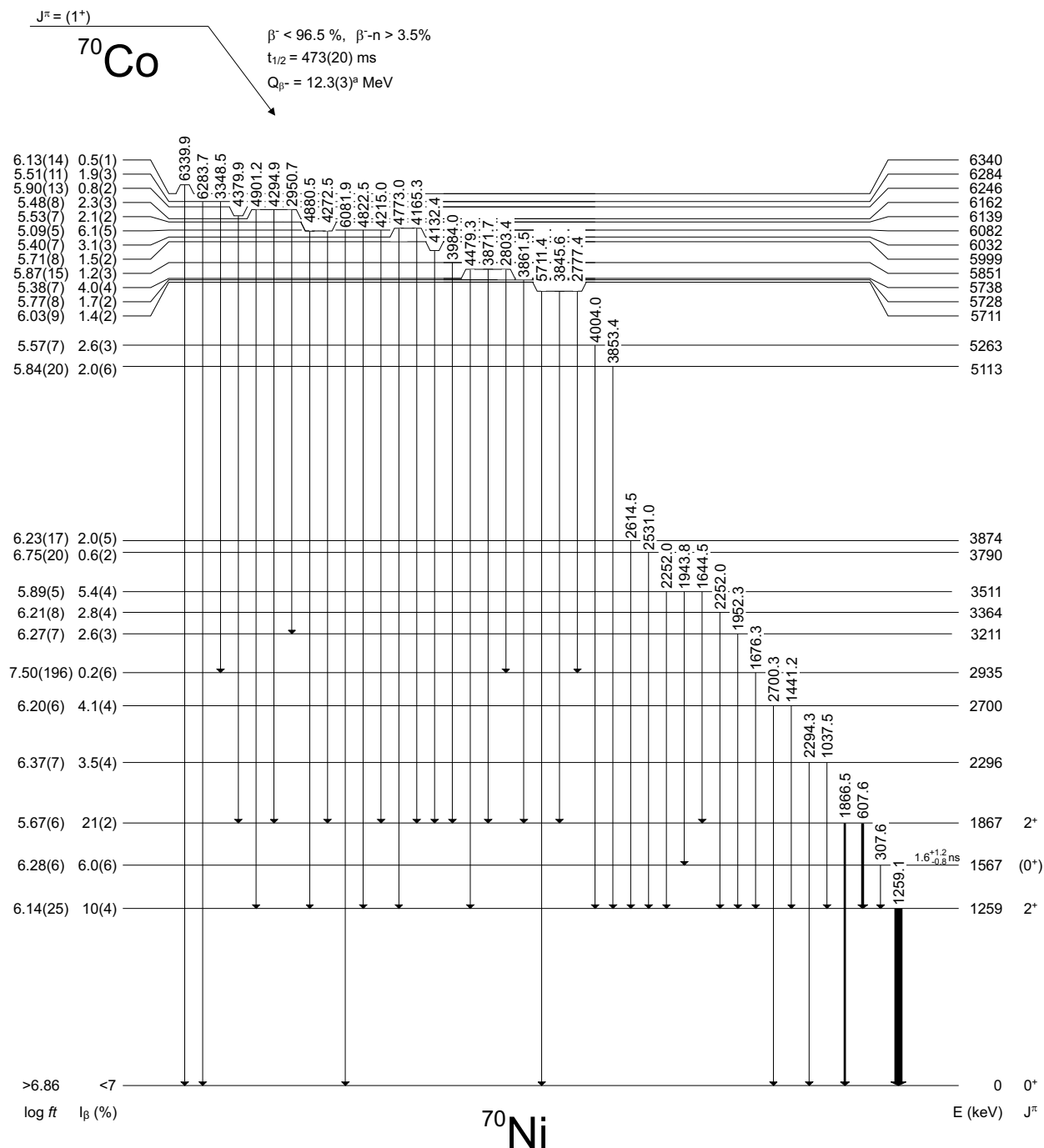


Figure 4.41: Decay scheme for the long-lived, low-spin, ^{70}Co isomer. States in ^{70}Ni are labeled with an energy in keV and the spin in parity (if known) on the right. On the left, β -decay branching ratios and $\log_{10} ft$ values are shown. ^a Q -value taken from Ref. [56].

SeGA, the 307.6-keV peak is not apparent in Fig. 4.42a. However, the 307.6-keV transition is clearly observed in the β -gated ^{70}Co correlated SeGA spectrum shown in Fig. 4.42b.

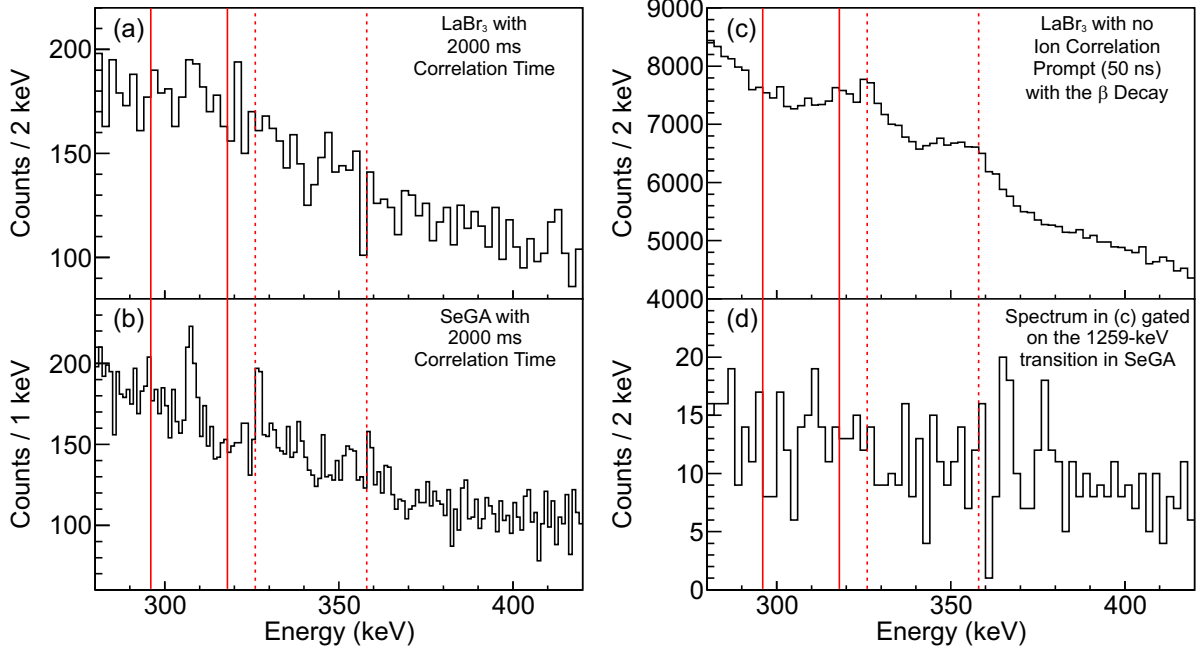


Figure 4.42: (a) and (b) Spectrum of γ -rays recorded in the LaBr₃ and SeGA detectors, respectively, coincident with a ^{70}Co decay event in the segmented plastic scintillator. (c) Spectrum of γ -rays recorded in the LaBr₃ coincident with a decay event in the segmented plastic scintillator. (d) Spectrum shown in panel (c) gated on the 1259.1-keV transition in SeGA. In panels (c) and (d) the coincidence window between the LaBr₃ detectors and PSPMT was 50 ns and in (d) the LaBr₃-SeGA coincidence window was 600 ns. In all panels the set of solid red and dashed red bars represent the energy windows used for the peak and background regions of interest, respectively.

An attempt was made to forgo ion correlations and examine the β -gated LaBr₃ energy spectrum. Since the PSPMT and LaBr₃ detectors have good time resolution, the coincidence window was shortened from 10 μs to 50 ns to eliminate random coincidences. The β -gated LaBr₃ energy spectrum in the region of the 307.6-keV transition is shown in Fig. 4.42c. The number of implanted ^{70}Co ions was a relatively small component of the total implanted ions and there is no evidence of the 307.6-keV peak in Fig. 4.42c. The 307.6-keV transition is known to feed the 1259-keV 2_1^+ state which decays by a 1259.1-keV γ -ray. A gate on the 1259.1-keV γ -ray recorded in SeGA was placed on the spectrum shown in Fig. 4.42c and the resulting spectrum is presented in Fig. 4.42d. The LaBr₃-SeGA coincidence window was 600 ns. With the present statistics, and the detection efficiencies of the 307.6-keV transition

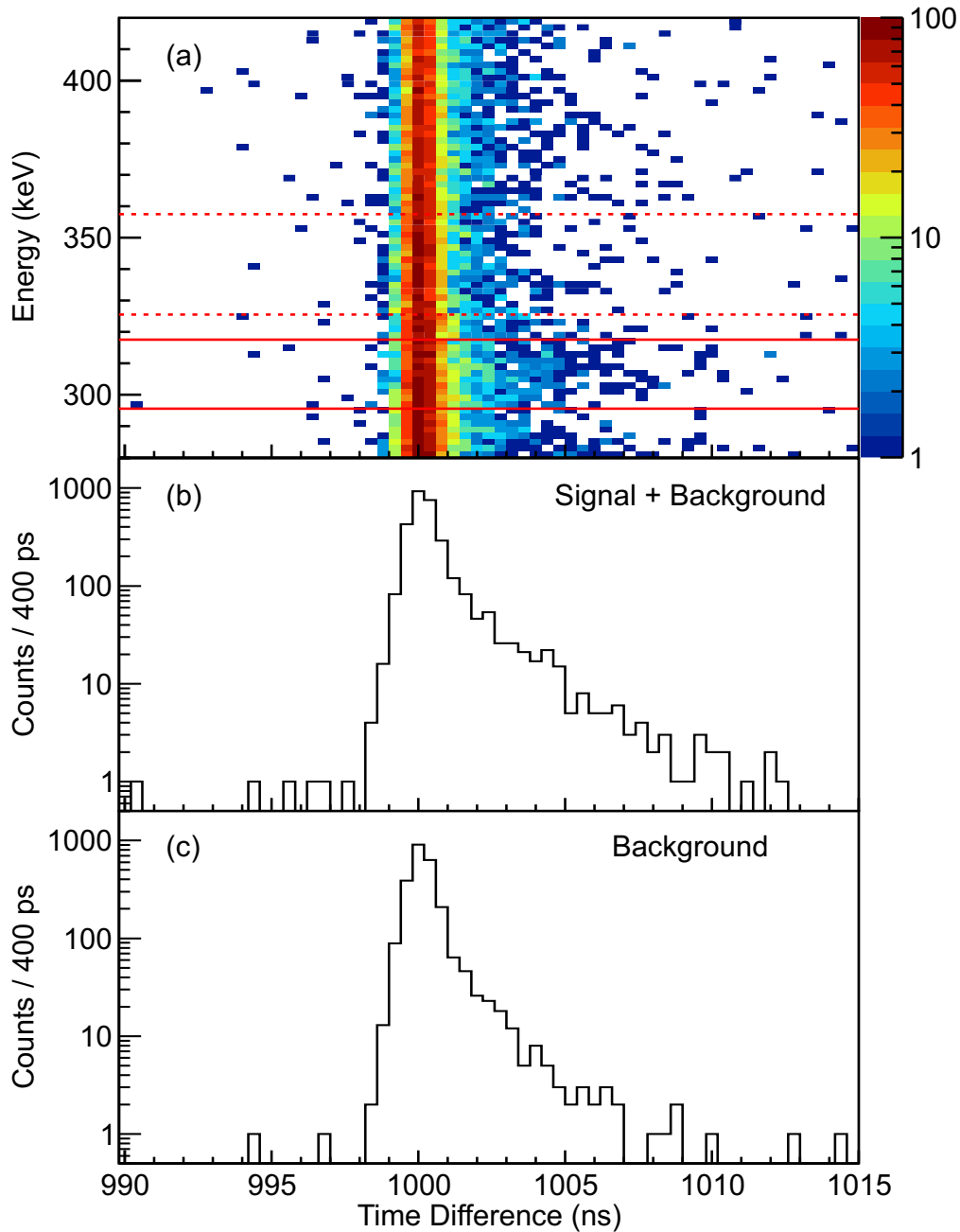


Figure 4.43: (a) Two-dimensional spectrum of γ -rays recorded in the LaBr_3 detectors coincident with a decay event in the segmented plastic scintillator vs. time difference between the LaBr_3 and segmented plastic scintillator. The solid red and dashed red bars denote the energy windows used for the peak and background regions of interest (ROI), respectively. (b) and (c) Time-difference spectra (LaBr_3 - segmented plastic scintillator) obtained by projecting the spectrum in (a) onto the time-difference axis over the regions between the solid (peak ROI) and dashed (background ROI) red lines, respectively.

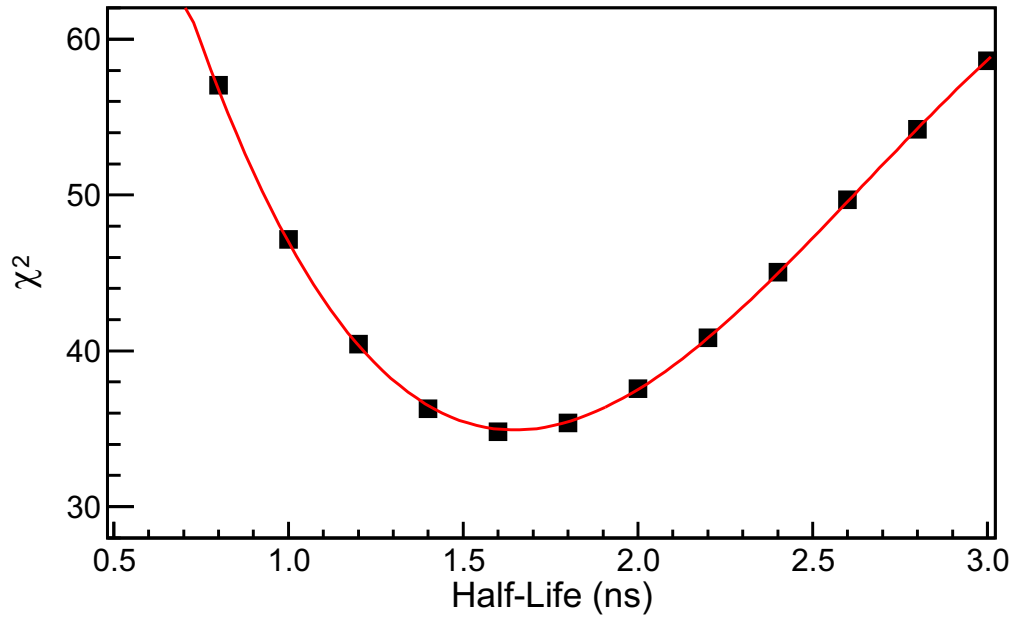


Figure 4.44: χ^2 as a function of trial half-life used in each convolution fit, shown as black squares, and quadratic fit, shown in red, for interpolation between points.

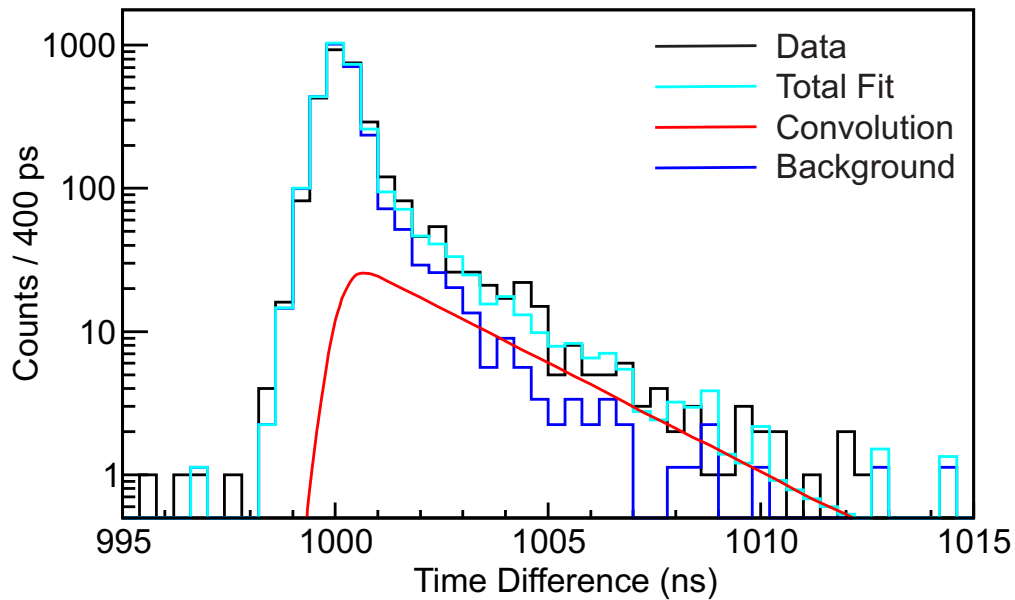


Figure 4.45: Best fit results for the lifetime of the (0_2^+) state in ^{70}Ni . In black and blue are the time-difference spectra for the peak and background ROIs shown in Figs. 4.43b and 4.43c, respectively. The convolution of the detector response with the best-fit half-life is shown in Red and the total fit of background plus convolution is shown in cyan.

in the LaBr_3 detectors and the 1259.1-keV transition in SeGA, 35(7) counts are expected in the 307.6-keV peak in Fig. 4.42d. Based on the LaBr_3 resolution and the binning of Fig.

4.42d, a 307.6-keV peak would be ≈ 4 counts in height, which is smaller than the variation in the background. This level of statistics precludes the use of $\beta\gamma\gamma$ timing techniques.

Since no strong peak was observed in the LaBr₃ spectrum in Fig. 4.42a the number of counts expected in the peak ROI was deduced from the simulated γ -ray detection efficiencies of SeGA, shown in Fig. 3.40, and the measured ratio of efficiencies (LaBr₃/SeGA) presented in Fig. 3.44. The peak ROI is denoted with solid-red vertical lines in Figs. 4.42a and 4.43a and covers the region of 296 to 318 keV. The background ROI, denoted with dashed-red vertical lines in Figs. 4.42a and 4.43a, was taken directly above the peak ROI from 326 to 358 keV and the corresponding background spectra were scaled appropriately in the fit. The two small peaks observed in Fig. 4.42b at 327.0 keV from ⁶⁸Co and 339.6 keV from ⁷⁰Cu contaminate the background ROI but have no measurable half-lives and thus did not affect the analysis.

The time-difference spectra between γ -rays, detected in the LaBr₃ detectors, and coincident β decays, detected in the segmented plastic scintillator, was extracted by projecting the two-dimensional LaBr₃ energy vs. time-difference spectrum, shown in Fig. 4.43a, onto the time-difference axis for each of the two regions. An artificial offset of 1000 ns was added to the time-difference to avoid negative time differences. The time-difference spectra (LaBr₃ - segmented plastic scintillator) obtained from projecting the spectrum in (a) onto the time-difference axis over the regions between the solid (peak ROI) and dashed (background ROI) red lines are shown in Figs. 4.43b and 4.43c, respectively.

Based on the total counts expected in the peak and the total counts recorded in the background ROI the background spectrum was scaled to contain the proper number of counts. Then, using the techniques described in Section 3.8, a series of trial lifetimes were convolved with the measured detector response and the χ -square minimization procedure

was used to extract the half-life and associated error for the (0_2^+) state in ^{70}Ni . The χ^2 as a function of trial half-life from each fit is presented in Fig. 4.44. The black squares are the χ^2 values for each trial half-life, and the red line is a quadratic fit for interpolation between points.

The half-life for the (0_2^+) state was taken from the half-life corresponding to the minimum of the chi square distribution in Fig. 4.44. The statistical error was determined from the half-life values one χ^2 unit from the minimum. Systematic errors were investigated by varying quantities such as the ratio of counts in the peak to counts in the background, the centroid of the underlying Gaussian component of the convolution, and the magnitude of the DOI correction. All errors were added in quadrature. A value of $1.65_{-0.25}^{+0.30}$ ns was obtained for the half-life for the (0_2^+) state in ^{70}Ni . The best fit is shown in Fig. 4.45. In Fig. 4.45, the black and blue (blue is scaled) are the time-difference spectra obtained for the peak and background ROIs from Figs. 4.43b and 4.43c, respectively. The convolution of the detector response with the best-fit 1.65-ns half-life is shown in Red. The total fit of the scaled background plus convolution is shown in cyan.

Chapter 5

Discussion and Outlook

In this chapter the significance of the present results are discussed. In particular, the results suggest the presence of shape coexistence in ^{68}Ni and provide evidence that shape coexistence extends further along the Ni isotopic chain into ^{70}Ni . Comparisons with advanced shell model calculations are made and provide some insight into the importance of various excitations and configurations to describing the structures of $^{68,70}\text{Ni}$. At the conclusion of this chapter, an outlook is provided to direct further investigations in the region.

5.1 Shape Coexistence in $^{68,70}\text{Ni}$

The present results report new lifetime and branching ratio measurements for $^{68,70}\text{Ni}$ that can be used to deduce transition probabilities for $E0$ and $E2$ transitions. Measured lifetimes for excited states in $^{68,70}\text{Ni}$, both from the present work and the literature, are displayed in Table 5.1. Additionally, measured branching ratios for several transitions connecting these states are also presented along with $\rho^2(E0)$ and $B(E2)$ values determined using half-lives and branching ratios with Eqs. (2.39) and (2.28), respectively.

These values extracted from experiment, shown in Table 5.1, are compared with the results of shell model calculations employing the A3DA $[(0f1p0g_{9/2}1d_{5/2})^{\pi\nu}]$ model space] and LNPS $[(0f1p)^{\pi}(0f1p0g_{9/2}1d_{5/2})^{\nu}]$ model space] effective interactions in Fig. 5.1. Additional shell-model calculations, with effective interactions [65–67] over model spaces lacking proton

Table 5.1: Half-lives, branching ratios, and either absolute $B(E2)$ in $e^2\text{fm}^4$ or $\rho^2(E0)$, depending on the nature of the transition.

	J_i^π	$t_{1/2}$	J_f^π	BR	$B(E2)$	$\rho^2(E0)$
^{68}Ni	0_2^+	272(3) ns	0_1^+	1.0	-	0.0075(1)
	2_1^+	0.31(5) ps ^a	0_1^+	$0.999^{+0.001}_{-0.05}$	52.5(84)	-
			0_2^+	$1.2(3)\times 10^{-3}$	147(46)	-
	0_3^+	0.57(5) ns	0_1^+	< 0.0173	-	< 0.0050
			0_2^+	< 0.0018	-	< 0.0258
			2_1^+	> 0.981	39.0(34)	-
^{70}Ni	2_1^+	1.04(17) ps ^b	0_1^+	1.0	172(28) ^b	-
	(0_2^+)	$1.65^{+0.30}_{-0.25}$ ns	2_1^+	> 0.66	> 70	-
			0_1^+	< 0.33	-	< 0.54

^a from Ref. [22] ^b from Ref. [64]

excitations, successfully reproduce the energy of the 0_2^+ in ^{68}Ni state but fail to predict both the 0_3^+ [18, 19] state in ^{68}Ni and the (0_2^+) [23] state in ^{70}Ni , and are not considered here.

Beginning with the 0_2^+ in ^{68}Ni , the deduced $B(E2 : 0_2^+ \rightarrow 2_1^+)$ value of 147(46) $e^2\text{fm}^4$ agrees well with both the A3DA and LNPS interactions, which give 168 and 182 $e^2\text{fm}^4$, respectively. The observation of this strong collective transition $0_2^+ \rightarrow 2_1^+$ lends experimental support that the 2_1^+ and 0_2^+ have similar configurations as predicted by the calculations [7].

The 0_2^+ state was further investigated within the framework of a two-level mixing model, discussed in Sec. 1.3, assuming the 0_2^+ state can be described by the mixing of spherical and deformed configurations. Using Eq. (2.47) and the $B(E2)$ values for the $2_1^+ \rightarrow 0_2^+$ and $2_1^+ \rightarrow 0_1^+$ transitions, the mixing angle, θ , was deduced and used to calculate a mixing amplitude of $\cos^2(\theta) = 0.74(7)$. This value agrees well with complimentary relative cross section measurements for the population of the 0_1^+ and 0_2^+ states in the $^{66}\text{Ni}(t,p)^{68}\text{Ni}$ reaction [70] which resulted in a lower limit of $\cos^2(\theta) > 0.7$. While the mixed and closed-shell configurations could not be distinguished in Ref. [70], the present results strongly favor mixing.

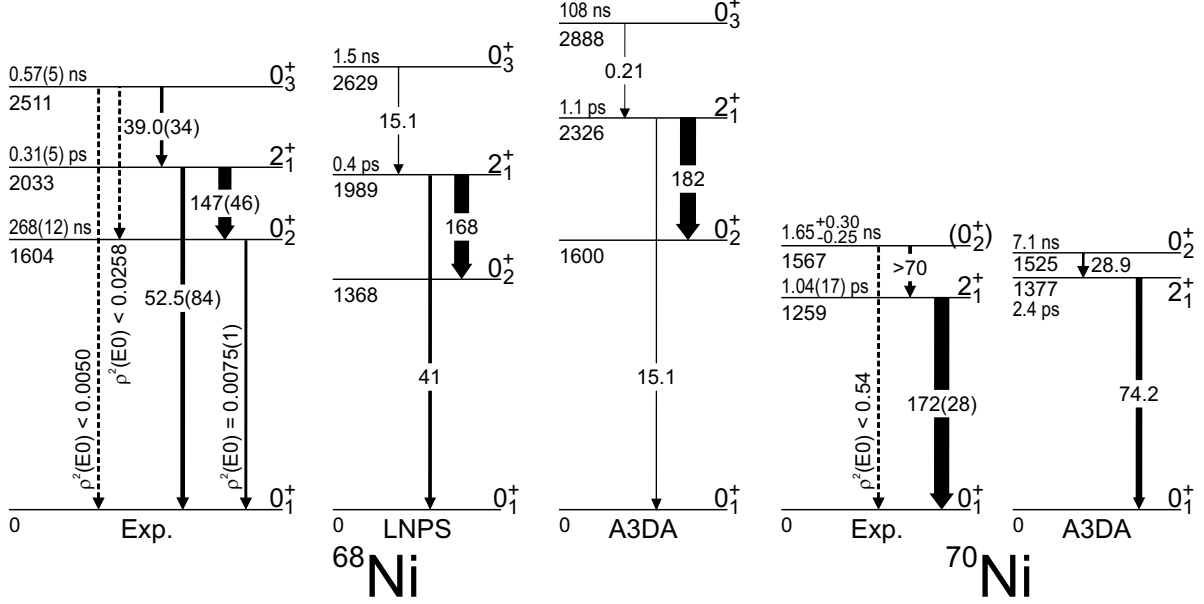


Figure 5.1: Half-lives and transition strengths of the lowest four states in ^{68}Ni (left) and the lowest three states in ^{70}Ni (right) compared with predictions of advanced shell model calculations using the LNPS [21] and A3DA [68] effective interactions. Half-lives of the states, when known, are given on the upper left side of each level with the associated energies (in keV) on the lower left side. Unobserved transitions are indicated by dotted lines. Electric monopole transition strengths are given for the $E0$ transitions, while $B(E2)$ values, in units of $e^2\text{fm}^4$, are given for $E2$ transitions. Experimental values for the 2_1^+ state half-life and $B(E2)$ for ^{70}Ni are adopted from Ref. [64]. Note that, while LNPS predictions of the ^{70}Ni $B(E2 : 0_2^+ \rightarrow 2_1^+)$ value have not been published so far, Ref. [69] indicates a calculated $B(E2 : 2_1^+ \rightarrow 0_1^+)$ value of $102 e^2\text{fm}^4$ with this interaction (not shown).

Using Eq. (2.44), the measured $\rho^2(E0)$ for the $0_2^+ \rightarrow 0_1^+$ transition, and the mixing amplitude, $\cos^2(\theta)$, the difference in mean square charge radii between the 0_2^+ and 0_1^+ states was determined to be $\Delta\langle r^2 \rangle = 0.17(2)\text{fm}^2$. Assuming a spherical 0_1^+ state, the absolute value of the intrinsic quadrupole moment of the 0_2^+ state is $|Q_0| = 93(5) \text{efm}^2$, which agrees well with the both the A3DA and LNPS predictions of $Q_0 = -95 \text{efm}^2$ [18] and $|Q_0| = 93 \text{efm}^2$ [8], respectively.

Examining the 0_3^+ state in ^{68}Ni , the measured half-life of 0.57(5) ns is much shorter than the value of the A3DA prediction of 108 ns [21], but compares more favorably with the 1.5-ns [21] half-life from the LNPS predictions. As such, the absolute $B(E2 : 0_3^+ \rightarrow 2_1^+)$ of

39.0(34) $e^2\text{fm}^4$ deduced from experiment is significantly larger than the 0.21 $e^2\text{fm}^4$ from the A3DA calculations, but again agrees better with the 15.1 $e^2\text{fm}^4$ from the LNPS calculations.

The current work is only able to place limits on the $0_3^+ \rightarrow 0_2^+$ and $0_3^+ \rightarrow 0_1^+$ $E0$ transition branches. Using the branching ratio limits, and the newly measured half-life of the 0_3^+ state, limits on $\rho^2(E0)$ of < 0.0258 and < 0.0050 can be placed for the former and the latter. Due to the more complicated configurations predicted by theory for the 0_3^+ state, a treatment within the two-level mixing model, similar to what was done for the 0_2^+ state, would not be instructive.

Transitioning from ^{68}Ni to ^{70}Ni , the A3DA calculations predict a deepening of the prolate potential well [7] and a concomitant drop in the energy of the associated prolate-deformed 0^+ state from 2511 keV in ^{68}Ni to 1525 keV in ^{70}Ni . The deepening of the prolate well is explained by the strengthening of the attractive $\nu 0g_{9/2} - \pi 0f_{5/2}$ and repulsive $\nu 0g_{9/2} - \pi 0f_{7/2}$ monopole interactions of the tensor force with added $\nu 0g_{9/2}$ occupancy. These interactions serve to decrease the energy difference between the $\pi 0f_{7/2}$ and $\pi 0f_{5/2}$ single particle states increasing the likelihood of excitations into the $\pi 0f_{5/2}$, which is the dominant proton excitation in the prolate-deformed 0^+ states in $^{68,70}\text{Ni}$ [7, 23].

In the present work, the (0_2^+) state is observed at 1567 keV, in good agreement with the energy value of 1525 keV predicted by the A3DA calculations. The work of Ref. [23] proposed the 2^+ state, observed at 1867 keV in the present work, and the 2508-keV 4^+ state, not populated in the present work, as members of a deformed band built on the (0_2^+) state. Their claim was based on the absence of corresponding states at 1867 and 2508 keV in shell-model calculations excluding proton excitations. The strong E_γ^{-5} dependence in the $B(E2)$ favors the 1867-keV $2_2^+ \rightarrow 0_1^+$ transition over the 300-keV $2_2^+ \rightarrow (0_2^+)$ transition. The predicted ratio of $B(E2; 2_2^+ \rightarrow 0_2^+) / B(E2; 2_2^+ \rightarrow 0_1^+)$ of 400 [23] precluded observation of

the $2_2^+ \rightarrow (0_2^+)$ transition both in singles and in coincidence with the 1643.5-keV transition.

The A3DA calculations predict a value of 7.2 ns [68] for the half-life of the (0_2^+) state, which is the correct order of magnitude when compared with the measured half-life of $1.65_{-0.25}^{+0.30}$ ns. The experimental value for the $B(E2 : 0_2^+ \rightarrow 2_1^+)$ has a lower limit (1σ) of > 70 efm^2 based on the $> 66\%$ branch for the 307.5-keV $0_2^+ \rightarrow 2_1^+$ transition. If one assumes a 100% γ -ray branch then the value becomes 123_{-18}^{+19} efm^2 . Regardless, the $B(E2 : 0_2^+ \rightarrow 2_1^+)$ of 28.9 efm^2 predicted by the A3DA calculations is lower than the experimental lower limit.

Overall, while both the A3DA and LNPS calculations correctly predict the energies of all the states shown in Fig. 5.1, the tenuous agreement for the half-lives of the 0_3^+ state in ^{68}Ni and the 0_2^+ state in ^{70}Ni indicates there is room for improvement on the theoretical front. The inability to treat the 0_3^+ state in ^{68}Ni within the framework of the two-level mixing model precludes extraction of the intrinsic quadrupole moment and any strong statements about experimental evidence of triple shape coexistence. However, the quantitative description of the 0_2^+ verifies the presence of shape coexistence in ^{68}Ni .

5.2 Analysis of β -Decay Strength and Intensity Distributions in $^{68,70}\text{Ni}$

In this section, the cumulative β -decay strength and intensity distributions are presented and compared with shell-model calculations. Experimentally, the β -decay feedings were determined by the balance of absolute γ -ray intensity recorded in and out of each level. Since these feedings are based on γ -ray intensity balances they are referred to as “apparent” feedings. From the apparent β -decay feedings and a measurement of the β -decay half-life, the partial half-life is calculated using Eq. (2.10). The Fermi integral is evaluated for each

state using Eq. (2.12).

$B(GT)$ values are determined using Eq. (2.11) assuming $B(F) \equiv 0$. While this assumption is not entirely true, the majority of the Fermi strength will be to the isobaric analogue state, which for neutron-rich nuclei, is outside the β -decay Q-value window. This is due to an increase in the Coulomb energy with the conversion of a neutron to a proton. In the case of $^{68,70}\text{Ni}$ the isobaric analogue state would be located around ≈ 15 MeV of excitation energy. Furthermore, since the majority of the spin and parities remain unknown in $^{68,70}\text{Ni}$, some ambiguity regarding the character of β -decay transitions exists, and the experimentally determined cumulative $B(GT)$ values presented herein will contain contributions from forbidden decay.

Shell-model calculations presented in this section were performed using the $0f1p0g_{9/2}0g_{7/2}$ model space for neutrons. The proton configurations were fixed in these calculations such that Ni isotopes possessed a filled $Z = 28$ shell, while Co isotopes had a filled $Z = 28$ shell with a hole in the $\pi 0f_{7/2}$ single-particle state. The GXFP1A Hamiltonian [71] was used for the $0f1p$ portion of the model space while the $0g$ part was created using the N^3LO interaction [72] with a V_{lowk} renormalization into 6 major oscillator shells. The effective interaction was created using many-body perturbation theory up to second order [73]. Single-particle energies were obtained from relative binding energies and low-lying excited states in $^{69,70}\text{Ni}$, ^{69}Co , and ^{71}Cu . The single-particle energy spacings between the $\nu 0f_{7/2} - \nu 0f_{5/2}$ and $\nu 0g_{9/2} - \nu 0g_{7/2}$ were set to around 6 MeV. A quenching factor of 0.6 was applied to all Gamow-Teller strengths.

5.2.1 Short-Lived, High-Spin, ^{70}Co Isomer

The configuration of the short-lived ^{70}Co isomer was taken to be $(\nu 0g_{9/2})^3(\pi 0f_{7/2})^{-1}$ relative to the closed $Z = 28$ proton shell and $N = 40$ neutron subshell closures. A 6^- spin and parity from the coupling of the $\nu 0g_{9/2}$ neutron and $\pi 0f_{7/2}$ proton hole was used. States in ^{70}Ni were formed from all possible neutron one-particle one-hole ($1p - 1h$) excitations relative to ^{70}Co . A comparison between the apparent cumulative β -decay intensity distribution from experiment (black line with salmon error band) with the theoretical cumulative β -decay intensity distribution from the shell model calculations (dark blue dashed line) is presented in Fig. 5.2. The vertical red dashed line represents the 7792-keV neutron separation energy [22].

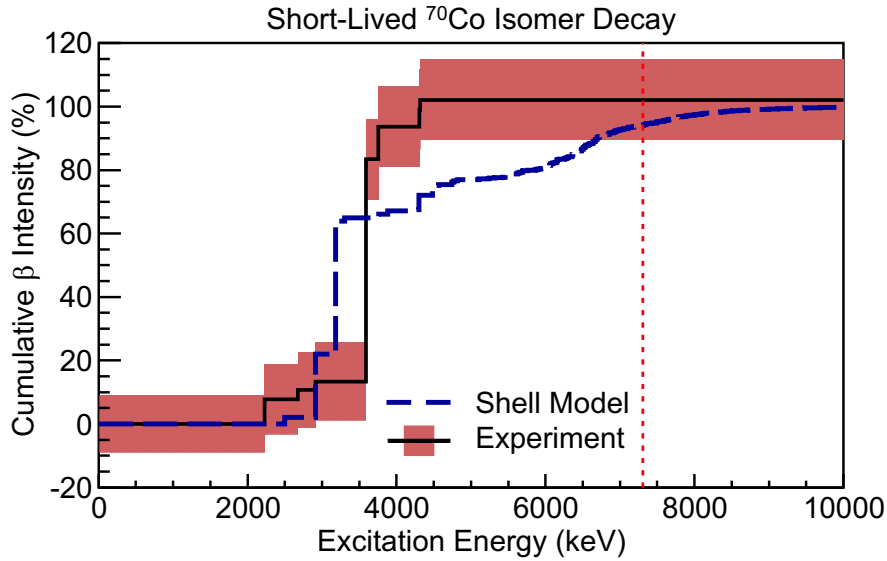


Figure 5.2: Apparent cumulative β -decay intensities deduced from the experimental decay scheme in Fig. 4.36 (black line with salmon error bars) compared with shell model calculations (dashed dark blue line).

Reasonable agreement between the experimental and theoretical cumulative β -decay intensities is obtained and the calculation gives a 104.5 ms half-life which agrees quite well with the 104(2) ms obtained from the present work. A comparison between the apparent cumulative β -decay strength distribution from experiment (black line with turquoise error

band) with the theoretical cumulative β -decay strength distribution from the shell model calculations (dark blue dashed line) is presented in Fig. 5.3. Again vertical red dashed line represents the 7792-keV neutron separation energy [22].

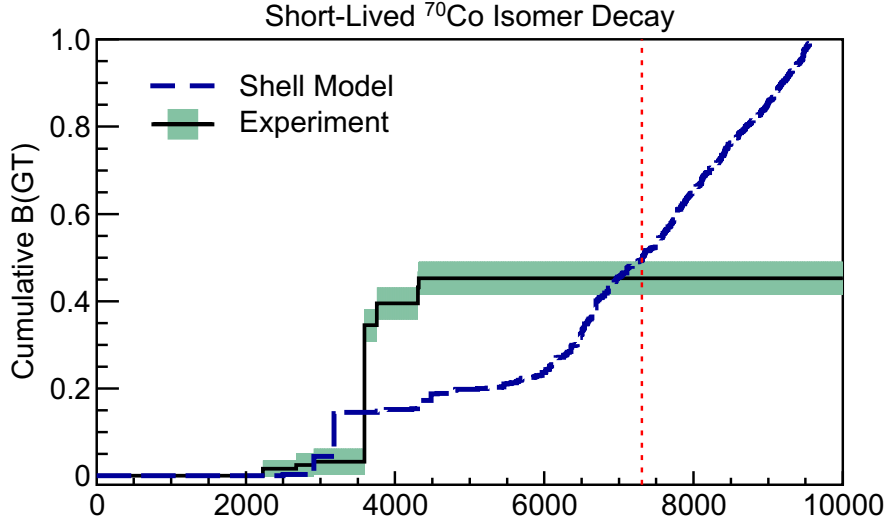


Figure 5.3: Apparent cumulative β -decay intensities deduced from the experimental decay scheme in Fig. 4.36 (black line with turquoise error bars) compared with shell model calculations (dashed dark blue line).

In both the experimental and theoretical strength distributions the majority of the strength is to higher-lying negative parity 5^- , 6^- , and 7^- states. This is expected since β decay of the 6^- parent to the 0^+ , 2^+ , 4^+ , and 6^+ states of the ^{70}Ni yrast band are forbidden, and thus significantly hindered. Low-energy states starting around 3592 keV in ^{70}Ni are populated by $0\nu f_{5/2}$ to $0\pi f_{7/2}$ decays, while the steady rise starting at ~ 6 MeV experimental distribution is most likely due to contributions from $\nu 1p$ to $\pi 1p$, $\nu 0f_{5/2}$ to $\pi 0f_{5/2}$, and $\nu 0g_{9/2}$ to $\pi 0g_{9/2}$ decays which create higher energy proton hole states in ^{70}Ni .

Experimentally, most ($\sim 70\%$) of the apparent β -decay feeding is to the 3592-keV (6^-) state. In a complimentary experiment, not detailed in this dissertation, a total absorption spectroscopy (TAS) experiment was performed on the decay of this ^{70}Co isomer [29]. A comparison of the apparent β -decay feedings between the present work and the TAS mea-

surement suggests that while most of the β -decay feeding does indeed go to the 3592-keV (6^-), state the present high-resolution spectroscopy attributes a factor of 2 excess feeding to the 3592-keV (6^-) state. This is presumably due to the pandemonium effect [74] where a large number of undetected low-intensity transitions feed this state from several higher-lying states. The pandemonium effect is unavoidable in the present low-efficiency high-resolution spectroscopy experiment, but is mitigated in TAS due to the high intrinsic γ -ray detection efficiencies (up to $\sim 85\%$) of TAS detectors [75].

In addition, the TAS measurement of Ref. [29] observes a strong preference for γ -ray emission over β -delayed neutron emission above the neutron separation energy. In the present work no evidence of β -delayed neutron emission is observed consistent with the TAS measurement. The origin of this behaviour as explained by Ref. [29] is poor spectroscopic overlap between neutron-unbound states in ^{70}Ni and low-lying states in ^{69}Ni which hinders neutron emission.

The overall good agreement between the present work, the TAS measurement, and the shell model calculation suggests that the short-lived, high-spin, ^{70}Co isomer is well described as a spherical 6^- state with a $(\nu 0g_{9/2})^3 (\pi 0f_{7/2})^{-1}$ configuration.

5.2.2 Long-Lived, Low-Spin, ^{70}Co Isomer

The configuration of the long-lived, low-spin, ^{70}Co isomer was taken to be $(\nu 0g_{9/2})^4 (\nu 1p_{1/2})^{-1} (\pi 0f_{7/2})^{-1}$ relative to the closed $Z = 28$ proton shell and $N = 40$ neutron subshell closures. Within the framework of the spherical shell model, a 3^+ spin and parity from the coupling of the $\nu 1p_{1/2}$ and $\pi 0f_{7/2}$ holes was adopted from Ref. [12]. As before, states in ^{70}Ni were formed from all possible neutron one-particle one-hole ($1p - 1h$) excitations relative to ^{70}Co . A comparison between the apparent cumulative β -decay intensity distribution from experi-

ment (black line with salmon error band) with the theoretical cumulative β -decay intensity distribution from the shell model calculations (dark blue dashed line) is presented in Fig. 5.4. The vertical red dashed line represents the 7307-keV neutron separation energy [59].

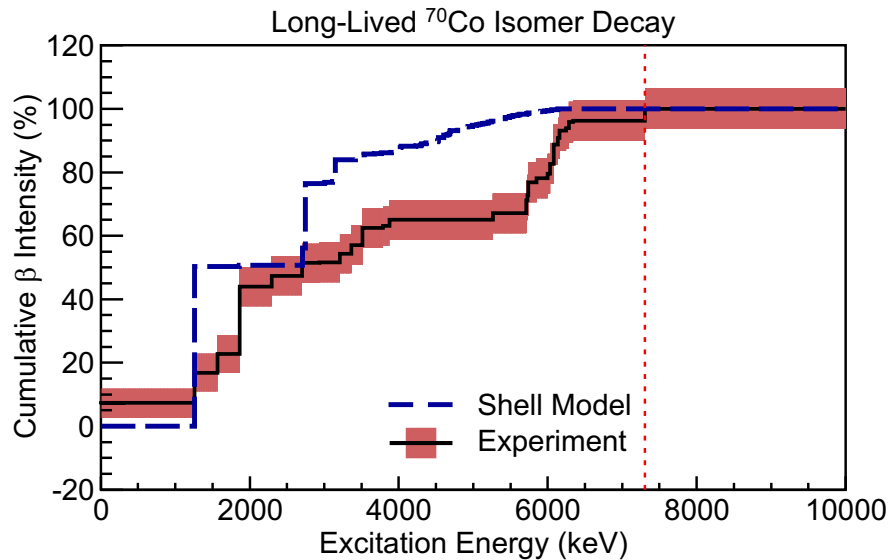


Figure 5.4: Apparent cumulative β -decay intensities deduced from the experimental decay scheme in Fig. 4.41 (black line with salmon error bars) compared with shell model calculations (dashed dark blue line).

The nature of the β -decay from the long-lived, low-spin, isomer is most likely identical to that of the short-lived, high-spin, isomer, whereby the low-lying Gamow-Teller strength is dominated by the $\nu 0f_{5/2}$ to $\pi 0f_{7/2}$ decays while the rise at ~ 6 MeV in the experimental distribution is again due to contributions from $\nu 1p$ to $\pi 1p$, $\nu 0f_{5/2}$ to $\pi 0f_{5/2}$, and $\nu 0g_{9/2}$ to $\pi 0g_{9/2}$ decays which leave higher energy proton hole states in ^{70}Ni .

A comparison between the apparent cumulative β -decay strength distribution from experiment (black line with turquoise error band) with the theoretical cumulative β -decay strength distribution from the shell model calculations (dark blue dashed line) is presented in Fig. 5.5. Again, the vertical red dashed line represents the 7307-keV neutron separation energy [59].

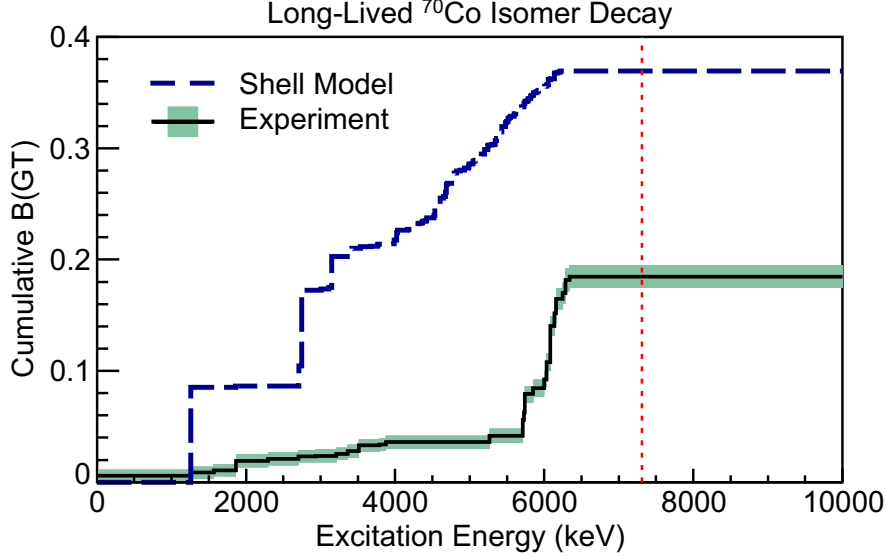


Figure 5.5: Apparent cumulative β -decay intensities deduced from the experimental decay scheme in Fig. 4.41 (black line with turquoise error bars) compared with shell model calculations (dashed dark blue line).

The calculation significantly overpredicts β -decay feeding to the 1260-keV 2_1^+ state. As a result, the β -decay strength distribution is also discrepant with experimental results. Despite this discrepancy, the calculation provides a reasonable prediction of 592 ms for the half-life of the long-lived, low-spin, ^{70}Co isomer for which the experimentally measured value is 450(13) ms. The large discrepancy in the feeding pattern points to a deficiency in our understanding of the configuration of the long-lived, low-spin, ^{70}Co isomer. It suggests that the long-lived, low-spin, ^{70}Co isomer is not well described by the spherical $(\nu 0g_{9/2})^4(\nu 1p_{1/2})^{-1}(\pi 0f_{7/2})^{-1}$ configuration, but instead has a more complicated configuration and/or an incorrect spin and parity assignment.

Recent large-scale shell-model calculations using the A3DA interaction [76] suggest that long-lived ^{70}Co isomer is prolate deformed with ~ 3 protons and ~ 3 neutrons on average excited across $Z = 28$ and $N = 40$, respectively. Based on the evidence of the descending $1/2^-$ intruder orbital in the odd- A cobalt isotopes [15, 16, 77] with added neutron occupancy

of the $\nu 0g_{9/2}$, a likely configuration for the long-lived ^{70}Co isomer involves the coupling of the $[301]\nu p_{1/2}$ and $[321]\pi p_{3/2}$ Nilsson orbitals [55]. This would yield 1^+ and 0^+ states with the 1^+ located lower in energy [78].

Additional support for a 1^+ spin and parity assignment can be obtained by examining the spin and parity of states fed in β -decay. The strongest feeding is to the 1867-keV 2_2^+ state ($\approx 21\%$) followed by the 1260-keV 2_1^+ state ($\approx 10\%$). While the feeding of 2^+ states alone does not discriminate between 1^+ and 3^+ assignments, the lack of feeding to the 2229-keV 4_1^+ and 2508-keV (4_2^+) [23] states, but relatively strong feeding to the 1567-keV (0_2^+) state, favors the 1^+ assignment.

The large feeding to the 2_2^+ compared to the 2_1^+ , despite the disadvantage from the decay energy dependence of the Fermi integral, suggests similarity in the underlying configurations between the long-lived, low-spin, ^{70}Co isomer and the 2_2^+ state in ^{70}Ni . Based on the A3DA calculation results [7], the 0_2^+ and 2_2^+ are expected to be prolate deformed and have configurations with a large contribution from proton excitations. This lends further support for a prolate-deformed 1^+ long-lived, low-spin, ^{70}Co isomer with a configuration comprised of multiple particle-hole excitations.

5.2.3 Long-Lived, Low-Spin, ^{68}Co Isomer

Analogous to the long-lived ^{70}Co isomer, the configuration of the long-lived ^{68}Co isomer was taken to be $(\nu 0g_{9/2})^2(\nu 1p_{1/2})^{-1}(\pi 0f_{7/2})^{-1}$, relative to ^{68}Ni , and the same 3^+ spin and parity from the coupling of the $\nu 1p_{1/2}$ and $\pi 0f_{7/2}$ holes was adopted from Ref. [12]. States in ^{68}Ni were formed from all possible neutron one-particle one-hole ($1p - 1h$) excitations relative to ^{68}Co . A comparison between the apparent cumulative β -decay intensity distribution from experiment (black line with salmon error band) with the theoretical cumulative β -decay

intensity distribution from the shell model calculations (dark blue dashed line) is presented in Fig. 5.6. The vertical red dashed line represents the 7307-keV neutron separation energy [59].

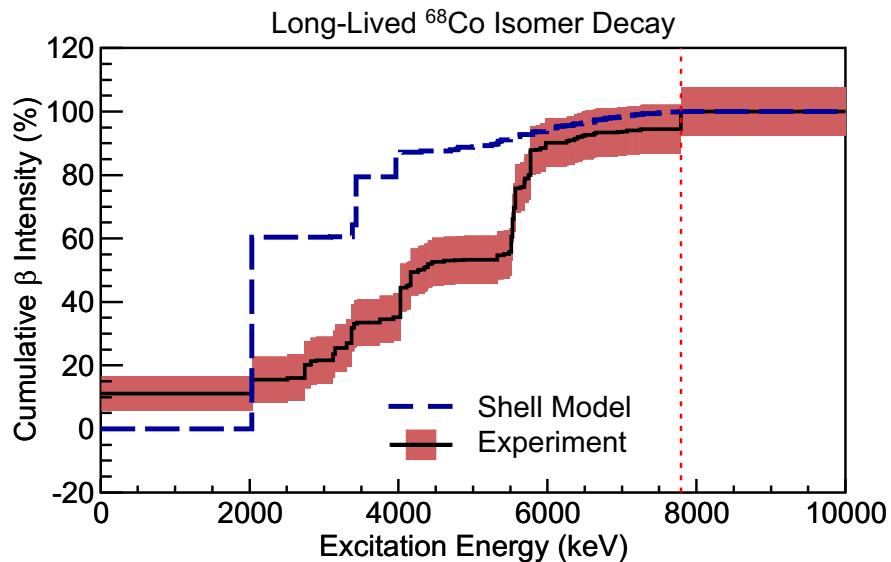


Figure 5.6: Apparent cumulative β -decay intensities deduced from the experimental decay scheme in Fig. 4.6 (black line with salmon error bars) compared with shell model calculations (dashed dark blue line).

Just as with the decay of ^{70}Co , it is likely that the low-lying Gamow-Teller strength is dominated by the $0\nu f_{5/2}$ to $0\pi f_{7/2}$ decays while the rises at ~ 4 MeV and ~ 6 MeV in the experimental distribution are due to contributions from $\nu 1p$ to $\pi 1p$, $\nu 0f_{5/2}$ to $\pi 0f_{5/2}$, and $\nu 0g_{9/2}$ to $\pi 0g_{9/2}$ decays, which leave higher-energy proton hole states in ^{68}Ni .

A comparison between the apparent cumulative β -decay strength distribution from experiment (black line with turquoise error band) with the theoretical cumulative β -decay strength distribution from the shell model calculations (dark blue dashed line) is presented Fig. 5.7. Again, the vertical red dashed line represents the 7307-keV neutron separation energy [59].

The poor agreement between the calculated and experimental strength and intensity distributions closely mirrors that of the long-lived, low-spin, ^{70}Co isomer. The calculation

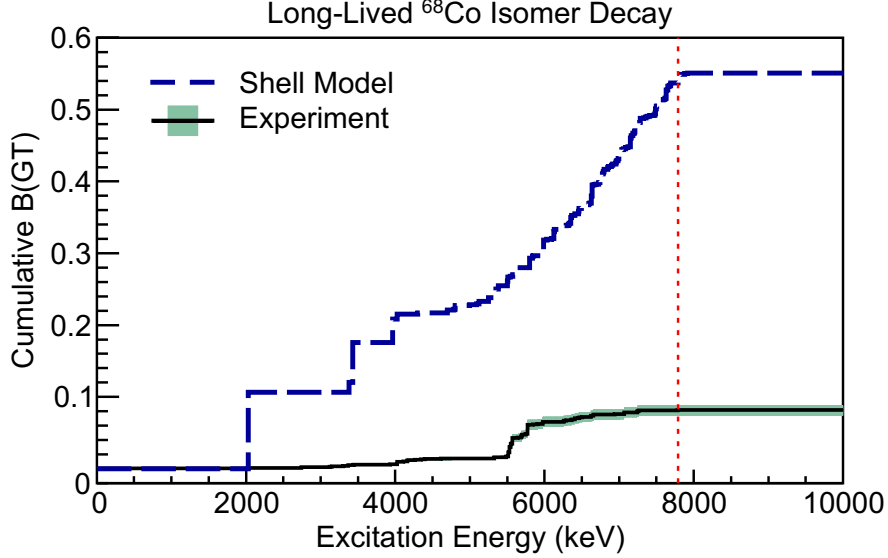


Figure 5.7: Apparent cumulative β -decay intensities deduced from the experimental decay scheme in Fig. 4.6 (black line with turquoise error bars) compared with shell model calculations (dashed dark blue line).

significantly overpredicts β -decay feeding to the 2_1^+ state, and the 115 ms half-life predicted by the calculation is very different than the measured value of 2330^{+790}_{-460} ms. Similar to the long-lived, low-spin, ^{70}Co isomer, the long-lived, low-spin, ^{68}Co isomer is also not well described by the spherical $(\nu 0g_{9/2})^2(\nu 1p_{1/2})^{-1}(\pi 0f_{7/2})^{-1}$ configuration and it likely possesses a more complicated configuration and/or an incorrect spin and parity assignment.

Recently, two other spin and parity assignments have been proposed for long-lived, low-spin, ^{68}Co isomer. The most recent spin and parity assignment is (2^-) from the coupling of the same downsloping $[321]1/2^+$ proton (originating from the spherical $\pi 1p_{3/2}$) orbital with the, also downsloping, $[431]3/2^+$ and $[440]1/2^+$ neutron (originating from the spherical $\nu 0g_{9/2}$) orbitals, at prolate deformation [21]. Experimentally-determined $\log ft$ values provide some support for this interpretation, since all β decays to $0, 2, 4^+$ states appear to be first-forbidden decay ($\log ft > 6$). However, the large $\log ft$ value (~ 7) for the decay to the 3301-keV (3^-) state, which should be an allowed decay, is conflicting.

A more plausible spin and parity assignment of 1^+ was proposed in Ref. [55], deduced from the large β -decay feeding to this isomer from the 0^+ ground state of ^{68}Fe . The 1^+ state is explained by the coupling of the $[321]1/2^-$ proton (originating from the spherical $\pi 1p_{3/2}$) and $[301]1/2^-$ neutron (originating from the spherical $\nu 1p_{1/2}$) orbitals at modest prolate ($\beta \approx 0.2$) deformation.

Given the recent predictions of the large-scale shell model calculations using the A3DA interaction for ^{70}Co [76], and the already-discussed systematics of intruder states in the region, this (1^+) isomer would likely be quite similar in configuration to ^{70}Co . Just like the case of ^{70}Co , the coupling of the $[321]1/2^-$ proton (originating from the spherical $\pi 1p_{3/2}$) and $[301]1/2^-$ (originating from the spherical $\nu 1p_{1/2}$) neutron states should give rise to a 1^+ state and a 0^+ state slightly higher in energy [78]. Based on the β -decay scheme presented in Ref. [55], a second state at an energy of 45 keV above the (1^+) isomer is present and also strongly fed by the β decay of the 0^+ ground-state of ^{68}Fe .

Based on the γ -ray coincidences and the established ^{68}Co level scheme, the work of Ref. [55] deduced an internal conversion coefficient of $\alpha = 1.0(4)$ for the 45-keV transition. Values of $\alpha = 0.52$ and $\alpha = 0.37$ [34] are expected for the internal coefficient for $E1$ and $M1$ multipolarities, respectively. Assuming an $E1$ transition the 45+x could have a spin and parity of 2^- , which is discrepant with the $\log ft$ of 4.7(3) for the decay to this state.

However, the present work contains a factor of ~ 5 increase in statistics over Ref. [55]. A measurement of the internal conversion coefficient, using the same techniques, gives a value of 0.18(10). The experimentally-deduced α of 0.18(10) compares more favorably with the $\alpha = 0.37$ for an $M1$ transition, suggesting that the state above the isomer is the same parity with $J = \pm 1$. Since the ground state of ^{68}Fe is a 0^+ state, it is most likely that the 45+x state in Ref. [55], fed strongly by β -decay, is also a 0^+ state. Therefore the expected 0^+

and 1^+ states, close to one another in energy, from the coupling of the $[321]1/2^-$ proton (originating from the spherical $1\pi p_{3/2}$) and $[301]1/2^-$ (originating from the spherical $1\nu p_{1/2}$) neutron orbitals, appear to be supported by current experimental evidence.

While the 1^+ spin and parity is the favored assignment for the long-lived ^{68}Co isomer, the present spectroscopic evidence is not sufficient to make a definitive argument. Many states in ^{68}Ni have only tentative spin and parity assignments and thus further information about the spins and parities of additional strongly fed states, such as the 4163-, 5512-, 5529-, 5548-, 5566-, and 5774-keV states, would help make a more substantive argument about the spin and parity of the long-lived, low-spin, ^{68}Co isomer.

5.3 Outlook

The results of this work constitute a quantitative description of excited 0^+ states in the neutron-rich nickel isotopes near the $N = 40$ subshell closure, and have demonstrated that shape coexistence occurs in ^{68}Ni . However, there are many questions that remain unanswered. Does triple shape coexistence, like that of ^{186}Pb , occur in ^{68}Ni ? How far along the Ni isotopic chain does shape coexistence extend and how does it compare with current theoretical predictions? What is the nature of the β -decaying isomers in the neutron-rich Co isotopes and what are their implications for shape coexistence in the Co isotopes?

These questions will require a large effort from experiment and theory alike. In order to determine the existence of triple shape coexistence in ^{68}Ni , as predicted by large-scale shell model calculations [5,7–9], measurements of the $0_3^+ \rightarrow 0_2^+$ and $0_3^+ \rightarrow 0_1^+$ $E0$ transitions must be made. Together with the newly-measured 0_3^+ state half-life, the electric monopole transition strength could be determined and related to the difference in mean square charge

radii between the 0_3^+ and 0_2^+ , 0_1^+ states.

Further investigation into the nature of the (0_2^+) state in ^{70}Ni must be performed to conclusively extend shape coexistence further along the Ni isotopic chain. First confirmation of the 0^+ spin and parity is required and then observation of the $(0_2^+) \rightarrow 0_1^+$ $E0$ transition coupled with a more precise half-life measurement will be needed to deduce the electric monopole transition strength and extract the difference in mean square charge radii between the (0_2^+) and 0_1^+ states.

From a theoretical standpoint, the ability to more accurately reproduce excited-state half-lives and electromagnetic transition probabilities is important for understanding the underlying nucleon configurations and thus the migration of single-particle states. Additionally, $E0$ transition strengths from theory, reportedly close on the horizon, would be of interest to further investigate shape coexistence across the nuclear chart.

Further experimental investigation of the β -decaying Co isomers is also important. All attempts thus far to identify transitions connecting the presumed prolate and spherical β -decaying isomers in $^{68,69,70}\text{Co}$ have been unsuccessful. Thus the energy separations are unknown and even their ordering remains unclear. Precision mass measurements are needed to determine the mass of each isomer. Total absorption spectroscopy (TAS) measurements of $^{68,69,70}\text{Co}$ β decay would allow experimental determination of the Gamow-Teller strength distribution. Comparison of level schemes, lifetimes, and β -decay strength distributions between experiment and large scale shell-model calculations for $^{68,69,70}\text{Co}$ would provide stringent tests of competing theoretical descriptions.

APPENDICES

Appendix A

Identification of Additional Peaks

Observed in Pulse Shape Analysis

Not Affiliated With the $0_2^+ \rightarrow 0_1^+$

Transition in ^{68}Ni

In this appendix the low-energy peaks observed in the pulse-shape analysis results from the GeDSSD, not affiliated with the $0_2^+ \rightarrow 0_1^+$ transition in ^{68}Ni , are discussed.

The 141.4-keV transition in Fig. 3.23 comes from the decay of the 242.6-keV isomeric state in ^{70}Cu which has a half-life of 6.6 s [59]. The 185.0-keV, 239.2-keV, and 352.1-keV are room background lines from ^{226}Ra , ^{212}Pb , and ^{214}Pb , respectively.

The peak at 92.6-keV is from the decay of the 93.3-keV $1/2^-$ state in ^{67}Zn [79]. The first pulse energies coincident with the 92.6-keV second pulse energy peak from Fig. 3.28 are shown in Fig. A.1a. γ rays, detected in SeGA, coincident with the 92.6-keV second pulse energy peak from Fig. 3.28 are presented in Fig. A.1b.

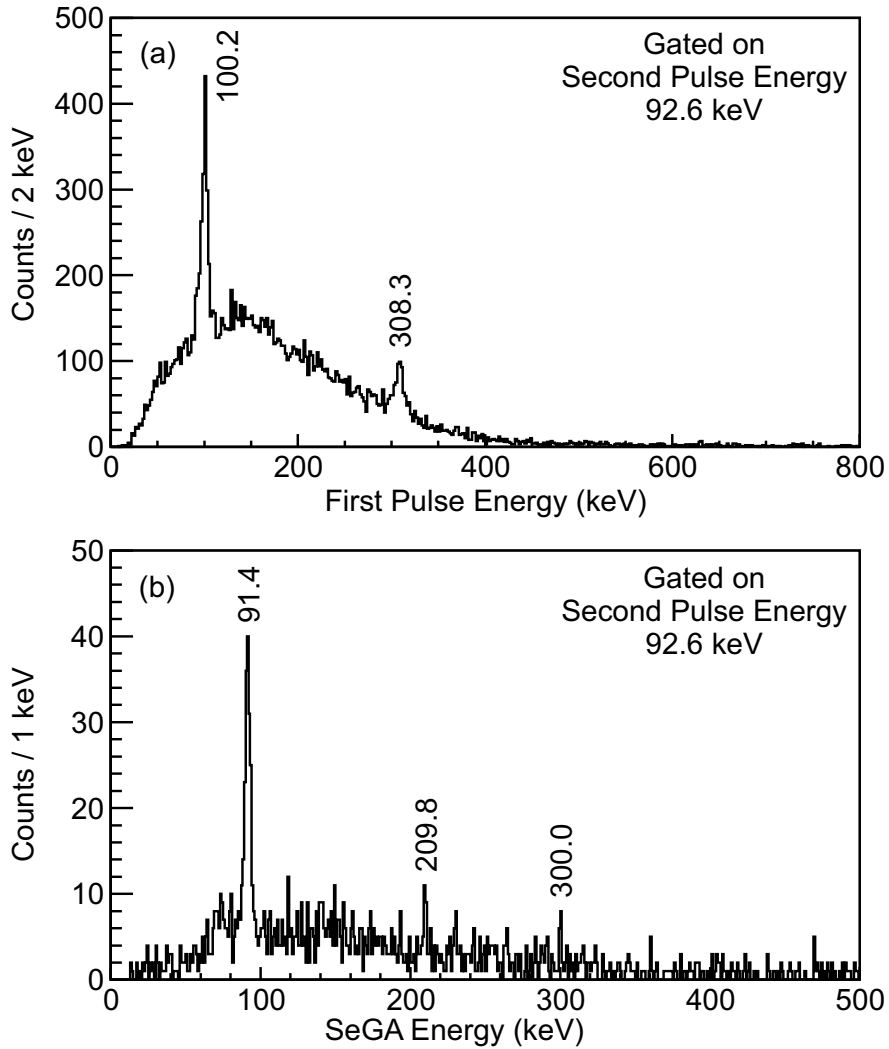


Figure A.1: (a) Coincident first rise energies of double pulses with a 92.6-keV second rise energy. (b) Gamma rays recorded in SeGA coincident with double pulses recorded in the GeDSSD with the energy of the second rise in the 92.6-keV peak.

The 92.6-keV transition observed in Fig. 3.23 was placed as the $(1/2^- \rightarrow 5/2^-)$ transition in ^{67}Zn . The 93-keV state $1/2^-$ state in ^{67}Zn has a half life of $9.07(4) \mu\text{s}$ and is fed both directly and indirectly through the β decay of ^{67}Cu [79]. The coincident γ rays with energies of 91.4, 209.8, and 300.0 keV, shown in Fig. A.1b, are known to feed, directly or indirectly, the 93-keV state [79].

The GeDSSD is sensitive to both electrons and low-energy γ rays and as such both were observed in the first rise energy spectrum in Fig. A.1a. The energy recorded in Fig.

A.1a can be from just the β -decay electron, just a β -delayed γ -ray if the β -decay indirectly populates the 93-keV state and the electron and γ -ray deposit energy in different strips of the detector, or a combination of the sum of the β -decay electron and β -delayed γ -ray energy if the depositions occur in the same strip.

The broad and continuous distribution is from the β -decay electrons both with and without summing of β -delayed γ -rays. The isolated γ -ray events are the 100.2- and 308.3-keV peaks shifted in energy by ≈ 8.5 keV. The origin of this energy shift remains unknown.

The peak at ≈ 175 keV is the decay of the 174.9-keV $5/2^-$ state [80] in ^{71}Ge populated by secondary fragmentation of the GeDSSD crystal under heavy-ion implantation. The γ rays detected in SeGA coincident with the 175-keV second pulse energy peak in the GeDSSD are presented Figure A.2.

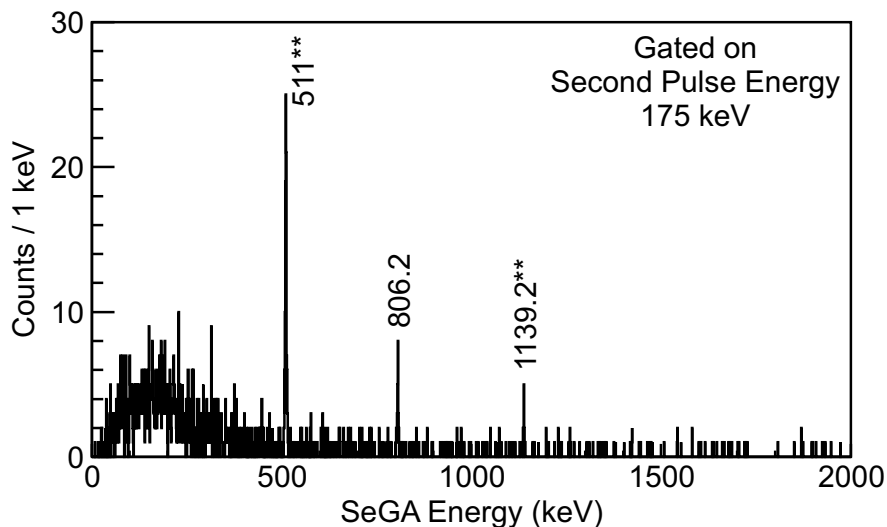


Figure A.2: Gamma rays recorded in SeGA coincident with double pulses recorded in the GeDSSD with the energy of the second rise in the 175-keV peak. The 511- and 1139.2-keV peaks, labeled with two asterisks, are coincident with the decay of the 0_2^+ state in ^{68}Ni during events where there was incomplete energy collection for the pair-production or internal conversion decay processes. The 806.2-keV peak is new and remains unidentified.

In Fig. A.2, the 511- and 1139.2-keV peaks, labeled with two asterisks, are coincident with the decay of the 0_2^+ state in ^{68}Ni during events where incomplete energy collection

for the pair-production or internal conversion decay processes occurred. The peak at 806.2 keV is new from this work and remains unidentified. The 24-keV peak observed in the first rise energy spectrum in work of Ref. [81] during the commissioning of the GeDSSD was not observed in the present work. Prior experiments damaged the detector enough to preclude low amplitude double pulse detection and have degraded the energy resolution.

The unresolved high-energy tail of the 175-keV peak in Fig. 3.28b is from the 190-keV transition which depopulates the 2742-keV ($13/2^+$) state feeding the 2552-keV ($13/2^+$) state in ^{69}Cu [52], the granddaughter of ^{69}Co which was implanted in the GeDSSD. The γ rays detected in SeGA coincident with the 190-keV second pulse energy peak in the GeDSSD are presented in Fig. A.3.

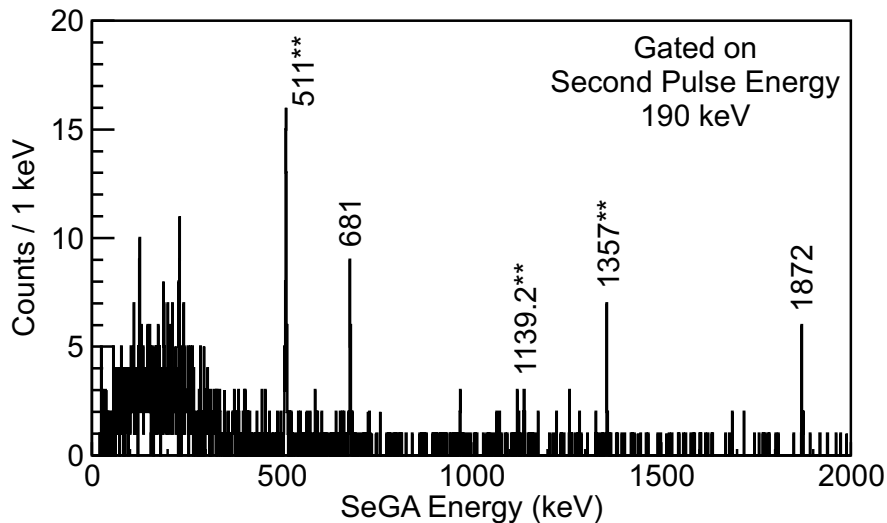


Figure A.3: Gamma rays recorded in SeGA coincident with double pulses recorded in the GeDSSD with the energy of the second rise in the 190-keV peak. The 511-keV peak, labeled with two asterisks, was coincident with the decay of the 0_2^+ state in ^{68}Ni during events where there was incomplete energy collection for the pair-production or internal conversion decay processes. The 1357-keV peak was coincident with an unresolved and unidentified ≈ 200 keV second pulse energy. The 681- and 1870-keV transitions are from the 680.6-1872.3-keV γ -ray cascade that depopulates the 2552-keV state in ^{69}Cu [52].

In Fig. A.3, the 511-keV peak, labeled with two asterisks, is again from the coincidence with the the decay of the 0_2^+ state in ^{68}Ni in events with incomplete energy collection for the

pair-production or internal conversion decay processes. The 1357-keV peak was coincident with an unresolved and unidentified ≈ 200 keV second pulse energy. The 681- and 1870-keV transitions are from the 680.6-1872.3-keV γ -ray cascade that depopulates the 2552-keV state in ^{69}Cu [52].

Appendix B

$\beta\gamma\gamma$ and $\beta\gamma\gamma$ -double-pulse

Coincidences Observed Following the

β -Decay of the Long-Lived, Low-Spin,

^{68}Co Isomer

In this appendix the $\beta\gamma\gamma$ and $\beta\gamma\gamma$ -double-pulse coincidences observed during the β -decay of ^{68}Co into ^{68}Ni are presented. These coincidences were used to identify and place levels in the low-energy ^{68}Ni level scheme.

$\beta\gamma\gamma$ Coincidences

While several transitions are observed following the β -decay of ^{68}Co , the 2032.9-keV $2_1^+ \rightarrow 0_1^+$ transition is the most intense transition listed in Table 4.1. The 2032.9-keV transition collects significant intensity from higher lying states, and as such several coincidences are observed. The $\beta\gamma\gamma$ coincidence spectrum gated on the 2032.9-keV $2_1^+ \rightarrow 0_1^+$ transition are shown in Fig. B.1.

A strong coincidence with a 709.3-keV γ ray is shown in Fig. B.1. The 709.3-keV transition, along with the 1139.2-keV and 2742.2-keV transitions, is known to depopulate

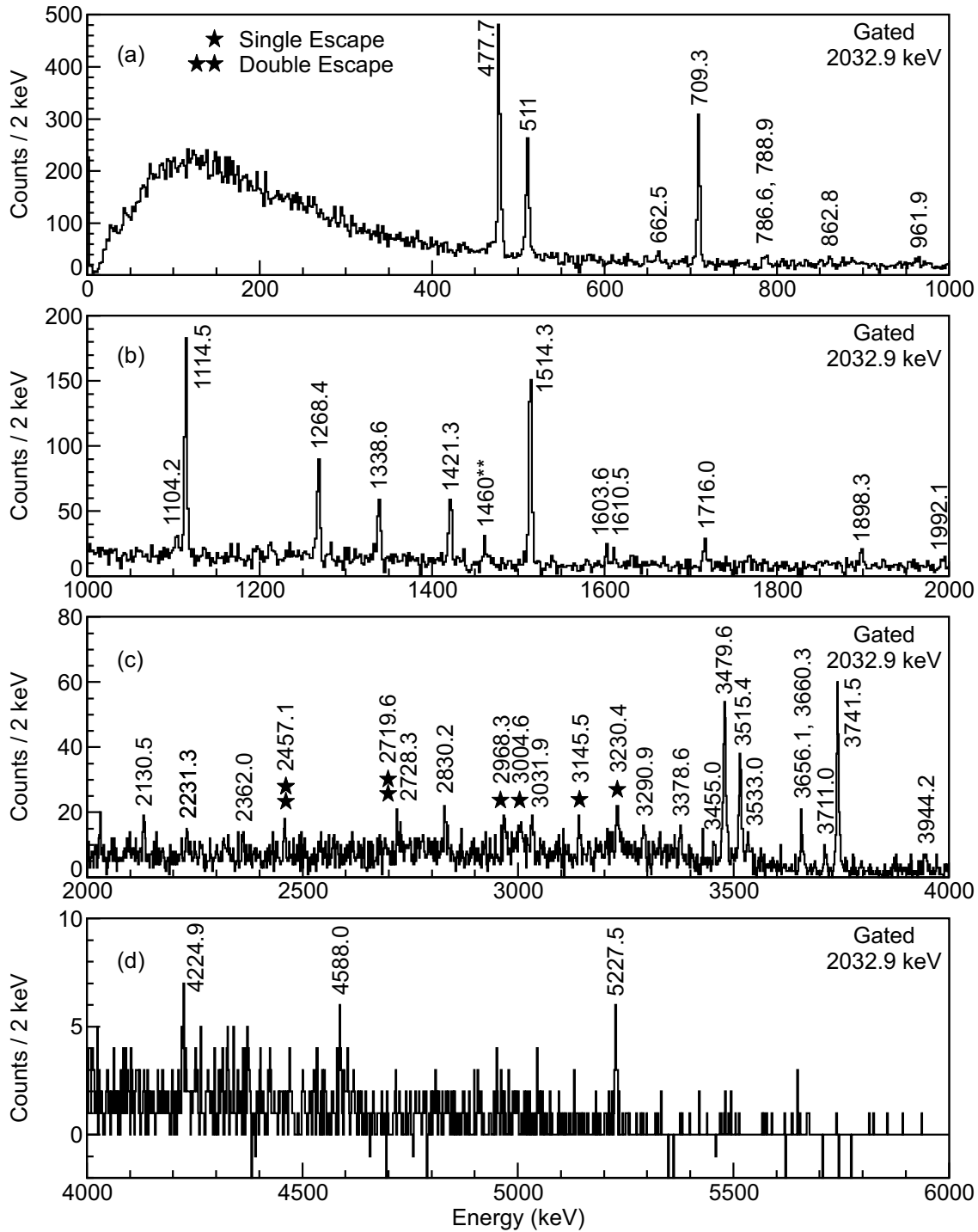


Figure B.1: Background-subtracted $\beta\gamma\gamma$ coincidence spectra gated on the 2032.9-keV $2_1^+ \rightarrow 0_1^+$ transition in ^{68}Ni . The background was taken symmetrically either side of the 2032.9-keV peak. Coincident transitions are labeled with their energies and, when applicable, single and double-escape peaks are denoted with one or two stars, respectively, in addition to the energy of the peak.

the 2742-keV 2_2^+ state. The $\beta\gamma\gamma$ coincidence spectra gated on the 709.3-keV, 1139.2-keV, and 2742.2-keV transitions are shown in Figs. B.2a, B.2b, and B.2c, respectively while the sum of the coincidence spectra from all three gates is presented in Fig. B.2d.

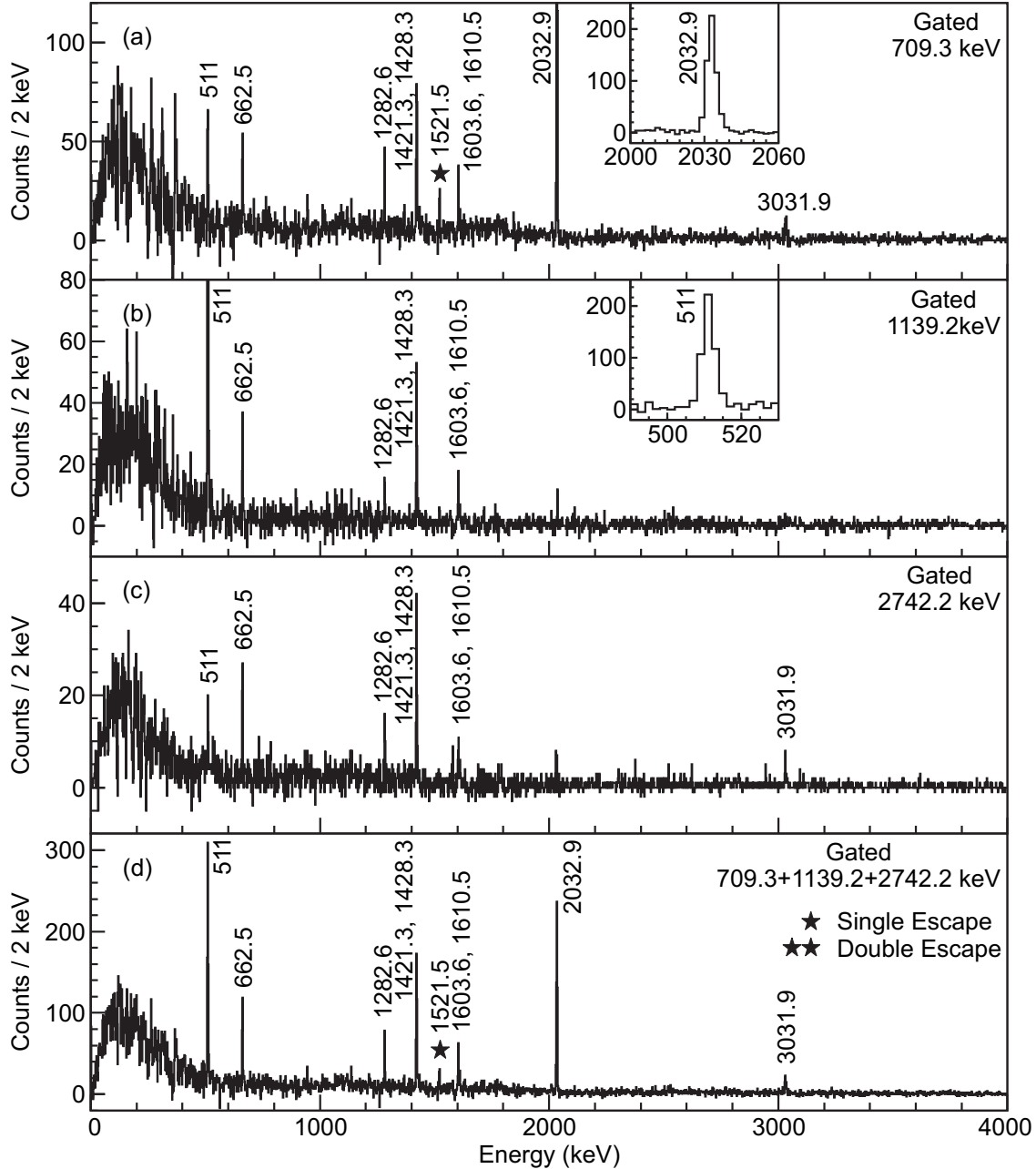


Figure B.2: Background-subtracted $\beta\gamma\gamma$ coincidence spectra gated on the (a) 709.3-keV, (b) 1139.2-keV, (c) 2742.2-keV, and (d) sum of the 709.3-, 1139.2-, and 2742.2-keV transitions. The background was taken symmetrically either side of each respective peak region. Coincident transitions are labeled with their energies and, when applicable, single-escape peaks are denoted with one star in addition to the energy of the peak. The insets in (a) and (b) show the full heights of the 2032.9-keV and 511-keV peaks truncated in (a) and (b), respectively.

Together, the $\beta\gamma\gamma$ coincidences present in Figs. B.1 and B.2 verify most of the ^{68}Ni low energy level-scheme in Fig. 4.1. In addition, several new γ rays are observed in Figs. 4.2,

B.1, and B.2. Using the $\beta\gamma\gamma$ coincidences, presented in Fig. B.3 many of these γ rays were placed in the ^{68}Ni level scheme.

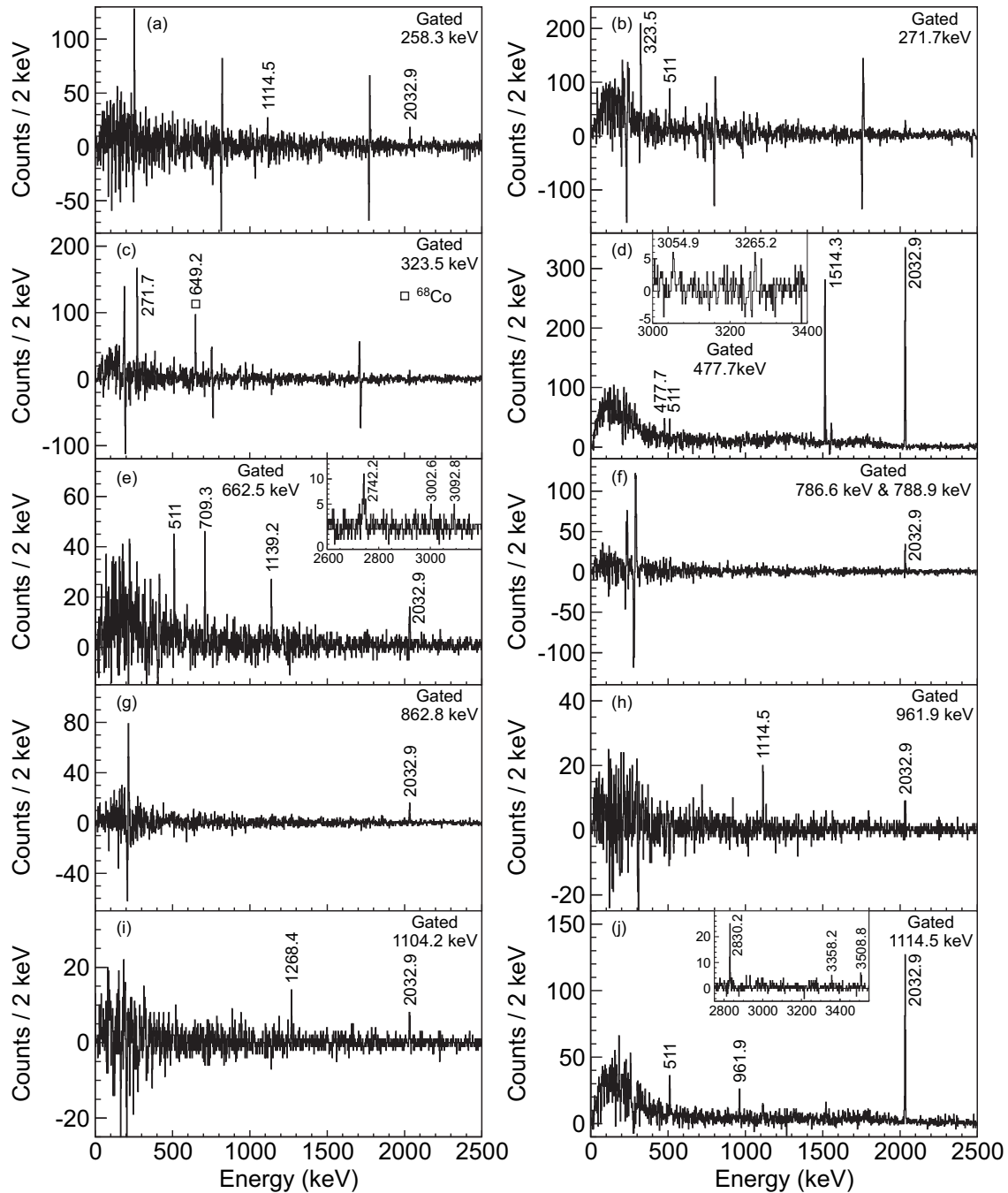


Figure B.3: Background-subtracted $\beta\gamma\gamma$ coincidence spectra. Coincident transitions are labeled with their energies. All insets display additional ranges of their respective spectra. The open square symbol used on (c) represents a contaminating 649.2-327.0-keV coincidence from ^{68}Co . A single asterisk after an energy label signifies the transition was observed exclusively in coincidence, and two asterisks following an energy label identifies a coincidence with contaminating transition.

Figure B.3: (cont'd)

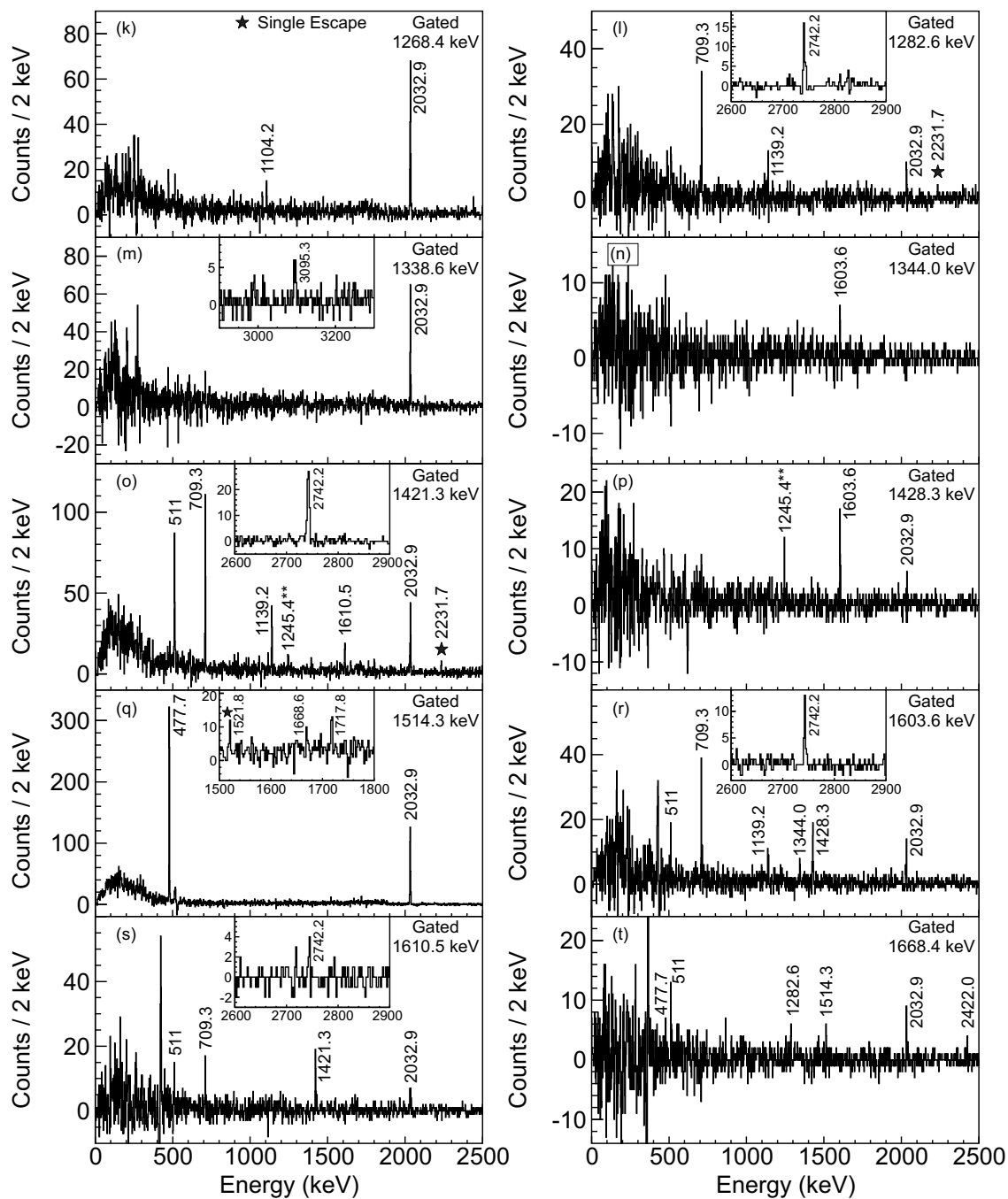


Figure B.3: (cont'd)

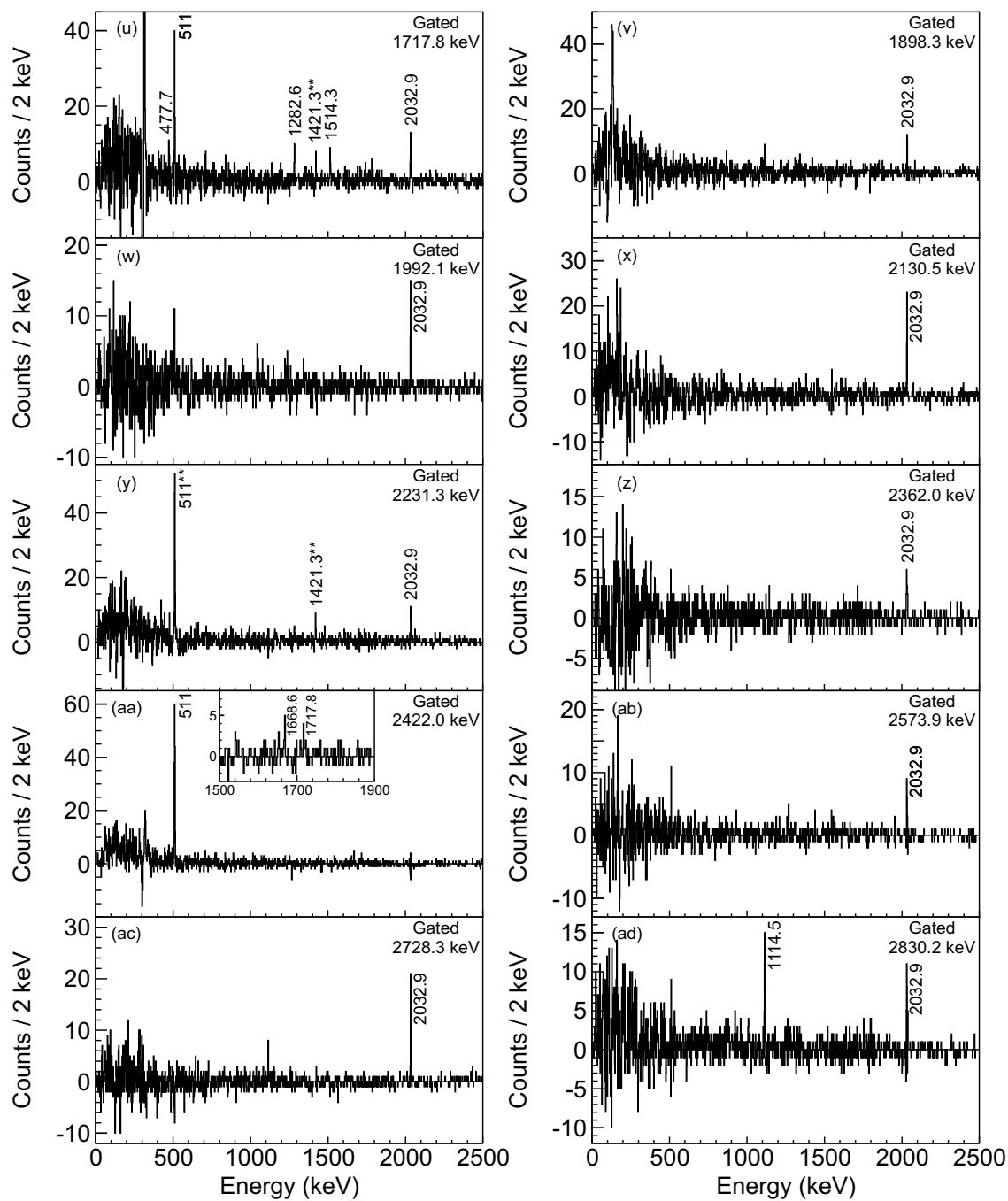


Figure B.3: (cont'd)

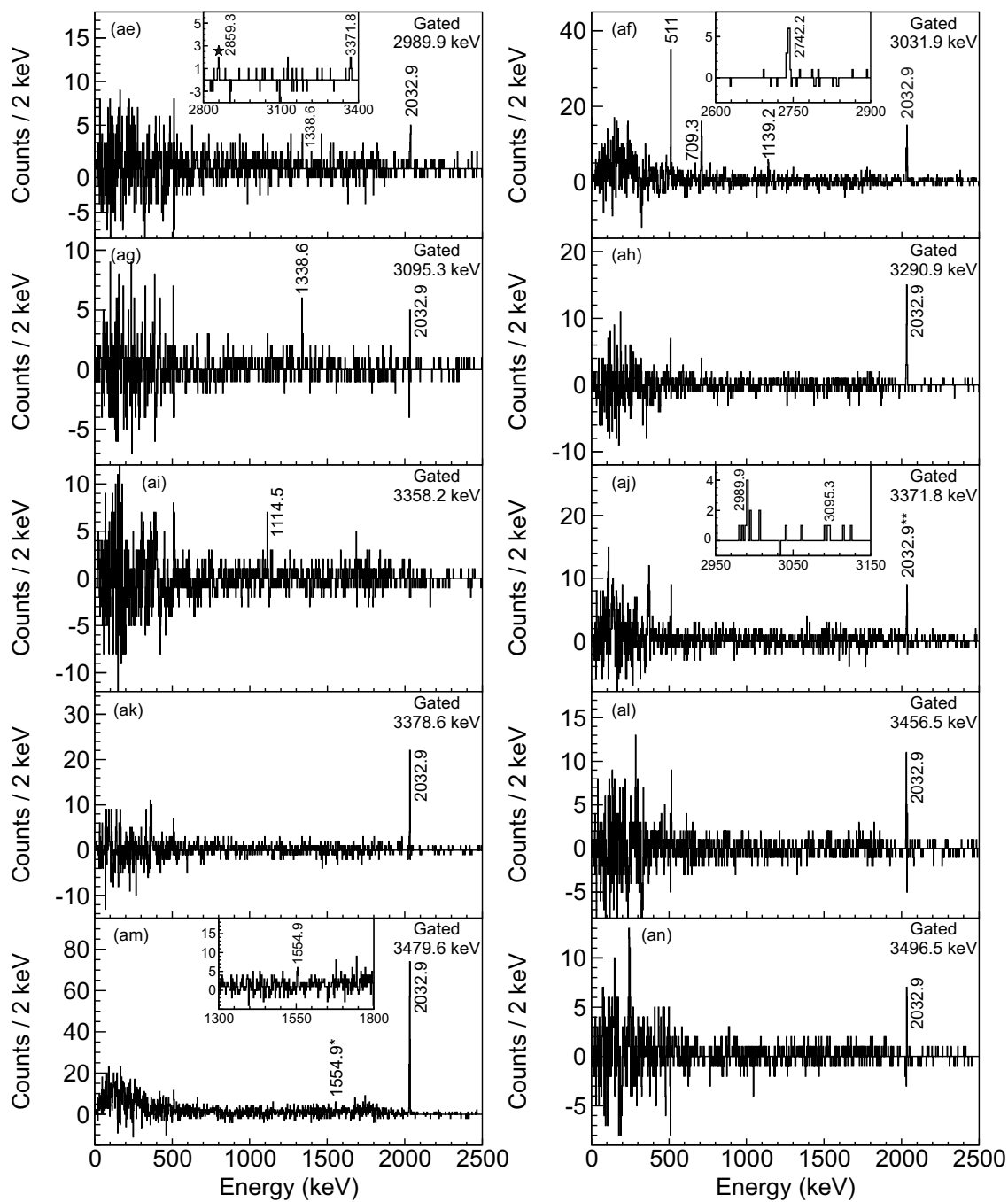


Figure B.3: (cont'd)

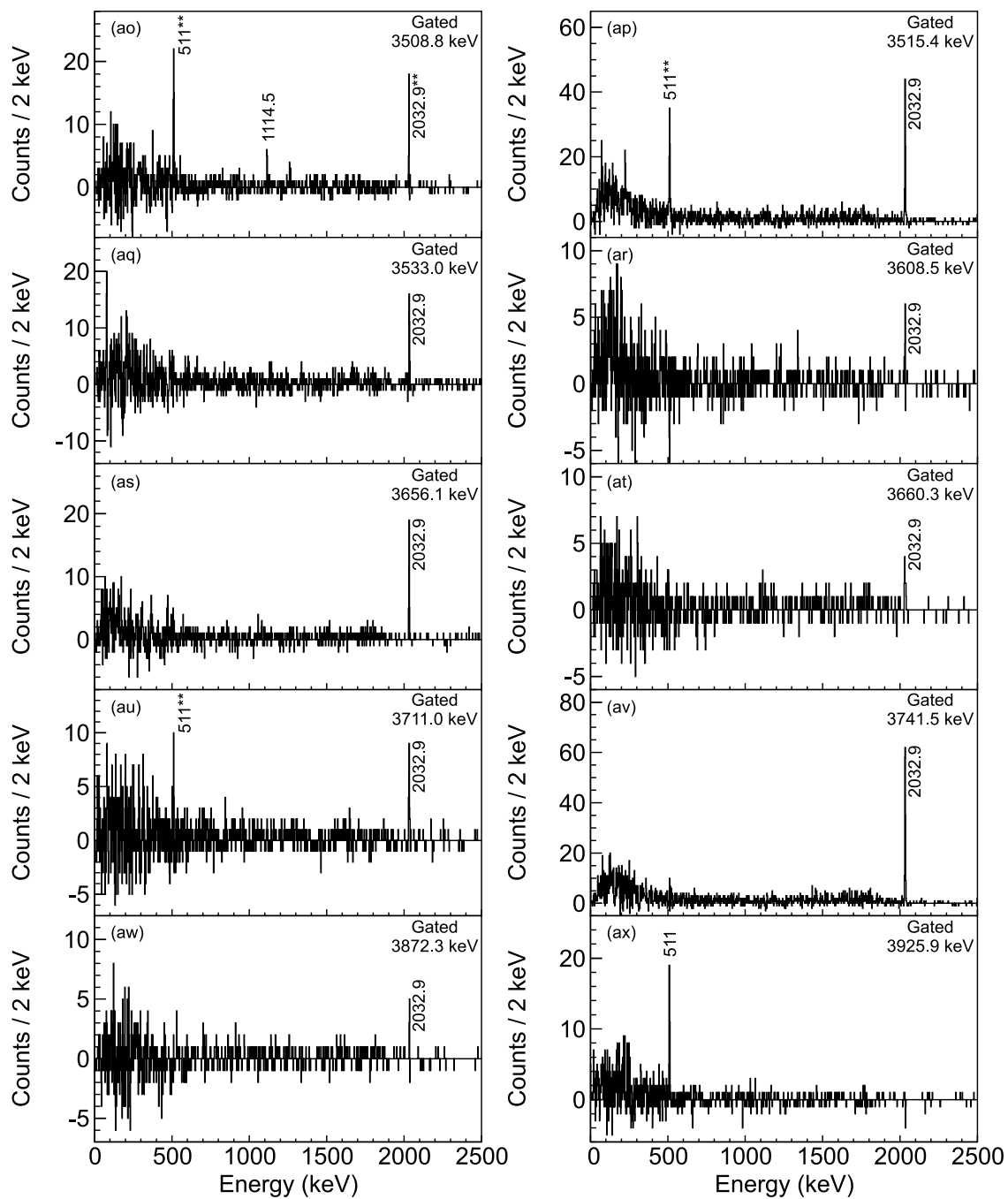
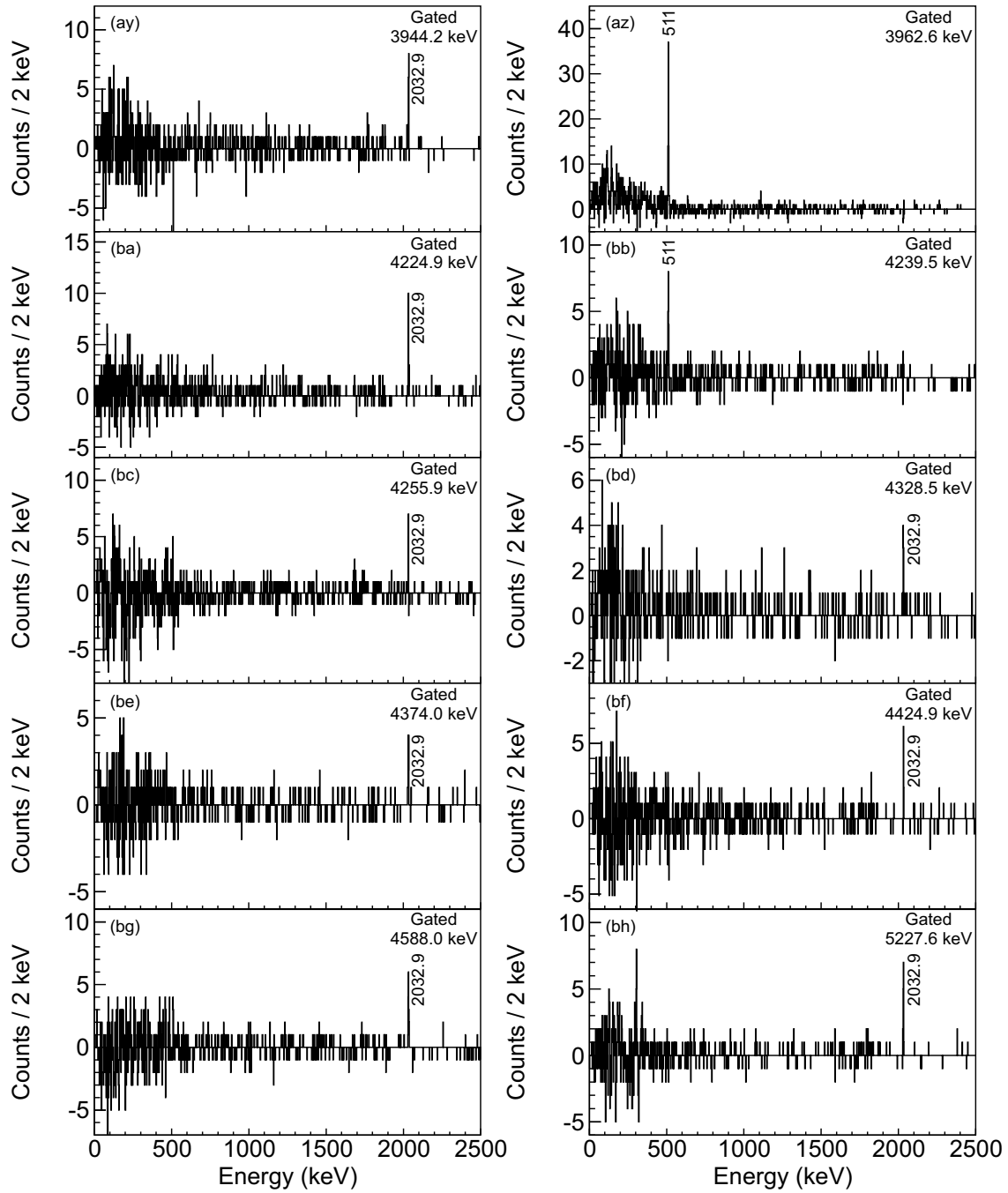


Figure B.3: (cont'd)



The 258.3-keV transition was first identified in the work of Ref. [20] and was placed depopulating a 3405-keV level. The 258.3-keV transition was also observed in later work and the 3405-keV state was assigned a tentative (4^+) spin and parity [82]. Figure B.3a shows the 258.3-1114.5-keV and 258.3-2032.9-keV coincidences thereby supporting the placement of the 258.3-keV depopulating the 3405-keV (4^+) state [82] feeding the 3147-keV 4^+ state [12].

The 271.7- and 323.5-keV transitions were first identified following the β decay of the short-lived, high-spin, ^{68}Co isomer [12]. The former depopulates a 3444-keV ($6^-, 7^-$) state feeding a 3120-keV (5^-) state while the latter depopulates the 3120-keV state feeding the isomeric 2847-keV 5^- state [83]. The work of Ref. [82] also observed these transitions, updated the energies of the two higher-lying states to 3442.6-keV and 3118.9-keV, and postulated (5^-) and (4^-) spins and parities for the two, respectively. Recently the 271.7-keV transition was also observed following β decay of ^{68}Co selectively populated by the β decay of ^{68}Fe [21].

In the present work a strong 271.7-323.5-keV coincidence is observed in Figs. B.3b and B.3c. Based on the absolute intensities and the observed coincidences the placement of these two transition is supported. The 595.5-keV transition [12, 82], parallel to the 271.7-323.5-keV cascade, is obscured in Fig. 4.2 by the 594.3-keV transition from ^{69}Ni [84] populated in the decay of ^{69}Co , a randomly correlated beam contaminant. The the 814.5-keV $5^- \rightarrow 2_1^+$ transition is not observed coincident with the β decay in Fig. 4.2 due to the 0.86(5) ms half life of the isomeric 2847-keV 5^- state [83] but is observed in γ -ray singles. The absolute intensities of the 814.5-keV and 271.7-keV transitions match within error suggesting that the 595.5-keV transition is weak compared to the 323.5-keV transition consistent with the results of Ref. [82].

The 477.7-keV transition [12] is known to depopulate the 2511-keV 0_3^+ state [20] feeding the 2032.9-keV 2_1^+ state. The work of Ref. [12] also identified a 1515-keV transition feeding

2511-keV 0_3^+ state from a 4025-keV (2^+) state. The 4024.6-keV ground-state transition is also observed in Fig. 4.2. In the present work strong 477.7-2032.9-keV, 477.7-1514.3-keV, and 1514.3-2032.9-keV coincidences are observed in Figs. B.3d and B.3q consistent with the current placement of the 477.7-keV and 1514.3-keV transitions. A weak 477.7-511-keV coincidence is observed in Fig. B.3d most likely from pair production originating from high-energy γ -rays feeding the 2511-keV 0_3^+ state. The 477.7-477.7-self coincidence observed in Fig. B.3d is new to this work and remains unexplained.

Two weaker coincidences between the 477.7-keV and 3054.9-keV and 3265.2-keV transitions are present in the inset of Fig. B.3d. If placed above the 1514.3-keV transition 8(2) 3054.9-1514.3-keV and 5(2) 3265.9-1514.3-keV coincidences would be expected of which zero are observed in each case. Therefore, the 3054.9-keV and 3265.2-keV transitions are placed feeding the 2511-keV state directly, depopulating a new state at 5566 keV, for which the ground state transition is observed in Fig. 4.2, and a previously identified 5774-keV state [21], respectively.

Two additional transitions are also placed depopulating the new 5566-keV level. The 3533.0-keV transition, observed in coincidence with the 2032.9-keV transition in Figs. B.1 and B.3aq, was placed feeding the 2033-keV 2_1^+ state from the 5566-keV level. A new 3962.6-keV transition observed in coincidence with 511-keV γ rays in Fig. B.3az, and the $0_2^+ \rightarrow 0_1^+$ $E0$ transition in Fig. 4.4 and was placed feeding the 1603-keV 0_2^+ state from the 5566-keV level.

In addition to the strong 1514.3-477.7-keV coincidence, three additional γ -ray coincidences with the 1514.3-keV transition are also present in Fig. B.3q. The coincidence at 1521.8 keV is from the single-escape peak of the 2032.9-keV transition. The other two transitions at 1668.6 keV and 1717.8 keV were placed feeding the 4025-keV (2^+) state from two

levels at 5693 and 5744 keV, respectively. A 3660.3-keV transition, observed in coincidence with the 2032.9-keV transition in Figs. B.1 and B.3at, is also placed depopulating the new 5693-keV level feeding the 2033-keV 2_1^+ state.

For the 1668.6-keV transition, the 1514.3-1668.6-keV coincidence is seen in Fig. B.3t and a 1668.6-2422.0-keV coincidence observed in Figs. B.5q, and B.3aa. A 1668.6-1282.6-keV coincidence is also observed in Figs. B.5l and B.5t, which is expected since the 1282.6-keV transition [21] feeds the 2742-keV 2_2^+ state from the 4025-keV (2^+) state.

The 1717.8-1514.3-keV coincidence is seen in Fig. B.3t. The 1717.8-2422.0-keV coincidence is observed in Figs. B.3u and B.3Ac. Additional coincidences between the 1717.8-keV transition and the 1282.6-keV, 1514.3, and 477.7-keV transitions in Fig. B.3u further support the placement of the 1717.8-keV transition feeding the 4025-keV (2^+) state. The coincidence with the 2032.9-keV transition in Fig. B.3u is predominately contamination from the unresolved 1716.0-keV transition seen in coincidence with the 2032.9-keV transition in Fig. B.1. The 1716.0-keV transition was placed feeding the 2033-keV 2_1^+ state from a new 3749-keV level. The peak at 1421.3-keV in Fig. B.3u, denoted with two asterisks, is the 1421.3-keV transition that feeds the 2742-keV 2_2^+ state from the 4163-keV (2^+) state detected in coincidence with the 1720-keV double escape peak from the 2742.2-keV transition that is also unresolved from the 1717.8-keV transition.

The 1992.1-2032.9-keV coincidence present in Figs. B.3w and B.1 places the new 1992.1-keV transition feeding the 2033-keV 2_1^+ state from the known 4025-keV (2^+) state.

In the present work, five transitions have been placed depopulating the 4025-keV (2^+) state with energies of 4024.6-keV, 2422.0-keV, 1992.1-keV, 1514.3-keV and 1282.6-keV. The background-subtracted $\beta\gamma\gamma$ coincidence spectrum gated on the sum of those five transitions is presented in Fig. B.4. In the summed coincidence spectrum presented in Fig. B.4 the

1668.6-keV and 1717.8-keV transitions are clearly observed and therefore confidently placed feeding the 4025-keV (2^+) state in the ^{68}Ni level scheme.

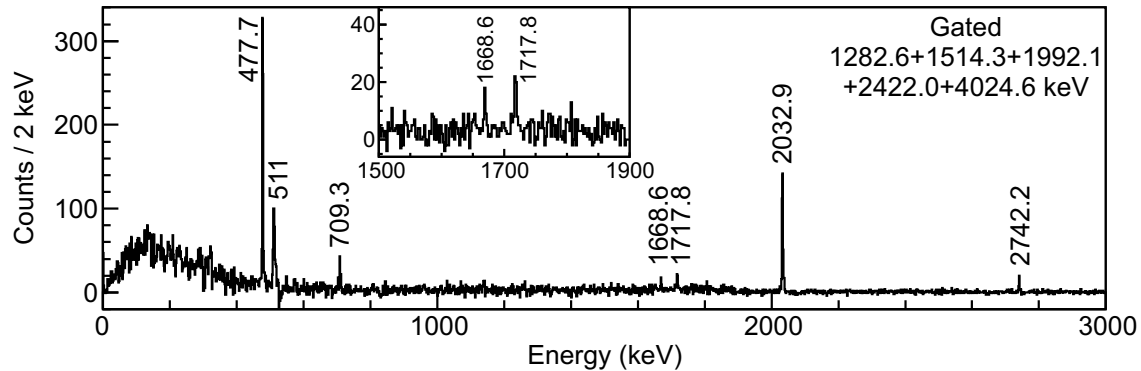


Figure B.4: Background-subtracted $\beta\gamma\gamma$ coincidence spectra gated on the sum of the 1282.6-keV, 1514.3-keV, 1992.1-keV, 2422.0-keV, and 4024.6-keV transitions. The background was taken symmetrically either side of each respective peak region. Coincident transitions are labeled with their energies. The inset shows a zoomed-in view of the 1500 to 1900 keV region of the spectrum.

The 662.5-keV transition is known to depopulate the 3405-keV (4^+) state [20,82] feeding the 2742-keV 2_2^+ state. Two coincidences between the 662.5-keV γ ray with new 3002.6-keV and 3092.8-keV γ rays are present in the inset of Fig. B.3e. These transitions are placed feeding the 3405-keV (4^+) state from two new levels at 6407 keV and 6498 keV.

A new doublet around ≈ 787 keV was observed in coincidence with the 2032.9-keV transition in Fig. B.3f. Though unresolved, a fit comprised of two Gaussians plus a linear background was performed extracting two peaks with energies of 786.6(4) and 788.9(2) keV. Gating either side of the doublet revealed exclusive coincidence with the 2032.9-keV suggesting that both transitions directly feed the 2032.9-keV 2_1^+ state from two new levels at 2820 and 2822 keV. The strong coincidence between the doublet and 2032.9-keV transition is shown in Figure B.3f.

A coincidence between a new 862.8-keV γ -ray and the 2032.9-keV transition is shown in Fig. B.3g, placing a new level at 2896 keV. The 961.9-keV transition is also new to this work

and is observed in coincidence with the 1114.5-keV and 2032.9-keV transitions in Fig. B.3h. Based on the coincidence relationships the 961.9-keV transition depopulates a new 4109-keV level feeding the feeding the 3147-keV 4^+ state [12].

The 1114.5-keV transition, first observed in the work of Ref. [12], feeds the 2032.9-keV 2_1^+ state from a 3148-keV 4^+ state [12,19–21,82]. Coincidence is observed between a new 961.9-keV γ ray and the 1114.5-keV transition in Figs. B.3h and B.3j and with the 2032.9-keV transition in Figs. B.3h and B.1. A new 2830.2-keV transition is also seen in coincidence with the 1114.5-keV transition in Figs. B.3j and B.3ad and also with the 2032.9-keV transition in Figs. B.3j and B.1. The 961.9-keV transition was placed feeding the 3148-keV 4^+ state from a new 4109-keV level while the 2830.2-keV transition is also placed feeding the 3148-keV 4^+ state from the 5977-keV level also new to this work. A 3944.2-keV transition, observed in coincidence with the 2032.9-keV transition in Fig. B.3ay, is also placed depopulating the 5977-keV level.

Two weaker coincidences between the 1114.5-keV transition and new 3358.2-keV and 3508.8-keV transitions are shown in the inset of Fig. B.3j and Figs. B.3ai and B.3ao, respectively. These two transitions are placed feeding the 3148-keV 4^+ state directly from two new levels at 6506 keV and 6656 keV. The coincidences between the 3508.8-keV transition and the 2032.9-keV and 511-keV γ -rays are due to contamination in the gate from the 3515.4-keV transition (see Fig. B.3ap) and the 3514-keV single-escape peak of the 4024.6-keV transition, respectively.

Coincidences between the new 1104.2-keV γ ray and the 1268.4-keV transition are observed in Figs. B.3i and B.3k. A 1104.2-2032.9-keV coincidence is also present in Figs. B.3i and B.1 along with a strong 1268.4-2032.9-keV coincidence in Figs. B.3k and B.1. The 1268.4-keV transition was first observed in the Ref. [20] and placed feeding the 2032.9-keV 2_1^+

state from a new level at 3301 keV. Subsequent studies [21,82] also observed the 1268.4-keV transition and confirmed its placement. The present work places the 1104.2-keV transition depopulating a new level at 4405 keV feeding the 3301-keV level which in turn decays by the 1268.4-keV transition to the 2032.9-keV 2_1^+ state.

The 1338.6-keV transition, observed in coincidence with the 2032.9-keV transition in Figs. B.3l and B.1, is new to this work. There is also coincidence between the 1338.6-keV transition and another new γ ray at 3095.3 keV. Based on the absolute intensities and the observed coincidences the 1338.6-keV transition was placed feeding the 2033-keV 2_2^+ state from a new 3372-keV level, which is fed by the 3095.3-keV transition from another new level at 6467 keV. The 3371.8-keV ground-state transition is observed in the β -delayed γ -ray spectrum shown in Fig. 4.2.

The 1421.3-keV transition is known to feed the 2742-keV 2_2^+ state from the 4163-keV (2^+) state [21]. The 1610.5-keV transition is new to this work and placed feeding the 4163-keV (2^+) state from the 5774-keV level [21] based on the 1421.3-1610.5-keV coincidence observed in Figs. B.3o and B.3s. The 1610.5-709.3-keV coincidences displayed in Figs. B.2a, B.2d, and B.3s and the 1610.5-2032.9-keV coincidences present in Figs. B.3s and B.1 originate from the 1610.5-1421.3-709.3-2032.9-keV γ -ray cascade. The 1610.5-2742.2-keV coincidence is also present in Figs. B.2c, B.2d, and B.3s from the 1610.5-1421.3-2742.2-keV γ -ray cascade. The coincidence with the 1245.4-keV transition, denoted with two asterisks, present in both Figs. B.3o and B.3p is from a coincidence with a 1424.0-keV transition from an unknown source that contaminates each respective gate.

The 1603.6-keV and 1428.3-keV transitions are both new to this work. The 1603.6-keV transition is observed in coincidence with the 709.3-keV, 1139.2-keV, and 2742.2-keV transitions in Figs. B.3r and B.2d, and Figs. B.2a, B.2b, and B.2c, respectively. A 1603.6-

1428.3-keV coincidence is also observed in Figs. B.3r and B.3p. Based on the absolute intensities and coincidence relationships the 1603.6-keV transition was placed feeding the 2742-keV 2_2^+ state from a new level at 4346-keV, which is fed by the 1428.3-keV transition from the known 5774-keV level [21]. The 1603.6-511-keV coincidence observed in Fig. B.3r is predominantly due to the pair-production decay mode of the coincident $0_2^+ \rightarrow 0_1^+$ $E0$ transition. Once again the coincidence with the 1245.4-keV, denoted with two asterisks, present in both Figs. B.3o and B.3p is from a coincidence with a 1424.0-keV transition that contaminates each respective gate.

An additional coincidence between the 1603.6-keV transition and a new 1344.0-keV γ ray is present in Figs. B.3n and B.3r. A strong coincidence between a new 3656.1-keV γ ray and the 2032.9-keV transition is present in Figs. B.3as and B.1. Both coincidence relationships place a new level at 5689 keV.

The 1898.3-2032.9-keV coincidence observed in Fig. B.3v is also present in Fig. B.1 placing a new level at 3931 keV depopulated by the new 1898.3-keV transition feeding the 2033-keV 2_1^+ state. The new 2130.5-keV transition is seen in coincidence with the 2032.9-keV γ ray in Figs. B.3x and B.1 and was placed feeding the 2033-keV 2_1^+ state from the known 4163-keV (2^+) state.

The 2032.9-2231.3-keV coincidence observed in Figs. B.3y and B.1 places a new level at 4264 keV depopulated by the new 2231.3-keV transition which feeds the 2033-keV 2_1^+ state. The coincidences between the 2231.3-keV γ with the 511-keV and 1421.3-keV γ rays, denoted with two asterisks in Fig. B.3y, arise from coincidences with the single escape peak from the 2742.2-keV transition which is unresolved with the 2231.3-keV transition.

A coincidence between a new 2362.0-keV γ ray and the 2032.9-keV transition is observed in Figs. B.3y and B.1. The 2362.0-keV transition was placed feeding the 2033-keV 2_1^+ state

from a new 4394 keV level. A new 2573.9-keV γ is shown in coincidence with the 2032.9-keV transition in Figs. B.3ab and B.1. The 2573.9-keV transition was placed feeding the 2033-keV 2_1^+ state from a new level at 4607 keV. The 4607.2(5)-keV ground-state transition is observed in Fig. 4.2).

The coincidence between a new 2728.3-keV γ ray with the 2032.9-keV transition is shown in Figs. B.3ab and B.1. The 2728.3-keV transition was placed feeding the 2033-keV 2_1^+ state from a new level at 4761 keV.

The new 2989.9-keV γ ray is observed in coincidence with the 3371.8-keV γ ray, and associated 2859.3-keV single escape peak, in Fig. B.3ae. In addition, coincidences between the 2989.9-keV γ ray and the 1338.6-keV and 2032.9-keV transitions are also present in Fig. B.3ae. When gating on the 3371.8-keV transition, shown in Fig. B.3aj, the 2989.9-keV and 3095.3-keV transitions are observed in coincidence. Coincidences between the 3095.3-keV transition and the 1338.6-keV and 2032.9-keV γ rays are shown in Fig. B.3ag. The 3371.8-keV transition was placed as the ground state transition for the 3372-keV level fed by the 2989.9-keV and 3095.3-keV transitions from two new levels at 6361 and 6467 keV, respectively.

The coincidence with the 2032.9-keV transition in Fig. B.3aj, labeled with two asterisks, results from contamination of the gate from the 3378.6-keV transition. The 3378.6-2032.9-keV coincidence is shown in Fig. B.3ak and the 3378.6-keV was placed feeding the 2033-keV 2_1^+ state from a new level at 5411 keV.

The 3031.9-keV transition was placed feeding the 2742-keV 2_2^+ state. Strong 3031.9-1139.2-keV coincidences are seen in Figs. B.2b, B.2d, and B.3af. In addition the 3031.9-709.3-keV coincidences observed in Figs. B.2a, B.2d, and B.3af, 3031.9-2032.9-keV coincidences seen in Figs. B.1 and B.3af, and 3031.9-2742.2-keV coincidences present in Figs.

B.2c, B.2d, and B.3af all support the placement of the 3031.9-keV transition feeding the 2742-keV 2_2^+ state from the known 5774-keV level [21].

The 3290.9-keV and 3456.5-keV γ rays are both new to this work and are observed in coincidence with the 2032.9-keV transition, exclusively, in Fig. B.1 and Figs. B.3ah and B.3al, respectively. The 3290.9-keV and 3456.5-keV transitions are placed directly feeding the 2033-keV 2_1^+ state from two new levels at 5243 keV and 5489 keV, respectively.

The 3479.6-keV transition, first observed in the work of Ref. [12], was placed feeding the 2033-keV 2_1^+ state from a 5513-keV level [12]. The strong 3479.6-2032.9-keV coincidence is observed in Figs. B.1 and B.3am confirms this placement. A second coincidence between the 3479.6-keV transition and a new 1554.9-keV transition is also present in Fig. B.3am. The 1554.9-keV γ -ray is too weak to see in the β -gated γ -ray singles spectrum shown in Fig. 4.2 and placed above the 3479.6-keV transition in the γ -ray cascade feeding the 5513-keV level from a new level at 7067-keV.

A coincidence between a new 3496.5-keV γ ray and the 2032.9-keV transition is observed in Fig. B.3an, placing a new level at 5529 keV for which the 5528.7-keV ground-state transition is observed in Fig. 4.2. A new 3925.9-keV transition observed in coincidence with 511-keV γ rays in Fig. B.3ax, and the $0_2^+ \rightarrow 0_1^+$ $E0$ transition in Fig. 4.4 and was placed feeding the 1603-keV 0_2^+ state from the 5529-keV level.

A strong coincidence between the 3515.4-keV and 2032.9-keV transitions is observed in Figs. B.1 and B.3ap. The 3515.4-keV transition was first observed in the work of Ref. [12] and subsequently by Ref. [21] and was placed feeding the 2033-keV 2_1^+ state from a 5549-keV level [12, 21]. The present work confirms this placement. The 3515.4-511-keV coincidence, denoted with two asterisks in Fig. B.3aq, results from the 3513.6-keV single escape peak from the 4024.6-keV transition that unresolved from the 3515.4-keV transition.

The 3608.5-keV γ ray was observed in coincidence with the 2032.9-keV transition in Fig. B.3ar placing a new level at 5641 keV. The 3711.0-keV transition was placed feeding the 2033-keV 2_1^+ state from the 5743-keV level, discussed earlier in this section, based on the 3711.0-2032.9-keV coincidences observed in Figs. B.1 and B.3au. The 3711.0-511-keV coincidence observed in Fig. B.3au is from the 3713.9-keV single escape peak of the 4224.9-keV transition. The absolute intensity of the 3711.0-keV adjusted accordingly to correct for this contamination.

A strong coincidence between the 3741.5-keV and 2032.9-keV transitions is observed in Figs. B.1 and B.3av. The 3741.5-keV transition was first observed in the work of Ref. [12] and subsequently by Ref. [21] and was placed feeding the 2033-keV 2_1^+ state from a 5774-keV level [12, 21]. The present work confirms this placement.

The new 3872.3-keV transition was coincident with the 2032.9-keV transition in Fig. B.3aw and was placed feeding the 2033-keV 2_1^+ state from a new level at 5905 keV. The 4224.9-keV level is also new to this work and is shown in coincidence with the 2032.9-keV transition in Figs. B.1 and B.3ba placing a new level at 6258 keV.

A new 4239.5-keV transition is shown in coincidence with 511-keV γ rays and the $0_2^+ \rightarrow 0_1^+$ $E0$ transition in Figs. B.3bb and 4.4 and was placed feeding the 1603-keV 0_2^+ state from a new level at 5843 keV.

The 4255.9-keV, 4328.5-keV, 4374.0-keV, 4424.9-keV, 4588.0-keV, and 5227.6-keV transitions are all new to the present work and observed in coincidence with the 2032.9-keV transition in Figs. B.3bc, B.3bd, B.3be, B.3bf, Figs. B.3bg and B.1, and Figs. B.3bh and B.1, respectively, and are placed feeding the 2033-keV 2_2^+ state from new levels at 6289, 6361, 6407, 6458, 6621, and 7260 keV. These coincidences are summarized in Table 4.2.

$\beta\gamma\gamma$ -double-pulse Coincidences

The unambiguous identification of the $0_2^+ \rightarrow 0_1^+$ $E0$ transition coupled with the high statistics in the present work permits examination of $\beta\gamma\gamma$ -double-pulse quadruple coincidences. The background subtracted quadruple coincidence spectra are presented in Fig. B.5 and allow placement of several transitions listed in Table 4.3. In each case the background was taken symmetrically, directly above and below, the peak of interest.

The $\beta\gamma\gamma$ -double-pulse coincidences in Fig. B.5 allow identification and placement of weak transitions. Stronger transitions observed earlier in this section also show coincidences in Fig. B.5 but will not be discussed any further.

A new 1579.2-keV γ -ray is observed in coincidence with both the 1421.3- and 1139.2-keV transitions in Fig. B.5g. The weak intensity of the 1579.2-keV transition precludes observation of 1421.3-1579.2-keV and 1139.2-1579.2-keV coincidences in Figs. B.5d and B.5a, respectively. The 1579.2-keV transition was placed feeding the 4164-keV (2^+) state from the 5743-keV level identified earlier in this section.

The 1540.7-keV transition is also new to this work and observed in coincidence with the 1139.2-keV transition in Fig. B.5f. The 1540.7-keV transition was placed feeding the 2742-keV 2_2^+ state from a new level at 4283 keV.

A coincidence between a new 1631.2-keV γ ray and the 1139.2-keV transition is observed in Fig. B.5j, placing a new level at 4373 keV. In Figs. B.5k and B.5p a coincidence between a new 1641.3-keV and 2529.8-keV transitions. Based on the absolute intensities and the lack of any other coincidences the 2529.8-keV transition was placed feeding the 1603.5-keV 0_2^+ state from a new level at 4132 keV and the 1641.3-keV transition was placed feeding that new 4132-keV level from the known 5774-keV level [12].

In Fig. B.5m a coincidence is present between a new 1713.3-keV γ -ray and the 1139.2-keV transition. The 1713.3-keV transition was placed feeding the 2742-keV 2_2^+ state from a new 4456-keV level. The weak intensity of the 1713.3-keV transition precludes observation of the 1139.2-1713.3-keV coincidence in Fig. B.5a. These coincidences are summarized in Table 4.2.

The remainder of the transitions listed in Table 4.3 displayed no coincidences (other than with 511-keV γ rays) and as such are hard to place precisely in the ^{68}Ni level scheme. However, the coincidence with the $0_2^+ \rightarrow 0_1^+$ $E0$ transition requires that they feed the 1603-keV 0_2^+ state either directly or indirectly.

An attempt was made to match energy sums of unplaced transitions with observed levels with other observed levels or energy sums. Several transitions were placed using this technique. The 1366.4-keV and 1400.3-keV transitions were placed feeding the 4164-keV level depopulating the new 5530-keV and 5565-keV levels discussed previously in this section.

The sum of the 1705.3-keV transition with the 2742-keV level and the sum of the 2860.8-keV transition with the 1603-keV level both sum to a new level at 4448 keV. Furthermore, if the 2860.8-keV transition were located above the 1139.2-keV, 1421.3-keV, or 2422.0-keV (or any transition lower in energy) the expected number of coincidences would be readily observed, supporting this placement. The two energy sums match each other within 0.05 keV lending further credibility.

The sum of the 2947.1-keV γ -ray with the 2742-keV state gives a state with an energy of 5689 keV and the sum of the 3235.0-keV γ -ray with the 2742-keV state gives a state with an energy of 5977 keV. The 5689-keV and 5977-keV levels were already mentioned earlier in this section.

The sum of the 3218.4(11)-keV transition with the 4025-keV state, 4500.1(3)-keV tran-

sition with the 2742-keV state, and the 5639.8(8)-keV transition with the 1603-keV state all yield an energy of ≈ 7242 -keV and are consistent within a 1σ error. Examining the β -gated γ -ray singles spectrum, shown in Fig. B.1, a 7240.5(10) keV transition is observed which in the limit of 2σ is consistent with the weighted average energy of the three sum energies mentioned above. Therefore the 3218.4-keV, 4500.1-keV, and 5639.8-keV transitions are all placed depopulating a new 7242-keV state.

The sum of the 4198.7.1-keV γ -ray with the 2742-keV state and the sum of the 5337.7-keV γ -ray with the 1603-keV both give an energy of 6941 keV. Since the two sums match each other within 0.25 keV the placement of a new level at 6941-keV, depopulated by those two transitions, can be made with reasonable confidence.

The 5395.8-keV, 5978.0-keV, and 6178.6-keV transitions were placed feeding the 1603-keV 0_2^+ state since it is unlikely that they originate from states above the 7792(4)-keV [56] neutron separation energy, placing new levels at 6999, 7581, and 7782 keV, respectively.

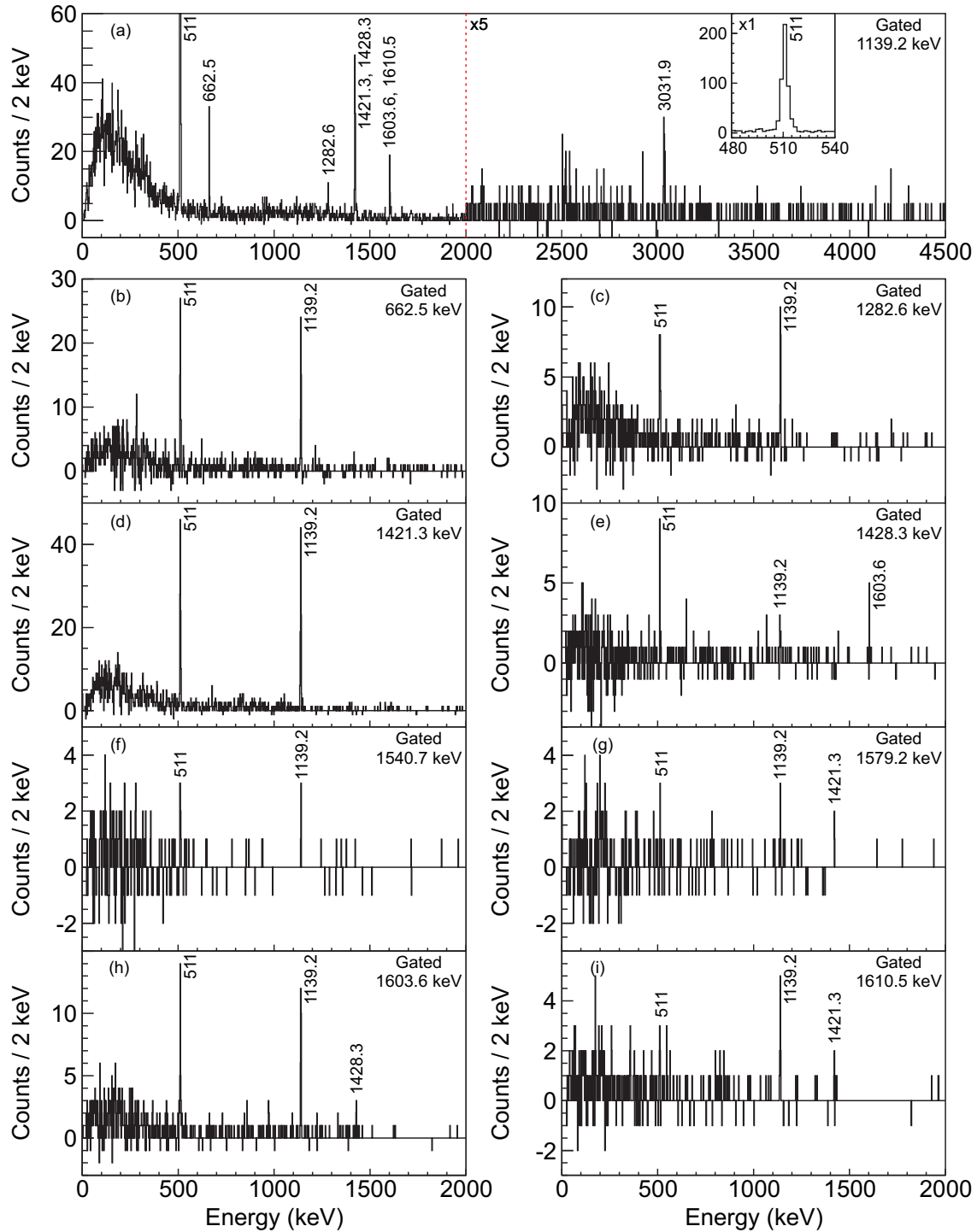
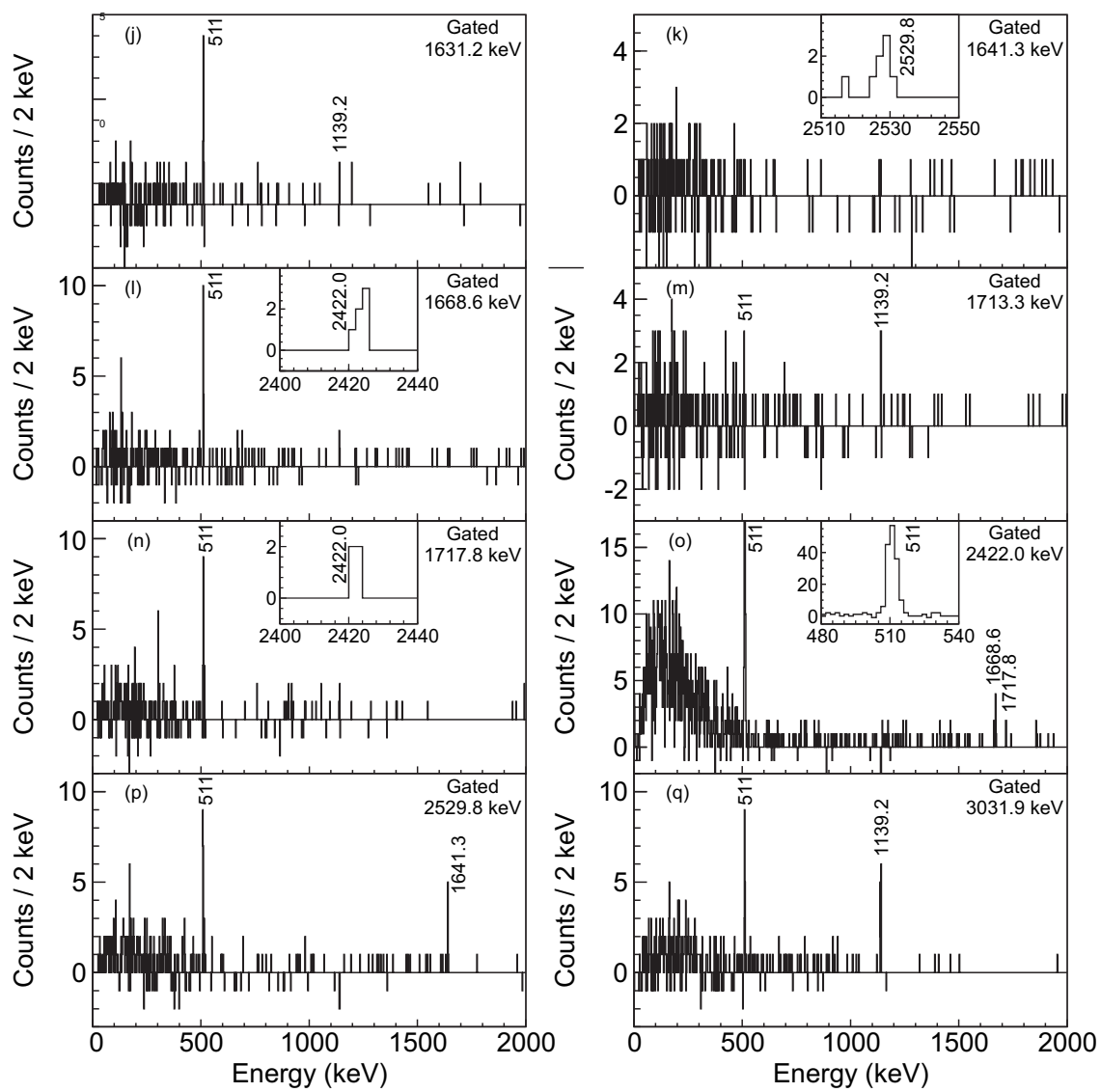


Figure B.5: Background-subtracted $\beta\gamma\gamma$ -double-pulse coincidence spectra recorded in coincidence with the detection of the $0_2^+ \rightarrow 0_1^+$ $E0$ transition in ^{68}Ni . The background was taken symmetrically either side of the peak except. The inset in (a) shows the full height of the 511-keV peak cut off in the spectrum displayed in (a). The inset in panel (k) shows the region between 2510 and 2550 keV for the spectrum in (k). The insets in panels (l) and (n) show the region between 2400 and 2440-keV for the same spectrum in each panel. The inset in (o) shows the full height of the 511-keV peak cut off in the spectrum displayed in (o).

Figure B.5: (cont'd)



Appendix C

$\beta\gamma\gamma$ Coincidences Observed Following the β -Decay of the Short-Lived, High-Spin, ^{70}Co Isomer.

In this appendix the $\beta\gamma\gamma$ coincidences observed following the β -decay of the short-lived, high-spin, ^{70}Co isomer are presented. These coincidences were used to identify and place levels in the low-energy ^{70}Ni level scheme. $\beta\gamma\gamma$ coincidence spectra are shown in Fig. C.1 for all ten transitions listed in Table 4.9. In Fig. C.1 all coincidences belonging to ^{70}Ni affiliated with the short-lived, high-spin, ^{70}Co isomer are labeled with an energy while transitions affiliated with the long-lived, low-spin, ^{70}Co isomer are denoted with black squares.

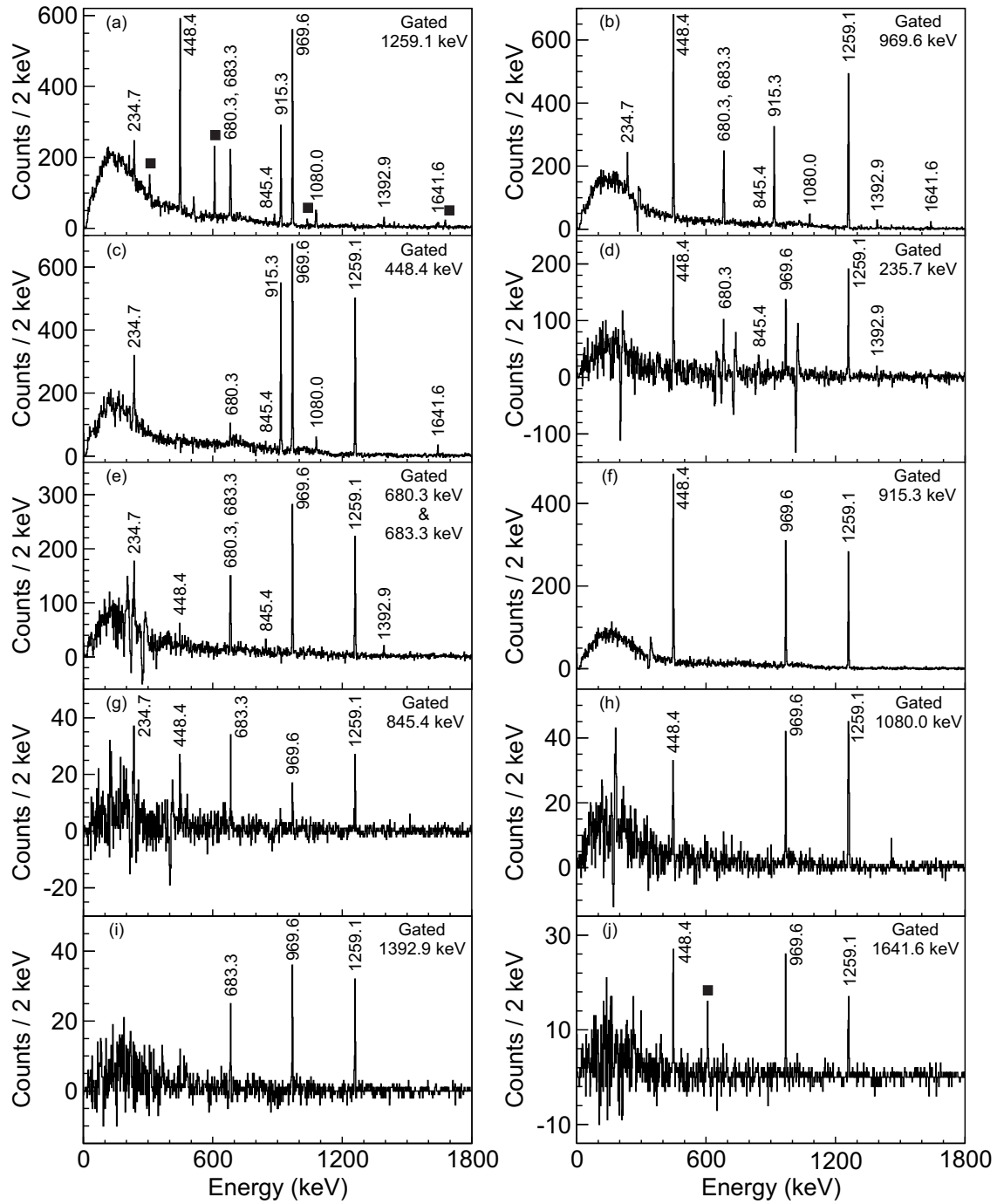


Figure C.1: Series of background subtracted $\beta\gamma\gamma$ coincidence spectra correlated to the decay of the short-lived, high-spin, ^{70}Co isomer. The background was taken symmetrically either side of the peak except where other γ rays interfered, in which case the background was taken above as close as possible to the peak of interest. Transitions affiliated with the long-lived, low-spin, ^{70}Co isomer are denoted with black squares.

The γ rays coincident with the 1259.1-keV ($2_1^+ \rightarrow 0_1^+$) transition are shown in Fig. C.1a. Since the 1259.1-keV transition collects intensity from the decay of both ^{70}Co isomers, transitions affiliated with the decay of the long-lived, low-spin, isomer, denoted by black squares in Fig. C.1a, are present and discussed in the next section. Based on the existing knowledge of the ^{70}Ni level scheme the strong 1259.1-969.6-keV coincidences observed in Figs. C.1a and C.1b, 1259.1-448.5-keV coincidences observed in Figs. C.1a and C.1c, and 448.5-969.6-keV coincidences observed in Figs. C.1b and C.1c are expected.

In the present work 1030(60) 1259.1-969.6-keV coincidences and 1277(65) 448.4-969.6-keV coincidences are expected of which 1085(50) and 1337(65) are observed, respectively, thereby validating the coincidence spectroscopy techniques used herein. All other coincidences presented in this work were verified in this same manner.

Coincidence with a 234.7-keV transition is observed in Figs. C.1a, C.1b, and C.1c. In turn Fig. C.1d, gated on the 234.7-keV transition, shows strong coincidences with the 448.4-keV, 969.6-keV, and 1259.1-keV transitions. Based on the absolute intensities, and the recorded number of 234.7-448.4-keV coincidences, the 234.7-keV transition was placed feeding the 2677-keV 6_1^+ state from the 2912-keV (5^-) state as reported by Ref. [23].

In Fig. C.1f the γ rays coincident with the 915.3-keV transition are presented. The spectrum is very clean and strong coincidences with the 448.4-keV, 969.6-keV, and 1259.1-keV transitions are observed with no other coincidences present. The proposed placement of the 915.3-keV transition depopulating a state at 3592 keV feeding the 2677-keV 6_1^+ state [23] is certainly correct.

The coincidence spectra for the 845.4-keV and 1080.0-keV transitions are shown in Figs. C.1g and C.1h. In Fig. C.1g there are coincidences with between the 845.4-keV transition and the 234.7-keV, 448.4-keV, 969.6-keV, and 1259.1-keV transitions. Based on the recorded

coincidences and the absolute intensities we support the placement of the 845.4-keV transition depopulating the new 3757-keV (7^-) state and feeding the proposed 2912-keV (5^-) state.

In Fig. C.1h the 1080.0-keV transition is observed in coincidence with the 448.5-keV, 969.6-keV, and 1259.1-keV transitions. Furthermore, the 1080.0-keV transition is not in coincidence with either the 234.7-keV or the 683.3-keV transitions suggesting that it runs in parallel with them. The current results support the conclusion of Ref. [23] that the 1080.0 depopulates the 3757-keV (7^-) state and feeds the 2677-keV 6_1^+ state.

The observation of the 1392.9-keV is new to this work. In Fig. C.1i strong coincidences are observed with 683.3-keV, 969.6-keV, and 1259.1-keV transitions with no other coincidences observed. Based on the recorded coincidences and lack of coincidences with transitions higher in the level scheme the 1392.9-keV is proposed to depopulate a new state at 4305 keV feeding the 2912-keV (5^-) state.

In the present work the 683.3-keV transition is observed to be self coincident. In the β -gated γ -ray singles spectrum, shown in Fig 4.22b, a peak with an anomalous large width and a centroid of ≈ 682 keV is observed. In Fig. C.1e the γ rays coincident with the wide ≈ 682 -keV peak are presented. In addition to a strong self coincidence, strong coincidences with 969.6-keV and 1259.1-keV are observed along with weaker coincidences with 234.7-keV, 448.4-keV, 845.4-keV, and 1392.9-keV. Looking closely at the other coincidence spectra for coincidences between only one of the transitions in the doublet we observe four such cases. In Figs. C.1c and C.1d, 448.4-680.3-keV and 234.7-680.3-keV coincidences are observed, respectively. This would place the 845.4-keV and 1392.9-keV transitions parallel to the new 680.3-keV transition, which is supported by the 845.4-683.3-keV and 1392.9-683.3-keV coincidences observed in Figs. C.1g and C.1i, respectively. This suggests that a 680.3-keV

transition feeds the 2912-keV (5^-) state from the 3592-keV (6^-) state. The intensity of the 680.3-keV and 683.3-keV transitions were deduced from the recorded coincidences. There were 402(30) counts in the self coincidence that when divided by two and corrected for efficiency gives 4660(415) counts. This is how many events in singles flow through the 680.3-683.3-keV γ -ray cascade. However there is also the 680.3-234.7-keV γ -ray cascade. There are 139(25) counts in the 680.3-234.7-keV coincidence, and corrected for the 234.7-keV γ -ray efficiency gives 1910(350) counts. The sum of those two cascades is the number of counts in the doublet that belong to the 680.3-keV transition while the remainder are attributed to the 683.3-keV transition. Using this information coupled with the number of counts in the doublet, obtained from the β -delayed γ -ray singles, the absolute intensities, reported in Table 4.9, were deduced.

The last transition new to this work is the 1641.6-keV γ ray. In Fig. C.1j strong coincidences between 1641.6-keV transition and the 448.4-keV, 969.6-keV, and 1259.1-keV transitions are observed. The 1641.6-keV transition is also a doublet evidenced by the width of the peak in Fig. 4.22d and the results of the isomer separation in Fig. 4.35e. Thankfully the two transitions composing the \approx 1642-keV doublet are affiliated exclusively with the decay of different ^{70}Co isomers making the analysis more straightforward than that of the \approx 682-keV doublet. The contaminating 1643.5-607.5-keV coincidence, denoted by the black square in C.1j will be discussed in the next section. Based on the observed coincidences the 1641.6-keV transition most likely feeds the 2677-keV 6_1^+ state placing a new level at 4319 keV.

A summary of all observed coincidences is shown in Table 4.10

Appendix D

$\beta\gamma\gamma$ Coincidences Observed Following the β -Decay of the Long-Lived, Low-Spin, ^{70}Co Isomer.

In this appendix the $\beta\gamma\gamma$ coincidences observed following the β -decay of the long-lived, low-spin, ^{70}Co isomer are presented. These coincidences were used to identify and place levels in the low-energy ^{70}Ni level scheme. Figure D.1 presents a series of $\beta\gamma\gamma$ coincidence spectra for γ rays observed following the decay of the long-lived, low-spin ^{70}Co isomer.

In Fig. D.1a the γ rays coincident with a new 1037.5-keV γ ray are shown. The 1259.1-1037.5-keV coincidence observed in Fig. D.1a is also observed in Fig. 4.37a. The 1037.5-keV transition was placed feeding the 1259.1-keV 2_1^+ state from a new level at 2296 keV. In singles there is a 2294.3-keV transition not in coincidence with any other γ rays which, despite the ≈ 2 keV energy difference, is proposed to be the ground-state transition for this new state.

In Figs. D.1b and 4.37a a coincidence between a new 1441.2-keV transition and the 1259.1-keV γ ray is observed, which places a new level at 2700 keV. Furthermore, a relatively intense transition is observed in β -gated γ -ray singles at 2700.3 keV, not in coincidence with any other γ rays, and is presumed to be the ground-state transition for the new level.

A strong coincidence between a new 1676.3-keV γ -ray with the 1259.1-keV transition is

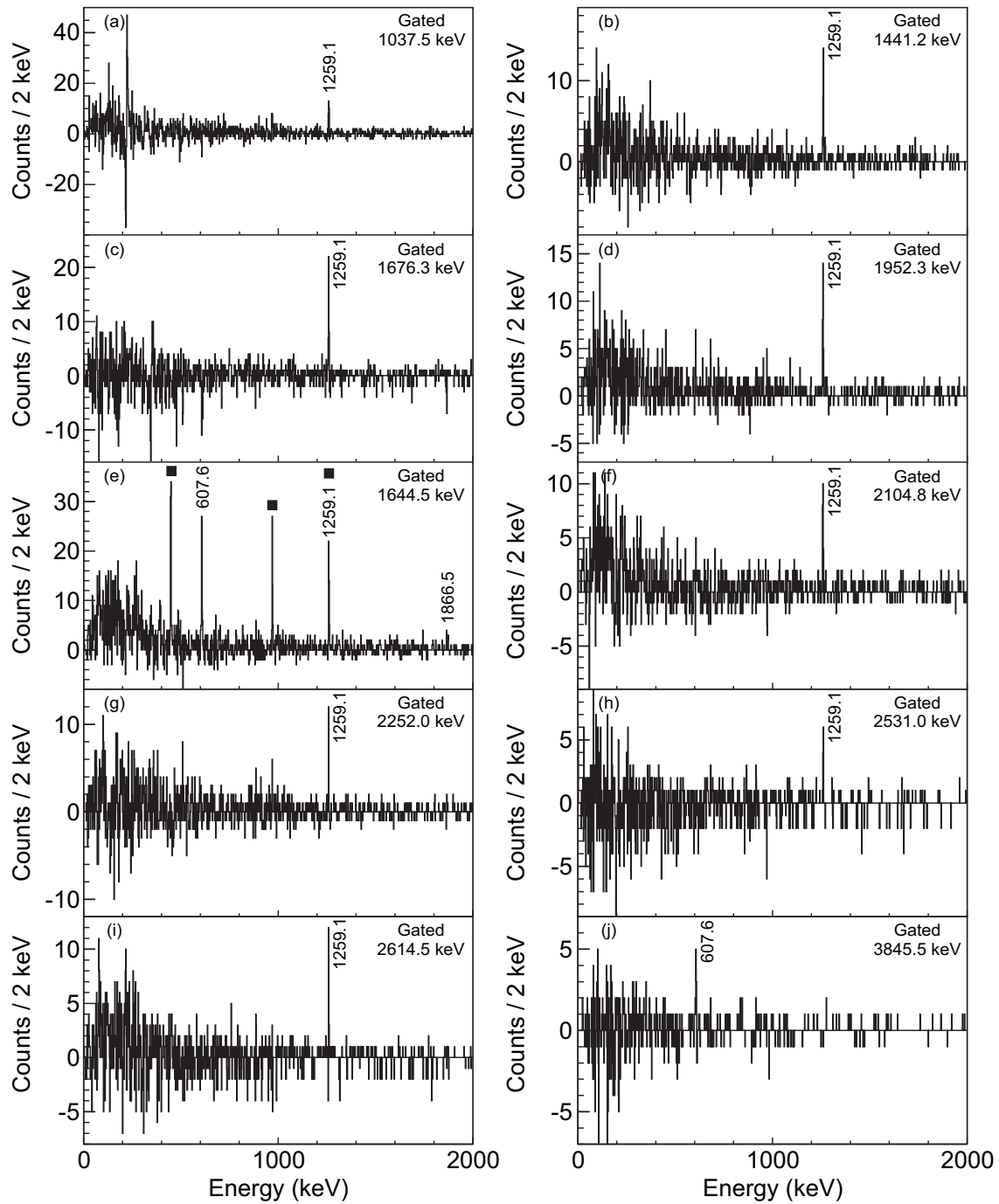
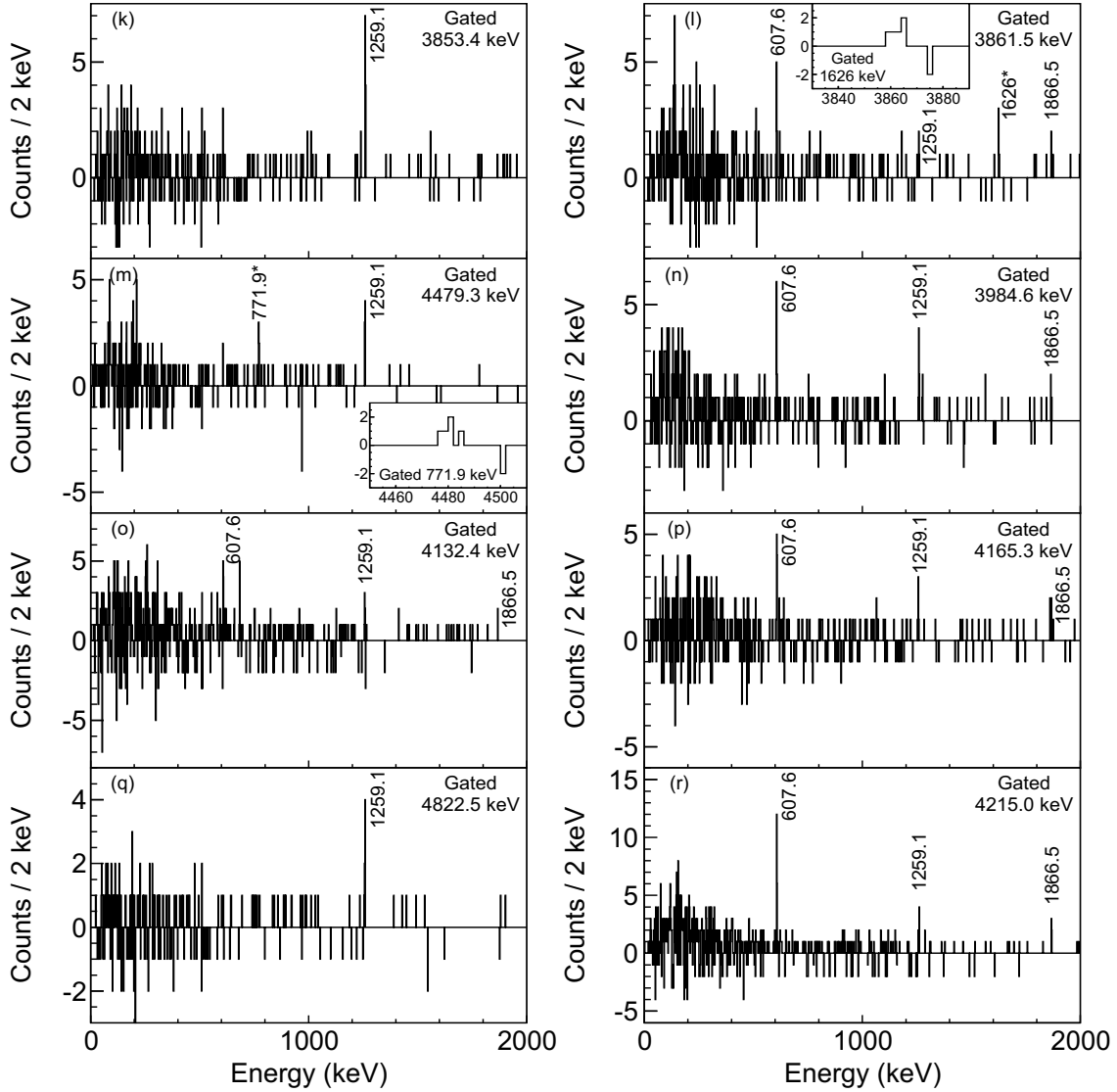


Figure D.1: Series of background subtracted $\beta\gamma\gamma$ coincidence spectra correlated to the decay of the long-lived, low-spin, ^{70}Co isomer. The background was taken symmetrically either side of the peak except where other γ rays interfered, in which case the background was taken above as close as possible to the peak of interest. Transitions affiliated with the short-lived, high-spin, ^{70}Co isomer are denoted with black squares. Transitions observed in coincidence but not in singles are denoted with asterisks. The insets in (l) and (m) show the $\beta\gamma\gamma$ coincidence spectra gated on the 1626-keV and 771.9-keV transitions.

Figure D.1: (cont'd)

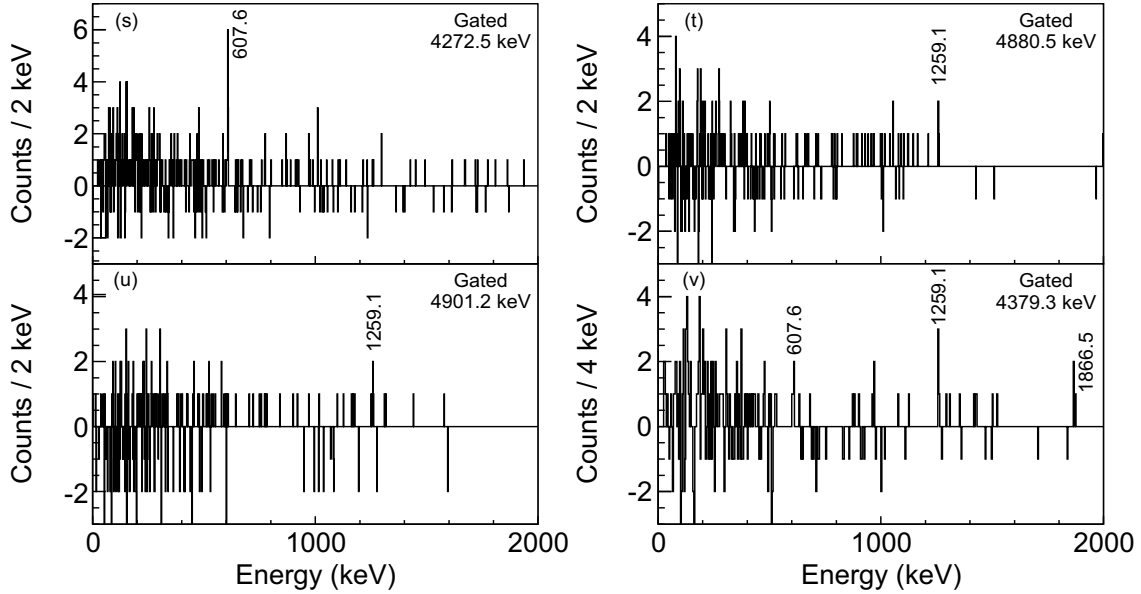


shown in Figs. D.1m and Fig. 4.37a, placing a new level at 2935 keV.

In Fig. D.1d the γ rays coincident with the 1952.3-keV γ ray, first identified by Ref. [23], are shown. The coincidence is also observed in Fig. Fig. 4.37a. In Ref. [23] a 1950-keV transition was observed in coincidence with the 1259.1-keV transition and placed feeding the 1259-keV 2_1^+ state from a new level at 3209. The present results support this placement and updates the energy to 3211 keV for the new level.

The γ rays coincident with a new 1644.5-keV transition are shown in Fig. D.1e. This γ

Figure D.1: (cont'd)



ray is unresolved from the 1641.6-keV transition, affiliated with the decay of the short-lived, high-spin, ^{70}Co isomer, and as such the coincidence spectrum is contaminated with the 448.4-, 969.6, and 1259.1-keV transitions, identified by black squares in Fig. D.1e. However, some coincidences with the 1259.1-keV transition are not contaminants, and a strong coincidence with the 607.6-keV ($2_2^+ \rightarrow 2_1^+$) transition is observed both in Figs. D.1e and 4.38a. A weaker coincidence is observed with the 1866.5-keV transition as well in Figs. D.1e and 4.38c. This places the 1644.5-keV γ ray feeding the 1867-keV 2_2^+ state from the same 3511-keV level identified above. A third transition with an energy of 2252.0-keV, observed in coincidence with the 1259.1-keV transition in Fig. D.1g, was placed depopulating the same 3511-keV level and is believed to feed the 1259.1-keV 2_1^+ state.

In Fig. D.1f a strong coincidence between a new 2104.8-keV γ -ray and the 1259.1-keV transition is observed, placing a new level at 3364 keV. The 2104.8-1259.1-keV coincidence is also present in Fig. 4.37a.

In Fig. D.1h a new 2531.0-keV γ ray is shown in coincidence with the 1259.1-keV tran-

sition placing a new level at 3790 keV.

A coincidence between a new 2614.5-keV γ -ray and the 1259.1-keV transition is present in Figs. D.1i and 4.37b, placing a new level at 3874 keV. In β -gated γ -ray singles there is a contaminant transition in the 2614-keV region so the intensity of the transition was determined using the efficiency-corrected 15(4) 1259.1-2614.5-keV coincidences.

In Fig. D.1i the γ -rays coincident with a new 3845.5-keV γ -ray are shown. Figures D.1i and 4.37a show a coincidence with 607.6-keV placing a new level at 5712 keV. Furthermore, a new 5711.4-keV γ -ray was identified in β -gated γ -ray singles, and is assumed to be the ground-state transition for this new level. A new 2777.4-keV γ -ray was also placed depopulating the new 5712-keV level and feeding the new 2935-keV level based off energy differences, but no coincidences were observed to support this placement.

γ rays coincident with a new 3853.4-keV γ -ray are shown in Fig. D.1k. A strong coincidence with the 1259.1-keV transition is observed, placing an new level at 5112 keV.

In Fig. D.1l coincidences between a new 3861.5-keV γ ray and the 607.6-keV, 1259.1-keV, and 1866.5-keV transitions are observed, placing a new level at 5728 keV. There is an additional coincidence with a 1626-keV γ ray, which is also observed in the inset in Fig. D.1l obtained by gating on the 1626-keV region. However, without the γ -gated decay curve to confirm the affiliation of the 1626-keV γ ray with the decay of the long-lived ^{70}Co isomer, it cannot be confidently placed in the decay scheme.

Figure D.1m a coincidence between a new 4479.3-keV γ ray and the 1259.1-keV transition is observed, placing a new level at 5738 keV. There were 5(1) 4479.3-1259.1-keV coincidences expected and 6(2) are recorded. Additionally two other transitions were placed depopulating this level based on energy differences. A 3871.7-keV transition was placed feeding the 1867-keV 2_2^+ state and a 2803.4-keV transition was placed feeding the 2935-keV level. These

placements are not based off any recorded coincidences and it is also possible that the 3871.7-keV transition could depopulate a 5130-keV level, for which the unplaced 5130-keV transition could be the ground-state transition. A second coincidence with a 772.0-keV γ ray is also observed in Fig. D.1m which in turn is seen in the inset obtained by gating on the 772-keV region. However without a γ -gated decay curve to confirm the 772.0-keV transition's affiliation with the decay of either ^{70}Co isomer it cannot be placed in the decay scheme.

In Fig. D.1n coincidences between a new 3984.6-keV γ ray and the 607.6-keV, 1259.1-keV, and 1866.5-keV transitions are observed, placing a new level at 5850 keV. Figures D.1o and D.1p show coincidences between new 4132.4-keV and 4165.3-keV γ -rays, respectively, with the 607.6-keV, 1259.1-keV, and 1866.5-keV transitions. These coincidences place new levels at 5999 keV and 6032 keV. A 4771.6-keV γ ray was also placed depopulating the new 6032-keV level, feeding the 1259.1-keV 2_1^+ state, based off energy differences but no coincidences were observed to support this placement.

γ rays coincident with a new 4822.5-keV γ -ray are shown in Fig. D.1q. A coincidence with the 1259.1-keV transition is observed, placing an new level at 6082 keV. In Fig. D.1r coincidences between a new 4215.0-keV γ ray and the 607.6-keV, 1259.1-keV, and 1866.5-keV transitions are observed, and therefore the 4215.0-keV transition most likely depopulates the same new 6082-keV level. A 6081.9-keV γ ray was observed in β -delayed γ -ray singles and was placed as the ground state transition for the new 6082-keV level.

In Fig. D.1s a new 4272.5-keV γ ray is shown in coincidence with the 607.6-keV transition, placing a new level at 6139-keV. Another new γ ray at 4800.5-keV is observed in coincidence with the 1259.1-keV transition in Figure D.1t, which places it depopulating this same new 6139-keV level.

In Fig. D.1u a coincidence between a new 4901.2-keV γ ray with the 1259.1-keV transition is observed, placing a new level at 6160 keV. Based on calculated energy differences between levels the 2950.7-keV transition has also been placed depopulating this new 6160-keV level and feeding the new 3211-keV level. However, no coincidences are present to verify that placement.

In Fig. D.1v a new 4379.9-keV γ ray is shown in coincidence with the 607.6-keV, 1259.1-keV, and 1866.5-keV transitions, placing a new level at 6246 keV.

Also placed in the decay scheme for the long-lived, low-spin, ^{70}Co isomer are two new levels at 6284 keV and 6340 keV for which only the 6283.8-keV and 6339.9-keV ground-state transitions are observed. No coincidences with either 607.6-keV or 1259.1-keV transitions were observed.

BIBLIOGRAPHY

BIBLIOGRAPHY

- [1] Professor E. Rutherford F.R.S. Lxxix. the scattering of α particles by matter and the structure of the atom. *Philosophical Magazine Series 6*, 21(125):669–688, 1911.
- [2] Crc handbook of chemistry and physics, 94th ed. <http://www.hbcnetbase.com/>, 2013.
- [3] B. A. Brown. *Lecture Notes in Nuclear Structure Physics*. Michigan State University, 2010.
- [4] Takaharu Otsuka, Toshio Suzuki, Rintaro Fujimoto, Hubert Grawe, and Yoshinori Akaishi. Evolution of nuclear shells due to the tensor force. *Phys. Rev. Lett.*, 95:232502, Nov 2005.
- [5] S. M. Lenzi, F. Nowacki, A. Poves, and K. Sieja. Island of inversion around ^{64}Cr . *Phys. Rev. C*, 82:054301, Nov 2010.
- [6] Kris Heyde and John L. Wood. Shape coexistence in atomic nuclei. *Rev. Mod. Phys.*, 83:1467–1521, Nov 2011.
- [7] Yusuke Tsunoda, Takaharu Otsuka, Noritaka Shimizu, Michio Honma, and Yutaka Utsuno. Novel shape evolution in exotic ni isotopes and configuration-dependent shell structure. *Phys. Rev. C*, 89:031301, Mar 2014.
- [8] A Poves. Shape coexistence: the shell model view. *Journal of Physics G: Nuclear and Particle Physics*, 43(2):024010, 2016.
- [9] T Otsuka and Y Tsunoda. The role of shell evolution in shape coexistence. *Journal of Physics G: Nuclear and Particle Physics*, 43(2):024009, 2016.
- [10] J L Wood and K Heyde. A focus on shape coexistence in nuclei. *Journal of Physics G: Nuclear and Particle Physics*, 43(2):020402, 2016.
- [11] J. Elseviers, A. N. Andreyev, S. Antalic, A. Barzakh, N. Bree, T. E. Cocolios, V. F. Comas, J. Diriken, D. Fedorov, V. N. Fedosseyev, S. Franchoo, J. A. Heredia, M. Huyse, O. Ivanov, U. Köster, B. A. Marsh, R. D. Page, N. Patronis, M. Seliverstov, I. Tsekhanovich, P. Van den Bergh, J. Van De Walle, P. Van Duppen, M. Venhart,

- S. Vermote, M. Veselský, and C. Wagemans. Shape coexistence in ^{180}Hg studied through the β decay of ^{180}Tl . *Phys. Rev. C*, 84:034307, Sep 2011.
- [12] W. F. Mueller, B. Bruyneel, S. Franchoo, M. Huyse, J. Kurpeta, K. Kruglov, Y. Kudryavtsev, N. V. S. V. Prasad, R. Raabe, I. Reusen, P. Van Duppen, J. Van Roosbroeck, L. Vermeeren, L. Weissman, Z. Janas, M. Karny, T. Kszczot, A. Płochocki, K.-L. Kratz, B. Pfeiffer, H. Grawe, U. Köster, P. Thirolf, and W. B. Walters. β decay of ^{66}Co , ^{68}Co , and ^{70}Co . *Phys. Rev. C*, 61:054308, Apr 2000.
- [13] B. Pritychenko, M. Birch, B. Singh, and M. Horoi. Tables of $\{E2\}$ transition probabilities from the first states in even-even nuclei. *Atomic Data and Nuclear Data Tables*, 107:1 – 139, 2016.
- [14] C. Guénaut, G. Audi, D. Beck, K. Blaum, G. Bollen, P. Delahaye, F. Herfurth, A. Kellerbauer, H.-J. Kluge, J. Libert, D. Lunney, S. Schwarz, L. Schweikhard, and C. Yazidjian. High-precision mass measurements of nickel, copper, and gallium isotopes and the purported shell closure at $n = 40$. *Phys. Rev. C*, 75:044303, Apr 2007.
- [15] D. Pauwels, O. Ivanov, N. Bree, J. Büscher, T. E. Cocolios, J. Gentens, M. Huyse, A. Korgul, Yu. Kudryavtsev, R. Raabe, M. Sawicka, I. Stefanescu, J. Van de Walle, P. Van den Bergh, P. Van Duppen, and W. B. Walters. Shape isomerism at $n = 40$: Discovery of a proton intruder state in ^{67}Co . *Phys. Rev. C*, 78:041307, Oct 2008.
- [16] D. Pauwels, O. Ivanov, N. Bree, J. Büscher, T. E. Cocolios, M. Huyse, Yu. Kudryavtsev, R. Raabe, M. Sawicka, J. Van de Walle, P. Van Duppen, A. Korgul, I. Stefanescu, A. A. Hecht, N. Hoteling, A. Wöhr, W. B. Walters, R. Broda, B. Fornal, W. Krolas, T. Pawlat, J. Wrzesinski, M. P. Carpenter, R. V. F. Janssens, T. Lauritsen, D. Seweryniak, S. Zhu, J. R. Stone, and X. Wang. Structure of $^{65,67}\text{Co}$ studied through the β decay of $^{65,67}\text{Fe}$ and a deep-inelastic reaction. *Phys. Rev. C*, 79:044309, Apr 2009.
- [17] M. Bernas, Ph. Dessagne, M. Langevin, J. Payet, F. Pougheon, and P. Roussel. Magic features of ^{68}Ni . *Physics Letters B*, 113(4):279 – 282, 1982.
- [18] S. Suchyta, S. N. Liddick, Y. Tsunoda, T. Otsuka, M. B. Bennett, A. Chemey, M. Honma, N. Larson, C. J. Prokop, S. J. Quinn, N. Shimizu, A. Simon, A. Spyrou, V. Tripathi, Y. Utsuno, and J. M. VonMoss. Shape coexistence in ^{68}Ni . *Phys. Rev. C*, 89:021301, Feb 2014.
- [19] F. Recchia, C. J. Chiara, R. V. F. Janssens, D. Weisshaar, A. Gade, W. B. Walters, M. Albers, M. Alcorta, V. M. Bader, T. Baugher, D. Bazin, J. S. Berryman, P. F. Bertone, B. A. Brown, C. M. Campbell, M. P. Carpenter, J. Chen, H. L. Crawford, H. M. David, D. T. Doherty, C. R. Hoffman, F. G. Kondev, A. Korichi, C. Langer,

- N. Larson, T. Lauritsen, S. N. Liddick, E. Lunderberg, A. O. Macchiavelli, S. Noji, C. Prokop, A. M. Rogers, D. Seweryniak, S. R. Stroberg, S. Suchyta, S. Williams, K. Wimmer, and S. Zhu. Configuration mixing and relative transition rates between low-spin states in ^{68}Ni . *Phys. Rev. C*, 88:041302, Oct 2013.
- [20] C. J. Chiara, R. Broda, W. B. Walters, R. V. F. Janssens, M. Albers, M. Alcorta, P. F. Bertone, M. P. Carpenter, C. R. Hoffman, T. Lauritsen, A. M. Rogers, D. Seweryniak, S. Zhu, F. G. Kondev, B. Fornal, W. Królas, J. Wrzesiński, N. Larson, S. N. Liddick, C. Prokop, S. Suchyta, H. M. David, and D. T. Doherty. Low-spin states and the non-observation of a proposed 2202-keV, 0^+ isomer in ^{68}Ni . *Phys. Rev. C*, 86:041304, Oct 2012.
- [21] F. Flavigny, D. Pauwels, D. Radulov, I. J. Darby, H. De Witte, J. Diriken, D. V. Fedorov, V. N. Fedosseev, L. M. Fraile, M. Huyse, V. S. Ivanov, U. Köster, B. A. Marsh, T. Otsuka, L. Popescu, R. Raabe, M. D. Seliverstov, N. Shimizu, A. M. Sjödin, Y. Tsunoda, P. Van den Bergh, P. Van Duppen, J. Van de Walle, M. Venhart, W. B. Walters, and K. Wimmer. Characterization of the low-lying 0^+ and 2^+ states in ^{68}Ni via β decay of the low-spin ^{68}Co isomer. *Phys. Rev. C*, 91:034310, Mar 2015.
- [22] E.A. McCutchan. Nuclear data sheets for $a = 68$. *Nuclear Data Sheets*, 113(67):1735 – 1870, 2012.
- [23] C. J. Chiara, D. Weisshaar, R. V. F. Janssens, Y. Tsunoda, T. Otsuka, J. L. Harker, W. B. Walters, F. Recchia, M. Albers, M. Alcorta, V. M. Bader, T. Baugher, D. Bazin, J. S. Berryman, P. F. Bertone, C. M. Campbell, M. P. Carpenter, J. Chen, H. L. Crawford, H. M. David, D. T. Doherty, A. Gade, C. R. Hoffman, M. Honma, F. G. Kondev, A. Korichi, C. Langer, N. Larson, T. Lauritsen, S. N. Liddick, E. Lunderberg, A. O. Macchiavelli, S. Noji, C. Prokop, A. M. Rogers, D. Seweryniak, N. Shimizu, S. R. Stroberg, S. Suchyta, Y. Utsuno, S. J. Williams, K. Wimmer, and S. Zhu. Identification of deformed intruder states in semi-magic ^{70}Ni . *Phys. Rev. C*, 91:044309, Apr 2015.
- [24] W. Loveland, D. J. Morrissey, and G. T. Seaborg. *Modern Nuclear Chemistry*. John Wiley & Sons, Inc., New Jersey, 2006.
- [25] Jouni. Suhonen. *From Nucleons to Nucleus: Concepts of Microscopic Nuclear Theory*. Springer, Berlin, Heidelberg, 2007.
- [26] H. Bateman. Procedure cambridge philosophic society. *Math.Phys.Sci.*, 15:423, 1910.
- [27] H. Ohm, M. Zendel, S. G. Prussin, W. Rudolph, A. Schröder, K. L. Kratz, C. Ristori, J. A. Pinston, E. Monmand, F. Schussler, and J. P. Zirnheld. Beta-delayed neutrons and

- high-energy gamma-rays from decay of ^{137}I . *Zeitschrift für Physik A Atoms and Nuclei*, 296(1):23–33, 1980.
- [28] J. L. Tain, E. Valencia, A. Algora, J. Agramunt, B. Rubio, S. Rice, W. Gelletly, P. Regan, A.-A. Zakari-Issoufou, M. Fallot, A. Porta, J. Rissanen, T. Eronen, J. Äystö, L. Batist, M. Bowry, V. M. Bui, R. Caballero-Folch, D. Cano-Ott, V.-V. Elomaa, E. Estevez, G. F. Farrelly, A. R. Garcia, B. Gomez-Hornillos, V. Gorlychev, J. Hakala, M. D. Jordan, A. Jokinen, V. S. Kolhinen, F. G. Kondev, T. Martínez, E. Mendoza, I. Moore, H. Penttilä, Zs. Podolyák, M. Reponen, V. Sonnenschein, and A. A. Sonzogni. Enhanced γ -ray emission from neutron unbound states populated in β decay. *Phys. Rev. Lett.*, 115:062502, Aug 2015.
- [29] A. Spyrou, S. N. Liddick, F. Naqvi, B. P. Crider, A. C. Dombos, D. L. Bleuel, B. A. Brown, A. Couture, L. Crespo Campo, M. Guttormsen, K.-L. Kratz, A. C. Larsen, R. Lewis, P. Moller, S. Mosby, M. R. Mumpower, G. Perdikakis, C. J. Prokop, T. Renström, S. Siem, S. J. Quinn, and S. Valenta. Large fragmentation observed in the β -decay intensity of ^{70}Co . *Submitted*.
- [30] S. Raman, C.W. Nestor Jr., and P. Tikkanen. Transition probability from the ground state to the first-excited 2^+ state of even-even nuclides. *Atomic Data and Nuclear Data Tables*, 78(1):1 – 128, 2001.
- [31] J.L. Wood, E.F. Zganjar, C. De Coster, and K. Heyde. Electric monopole transitions from low energy excitations in nuclei. *Nuclear Physics A*, 651(4):323 – 368, 1999.
- [32] T. Kibdi and R. H. Spear. Electric monopole transitions between 0^+ states for nuclei throughout the periodic table. *AIP Conference Proceedings*, 769(1):442–445, 2005.
- [33] E. L. Church and J. Weneser. Electric-monopole transitions in atomic nuclei. *Phys. Rev.*, 103:1035–1044, Aug 1956.
- [34] T. Kibdi, T.W. Burrows, M.B. Trzhaskovskaya, P.M. Davidson, and C.W. Nestor Jr. Evaluation of theoretical conversion coefficients using bricc. *Nuclear Instruments and Methods in Physics Research Section A: Accelerators, Spectrometers, Detectors and Associated Equipment*, 589(2):202 – 229, 2008.
- [35] H. Mach, R.L. Gill, and M. Moszynski. A method for picosecond lifetime measurements for neutron-rich nuclei. *Nuclear Instruments and Methods in Physics Research Section A: Accelerators, Spectrometers, Detectors and Associated Equipment*, 280(1):49 – 72, 1989.

- [36] X. Wu, H. Blosser, D. Johnson, F. Marti, and R. C. York. The k500-to-k1200 coupling line for the coupled cyclotron facility at the nscl. In *Particle Accelerator Conference, 1999. Proceedings of the 1999*, volume 2, pages 1318–1320 vol.2, 1999.
- [37] D.J. Morrissey, B.M. Sherrill, M. Steiner, A. Stolz, and I. Wiedenhoefer. Commissioning the a1900 projectile fragment separator. *Nucl. Instrum. Methods Phys. Res. B*, 204(0):90 – 96, 2003. 14th International Conference on Electromagnetic Isotope Separators and Techniques Related to their Applications.
- [38] D. Bazin, O. Tarasov, M. Lewitowicz, and O. Sorlin. The program lise: a simulation of fragment separators. *Nuclear Instruments and Methods in Physics Research Section A: Accelerators, Spectrometers, Detectors and Associated Equipment*, 482(12):307 – 327, 2002.
- [39] C.J. Prokop, S.N. Liddick, B.L. Abromeit, A.T. Chemey, N.R. Larson, S. Suchyta, and J.R. Tompkins. Digital data acquisition system implementation at the national superconducting cyclotron laboratory. *Nucl. Instrum. Methods Phys. Res. A*, 741(0):163 – 168, 2014.
- [40] H. Tan, M. Momayezi, A. Fallu-Labruyere, Y. X. Chu, and W. K. Warburton. A fast digital filter algorithm for gamma-ray spectroscopy with double-exponential decaying scintillators. *IEEE Transactions on Nuclear Science*, 51(4):1541–1545, Aug 2004.
- [41] A. Fallu-Labruyere, H. Tan, W. Hennig, and W.K. Warburton. Time resolution studies using digital constant fraction discrimination. *Nucl. Instrum. Methods Phys. Res., Sect. A*, 579(1):247 – 251, 2007. Proceedings of the 11th Symposium on Radiation Measurements and Applications.
- [42] C.J. Prokop, S.N. Liddick, N.R. Larson, S. Suchyta, and J.R. Tompkins. Optimization of the national superconducting cyclotron laboratory digital data acquisition system for use with fast scintillator detectors. *Nucl. Instrum. Methods Phys. Res., Sect. A*, 792:81 – 88, 2015.
- [43] N. Larson, S.N. Liddick, M. Bennett, A. Bowe, A. Chemey, C. Prokop, A. Simon, A. Spyrou, S. Suchyta, S.J. Quinn, S.L. Tabor, P.L. Tai, Vandana Tripathi, and J.M. VonMoss. High efficiency beta-decay spectroscopy using a planar germanium double-sided strip detector. *Nucl. Instrum. Methods Phys. Res., Sect. A*, 727:59 – 64, 2013.
- [44] O. Sorlin, S. Leenhardt, C. Donzaud, J. Duprat, F. Azaiez, F. Nowacki, H. Grawe, Zs. Dombrádi, F. Amorini, A. Astier, D. Baiborodin, M. Belleguic, C. Borcea, C. Bourgeois, D. M. Cullen, Z. Dlouhy, E. Dragulescu, M. Górska, S. Grévy, D. Guillemaud-Mueller, G. Hagemann, B. Herskind, J. Kiener, R. Lemmon, M. Lewitowicz, S. M. Lukyanov,

- P. Mayet, F. de Oliveira Santos, D. Pantalica, Yu.-E. Penionzhkevich, F. Pougheon, A. Poves, N. Redon, M. G. Saint-Laurent, J. A. Scarpaci, G. Sletten, M. Stanoiu, O. Tarasov, and Ch. Theisen. ${}^{68}_{28}\text{ni}_{40}$: Magicity versus superfluidity. *Phys. Rev. Lett.*, 88:092501, Feb 2002.
- [45] S.N. Liddick, I.G. Darby, and R.K. Grzywacz. Algorithms for pulse shape analysis using silicon detectors. *Nuclear Instruments and Methods in Physics Research Section A: Accelerators, Spectrometers, Detectors and Associated Equipment*, 669:70 – 78, 2012.
- [46] Mohammad Alshudifat, R. Grzywacz, and S.V. Paulauskas. Development of a segmented scintillator for decay studies. *Physics Procedia*, 66:445 – 450, 2015. The 23rd International Conference on the Application of Accelerators in Research and Industry - {CAARI} 2014.
- [47] W.F. Mueller, J.A. Church, T. Glasmacher, D. Gutknecht, G. Hackman, P.G. Hansen, Z. Hu, K.L. Miller, and P. Quirin. Thirty-two-fold segmented germanium detectors to identify γ -rays from intermediate-energy exotic beams. *Nuclear Instruments and Methods in Physics Research Section A: Accelerators, Spectrometers, Detectors and Associated Equipment*, 466(3):492 – 498, 2001.
- [48] S.-C. Wu. Nuclear data sheets for $a = 214$. *Nuclear Data Sheets*, 110(3):681 – 748, 2009.
- [49] John A Cameron and Balraj Singh. Nuclear data sheets for $a=40$. *Nuclear Data Sheets*, 102(2):293 – 513, 2004.
- [50] M.J. Martin. Nuclear data sheets for $a = 208$. *Nuclear Data Sheets*, 108(8):1583 – 1806, 2007.
- [51] A. Ivan, K. C. Burr, Yiping Shao, and J. W. LeBlanc. Depth of interaction effect on timing resolution in pet block detectors. In *Nuclear Science Symposium Conference Record, 2004 IEEE*, volume 7, pages 4156–4158, Oct 2004.
- [52] C.D. Nesaraja. Nuclear data sheets for $a=69$. *Nuclear Data Sheets*, 115:1 – 134, 2014.
- [53] H. Mach, M. Lewitowicz, M. Stanoiu, F. Becker, J. Blomqvist, M.J.G. Berge, R. Boutami, B. Cederwall, Z. Dlouhy, B. Fogelberg, L.M. Fraile, G. Georgiev, H. Grawe, R. Grzywacz, P.I. Johansson, W. Klamra, S. Lukyanov, M. Mineva, J. Mrazek, G. Neyens, F. de Oliveir Santos, M. Pzfner, Yu.E. Penionzhkevich, E. Ramstrm, and M. Sawicka. Coupling of valence particles/holes to ${}^{68,70}\text{ni}$ studied via measurements of the $b(e2)$ strength in ${}^{67,69,70}\text{ni}$ and ${}^{71}\text{cu}$. *Nuclear Physics A*, 719:C213 – C216, 2003.

- [54] P.R. Bevington and D.K. Robinson. *Data reduction and error analysis for the physical sciences*. McGraw-Hill Higher Education. McGraw-Hill, 2003.
- [55] S. N. Liddick, B. Abromeit, A. Ayres, A. Bey, C. R. Bingham, M. Bolla, L. Cartegni, H. L. Crawford, I. G. Darby, R. Grzywacz, S. Ilyushkin, N. Larson, M. Madurga, D. Miller, S. Padgett, S. Paulauskas, M. M. Rajabali, K. Rykaczewski, and S. Suchyta. Low-energy structure of $^{66}_{27}\text{Co}_{39}$ and $^{68}_{27}\text{Co}_{41}$ populated through β decay. *Phys. Rev. C*, 85:014328, Jan 2012.
- [56] M. Wang, G. Audi, A.H. Wapstra, F.G. Kondev, M. MacCormick, X. Xu, and B. Pfeiffer. The ame2012 atomic mass evaluation. *Chinese Physics C*, 36(12):1603, 2012.
- [57] T. Kurtukian-Nieto, J. Benlliure, and K.-H. Schmidt. A new analysis method to determine β -decay half-lives in experiments with complex background. *Nuclear Instruments and Methods in Physics Research Section A: Accelerators, Spectrometers, Detectors and Associated Equipment*, 589(3):472 – 483, 2008.
- [58] M. Birch, B. Singh, I. Dillmann, D. Abriola, T.D. Johnson, E.A. McCutchan, and A.A. Sonzogni. Evaluation of beta-delayed neutron emission probabilities and half-lives for $z = 228$. *Nuclear Data Sheets*, 128:131 – 184, 2015.
- [59] J.K. Tuli. Nuclear data sheets for $a = 70$. *Nuclear Data Sheets*, 103(3):389 – 514, 2004.
- [60] K. H. Schmidt, C. C. Sahm, K. Pielenz, and H. G. Clerc. Some remarks on the error analysis in the case of poor statistics. *Zeitschrift für Physik A Atoms and Nuclei*, 316(1):19–29, 1984.
- [61] M. Pftzner, R. Grzywacz, M. Lewitowicz, and K. Rykaczewski. Experiments with isomeric beams. *Nuclear Physics A*, 626(12):259 – 262, 1997. Proceedings of the Third International Conference on Nuclear Physics at Storage Rings.
- [62] R. Grzywacz, R. Béraud, C. Borcea, A. Emsallem, M. Glogowski, H. Grawe, D. Guillemaud-Mueller, M. Hjorth-Jensen, M. Houry, M. Lewitowicz, A. C. Mueller, A. Nowak, A. Płochocki, M. Pfützner, K. Rykaczewski, M. G. Saint-Laurent, J. E. Sauvestre, M. Schaefer, O. Sorlin, J. Szerypo, W. Trinder, S. Viteritti, and J. Winfield. New island of μs isomers in neutron-rich nuclei around the $Z = 28$ and $N = 40$ shell closures. *Phys. Rev. Lett.*, 81:766–769, Jul 1998.
- [63] M. Sawicka, R. Grzywacz, I. Matea, H. Grawe, M. Pfützner, J. M. Daugas, M. Lewitowicz, D. L. Balabanski, F. Becker, G. Bélier, C. Bingham, C. Borcea, E. Bouchez, A. Buta, M. La Commara, E. Dragulescu, G. de France, G. Georgiev, J. Giovino, M. Górska, F. Hammache, M. Hass, M. Hellström, F. Ibrahim, Z. Janas, H. Mach,

- P. Mayet, V. Méot, F. Negoita, G. Neyens, F. de Oliveira Santos, R. D. Page, O. Perru, Zs. Podolyák, O. Roig, K. P. Rykaczewski, M. G. Saint-Laurent, J. E. Sauvestre, O. Sorlin, M. Stanoiu, I. Stefan, C. Stodel, Ch. Theisen, D. Verney, and J. Żylicz. Low energy levels in ^{72}Ni . *Phys. Rev. C*, 68:044304, Oct 2003.
- [64] O. Perru, O. Sorlin, S. Franchoo, F. Azaiez, E. Bouchez, C. Bourgeois, A. Chatillon, J. M. Daugas, Z. Dlouhy, Zs. Dombrádi, C. Donzaud, L. Gaudefroy, H. Grawe, S. Grévy, D. Guillemaud-Mueller, F. Hammache, F. Ibrahim, Y. Le Coz, S. M. Lukyanov, I. Matea, J. Mrazek, F. Nowacki, Yu.-E. Penionzhkevich, F. de Oliveira Santos, F. Pougheon, M. G. Saint-Laurent, G. Sletten, M. Stanoiu, C. Stodel, Ch. Theisen, and D. Verney. Enhanced core polarization in ^{70}Ni and ^{74}Zn . *Phys. Rev. Lett.*, 96:232501, Jun 2006.
- [65] A. F. Lisetskiy, B. A. Brown, M. Horoi, and H. Grawe. New $t = 1$ effective interactions for the $f_{5/2} p_{3/2} p_{1/2} g_{9/2}$ model space: Implications for valence-mirror symmetry and seniority isomers. *Phys. Rev. C*, 70:044314, Oct 2004.
- [66] M. Honma, T. Otsuka, T. Mizusaki, and M. Hjorth-Jensen. New effective interaction for $f_5p_{9/2}$ -shell nuclei. *Phys. Rev. C*, 80:064323, Dec 2009.
- [67] B. Cheal, E. Mané, J. Billowes, M. L. Bissell, K. Blaum, B. A. Brown, F. C. Charwood, K. T. Flanagan, D. H. Forest, C. Geppert, M. Honma, A. Jokinen, M. Kowalska, A. Krieger, J. Krämer, I. D. Moore, R. Neugart, G. Neyens, W. Nörthershäuser, M. Schug, H. H. Stroke, P. Vingerhoets, D. T. Yordanov, and M. Žáková. Nuclear spins and moments of ga isotopes reveal sudden structural changes between $n = 40$ and $n = 50$. *Phys. Rev. Lett.*, 104:252502, Jun 2010.
- [68] T. Otsuka. private communication.
- [69] K. Kolos, D. Miller, R. Grzywacz, H. Iwasaki, M. Al-Shudifat, D. Bazin, C. R. Bingham, T. Braunroth, G. Cerizza, A. Gade, A. Lemasson, S. N. Liddick, M. Madurga, C. Morse, M. Portillo, M. M. Rajabali, F. Recchia, L. L. Riedinger, P. Voss, W. B. Walters, D. Weisshaar, K. Whitmore, K. Wimmer, and J. A. Tostevin. Direct lifetime measurements of the excited states in ^{72}Ni . *Phys. Rev. Lett.*, 116:122502, Mar 2016.
- [70] J. A. Lay, L. Fortunato, and A. Vitturi. Investigating nuclear pairing correlations via microscopic two-particle transfer reactions: The cases of ^{112}Sn , ^{32}Mg , and ^{68}Ni . *Phys. Rev. C*, 89:034618, Mar 2014.
- [71] M. Honma, T. Otsuka, B. A. Brown, and T. Mizusaki. New effective interaction for pf -shell nuclei and its implications for the stability of the $n = z = 28$ closed core. *Phys. Rev. C*, 69:034335, Mar 2004.

- [72] D. R. Entem and R. Machleidt. Accurate charge-dependent nucleon-nucleon potential at fourth order of chiral perturbation theory. *Phys. Rev. C*, 68:041001, Oct 2003.
- [73] <https://github.com/manybodyphysics/cens>.
- [74] J.C. Hardy, L.C. Carraz, B. Jonson, and P.G. Hansen. The essential decay of pandemonium: A demonstration of errors in complex beta-decay schemes. *Physics Letters B*, 71(2):307 – 310, 1977.
- [75] A. Simon, S.J. Quinn, A. Spyrou, A. Battaglia, I. Beskin, A. Best, B. Bucher, M. Couder, P.A. DeYoung, X. Fang, J. Grges, A. Kontos, Q. Li, S.N. Liddick, A. Long, S. Lyons, K. Padmanabhan, J. Peace, A. Roberts, D. Robertson, K. Smith, M.K. Smith, E. Stech, B. Stefanek, W.P. Tan, X.D. Tang, and M. Wiescher. Sun: Summing nai(tl) gamma-ray detector for capture reaction measurements. *Nuclear Instruments and Methods in Physics Research Section A: Accelerators, Spectrometers, Detectors and Associated Equipment*, 703:16 – 21, 2013.
- [76] T. Otuska. Structure evolutions in exotic nuclei and nuclear forces. Presented at the RIKEN 2koma plus seminar, Wako, Japan.
- [77] S. N. Liddick, W. B. Walters, C. J. Chiara, R. V. F. Janssens, B. Abromeit, A. Ayres, A. Bey, C. R. Bingham, M. P. Carpenter, L. Cartegni, J. Chen, H. L. Crawford, I. G. Darby, R. Grzywacz, J. Harker, C. R. Hoffman, S. Ilyushkin, F. G. Kondev, N. Larson, M. Madurga, D. Miller, S. Padgett, S. V. Paulauskas, M. M. Rajabali, K. Rykaczewski, D. Seweryniak, S. Suchyta, and S. Zhu. Analogous intruder behavior near ni, sn, and pb isotopes. *Phys. Rev. C*, 92:024319, Aug 2015.
- [78] C. J. Gallagher and S. A. Moszkowski. Coupling of angular momenta in odd-odd nuclei. *Phys. Rev.*, 111:1282–1290, Sep 1958.
- [79] Huo Junde, Huang Xiaolong, and J.K. Tuli. Nuclear data sheets for $a = 67$. *Nuclear Data Sheets*, 106(2):159 – 250, 2005.
- [80] Khalifeh Abusaleem and Balraj Singh. Nuclear data sheets for $a = 71$. *Nuclear Data Sheets*, 112(1):133 – 273, 2011.
- [81] Scott Suchyta. *Studies of the Neutron-Rich Nuclei near $N = 40$ through Beta Decay*. PhD thesis, Michigan State University, 8 2014.
- [82] R. Broda, T. Pawłat, W. Królas, R. V. F. Janssens, S. Zhu, W. B. Walters, B. Fornal, C. J. Chiara, M. P. Carpenter, N. Hoteling, L. W. Iskra, F. G. Kondev, T. Lauritsen,

- D. Seweryniak, I. Stefanescu, X. Wang, and J. Wrzesiński. Spectroscopic study of the $^{64,66,68}\text{Ni}$ isotopes populated in $^{64}\text{Ni} + ^{238}\text{U}$ collisions. *Phys. Rev. C*, 86:064312, Dec 2012.
- [83] R. Broda, B. Fornal, W. Królas, T. Pawłat, D. Bazzacco, S. Lunardi, C. Rossi-Alvarez, R. Menegazzo, G. de Angelis, P. Bednarczyk, J. Rico, D. De Acuña, P. J. Daly, R. H. Mayer, M. Sferrazza, H. Grawe, K. H. Maier, and R. Schubart. $n = 40$ neutron subshell closure in the ^{68}Ni nucleus. *Phys. Rev. Lett.*, 74:868–871, Feb 1995.
- [84] E. Runte, K.L. Gippert, W.D. Schmidt-Ott, P. Tidemand-Petersson, L. Ziegeler, R. Kirchner, O. Klepper, P.O. Larsson, E. Roeckl, D. Schardt, N. Kaffrell, P. Peuser, M. Bernas, P. Dessagne, M. Langevin, and K. Rykaczewski. Decay studies of neutron-rich isotopes of manganese, iron, cobalt, nickel, copper and zinc. *Nuclear Physics A*, 441(2):237 – 260, 1985.